THE EFFECTS OF STEP EXCRESCENCES ON SWEPT-WING BOUNDARY-LAYER TRANSITION

A Dissertation

by

GLEN T. DUNCAN JR.

Submitted to the Office of Graduate and Professional Studies of
Texas A&M University
in partial fulfillment of the requirements for the degree of

DOCTOR OF PHILOSOPHY

Chair of Committee,	William S. Saric
Committee Members,	Helen L. Reed
	Edward B. White
	David A. Staack
Head of Department,	Rodney D. W. Bowersox

August 2014

Major Subject: Aerospace Engineering

ABSTRACT

The immense fuel savings and environmental benefits of reducing aircraft skin-friction drag through laminar flow is well known. However, obtaining substantial laminar flow on an aircraft in an operational environment has proven to be a difficult challenge due to surface imperfections (e.g. 2-D steps and gaps, surface roughness, bug-strikes, paint chips, etc.). One controllable imperfection is a 2-D step through requiring certain manufacturing tolerances between adjacent wing panels. Current methods for designing a laminar-flow aircraft require designing and manufacturing with overly-restrictive tolerances obtained from unswept flat-plate experiments. This research aims at giving designers more realistic manufacturing tolerances for a typical, swept-wing transport aircraft.

A 30° swept-wing model with a movable leading-edge extending to x/c = 0.15 is used in the flight environment and in a low-disturbance wind-tunnel to study the effect of 2-D step excrescences in a three-dimensional boundary layer. Forward- and aft-facing steps are modulated during the tests. The design of the test article and the internal actuation system is documented in detail. A structural and safety analysis is provided for the flight testing on a Cessna O-2A Skymaster. A flutter and handling-quality clearance flight proved the new test article is safe for the flight-testing experiments.

Pressure measurements are compared with computational results, infrared thermography is used to globally detect boundary-layer transition, and hotwire measurements provide details of the boundary-layer profiles in the vicinity of the steps. An analysis of the results is provided including comparisons of both the wind tunnel and flight environment, and from experimental studies of an unswept model of similar 2-D pressure gradient.

The crossflow instability is believed to dominate the transition process up to the critical step height, while the shear-layer instability dominates after the critical step height. The critical step height was found to be a function of unit Reynolds number. Also, the addition of leading-edge sweep with a similar 2-D pressure gradient substantially lowers the local Reynolds-based critical step height for forward-facing steps,

while it is similar for the aft-facing steps. However, a substantial increase in the conventional laminar-flow tolerances can be made confidently if a favorable pressure gradient is implemented.

DEDICATION

This work is dedicated to my loving parents Joan and Glen Duncan.

ACKNOWLEDGEMENTS

The presented research would not be possible without the help of many people throughout my time as an undergraduate and graduate student at Texas A&M University. I would first like to acknowledge that the funding for this effort was provided by Air Force Research Laboratories (AFRL) at Wright-Patterson Air Force Base through General Dynamics IT and by Northrop Grumman Corporation (NGC). Our program managers, Gary Dale and Juan Martinez, were supportive and helpful throughout the review board process for the flight experiment, and they set up technical meetings with other research groups. I would also like to thank NGC for giving our research team access to their experiments and for sharing their pre-publication data on their two-dimensional work. I have benefited from all of the technical meetings with AFRL and NGC by sharing research knowledge and strategies.

I first became involved in research during my undergraduate career at Texas A&M University under the supervision of Dr. Rodney Bowersox at the National Aerothermochemistry Laboratory. I would like to thank him for the research opportunity, the guidance of my research efforts, and the assistance during the application process for graduate school. I probably would not have continued my educational career to graduate school without the recommendation of Dr. Bowersox to my graduate advisor, Dr. William Saric.

I would like to thank Dr. William Saric for the opportunity to work under his supervision during my graduate career at both the Flight Research Laboratory and Klebanoff-Saric Wind Tunnel. He holds his students to a high standard in both academics and research, and I have greatly benefitted from his persistence for excellence. He consistently taught me to always keep the fine details of the research problem in mind, and encouraged me to work hard throughout my career. I'd also like to thank my committee members Dr. Helen Reed, Dr. Edward White, and Dr. David Staack for their guidance and support throughout the course of this research. They have frequently provided me with suggestions for improving the presented research. I would also like to thank Colleen Leatherman and Rebecca Mariano for handling all of the logistics for our research team.

Throughout the design and testing of the presented research, there have been several undergraduate and graduate students involved that I would like to thank. First, my partner in this research effort is Brian Crawford. His knowledge of electrical circuitry, instrumentation and programming have been crucial in the development of this project. David West also contributed to the success of the experiment; his attention to details and hard work throughout all stages of the project have been beneficial. Matthew Tufts is our main computationalist on the team and the CFD solutions for the project were performed by him. I'd like to also acknowledge the students that graduated and offered advice and assistance during the design of the test article: Simon Hedderman, Dr. Lauren Hunt, Thomas Williams, and Joshua Fanning. Ian Neel and Kristin Ehrhardt are undergraduates who also had important roles in this research

The flight testing aspect of this research would obviously not be possible without our test pilots Lee Denham, Lt Col Aaron Tucker, and Dr. Celine Kluzek. I appreciate them sharing their technical knowledge on flight testing, and keeping our flight team safe as we performed our experiments. I would like to acknowledge the efforts of our A&P mechanic Cecil Rhodes who has consistently maintained the aircraft to be in a safe and flyable condition for our flight team. I'd also like to thank the ground crew and co-pilot assistance provided by Brian Crawford, David West, Ian Neel, Matthew Tufts, Alex Craig, Jacob Cooper, Matthew Kuester, Bobby Ehrmann and Kristin Ehrhardt.

The assistance in the wind tunnel of the recently graduated students Dr. Rob Downs and Dr. Matthew Kuester in the wind tunnel is much appreciated. Dr. Downs helped with the earlier development of the mounting-bracket design inside the wind tunnel and assisted during the first wind tunnel campaign. Dr. Kuester was very flexible with sharing the wind tunnel's usage during the second wind tunnel campaign; he also provided assistance for our experiment throughout the entire campaign.

Finally, a huge thanks to my friends and family for their constant support throughout my educational career and making my time at Texas A&M University a great experience. I will cherish the weekly dinners I had with my wonderful sister, Lindsey, while she was at Texas A&M. I cannot thank my mother, Joan, and father, Glen, enough for their continual support and encouragement. My educational career at Texas A&M University would not be possible without them.

NOMENCLATURE

A	total disturbance amplitude
A_o	reference total disturbance amplitude, baseline at x/c = 0.05
ASU UWT	Arizona State University Unsteady Wind Tunnel
c	chord length, 1.372 m
crit	critical step height (typically used as a subscript)
$C\_$	5HP calibration coefficient of the subscript
$C_{p,3D}$	coefficient of pressure
$C_{p,2D}$	coefficient of pressure referenced normal-to-the-leading-edge, $[C_{p,3D}/\cos^2(\Lambda)]$
$C_{p,x}$	pressure-coefficient gradient against dimensional streamwise distance
CG	center of gravity
DAQ	data acquisition
DTC	digital temperature compensation
DREs	spanwise, periodic discrete roughness elements
EMI	electromagnetic interference
5HP	five-hole probe
FOS	factor of safety
FOS_c	component factor of safety (company rated forces compared to externally applied forces)
FOS_p	factor of safety to proof load
FOS_y	factor of safety to yield
FTE	flight-test engineer
I_{yy}	pitch moment of inertia
IR	infrared
ID	inner diameter

k	step height, forward-facing (+), aft-facing (-)
KIAS	knots indicated airspeed
KSWT	Klebanoff-Saric Wind Tunnel (Texas A&M University)
LE	movable Leading-Edge part of SWIFTER
M	Mach number
MB	static Main Body of SWIFTER
MSL	mean sea level
n	number of oscillations (aircraft clearance flight)
N	experimental amplification factor
$N_{baseline}$	experimental amplification factor of baseline cases ($k = 0$)
NTS	non-test surface
OS	number of overshoots ($n = OS/2$)
PDF	probability density function
PID	proportional integral derivative (a type of controller)
PIO	pilot-induced oscillations
Pk-Pk	peak-to-peak
PSD	power spectral density
p_s	freestream static pressure
$p_{surface}$	surface pressure
p_{edge}	static pressure, boundary-layer edge
$p_{\#}$	5HP pressure measurement for a specific hole number
q	dynamic pressure
r	adiabatic recovery factor, ($0.72^{0.5}$)
R	ideal gas constant
RD	rudder deflection (aircraft clearance flight)
Re'	unit Reynolds number

Re_c	chord Reynolds number
$Re_{k\infty}$	step-height Reynolds number based on freestream quantities
Re_{kk}	step-height Reynolds number based on undisturbed boundary-layer quantities at the roughness height
$Re_{\theta,AL}$	attachment-line momentum-thickness Reynolds number
RMS	root mean square
RMSE	root-mean-square error
RPM/RPS	revolutions per minute/revolutions per second
RTD	Resistance temperature detector
SEM	standard error of the mean
SWIFT	Swept-Wing In-Flight Testing (test-article acronym)
SWIFTER	Swept-Wing In-Flight Testing Excrescence Research (test-article acronym)
s	span length of test article, 1.067 m
s_k	surface distance, up to location of the step
s_{tr}	surface distance, up to transition location
std	standard deviation of the measurement
TAMU FRL	Texas A&M University's Flight Research Laboratory
Tu	freestream turbulence intensity
T	temperature
T_{aw}	adiabatic wall temperature
TEC	thermoelectric cooler
T_{edge}	temperature at boundary-layer edge
T_∞	freestream temperature
T_k	temperature at step height k
T_s	aircraft settling time
TS	test surface

T-S	Tollmien-Schlichting, boundary-layer instability
u	streamwise steady velocity
u'	temporal unsteady velocity
u'_{rms}	temporal root-mean-square unsteady velocity
u_{FS}	measured velocity with freestream hotwire probe
u_k	leading-edge-normal, undisturbed velocity at step height k
$u_{mean,z}$	u velocity averaged along the z direction
$u_{rms,z}$	u velocity root-mean-square along the z direction
U	total velocity
U_{edge}	boundary-layer edge velocity
U_∞	freestream velocity
x, y, z	model-fixed coordinates: leading-edge normal, wall-normal, leading-edge-parallel root to tip
x_t, y_t, z_t	tangential coordinates to inviscid streamline
X, Y, Z	aircraft coordinates: roll axis (towards nose), pitch axis (towards starboard), yaw axis (towards bottom of aircraft)
x_k	streamwise location of the excrescence
x_{tr}	streamwise location of the transition location of the step height of interest
$x_{tr,baseline}$	streamwise location of the baseline (k = 0 μm) transition location
α	model angle of attack
α_{offset}	chord-line angle offset (5HP relative to test article)
β	aircraft sideslip angle
β_{offset}	yaw angle that the test-article is offset from the aircraft centerline
γ	ratio of specific heats (1.4)
δ_{99}	boundary-layer thickness at which $u/U_{edge} = 0.99$
δ_{99}	boundary-layer height at $0.99U_{edge}$

δ^*	boundary-layer displacement thickness
ζ	damping ratio
θ	boundary-layer momentum thickness
θ_{AC}	pitch angle of aircraft
$\theta_{AC,offset}$	aircraft-pitch angle offset (5HP relative to test article)
θ_T	dimensional temperature variable
Λ	leading-edge sweep angle
μ	dynamic viscosity
μ_k	dynamic viscosity, step height k
ν	kinematic viscosity
ν_{edge}	kinematic viscosity, edge of boundary layer
ν_k	kinematic viscosity, step height k
ρ_k	density at step height k
τ	moment in the aircraft coordinates (subscripts X, Y, Z)
φ	aircraft bank angle
ω_d	damped frequency
ω_n	natural frequency

TABLE OF CONTENTS

Page

LIST OF FIGURES

Page

LIST OF TABLES

Page

I. INTRODUCTION

This dissertation describes the experimental research on the effect of step excrescences, both forward- and aft-facing, on the extent of laminar-flow on a swept leading edge in both the flight and wind tunnel environment. These experiments were tied closely with computational efforts (Tufts *et al.* 2013 [1-2]) all working at Texas A&M University's Flight Research Laboratory (FRL) and Klebanoff-Saric Wind Tunnel (KSWT).

In this introduction, the motivation, literature review, and experimental objectives are presented. A new test article was designed and fabricated to fit the needs of this study in both flight and wind tunnel. The bulk of the project was dedicated to modeling, designing and testing in the more demanding flight environment. Thus, comprehensive sections of the model design, structural analysis, safety analysis, ground static-load tests and clearance flights are included in this dissertation. The experimental methods used both in the wind tunnel and flight environment are documented in detail. Then, the results from each environment is presented separately. Finally, the main results are summarized and concluding remarks are made.

A. Motivation

Extending laminar flow over an aircraft's surface has been known to provide a significant skin-friction drag reduction. Skin friction accounts for about 50% of the total drag budget of a transport aircraft (Arnal & Archambaud [3]). If laminar flow can be sustained over a large transport aircraft's wings, tail surfaces, and nacelles, an estimated 15% reduction in drag can be achieved ([3]). This drag reduction can potentially allow heavier payloads, increased range capability, and lower overall fuel costs. For example, a substantial fuel savings of 29% is estimated for a transport aircraft with 113,400 kg payload and 10,000 nautical mile range at Mach = 0.75 if laminar flow is sustained to $x/c = 0.60$ of the wing and tail ([4]). The fuel savings in the Air Force fleet and commercial aircraft is of the order of 10^9 dollars per year.

Laminar flow can be attained through both passive and active control techniques. Favorable pressure gradients can be implemented to stabilize the boundary layer (natural laminar flow). Bleeding the boundary layer off through suction near the leading edge is a viable option for maintaining laminar flow. Also,

spanwise-periodic, discrete roughness elements (DREs) on a swept wing have shown success in delaying boundary-layer transition in the wind tunnel (Saric *et al.* [5]) and flight environment (Carpenter *et al.* [6], Carpenter [7]). However, in an operational environment, laminar flow is difficult to preserve due to surface imperfections. These surface imperfections can be organized into two main groups: 3-D roughness and 2-D roughness. 3-D roughness can describe distributed roughness, like the inherent background roughness of a painted or polished surface, or can describe isolated or discrete roughness, like fastener heads, bug strikes, paint chips, and ice accretion near the leading edge. Roughness that is spanwise (i.e. parallel to leading edge) is called 2-D roughness such as steps and/or gaps between adjacent skin-panels.

For a swept wing, which is typical for most transport aircraft, it is well known that polishing the leading-edge region can produce more laminar flow than a painted surface (Radeztsky *et al.* [8], Carpenter *et al.* [6], Carpenter [7]). However, sustaining a pristine leading edge can be difficult in an operational environment and this becomes mainly a maintenance problem. Fastener heads can be designed to be near flush on the surface to minimize the 3-D disturbances. Bug-strikes, paint chips, and ice accretion are all mainly environmental effects, and several methods have been used to minimize these events. Routine washing of the aircraft can be employed to remove bug strikes, and while in flight, leading-edge wipers can been used to remove bug strikes. Quality-control technicians can maintain an unchipped paint surface through occasional paint touch ups. Lastly, weeping wings and pneumatic boots have proven to be effective at preventing and removing ice buildup. The remaining set of surface imperfections, steps and gaps, can be controlled by setting appropriate manufacturing tolerances. Forward- and aft-facing steps will be the focus of this dissertation.

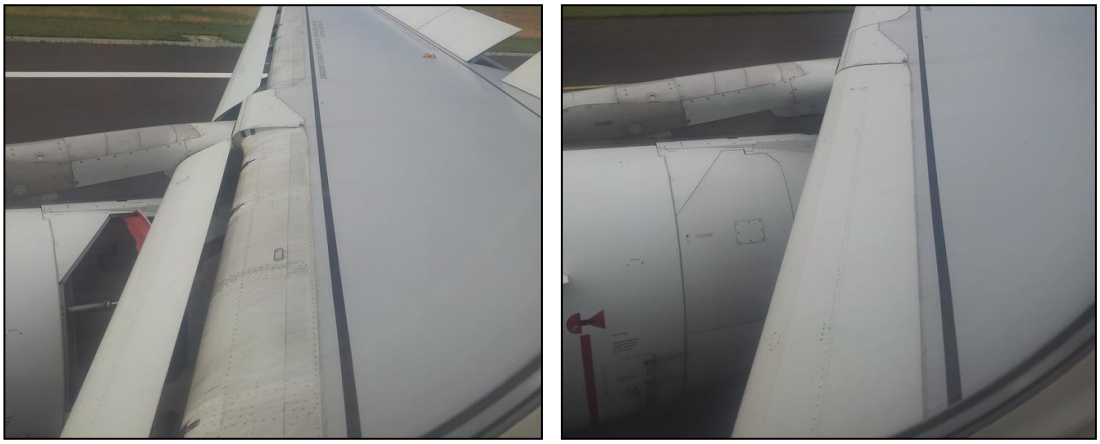

a) **b)**

Fig. 1 Airbus 319 leading-edge slats during landing, a) slats deployed, b) slats retracted

A typical transport aircraft has a critical, spanwise skin-panel interface approximately 0.1 to 0.2 m downstream of the leading edge (Drake *et al.* [9]). Two-dimensional steps and gaps are also inherent with the usage of leading-edge high-lift and anti-icing devices. A movable leading-edge slat interfacing with the static wing of an Airbus 319 is shown in Fig. 1; a potential site of a 2-D step and gap can be seen between the grey and white surfaces. Common design practice is to implement tight manufacturing tolerances, derived from flat-plate flow, on these skin-panels in an attempt to take advantage of the low-drag characteristics of laminar flow. Thus, these tight manufacturing tolerances cause manufacturing costs and fabrication time to increase. It is the goal of this work is to better understand the effect of 2-D steps on boundary-layer transition with the addition of a representative leading-edge sweep for a transport aircraft. When coupled with previous data of 2-D airfoil studies, a realistic database can eventually be established for excrescences near the leading edge of airfoils.

The appearance of steps and gaps typically occur near the leading edge in a region of accelerating flow, i.e. a favorable pressure gradient. For 2-D wings, the principal instability mechanism (Tollmien-Schlichting, T-S waves) is strongly attenuated. In the case of swept wings, the principal instability mechanism (crossflow waves) is amplified by the pressure gradient. Although this work builds on the 2-D work of NGC, keep in mind that the stability and breakdown processes may be fundamentally different.

B. Previous Experiments

Previous studies examining the effect of two-dimensional disturbances have almost exclusively focused on flat-plate flow (zero pressure gradient) as the canonical model for boundary-layers; linear stability theory can be applied for computational studies and relationships derived from the experiment can be easily resolved without having participating factors of pressure gradient or wall curvature. Since the ultimate application is an airfoil for aircraft, flat plates may deliver misleading results in the absence of pressure gradient and curvature. Moreover, it is imprudent to extrapolate flat-plate-derived tolerances to model pressure gradients, because pressure gradients are known to considerably affect boundary-layer transition. Investigations on specific airfoil designs can be performed, but this then can lead to limited results on that particular airfoil design.

During a technical experiment or application to aircraft design, scientists and engineers desire a confident condition in which the step height of the roughness begins to significantly influence the streamwise extent of boundary-layer transition. This condition is called the *critical roughness*, and several technical definitions have been implemented throughout the history of roughness research. The examination of critical roughness has been performed for quite some time; this review of previous experiments will only focus on research related to spanwise roughness.

One of the earlier experiments was in 1939 when Hood [10] studied how spanwise lapped joints (e.g. downward-sloped surface before a forward-facing step) affected the drag coefficient on an airfoil in the NACA high-speed wind tunnel. Tani & Hama [11] experimented with spanwise imperfections by placing different diameter cylindrical wires on the surface of a flat plate and airfoil in a wind tunnel; order of magnitude values for permissible roughness heights were documented. In 1943, Fage [12] investigated the effects of spanwise bulges (smooth hump), hollows (smooth dip), and ridges (forward-facing step followed directly by aft-facing step) on the transition location on a flat plate and a symmetric airfoil in a wind tunnel environment and created criteria for critical heights for the imperfections. Correlations were made that include the width (streamwise length) of the spanwise excrescences. Fage claimed that the shape of the excrescence does not have a major impact on the critical height. In 1946, Loftin [13] simulated the effect of spanwise, butt joints by creating a groove with a certain depth and width on a ‘low drag’ airfoil in the wind

tunnel environment. Smith & Clutter [14] performed experiments with spanwise cylindrical wires on a flat plate in a low-speed and high-speed wind tunnel. For the flat-plate experiment, it was claimed that 2-D roughness was the most sensitive with the smallest critical roughness-height Reynolds number ($Re_{kk,crit}$) compared to 3-D discrete discs and surface roughness. $Re_{kk,crit}$ is based on the undisturbed velocity at the roughness height (not freestream conditions). Also, Smith and Clutter stated that the pressure gradient, turbulence intensity, and location of roughness are minor effects on the $Re_{kk,crit}$. In 1972, Klebanoff & Tidstrom [15] performed a flat-plate experiment with 2-D circular roughness applied to the surface in a low-disturbance wind tunnel; they stated that the basic mechanism of 2-D roughness-induced transition is through the "destabilizing influence of the flow in the recovery zone on the existing disturbances which hastens the downstream development of the instability." They acknowledged that this stability-governed phenomenon is for smaller roughness heights, and that larger heights, which could be typical of a transport aircraft, would be governed by a shear-layer instability.

It is important to note that most of the previous experiments listed include spanwise roughness that has a forward-facing step followed by an aft-facing step (i.e. ridge); this type of spanwise roughness is not typical for a wing on a transport aircraft. The more practical spanwise surface imperfections in need of examination for a transport aircraft are separate forward- and aft-facing steps. Up to 1985, Holmes & Obara [16] reported that there did not exist step-height criteria for a wing with leading-edge sweep. They also disproved Fage's conclusions that the roughness shape did not affect the critical roughness through a series of flight tests with the X-21 and T-34C; they showed that a rounded edge of a forward-facing step, instead of sharp edge, allowed a significantly larger step height. It is believed that Fage's ridges created a separated region both forward and aft of the step and was dominated by a shear-layer instability; the rounded edge of the forward-facing step reduces the extent of the precarious separated region aft of the step.

More recently, Zuniga *et al.* [17] performed flight experiments at transonic conditions studying three combinations of gap and step effects on transition for a laminar flow, unswept model using a F-104G aircraft. Drake *et al.* (1996) [9] expanded on the configuration range from the previously mentioned F-104G experiment; however, these unswept experiments are difficult to compare to research of single steps due to the combination of both a step and gap. In 1999, Radeztsky *et al.* [8] concisely explored the effect of 2-D

roughness on an airfoil with leading-edge sweep in a low-disturbance wind tunnel. It was shown that the crossflow instability was insensitive to 2-D roughness for small roughness heights (<100 μm); but, the maximum roughness height was approximately 20% of the displacement thickness. Actual roughness heights from skin joints on transport aircraft could be much larger.

In 2005, Wang & Gaster [18] created a useful correlation to predict the transition location for both forward- and aft-facing steps on an unswept flat plate; the correlation is based on the differences in the instability amplification factor with and without a step. Similarly to Wang & Gaster, Crouch *et al.* [19] created a similar correlation model, but took into account the effect of a favorable and adverse pressure gradient.

Northrop Grumman Corporation (NGC) - Bender *et al.* (2007, 2013) [20-21], Drake & Bender (2009) [22], and Drake *et al.* (2008, 2010) [23-24] has extensively studied, in a low-disturbance environment, the effects of step height on transition for a flat plate including a pressure gradient and wedges. It was shown that a favorable pressure gradient, which is usually present on laminar-flow wings, can possibly relax the manufacturing tolerances of outer panels. However, in order to complete the knowledge of 2-D excrescence effects on transition, the effects of sweep need to be studied. A goal of the present work is to compare a swept-wing experiment directly to NGC's recent unswept studies and understand the effect of leading-edge sweep.

C. Boundary-Layer Instabilities and Swept-Wing Boundary-Layers

It is important to understand the different boundary-layer instability mechanisms that lead to boundary-layer transition for unswept and swept wings. Extrapolating data from 2-D to 3-D boundary layers on a swept-wing may lead to misleading results because of the differences in instability mechanisms. Two-dimensional airfoils are primarily subject to Tollmien-Schlichting (T-S) (streamwise) instabilities which are stabilized by accelerating (favorable) pressure gradients. On the other hand, swept-wings are affected by streamwise, crossflow, attachment-line, and centrifugal (Görtler) instabilities, as shown in Saric *et al.* [25] and Saric [26]. Acoustic disturbances and 2-D roughness significantly affect the streamwise instability. On the other hand, crossflow is sensitive to 3-D roughness and freestream turbulence (Reed & Saric [27] and

Saric *et al.* [25]) and is destabilized by an accelerating pressure gradient. Attachment-line and centrifugal instabilities can be controlled by specific geometric requirements on the model.

The crossflow instability is inherent with swept-wings and can be isolated and studied specifically if the other three instabilities are stabilized. Due to the focus of the present experiment, additional details of the crossflow instability will be documented. The crossflow instability was first discovered by Gray in 1952 [28]; streamwise streaks were observed using flow visualization techniques. These streaks are stationary vortical structures that are in line with the inviscid streamlines. Another major notable is that the streamlines are curved, as shown in Fig. 2, due to the leading-edge sweep and favorable pressure gradient. As the velocity reduces to zero at the wall within the boundary layer, the pressure gradient remains constant which causes a velocity component perpendicular to the local inviscid streamline; this velocity component is called crossflow. A schematic of the crossflow profile with the tangential, crossflow and total velocity components are shown in Fig. 3.

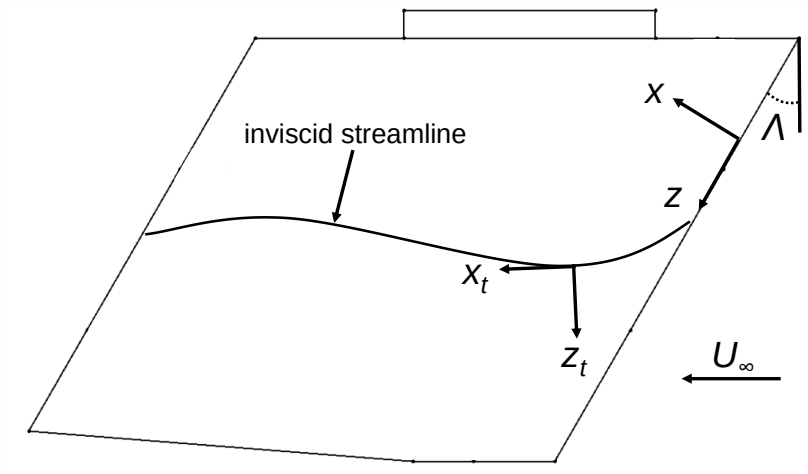

Fig. 2 Inviscid streamline over swept wing with model fixed coordinates (*x, y, z*) and tangential coordinates (x_t, y_t, z_t)

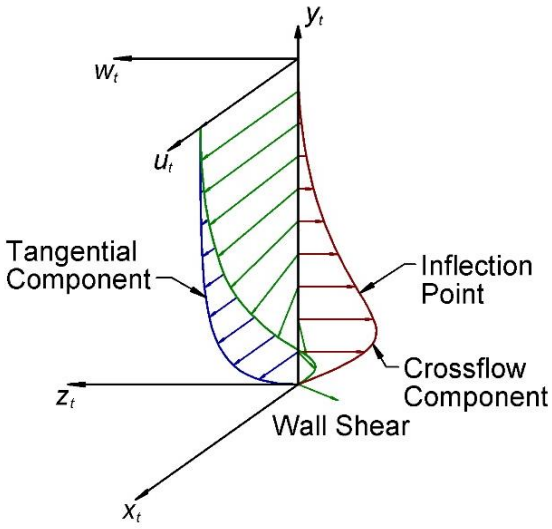

Fig. 3 Crossflow boundary-layer profile (Roberts [29])

The co-rotating vortical structure causes a periodic high and low wall shear stress; this is typically called crossflow streaking. These vortices can either be stationary or traveling waves, and transition is usually caused by either (not both). It is well known that boundary-layer transition studies require an acute attention to disturbances (freestream and surface roughness), especially analyzing the crossflow instability. Deyhle & Bippes [30] stated that when the combined freestream fluctuations are greater than a turbulence intensity, Tu = 0.2%, the crossflow instability becomes dominated by traveling waves instead of stationary waves. However, White *et al.* [31] proved that it is not this straightforward; stationary waves were observed with a Tu = 0.3% with a highly polished leading edge. The final application of this research, the flight environment, has low freestream disturbance levels, and therefore will most likely be dominated by stationary waves. Thus, it is necessary to utilize an experimental test facility that will guarantee that stationary crossflow waves will dominate the transition process; a low-disturbance wind tunnel and the flight environment will be utilized for the present experiment.

Most research on crossflow-dominated applications pays particular attention to 3-D roughness, and simply avoids 2-D roughness as it generally has little effect. While this is true for small 2-D roughness, real aircraft have many fairly large and difficult-to-avoid 2-D excrescences. In order to make laminar flow on

transport-class aircraft viable, additional research is needed to extend the progress made by NGC on unswept wedges to swept wings due to the possible interaction between crossflow waves and these large 2-D disturbances. Whereas the dominant instability (T-S) is stabilized in the unswept wedge, in the swept case the dominant instability (crossflow) is destabilized by the pressure gradient.

D. Experimental Objectives

The present research has the following objectives.

1. A test article will be designed to examine the effect of 2-D excrescences on a swept-wing model with capabilities for both flight and wind tunnel testing. Flight testing is favorable due to the directly-applicable transport unit Reynolds numbers and the disturbance environment in the experiment will match with that used in practice. The wind tunnel testing provides opportunities for detailed boundary-layer measurements.
2. Prior to flight testing with the new test article, a structural and displacement analysis will be performed alongside a detailed flight-safety analysis. Also, a series of static-load tests will proof the test article for the loads experienced in the flight environment and provide confidence to the structural analysis computations. Finally, flutter and handling-quality checks will clear the operational envelope for flight experimentation of the test article.
3. The critical step height for both forward- and aft-facing steps for swept-wing transition will be quantified for various freestream unit Reynolds numbers. A comparison will be made to the recent unswept work of NGC when the 2-D pressure gradient (normal to the leading edge) is similar, and the effect of leading-edge sweep will be quantified.
4. The interaction of a 2-D excrescence in a swept-wing boundary layer with a favorable pressure gradient will be analyzed through the measurement of streamwise, boundary-layer, velocity profiles upstream and downstream of the excrescence. These data will provide a detailed database for future computational validation.

II. EXPERIMENTAL CONFIGURATION AND DESIGN

Boundary-layer stability and transition experiments require a large attention to detail. Unintended problems in an experiment can manifest through the experimental facility or the test article used. For example, a conventional tunnel (i.e. tunnel with large velocity fluctuations) can provide misleading results for a crossflow experiment, with its high sensitivity to vortical disturbances. Also, model design is especially important to isolate the principle research problem currently being studied, and the test article obviously needs to be able to perform its function properly at all conditions in the experimental facility's environment.

The experimental model design is documented and compared to a similar previous experimental model. The experimental facilities are introduced and the integration with the model is detailed. At the maximum loading scenario of the test article, structural and displacement analyses are performed in order to ensure the safety and success of the experiment. As a final preparation for the beginning of the experiment, a series of static-load tests are cataloged and they provide confidence in the computations of the safety analysis.

A. Model Design

A versatile, efficient test article was desired to fit the needs of this excrescence research. The flight environment was crucial in order to provide low-disturbance, transport unit Reynolds numbers ($Re´$ = 4.00-5.50 x 10^6/m). Also, the wind-tunnel environment was important to provide fine details within the boundary layer, by the use of hotwire anemometry. A swept-wing model was developed to be capable of utilizing both of these environments. Configuration changes (i.e. step heights) were designed to be as quick as possible to maximize productivity. As a consequence, an internal actuator system was developed to provide accurate, rapid excrescence changes while in-flight and wind-on in the wind tunnel. Finally, a time-efficient method for creating a necessary temperature differential for the usage of IR thermography was developed into the model design.

The Swept-Wing In-Flight Testing Excrescence Research (SWIFTER) model was designed and fabricated for this excrescence research (shown in Fig. 4b); Advanced Technologies of Newport News, Virginia is the fabricator. In order to be applicable to most transport aircraft, the leading-edge sweep was chosen to be 30°. It is a natural-laminar-flow airfoil design; T-S waves are stabilized by a favorable pressure

gradient extending to x/c = 0.70. Görtler vortices are precluded by avoiding concave curvature forward of x/c = 0.70. Attachment-line instability and leading-edge contamination are both prevented by having an attachment-line momentum-thickness Reynolds number, $Re_{\theta,AL}$, smaller than the critical value of approximately 100 [32]: SWIFTER's maximum $Re_{\theta,AL}$ is approximately 80. Also in addition to the low $Re_{\theta,AL}$, the model has a free root end, not attached to turbulent boundary layers, to prevent leading-edge contamination in the flight environment. Thus, the crossflow instability is isolated and studied specifically with this model.

SWIFTER was derived from a previous swept-wing flight model, SWIFT, that successfully delayed crossflow dominated transition to turbulence using spanwise-periodic discrete roughness elements (Carpenter *et al.* [6], Carpenter [7]). It was decided that the same outer mold line (OML) as SWIFT would be used for the SWIFTER model with a chord of 1.372 m and a span of 1.067 m. This was beneficial due to the fact that the airfoil's pressure distribution and boundary-layer stability characteristics had been extensively studied (over seven years of experience), and the airfoil had been used for well over 700+ flight tests without a mishap. However, there were several improvements implemented on SWIFTER through the lessons learned and experienced gained with the SWIFT flight tests.

SWIFTER and SWIFT Structural Comparison

One of the first observable exterior changes made to SWIFTER was the addition of a midspan strut on the non-test side, as shown in Fig. 4. This midspan strut was added to minimize the relative displacements of the movable leading-edge part to the static test-surface part in the test region (centered around midspan). The forward regions of both the test and non-test side parts have a thicker wall in order to also minimize these relative displacements, as shown in Fig. 5ab. SWIFT's pylon mount assembly had the capability of adjusting the aircraft beta offset from centerline, β_{offset}, and it was decided that this angle adjustment was not necessary for SWIFTER due to the added complexity and the fact that the β_{offset} was never changed during the SWIFT campaign. In order to allow this angle adjustment, SWIFT's strut assembly had ball joints on the ends. Since SWIFTER did not have this angle adjustment, these ball joints were removed and replaced with rigid aluminum parts.

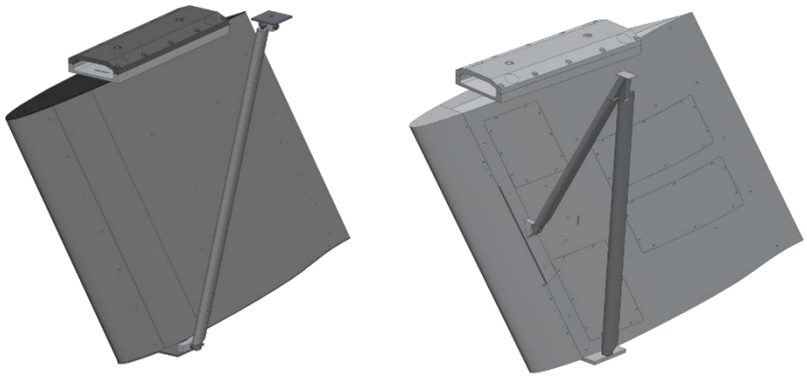

a) **b)**

Fig. 4 Test article comparison (non-test side view), a) SWIFT, b) SWIFTER

Another exterior change implemented on SWIFTER is the addition of non-test side access panels. During SWIFT flight operations, if instrumentation had to be adjusted or replaced inside the test article, the entire model had to be removed from the aircraft. Removal and re-install of SWIFT could take up to a full day to complete, while removal and re-install inside the wind tunnel could take up to two days. These easily removable panels allow access to all components inside the model and significantly improved both the flight and wind tunnel experiment's efficiency.

A main design change is the character and thickness of the wall of the test article. SWIFT has a stepped internal structure, in contrast to an ideal uniform wall thickness: a stepped structure was chosen because a uniform wall thickness results in increased fabrication complexity, time, and cost. The minimum wall thickness of SWIFT is 4.76 mm (0.188") and has areas up to 9.53 mm (0.375"). Thus, this lead to a significant weight increase and an overdesigned test article. SWIFT's designer portrayed that this overdesigned test article was due to time constraints, and a thinner wall could have still met the minimum factor of safety requirements for flight testing (McKnight [33]). Approximately 6 years later with improvements in fabrication processes and machines, it was decided that SWIFTER would have a uniform wall thickness of 3.18 mm (0.125") after consultation with the same fabricator. It was proved through structural analysis that the internal ribs and spar used inside SWIFT were not needed. However, the internal actuation system for SWIFTER required a much thicker forward region for both the test and non-test sides,

as shown in Fig. 5. The previously mentioned modifications to the test and non-test side parts lead to mass reduction of approximately 12.7 kg. Also, it was decided that the steel plates, on the root and tip of the airfoil, would be removed for the SWIFTER model. They simply acted as another fastening point for the two halves of the airfoil, but proved to be unnecessary. These steel plates had a combined mass of 5.9 kg. Thus, these airfoil structure modifications resulted in a total mass reduction from SWIFT to SWIFTER of approximately 18.6 kg. This significant weight decrease in the airfoil structure facilitated the design of the internal actuation system.

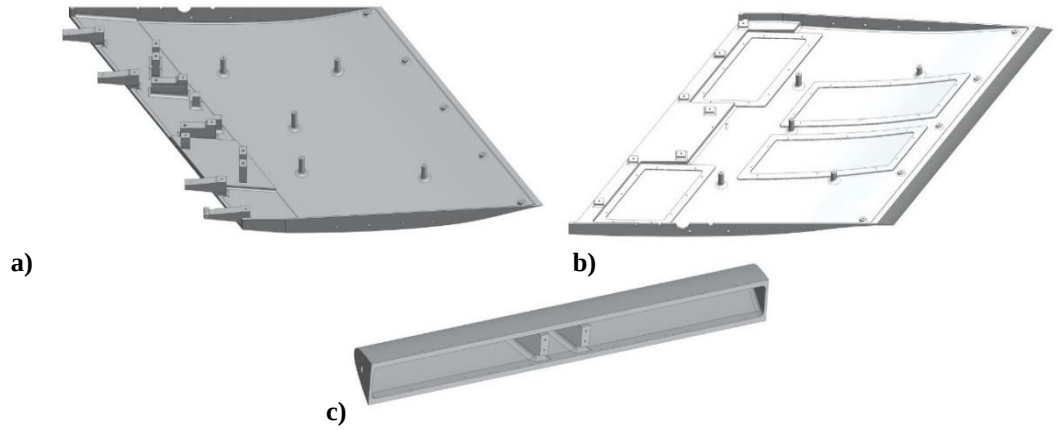

Fig. 5 Internal structure of SWIFTER, a) test side part, b) non-test side part, c) leading-edge part

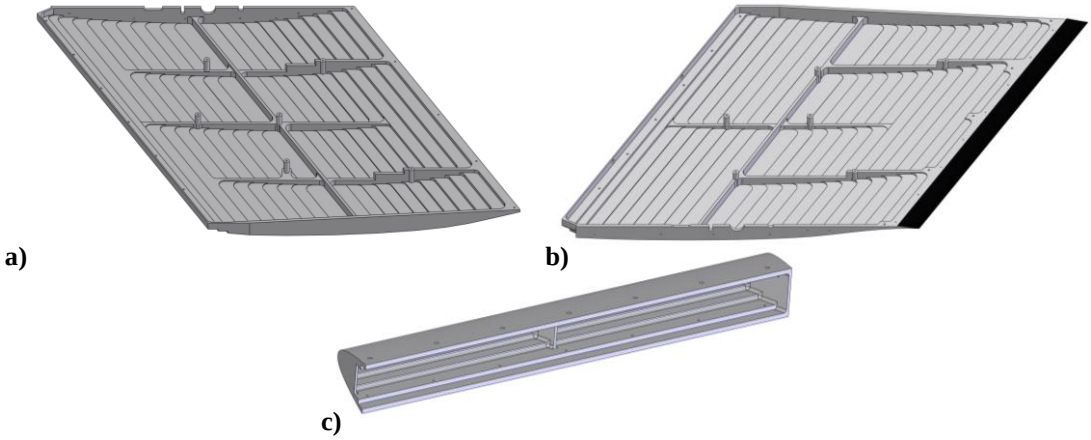

Fig. 6 Internal structure of SWIFT, a) test side part, b) non-test side part, c) leading-edge part

Internal Actuation System

There are several methods to create a forward- and aft-facing step at a specific streamwise location on a swept wing. One obvious method that can be implemented with swept-wing models is applying a thin sheet over the surface of the model. In-house experiments in the wind tunnel proved that this method is laborious and unreliable. It was difficult to maintain a low step-height uncertainty and prevent a wavy surface. Another potential method is to apply a shim at the mounting interface of the leading edge and main body assembly. This shim method has safety advantages for flight due to its static design, but limits the flight experiment to only one step height per flight. Also, depending on the number of step configurations planned and acceptable step-height uncertainties, the manufacturing of the shims can be costly. After comparing similar excrescence studies, the goal of the present experiment was to have less than or equal to ±25 μm step-height uncertainty across the entire span of the model. Lastly, an internal actuation system can be implemented to create a movable step-height interface. Depending on the actuator design, step heights can be modulated to less than 1 μm increments and configuration changes can be executed while in flight or wind-on in the wind tunnel. However, this movable design has additional challenges to prove safety of flight and it requires additional software and electrical support. The internal actuation system was selected for this present experiment, and the design accommodations and challenges will be discussed.

The internal actuation system had several design requirements: (1) low weight, (2) capability of supporting the leading-edge lift loads, (3) small enough to fit inside the airfoil structure, and (4) step-height uncertainty of 25 μm or better. A systems-engineering approach had to be used to incorporate several commercially made components into the aluminum structure. A holistic view of the structural, electrical, and operational impacts of the model had to be considered at all times. For example, it was easy to find a motor that would be capable of supporting the leading-edge lift loads, but they were typically larger motors that couldn't fit inside the model. To further complicate matters, most motors that produced enough force didn't have the fine resolution that this research demands. An overview of the actuation system will be first described and then details about each component will be documented.

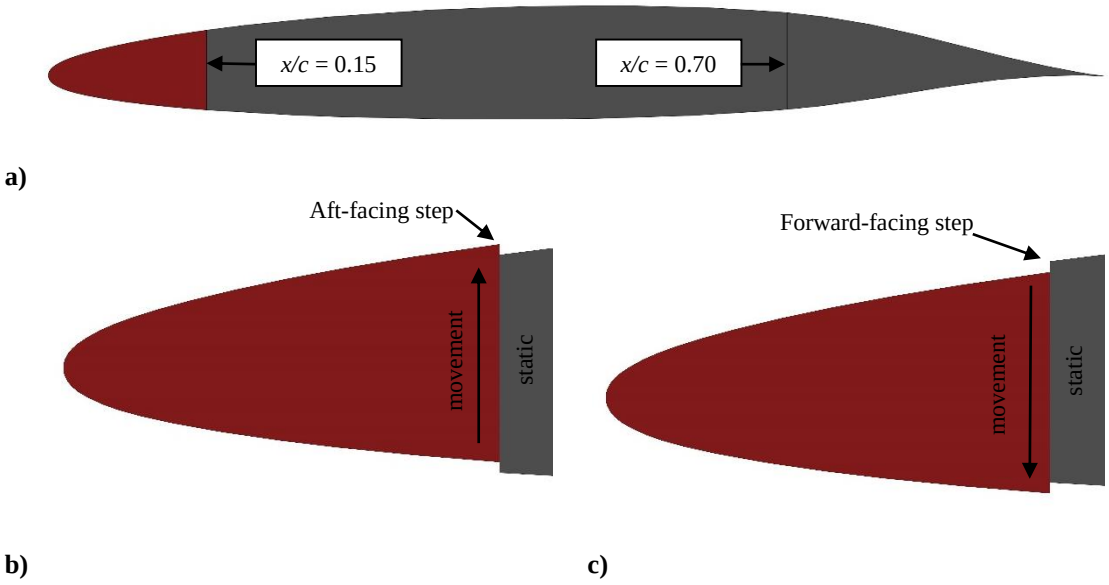

Fig. 7 Movable leading-edge schematic, a) SWIFTER airfoil with movable leading-edge highlighted maroon, excrescences located at *x/c* = 0.15, pressure minimum located at *x/c* = 0.70, b) aft-facing step motion, b) forward-facing step motion

SWIFTER has a separate movable leading-edge part (maroon part in Fig. 7), which is capable of two-dimensional movements through the internal actuation system: chordwise movements to produce gaps up to 20 mm normal to the leading edge and chord-plane-normal movements to produce ±5 mm steps. These excrescences are located at *x/c* = 0.15. The previously mentioned internal actuation system is shown in Fig. 8. There are a total of six internal linear actuators: four provide the step movements and two provide the gap movements. A pair of precision alignment shafts and linear sleeve bearings are used to ensure proper alignment of the leading-edge part and the rail guide assembly attached to the rest of the model. Configuration changes are initiated with gapping the movable leading edge forward by 500 μm (leading-edge-normal direction): this is to avoid binding of the two interfacing parts. The step-direction linear actuators are then engaged to produce the desired step height, as shown in Fig. 7bc. Lastly, the gap-direction linear actuators pull the leading-edge part back to seal the gap. All movements are controlled remotely via a control panel on the data-acquisition computer.

All lead screws and alignment shafts have mechanical locks to prevent them from unthreading due to vibration; this is important in the flight environment. The gap-direction lead screws have a nut that is

tightened against the part with the threaded hole. The step-direction lead screws and alignment shafts were fabricated with a rectangular end protruding outside the non-test surface. An exterior plate is fastened to the non-test side of the leading-edge part and it also has three rectangular holes. These holes line up with the protruding rectangular ends of the lead screws and shafts and prevent them from unthreading from the leading-edge part.

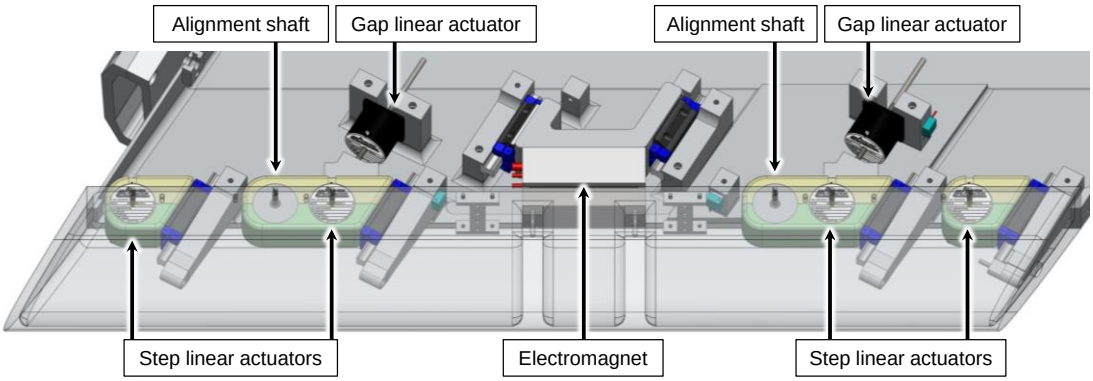

Fig. 8 Movable leading-edge actuation system (pressure side removed and movable leading edge transparent)

The main component of the internal actuator system is the linear actuator used to displace the leading edge in the step and gap direction. The 23A102A linear actuator stepper motor from Anaheim Automation was selected (shown in Fig. 9).

Fig. 9 23A102A linear actuator stepper motor from Anaheim Automation ([34])

The ¼-20 acme lead screw passes through the entire actuator housing; thus, this enables adjustable lead-screw length to fit any configuration. It is capable of producing an axial force of 450 N (100 lb) while traversing, mass of 0.5 kg, and the motor unit is only 51 mm (2.0”) tall (the maximum clearance is 76 mm, 3.0” inside the model). The axial travel per step is 6.4 μm and can be microstepped with a resolution of 0.8 μm (8 microsteps). The operating temperature range is from -20 °C to 50 °C, which is well beyond the temperature range needed.

The linear rail guides enable precision alignment and support of the leading-edge assembly as it translates in the chordwise direction. The 511U20B1 and 511H20D0 linear rail guides from Thomson were selected (shown in Fig. 10ab).

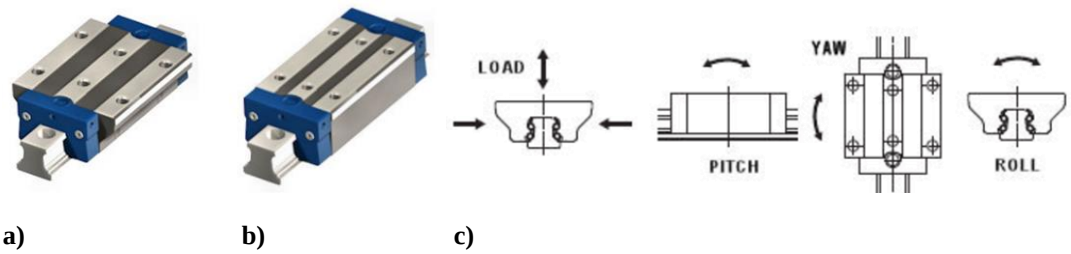

a) **b)** **c)**

Fig. 10 Linear rail guides from Thomson ([35]), a) 511U20B1 model (electromagnet), b) 511H20D0 model (actuation system), c) schematic for maximum rated loads and moments

Two different rail guides were used inside SWIFTER: the wide carriage model was used for mounting to the electromagnet aluminum block and the narrow carriage model was used to fit inside the leading edge. They both have identical rated loads and moments. The ratings for the dynamic load, pitch, yaw, and roll are 17,400 N (3,911 lb), 207 N·m (153 lb·ft), 207 N·m (153 lb·ft), and 205 N·m (151 lb·ft), respectively (illustrated in Fig. 10c). The static-load ratings are more than two times the dynamic ratings. The dynamic ratings are used in the component factor of safety analysis (see Structural and Displacement Analysis section), which enables the opportunity to change step configurations at the highest loading configuration in flight. The approximate weight of each rail and carriage system is approximately 2.5 lb. The rail material, AISI 52100 chrome alloy steel, has high stiffness and yield strength.

An electromagnet (Fig. 11), located at midspan (Fig. 8), is used to provide an additional locking mechanism of the movable leading part relative to the main body. The electromagnet is mounted to an aluminum block with carriages on each side. The carriages allow the electromagnet system to translate in the leading-edge-normal direction. This provides the opportunity to still use the electromagnet for different gap studies at $x/c = 0.15$ (gap studies are left to future experimenters). Lead screws and nuts are used to lock the gap movement of the electromagnet system through the two mounting columns aft of the electromagnet system. For the maximum pulling force, per manufacturer specifications, at least a 25 mm (1.0") thick low-carbon steel block must be used in conjunction with the electromagnet. This 25 mm (1.0") block is bolted to the inside of the leading-edge part.

Fig. 11 EM-3060-24C rectangular electromagnet from AEC Magnetics ([36])

The rated pulling force of this electromagnet is 6,700 N (1,500 lb) with the full magnetic face (76 mm x 152 mm, 3.0" x 6.0") touching the steel block. SWIFTER's design only allowed $^2/_3$ of the area to be touching the steel block, due to the limited internal thickness. After consultations with the manufacturer on this matter, the pulling force would only be able to support 4,500 N (1,000 lb) ($^2/_3$ of the maximum), and 1,100 N (250 lb) of shearing load (static frictional coefficient of 0.25). The electromagnet's mass is 4.1 kg and the steel block's mass is 1.4 kg.

In order to measure and monitor the step height and gap displacement during experimentation, a set of displacement sensors were incorporated into the design of the internal actuation system. If stepper motors are overloaded, they have the potential to stall and not actuate. The displacement sensors provide a stall detection technique. Two sensors are used for the step height in order to provide a spanwise uniformity

check and one gap sensor is used for the gap direction, as shown in Fig. 12a. The combination of small volume, low repeatability (order 10 μm or less), and measurement range greater than 25 mm (1.0") eliminated most displacement sensor possibilities. The ZX-PA series, analog position transducer (i.e. stringpot) from UniMeasure was selected for the displacement sensor (Fig. 12b). The stringpot has a flexible cable, in contrast to a rigid rod, which enables the usage for measurement of the moving leading-edge assembly relative to the static main body (the stringpot is mounted on the static main body). When the leading-edge part produces a gap, the cable flexes in this gap direction; thus, Pythagorean theorem needs to be used (knowing the gap displacement) to output a step height at all times.

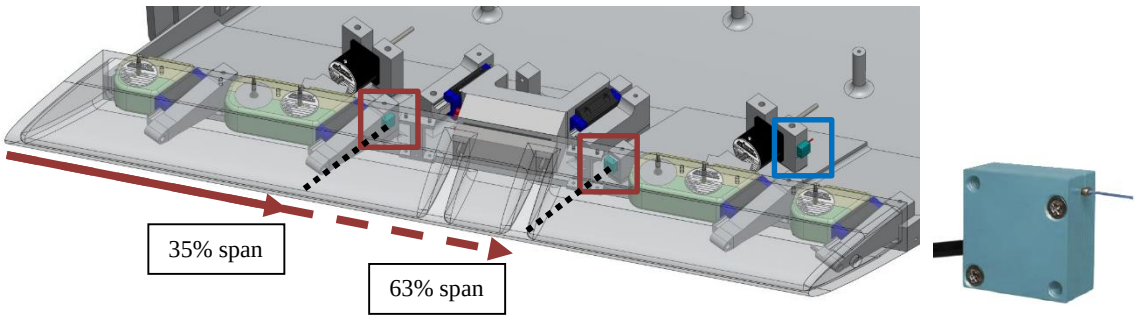

a) **b)**

Fig. 12 Displacement sensors, a) Maroon boxes – step sensors, blue box – gap sensor, b) ZX-PA series from UniMeasure ([37])

The ZX-PA series has a measurement range of 38 mm (1.5") and constantly has a cable tension of 1.1 N (0.2 lb). Based on a 16-bit DAQ system, a resolution of approximately 0.6 μm can be achieved. More importantly, the rated repeatability is 11.4 μm, and with the in-house calibration applied, the total uncertainty is ±18 μm. The operating temperature is -55 °C to 100 °C.

Leading-Edge Details

Two interchangeable leading-edge parts were fabricated for the present experiment. One leading-edge part had pressure taps installed, while the other did not. The pressure taps become 3-D disturbances and can potentially trip the boundary layer. If a tap on the leading-edge part trips to turbulence, a significant portion of the downstream test region is contaminated. Thus, initial tests use the pressure-tap leading-edge part to

measure the surface pressure profile, and then the polished leading-edge part is used for the infrared thermography campaign (the majority of the experiment).

The surface of the pressure-tap leading-edge part was not altered after receiving it from the fabricator and it has a brushed aluminum surface. The polished leading-edge part was initially sanded progressively with 400 to 4,000 grit (Norton brand) and then treated with a series of metal polishes (Granitize and Mothers brand) resulting in a residual roughness height of 0.2 μm RMS with a peak-to-peak value of 1.2 μm. One has to be extremely careful when sanding and polishing a surface interface because of the junction at $x/c = 0.15$. The edges were rounded off by a few hundred microns and had to be repaired. A two-part epoxy paint, with excellent sanding characteristics, was used to fill in the rounded edges. Then, the leading-edge part was match sanded to the painted test surface. Across the entire span of the model, the step-height uncertainty is approximately ±10 μm. The total uncertainty of the step height in flight is ±25 μm; the dominant term is the nonuniform, relative deformation of the leading-edge part with respect to the test surface.

In order to seal the leading-edge part to the main body, an expanded polytetrafluoroethylene gasket tape by Gore was applied to the leading edge. It has a 250 μm thickness when it is fully compressed. Kapton tape, with a thickness of 64 μm, is applied to the main body in order to provide an increase in static friction with the gasket material. The effective chord increase is less than 0.03%, but this is assumed to be negligible. This is the thinnest gasket that could be used confidently. Leak tests were performed prior to the flight tests. The model was pressurized and filled with smoke particles (0.3-2.5 μm diameter) to detect any leaks at the interface.

Heating Sheet

The global transition front was planned to be detected by infrared thermography in both the flight and wind tunnel environment. Without a temperature differential between the surface of the model and ambient, IR thermography cannot be used successfully. A cold soak at high altitude followed by a high-speed dive into higher temperatures has proven to create the necessary temperature differential for successful IR thermography (Carpenter *et al.* [6], Carpenter [7]). However, the wind tunnel does not have the capability of rapidly adjusting the freestream temperature. This cold-soak technique is time consuming: experience in

the flight environment has proven it takes approximately 20 to 30 minutes to achieve clear transition patterns. Several potential methods to achieve a temperature differential were examined that were compact, low weight, low cost, tolerable of the vibration environment in flight, and require no more than 500 W. Also, a uniform temperature across the surface was needed to have clear transition fronts. External heat lamps are not preferred due to the potential for infrared reflections (Freels [38]). After research of previous infrared thermography flight experiments (Fisher [39], Williams [40]), it was decided that the already proven and robust method of using a heating-wire sheet would be used to create the temperature differential.

Resistive heating wire is bonded to the interior face of the test-surface part with room temperature vulcanizing silicone, as shown in Fig. 13. Bathroom-tile heating wire is used specifically for this model. Two zones of heating are used due to the different thicknesses of aluminum on the test-surface part: this difference is due to structural considerations for the movable leading edge. The aft zone's skin is 3.2 mm thick, while the forward zone's skin is between 12.7 mm and 25.4 mm. In an effort to provide similar power to each zone, the power density is increased for the forward zone. The power density is modulated by adjusting the spacing of the wire lines: spacings of 12.7 mm and 25.4 mm were used for the forward and aft zones, respectively. The aft zone has 32.9 m of wire totaling a maximum of 300 W (350 W/m^2), while the forward zone has 19.5 m of wire totaling a maximum of 200 W (790 W/m^2). For reference, Fisher, in [39], portrays that a heating sheet with a power density of 400 W/m^2 is suitable to attain a 5 °C temperature differential for a transport-aircraft flight experiment.

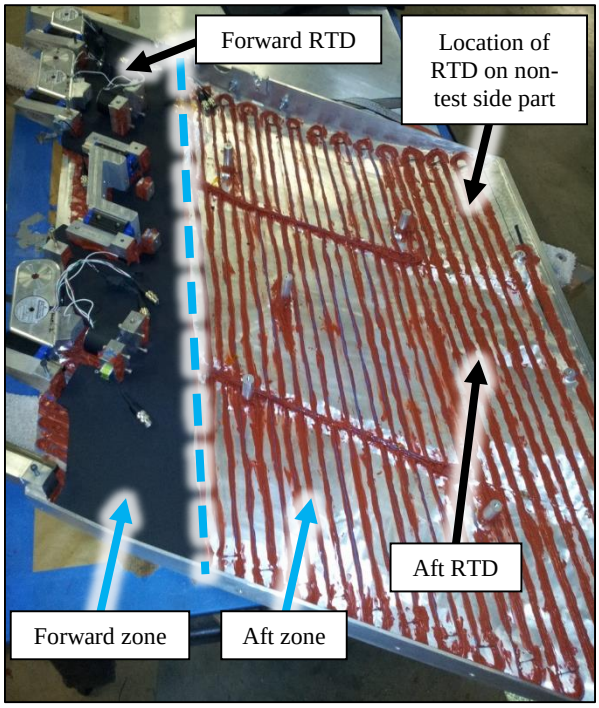

Fig. 13 Heating sheet and schematic of RTD locations (interior of test-side part shown)

Ideally, flush-mounted temperature sensors would be used to monitor the surface temperature at discrete locations for inputs to a proportional-integral-derivative (PID) controller for the heating sheet. Due to time constraints and the added complexity of the flush-mounted sensors, resistance temperature detectors (RTDs) were installed on the interior faces of the non-test and test side parts instead. A forward RTD and aft RTD were placed at a location where a reliable turbulent surface temperature could be monitored, as shown in Fig. 13. A Velcro turbulent trip strip was placed forward of the forward RTD location. The aft RTD is aft of the pressure minimum and therefore is always turbulent. A RTD was placed on the non-test side (unheated) part to represent a common temperature reference. A PID controller was programmed to maintain a 5 °C differential between the test-surface RTDs and the reference RTD. During experimentation, this typically led to a freestream temperature (measured with static temperature probe in freestream) and surface temperature (measured with infrared camera) differential between 1 to 4 °C. Also, the two independently controlled zones typically have comparable surface temperatures.

A 13 mm thick polyurethane insulating layer is overlaid on the heating wire to direct the heat towards the test surface. The insulating layer is the black cover on the forward zone, as shown in Fig. 13.

The usage of the heating sheet significantly improved the efficiency of the flight-test experiment, compared to the cold-soak method previously used with SWIFT. The heating sheet is turned on directly after takeoff. The test surface typically reaches a uniform, constant offset from the freestream by the time the aircraft reaches the test altitude (approximately 6,000 to 7,500 ft). Whereas, it was only with some difficulty that we could achieve two dives, the number of high-speed dives increased to 10 dives per flight. Additional safety information on the heating sheet is included in the Electrical Analysis section of the flight-test analysis.

Five-Hole Probe Mount

A new five-hole probe (5HP) mounting design was desired for the SWIFTER model. SWIFT's mount design begins with attaching the base of the 5HP to the end of an 'L' bracket. Then, this bracket was bolted to the non-test side of SWIFT through two bolts with adjustable washer shims, approximately 76 to 102 mm away from the surface. The chord-line angle offset (α_{offset}) could be adjusted through the washer shims and the torque of the bolts. The passed-down protocol was to use a plumb bob to mark the SWIFT chord line and the 5HP length on the ground of the hangar. The angle offset was calculated, and then the washer shims and/or torque of the bolts were modified to adjust the α_{offset} to the desired angle. This procedure could take up to several hours to complete, and there is potential for large human-measurement error.

SWIFTER's 5HP mount is shown in Fig. 14. The base of the 5HP was modified, through the 5HP manufacturer (Aeroprobe), to be press fit into a box channel. This box channel provides extra stiffness and minimizes probe-tip vibration. Brackets, as shown in Fig. 14b, are used to interface the box channel and the non-test surface of the model. The brackets were fabricated to have the identical airfoil contours at the streamwise location of the mounting holes. The α_{offset} of the 5HP was designed to be zero degrees. Thus, the installation of the 5HP could theoretically be installed with the same α_{offset} when the same bolt torque is applied. The box channel also had the ability to pitch, referenced to the root of the model, in order to create an aircraft-pitch offset, $\theta_{AC,offset}$. This improved mounting design, compared to SWIFT, proved to be beneficial operationally and experimentally due to its reliable mounting attitude and rapid

installation/removal. Additional details about the attitude measurements of the 5HP relative to the model are explained in the Five-Hole Probe section.

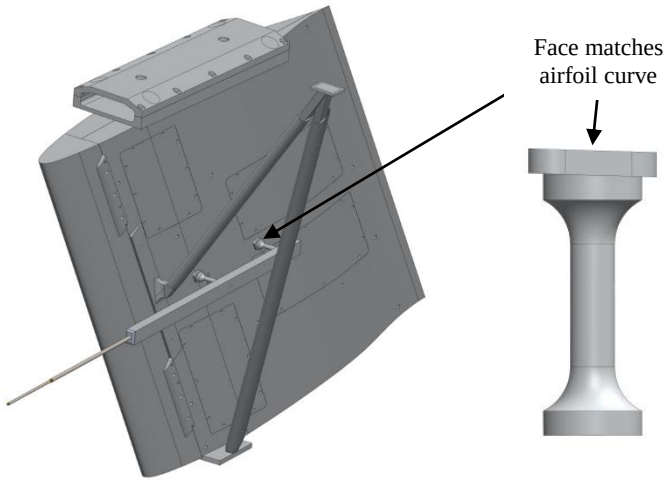

a) **b)**

Fig. 14 5HP mounted to SWIFTER, a) global view, b) close-up view of brackets

Gap-Insert Design

SWIFTER was designed to also be capable of studying gap excrescences at x/c = 0.15. Due to time constraints, gap excrescences were not studied in the flight environment and were only tested during a preliminary feasibility test in the wind tunnel. The gap-insert design is shown in Fig. 15. A static insert (teal) is applied to the non-test side and a movable insert (magenta) is applied to the test side.

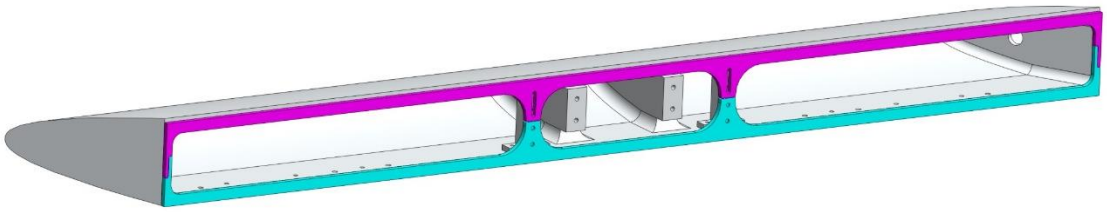

a)

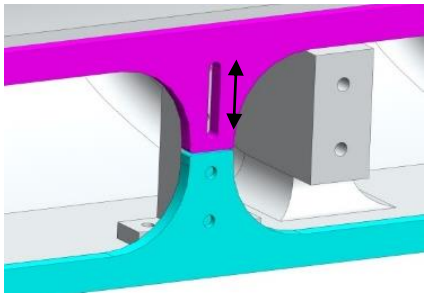

b)

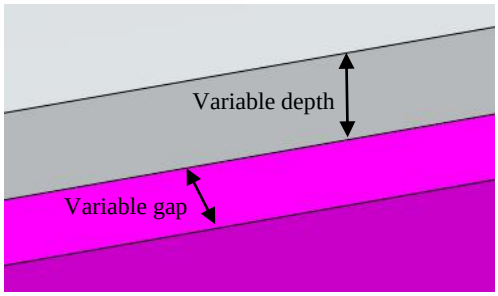

c)

Fig. 15 Gap excrescence design, a) full-span leading-edge view, b) movable (magenta) and static (teal) inserts, c) schematic of gap and depth variables

The inserts are fastened to the "I-beam" pylons inside the leading edge and are made out of Garolite. Compressible foam is applied to the aft face to allow variable gaps during the experiment, but still seals the leading edge to the main body. The slots in the movable insert provide an extra depth variable in addition to the main gap variable, as shown in Fig. 15c.

B. Experimental Facilities

Facility selection is important in boundary-layer and transition studies, especially when examining the crossflow instability with its high sensitivity to freestream disturbances. Preferably, this type of experiment would always be tested in flight, where the knowledge learned will be eventually utilized; but, safety concerns and resources hinder most researchers. Wind tunnel tests allow finer detailed measurement techniques, especially within the boundary layer. Also, the researcher has greater control over the experimental conditions, and wind tunnels usually permit longer duration testing. Performing this swept-wing experiment at Texas A&M University provided the unique opportunity to test in both the flight

environment (Flight Research Laboratory) and a low-disturbance wind tunnel (Klebanoff-Saric Wind Tunnel).

Flight Facility

SWIFTER was tested in the flight environment at Texas A&M University's Flight Research Laboratory (TAMU FRL). TAMU FRL began in 2005 with the usage of a 1968 Cessna O-2A Skymaster, as shown in Fig. 16. Unique exterior aspects of the aircraft include centerline-thrust twin engines, twin tail, high wing, and substantial optical access around the cabin.

The initial primary focus of the TAMU FRL was to extend boundary-layer transition through the use of DREs using the swept-wing test article SWIFT. As a part of this work, freestream disturbance measurements were performed using the O-2A on multiple occasions. A four-probe hotwire sting mount is fastened to the outboard, starboard hardpoint, as shown in Fig. 17. Carpenter *et al.* [6] and Carpenter [7] measured overall disturbance values of 0.05% to 0.07% of the freestream velocity. These values include acoustic disturbances and electronic noise. Fanning [41] extended these results by using temporal correlations to remove the electronic noise and acoustic sound from the hotwire measurements to obtain nominal values of 0.02% to 0.05%. These freestream disturbance values are suitable for a boundary-layer transition experiment. The O-2A has been adapted to suit many other research needs; plasma discrete roughness elements, shear-sensitive paint, LIDAR imaging, aerial photography, and air-quality measurements have been performed. A review of the TAMU FRL experiments using the O-2A is described in Tucker *et al.* [42].

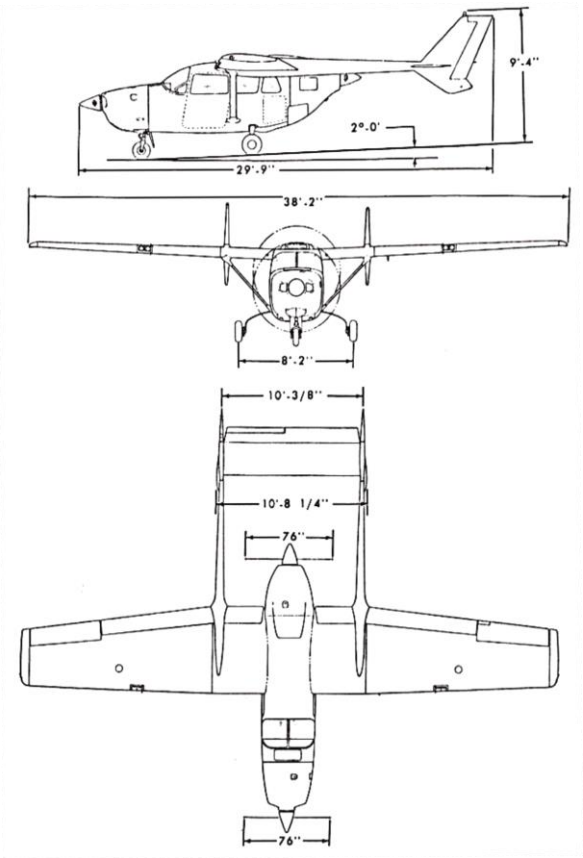

Fig. 16 Three-view dimensioned schematic of the Cessna O-2A Skymaster (Carpenter [7])

Similarly to SWIFT, SWIFTER is mounted on the port, outboard hardpoint of the O-2A, as shown in Fig. 17-18. The O-2A is a militarized version of the Cessna 337; it is a veteran of the Vietnam War. Target identification was the primary responsibility of the aircraft; several large windows around the cabin provide extensive optical access. SWIFTER can be easily seen at all times by all crew members; test pilot, copilot, and flight-test engineer (FTE). A large radio/communication rack is located in the rear of the cabin; this is an ideal place for the instrumentation packages behind the FTE (Fig. 20). Also, the four hardpoints are designed to carry heavy ordnances (e.g. machine guns, rockets, and bomblet dispensers). The US Air Force's experience with carrying heavy ordnances (up to 227 kg beneath each wing) on the O-2A helped significantly with the safety analysis of attaching SWIFTER. The centerline-thrust, twin-engine configuration provides a clean airflow over SWIFTER that is undisturbed by the front propeller. The hotwire

sting mount is attached to the O-2A during all SWIFTER flight experiments as a ballast on the starboard side; this added weight reduces the asymmetric loading created by SWIFTER.

Fig. 17 Cessna O-2A with SWIFTER attached to the port, outboard hardpoint and the hotwire sting mount attached to the starboard, outboard hardpoint

a) **b)**

Fig. 18 SWIFTER attached to O-2A, a) test side of SWIFTER and five-hole probe (5HP) (pilot perspective), b) non-test side of SWIFTER with dual-strut assembly and 5HP

SWIFTER is fastened to the O-2A's pylon assembly as shown in Fig. 19. The hotwire sting mount is fastened to an identical pylon assembly on the starboard wing. First, the two closed-loop eye hooks, bolted to the top pylon mount on SWIFTER, are inserted into the two cavities of the pylon. Hooks, inside the pylon, swing forward through the eye hooks and lock into position. At this point, SWIFTER is supported vertically

and cannot move forward in the streamwise direction. Four rocker arms are then tightened down onto the angled faces of the top pylon mount on SWIFTER; these arms restrain the test article from swaying along the aircraft's roll axis. Lastly, SWIFTER's strut assembly is bolted to the tie-down location; this fixture can be seen in Fig. 18b.

a) **b)**

Fig. 19 SWIFTER fastened to the O-2A's pylon assembly, a) front view, b) test-side view

SWIFTER limits the nominal maximum indicated airspeed of the O-2A from 192 KIAS to 170 KIAS. This limitation was developed from the safety analysis using the SWIFT test article under a worst-case loading scenario: a collision-avoidance maneuver at 170 KIAS with 30° bank and 2-g pull up ([43]). This nominal maximum indicated airspeed has an uncertainty greater than ±5 KIAS, and 175 KIAS was typically used as a do-not-exceed maximum airspeed during the experiment. In order to incorporate the largest loads on the test article, 175 KIAS was used to compute the pressure loading for the structural analysis of SWIFTER (see Structural and Displacement Analysis section). Typical test altitudes range from 3,000 ft to 8,500 ft MSL. Testing can occur up to 12,500 ft, but emphasis is placed on lower altitudes for the higher Reynolds numbers. A $Re´$ range of 4.00 to 5.50 x 10^6/m can be achieved (Re_c range of 5.50 to 7.50 x 10^6). Lower Reynolds numbers result in a larger aircraft pitch angle, θ_{AC}, which directly impacts the Λ (leading-edge sweep), as shown in Eq. (1). The previously mentioned Reynolds range results in a Λ range from 28° to 31°; Λ is assumed to be constant for the presented results.

$$\Lambda = 30° - \theta_{AC} \quad (1)$$

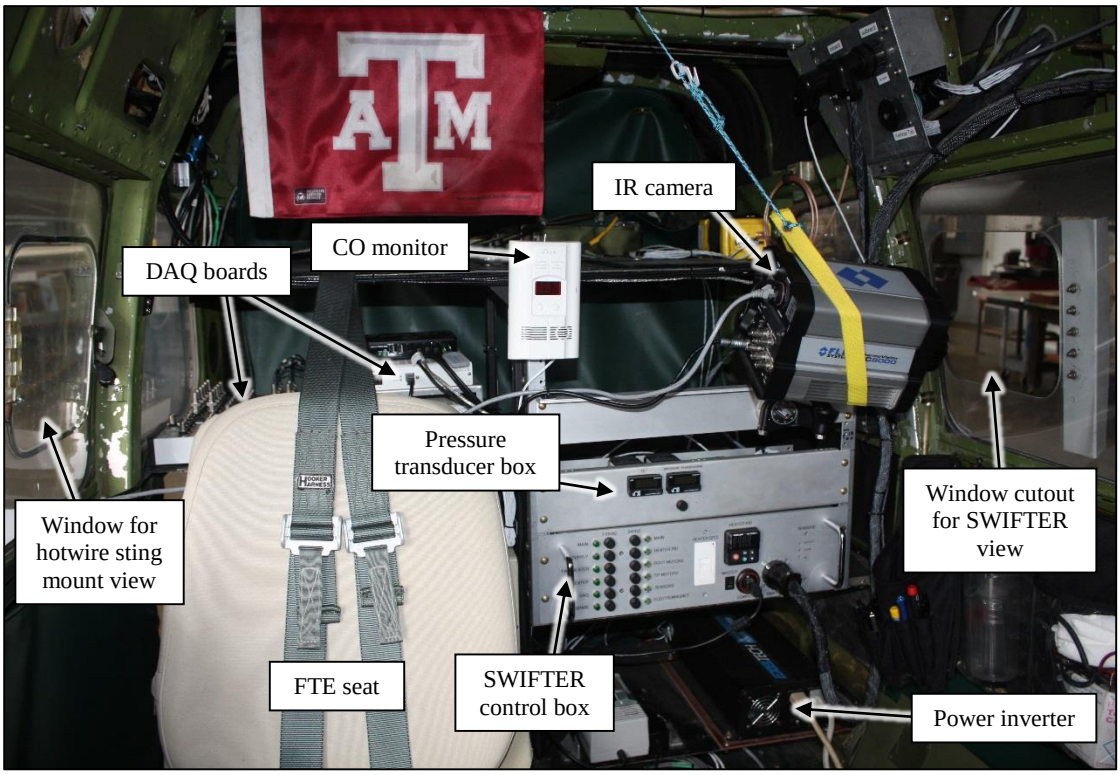

Fig. 20 Instrumentation rack typical experimental setup

A typical experimental setup for the O-2A's instrumentation rack is shown in Fig. 20. The starboard side of the instrumentation rack (left side of Fig. 20) has the data-acquisition (DAQ) boards with each BNC connector block and the aircraft's battery behind the FTE seat (not shown). The CO monitor is fastened to the center post between each side. The port side of the instrumentation rack has the aircraft's power inverter, SWIFTER control box, pressure-transducer box, and the IR camera. The FTE seat is on the starboard side, and the fourth O-2A seat (port side, rear) is removed for weight reduction and additional room for the FTE.

Additional information regarding experimental procedures, safety of flight, and a comparison with the SWIFT test article is included in the Flight-Test Analysis section.

The TAMU FRL operates out of Easterwood Airport in College Station, TX. The airport is owned by TAMU and is conveniently located within the main campus boundaries. Three intersecting runways, a FAA control tower, a general aviation terminal, and a commercial aviation terminal all comprise the entire airport. The multiple runway options are helpful in the event of high ground wind speed, with the restrictive crosswind limitations with SWIFTER attached (see Flight-Test Analysis section for more details). The control tower provides safe takeoff and landing operations, especially with the increased presence of other aircraft near the airport. Experimental operations are performed in two test areas; 15 nm west of College Station (test area 1) and 20 nm north of College Station (test area 2). The test areas are above low-population regions, free from FAA aircraft airways, and they have several landing options in the event of an emergency. Additional details regarding the test areas and flight operations at the TAMU FRL are included in [44-45].

Wind Tunnel Facility

For the wind tunnel experiments, SWIFTER will be installed into the low-disturbance Klebanoff-Saric Wind Tunnel (KSWT) at TAMU. The KSWT is the third reconstruction of the original tunnel first built by Phillip Klebanoff at the National Bureau of Standards in 1970. It was then moved to Arizona State University (ASU) in 1984 by William Saric (Saric 1992) and was called the ASU Unsteady Wind Tunnel (UWT). The primary research focus in the ASU UWT was boundary-layer stability and transition. The tunnel made its final move to TAMU in 2005 and several flow-quality improvements were made from the experience and lessons learned at ASU. In mid-2008, construction of the tunnel commenced and was fully operational by early-2009.

Hunt *et al.* [46] and Hunt & Saric [47] describe the flow-quality improvements of the tunnel, and the freestream environment was documented through hotwire measurements. In order to be near the range for recommended angles for maintaining attached flow (Reshotko *et al.* [48]), the first-stage diffuser angle (see Fig. 21) was transformed from the ASU UWT of 23° with screens to the KSWT of 5° with a new splitter plate. Also, the tunnel was widened 0.9 m and lengthened 0.3 m downstream of corner 4; this was done to reduce a region of increased disturbances due to potential poor flow recovery between corners 3 and 4. Lastly, by surrounding the motor by an acoustically-lined box, a source of acoustical disturbances was lessened. For an operational and experimental improvement, the air-cooled motor was moved outside the

tunnel and converted from a direct-drive to belt-drive fan assembly. This reduced a heat and disturbance source in the freestream. Within the range of 20-29 m/s for this tunnel, the reconstruction and improvements at TAMU lowered the turbulence intensities ([46]). More specifically at 25 m/s, a representative freestream velocity of the tunnel, the wall-normal fluctuation is 0.019% and the spanwise fluctuation is 0.023% both with 1 Hz to 10 kHz bandpass at TAMU, a decrease from 0.032% and 0.032% at ASU with 2 Hz to 1 kHz bandpass, respectively. Although different bandpasses are utilized, the broad TAMU bandpass validates the turbulence levels are lower than ASU. It is important to note that the transverse fluctuations, at all tunnel velocities in the KSWT, adhere to the suggested thresholds stated in Saric & Reshotko [49] in order to investigate boundary-layer stability and transition in the KSWT.

The KSWT is a closed-loop wind tunnel facility, as shown in Fig. 21. It has a 1.4 m by 1.4 m test section, and is capable of a maximum unit Reynolds number of 1.70 x 10^6/m. The *Re´* range tested for the present experiment was from 0.50 to 1.50 x 10^6/m, which corresponds to freestream velocity of approximately 8 m/s to 24 m/s. It is important to note that wall liners were not used for the present experiment. Previous studies in the KSWT have used wall liners to impose a spanwise-uniform pressure distribution in the test region. Wall liners are a significant time and resource investment. Preliminary tests with SWIFTER, without wall liners, lead to sufficient spanwise-uniformity, and it was decided that wall liners were not necessary for the actual test campaign. Static airfoil extenders on the root and tip of the model are used to simulate an infinite swept-wing in the test section, as shown in Fig. 22.

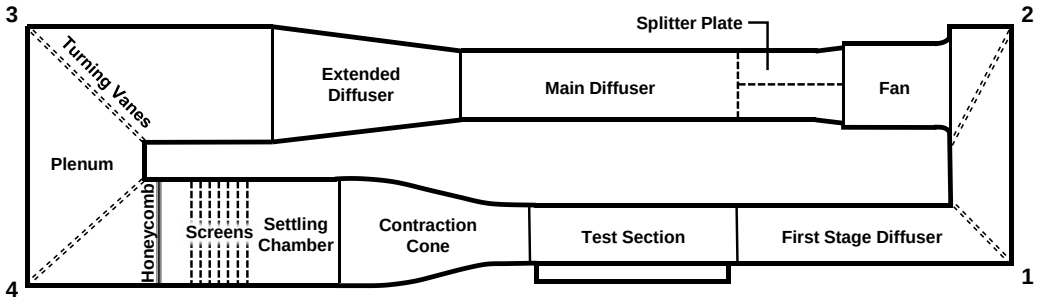

Fig. 21 Klebanoff-Saric Wind Tunnel schematic

Forward of the test section, a honeycomb plane and seven tensioned screens are used to reduce turbulent scales and increase flow uniformity. In order to minimize structural vibrations of the tunnel circuit or ground vibrations, the test section is placed on four pneumatic isolators. This is especially important for delicate hotwire measurements. The wind tunnel has three interchangeable test section windows: glass for optical access, acrylic with viewing ports for IR thermography access (Fig. 23a), and an articulated viewing window to accommodate the hotwire traverse (Fig. 23b). In order to minimize mass flow through the hole for the hotwire traverse's sting, a sealed pressure box encloses the entire length and height of the test section, including the hotwire traverse system (acrylic windows with gasket tape can be seen on right side of Fig. 23b).

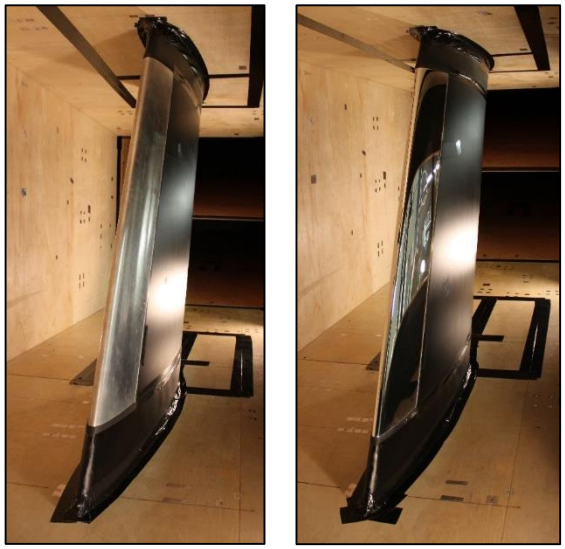

a) **b)**

Fig. 22 SWIFTER installed in test section with root and tip airfoil extenders, a) pressure-tap leading-edge part, b) polished leading-edge part

a) **b)**

Fig. 23 SWIFTER installed in KSWT,
a) infrared thermography setup, b) hotwire traverse setup

For the first set of tests, the window with viewing ports was used in conjunction with an infrared (IR) camera. This allows for rapid, detailed transition-location measurements. This will be used to map out the relation between step magnitude and transition location. The second set of tests utilizes the hotwire traverse system to characterize the boundary layer at multiple chord locations for multiple excrescence configurations.

SWIFTER was fastened to the KSWT's test section similar to previous swept-wing models. A large rectangular block with a cylindrical thru hole is bolted to a new angle-iron structure (Fig. 24a). This angle-iron structure is bolted to the existing bottom steel frame of the test section (Fig. 25a). A cylindrical part with an upper flange, which is bolted to SWIFTER, is inserted through the cylindrical thru hole of the rectangular block; the upper flange controls the vertical height of SWIFTER relative to the test section. Multiple model angles of attack can be set with the adjustable keyed slot and bottom flange. The root of the model (bottom of test section) is shown in Fig. 24a & 25a.

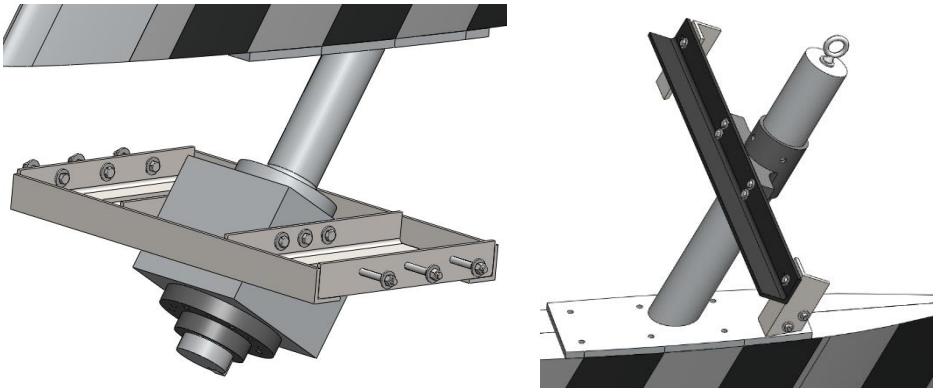

a) **b)**

Fig. 24 SWIFTER's mounting parts onto KSWT's test section, a) root of model, b) tip of model

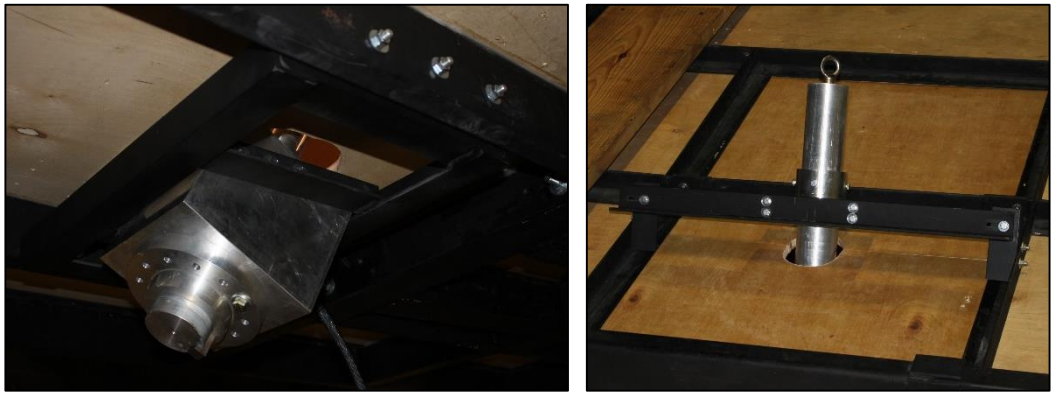

a) **b)**

Fig. 25 SWIFTER's mounting parts onto KSWT's test section (as installed), a) bottom view, b) top view

Fig. 24b & 25b portray the brackets used to fasten the tip of the model to the test section. A cylindrical part slides through a bracket with a cylindrical thru hole. This bracket is then bolted to the test section steel frame. In order to use the overhead crane to move the model, the cylindrical part has a closed eye hook on the end for tie straps to be inserted.

Details on the orientation of SWIFTER relative to the KSWT are provided in the KSWT Instrumentation for Freestream Characterization section.

C. Structural and Displacement Analysis

Safety of flight testing was a primary driver in the design process of SWIFTER. In order to calculate the loads experienced on the model during flight, a CFD analysis was initially performed and the pressure distributions were calculated by Matthew Tufts (Tufts *et al.* [1-2]). A simplified O-2A model was utilized; the fuselage, wings, port empennage, port wing strut, and port outboard pylon were modeled, as shown in Fig. 26. SWIFTER was modeled below the port outboard pylon with the dual-strut assembly, five-hole probe, and non-test side brackets, as shown in Fig. 26. Previous experience with the SWIFT project enabled the confident usage of this simplified aircraft model, the exclusion of the propeller wash, and the usage of the three-tier gridding method (Rhodes [50]). The grids were created using ANSYS ICEM and the CFD solution was computed using ANSYS Fluent. The CFD solution methods are second order, incompressible and pressure based. The flow was set to be turbulent after the pressure minimum to prevent separation; thus, this method provides a 'clean' pressure distribution.

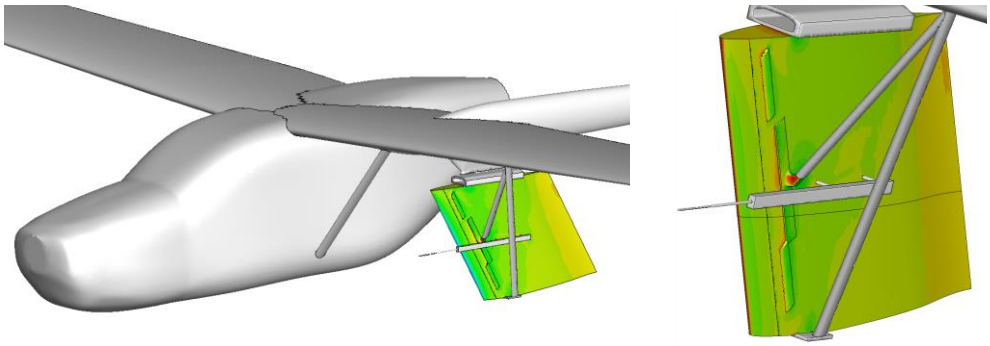

Fig. 26 CFD simulation of SWIFTER and O-2A with pressure isobars (Tufts *et al.* [1])

Three loading scenarios were computed: worst-case, experimental, and buckling. The worst-case scenario had the largest absolute lift produced by SWIFTER. The experimental scenario was modeled to investigate the relative deformation of the movable leading edge to the main body. The buckling scenario was modeled to study the effect of the compressive forces on the dual-strut assembly. All scenarios were simulated at 175 KIAS (maximum airspeed with model attached) and a summary of the CFD results is

shown in Table 1. The moment around the main mounting bolt on the channel assembly is also included for comparison.

Table 1 CFD load and moment summary

Scenario	α	Model Lift	Model Drag	Pitching moment around mounting bolt
Worst Case	+6.80°	527 lb	36 lb	139 ft·lb
Experimental	-4.00°	10 lb	17 lb	363 ft·lb
Buckling	-11.30°	-340 lb	945 lb	503 ft·lb

These pressure distributions were used as inputs to the stress and displacement analyses performed using the finite-element solver, Solidworks Simulation. Due to the software being incapable of inputting a 3-D pressure field, a pressure distribution slice at 60% span was chosen for the load input on the model. Midspan would have been preferred, but the five-hole probe and midspan-strut bracket are located at midspan and does not provide a representative distribution for the full span of the model. The 60% span slice proved to be a conservative lift estimation compared to the software-outputted CFD lift (Table 2). A simple integration between the pressure and suction side applied to the full span of the model provides the 60% span lift calculation. Due to its conservative nature, the 60% span pressure distribution was deemed suitable for the load input across the full span of the model.

Table 2 CFD lift and 60% span lift comparison

Scenario	CFD, Lift Calculation	60% Span, Lift Calculation	% Difference
Worst Case	527 lb	566 lb	+7.4%
Experimental	10 lb	28 lb	+180%
Buckling	-340 lb	-348 lb	+2.2%

Actuation System Analysis

An examination of the loads on the commercial components used for the leading-edge actuation system was first performed prior to the finite element analysis. Each component has a company-rated force it can support and each part must be able to withstand the leading-edge assembly's worst-case scenario with a

certain safety margin. The leading-edge part's worst-case scenario is not the worst-case scenario for the entire model; the buckling scenario is the worst-case scenario for the leading edge. A load summary for the leading-edge part is shown in Table 3. Also, the entire model must be able to withstand a 2-g, 30° bank collision avoidance maneuver. Thus, the leading-edge system must be able to withstand two times the leading-edge weight of 390 N (88 lb).

Table 3 Leading-edge part load summary

Scenario	Leading-Edge Lift	Leading-Edge Drag	Leading-Edge 2-g Weight
Worst Case	214 lb	36 lb	88 lb
Experimental	-75 lb	17 lb	88 lb
Buckling	-265 lb	95 lb	88 lb

A component factor of safety (FOS_c) quantity was created to compare the component's rated forces against the external forces applied in each direction in the aircraft coordinate system (*X*, *Y*, *Z*). *X* is the roll axis towards the nose, *Y* is the pitch axis towards the starboard side, and *Z* is the yaw axis towards the bottom of the aircraft. It is important to note that FOS_c is not the factor-of-safety to yield or ultimate. The FOS_c formulation for the *X* direction is shown below in Eq. (2).

$$FOS_{c,X} = \frac{\sum Component\ rated\ forces\ in\ X\ direction}{External\ forces\ applied\ in\ X\ direction} \tag{2}$$

The components under examination in the leading-edge assembly include the rail guides, linear actuators, and electromagnet. The rail-guide forces are calculated from the rated torque values each with a moment arm of 310 mm (12") for the *Z* forces and 150 mm (6") for the *Y* forces. Both moment arms are conservative values to provide a conservative force estimate. Each linear actuator can provide 890 N (200 lb) statically and 450 N (100 lb) dynamically. The dynamic force rating is the axial force the linear actuator can provide to translate the lead screw, while the static force is the axial force while stationary. More detail on the static-load tests to proof the above values is included in the Static-Load Tests section.

The electromagnet pulling force is 4,500 N (1,000 lb); this force is split up into components of 3,900 N (870 lb) in the *X*-direction and 2,200 N (500 lb) in the *Z*-direction. The maximum frictional force provided by the electromagnet in the step-direction (*Y*-direction) is 1,100 N (250 lb). A schematic of the force analysis in the *X* and *Z* direction is shown in Fig. 27. Two separate analyses were performed in the *Y* direction: linear rail-guide analysis (Fig. 28) and linear-actuator analysis (Fig. 29). The linear rail-guide analysis makes the assumption that all of the external force is applied directly to the rail guides. This is to simply examine the load capabilities of the rail guides. The electromagnet shear force and linear-actuator axial force are smaller than the rail-guide capabilities, as shown in the linear-actuator analysis, and thus, are the limiting factors in the *Y* direction.

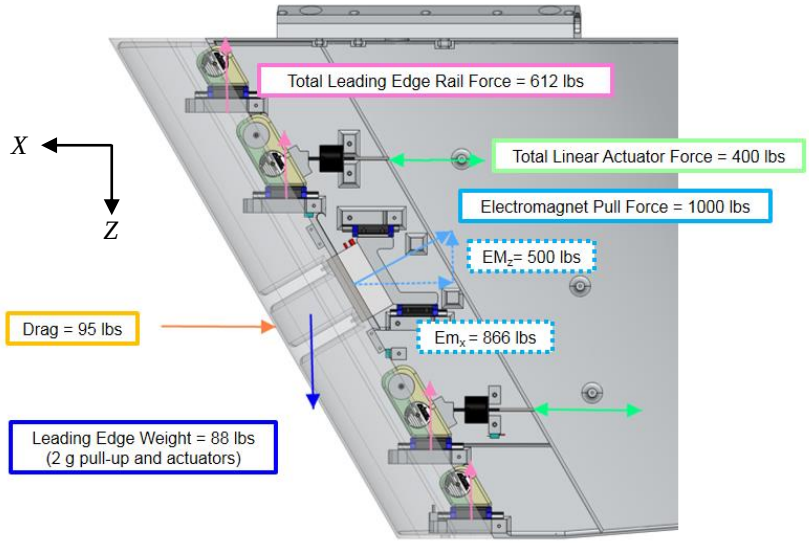

Fig. 27 Actuation system force analysis, in-plane, leading-edge part worst-case scenario

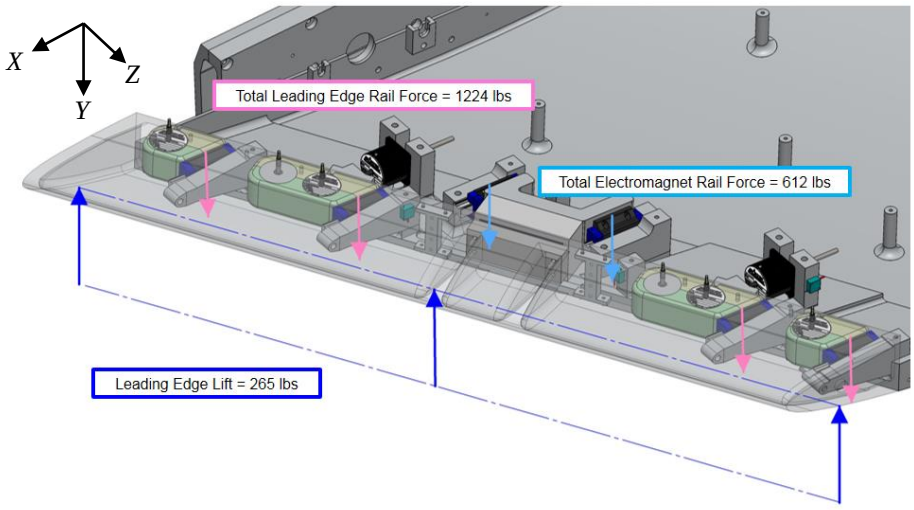

Fig. 28 Linear rail guide force analysis, lift-plane, leading-edge part worst-case scenario

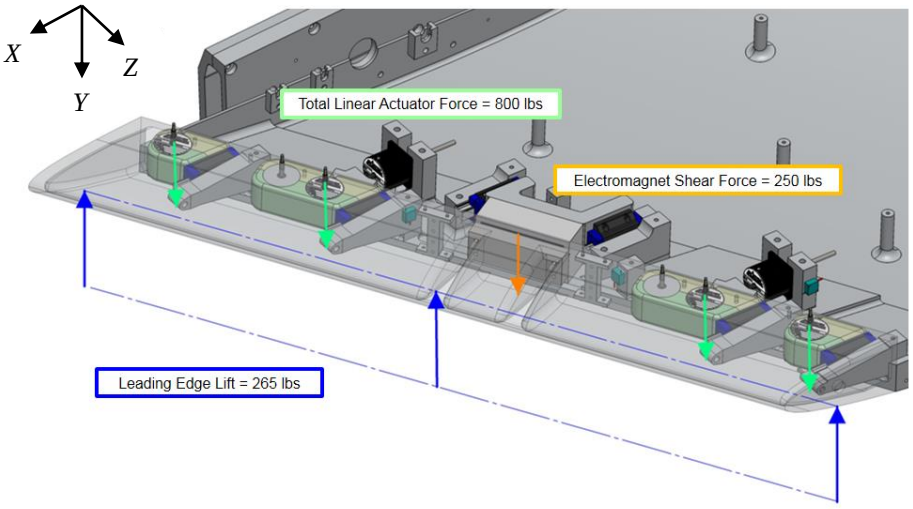

Fig. 29 Linear actuator force analysis lift-plane, leading-edge part worst-case scenario

A summary of the FOS_c in each direction is shown in Table 4. The minimum FOS_c is 3.0 without the electromagnet engaged and 4.0 with the electromagnet engaged (both for the *Y* direction linear actuators). An important note is that the step-direction linear actuators can produce a total of 1,780 N (400 lb) dynamically, while the maximum lift on the leading edge is 1,180 N (265 lb). This conditions portrays that

actuating the leading edge during any modelled scenario is possible. The worst possible scenario that could occur in flight is that the step-direction linear actuators stall and cause a misalignment of the leading edge relative to the main body. This scenario is a technical, experimental setup problem (i.e. this is not a safety problem). However, this scenario was never observed in any of the flight tests conducted.

Table 4 FOS_c comparison in each direction (minimum italicized)

Direction	***FOS*$_c$ (w/o EM)**	***FOS*$_c$ (w/ EM)**
X Direction	4.6	14.4
Y Direction (Rail Guides)	4.6	6.9
Y Direction (Linear Actuator)	3.0	4.0
Z Direction	7.0	12.6

Simulation Inputs

The inputs for the finite element analysis are the contact conditions between parts, restraining fixture points, and the external forces applied to the model. The understanding of each simulation input is important in order to ensure the real-life scenario and simulated scenario are as similar as possible.

The contact conditions between parts are addressed first. The leading-edge assembly, except the lead screws and smooth shafts, is fully bonded and is shown in blue in Fig. 30. This bonded assembly is a good assumption due to all of the components being rigidly fastened together with multiple bolts. Bearing connectors are applied to the lead screw and actuator housing interface. The lead screw is allowed to translate radially (about ±1 mm) inside of the actuator housing. The radial movement is allowed, but the axial movement is near zero. Radial and axial stiffness of the lead screw and housing interface are needed as inputs. If a radial force of approximately 450 N (100 lb) is considered and 1 mm radial movement is allowed, the calculated radial stiffness for the step-direction linear actuators is 445,000 N/m (2,540 lb/in) (350,000 N/m, 2,000 lb/in is used). The internal rotating bronze (SAE 660) nut provides the axial resistance. Using the material's Young's modulus of 100 GPa (14.5 x 10^6 psi) and axial length of the nut of 6.4 mm (0.25"), the calculated axial stiffness input for the step-direction linear actuators is 5.36 x 10^9 N/m (30.6 x 10^6 lb/in) (1.8 x 10^9 N/m, 10 x 10^6 lb/in is used). The step-direction lead screw ends are bonded to the leading edge and the gap-direction lead screw ends are bonded to the angular connector part.

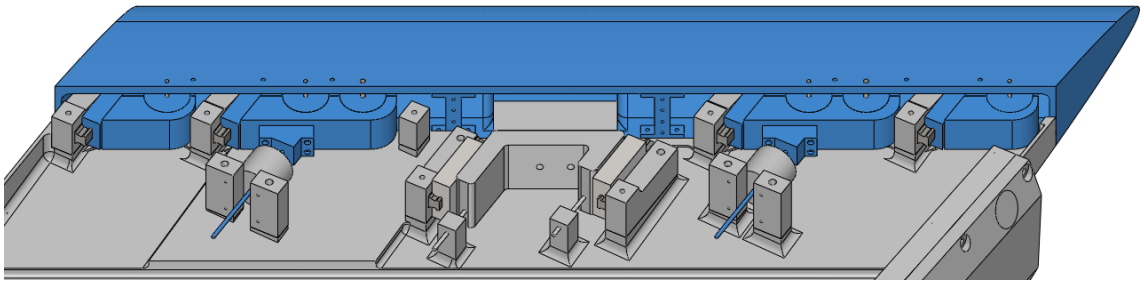

Fig. 30 Fully bonded contact condition for leading-edge assembly (shaded blue)

The gap-direction linear actuators have the same radial stiffness input as the step-direction linear actuators. However, the axial stiffness input is reduced to zero to allow axial movement of the lead screw inside the actuator housing. The gap-direction linear actuators have 450 N (100 lb) applied on each gap-direction lead screw pulling the movable leading edge into the model, as shown in Fig. 31. This is the maximum pulling dynamic force each actuator can produce. A reaction force of 450 N (100 lb) is applied on each of the test-surface pylons holding the gap-direction linear actuators. Also, the electromagnet is not engaged in the safety-of-flight simulations for conservative measure.

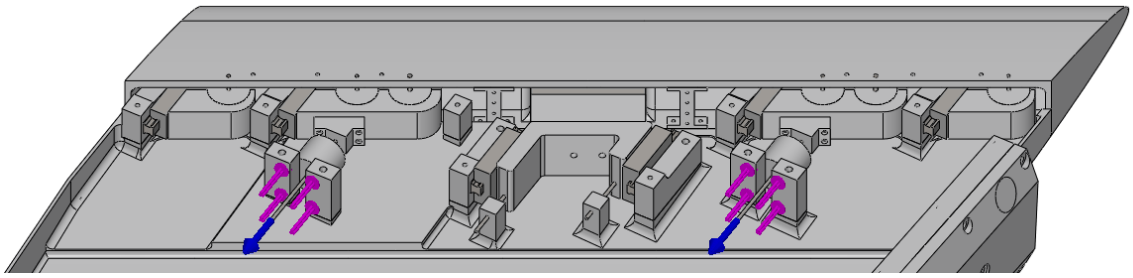

Fig. 31 Gap-direction linear actuator force schematic,
pulling force on lead screw (blue), reaction force on pylon (magenta)

A local friction boundary condition was applied between the movable leading edge and the main body. A static friction coefficient of 0.50 is used; this value was experimentally derived from in-house friction tests between the gasket tape and Kapton tape (gasket tape is applied to movable leading edge and Kapton

tape is applied to main body). The carriages and rail guides have a no-penetration boundary condition, which allows a realistic translation of the carriages along the rail guides. All other faces of contacting parts of the model are bonded together where there is a screw fastening the two parts together. A no-penetration boundary condition is applied everywhere else where there is not a screw.

Fixtures

SWIFTER has three main fixtures interfacing with the aircraft: eyebolts, rocker arms, and strut tie down. The eyebolts are fastened to the pylon mount, and the eye-hooks inside the outboard pylon assembly latch onto these two eyebolts. Once the eye-hooks are locked down, the model is restrained in the longitudinal (forward and aft) and vertical axes (weight), as shown in Fig. 32b. The rocker arms attached to the outboard pylon assembly are torqued towards SWIFTER's pylon-mount part. They are angled in a fashion that restrains the swaying motion of the test article; the restraining motion is the direction normal to the face on the pylon mount, as shown in Fig. 32a. The top of the dual-strut assembly is affixed with three screws fastened to the nut plates at the tie down location under the aircraft's wing. All three directions are restrained, as shown in Fig. 32c.

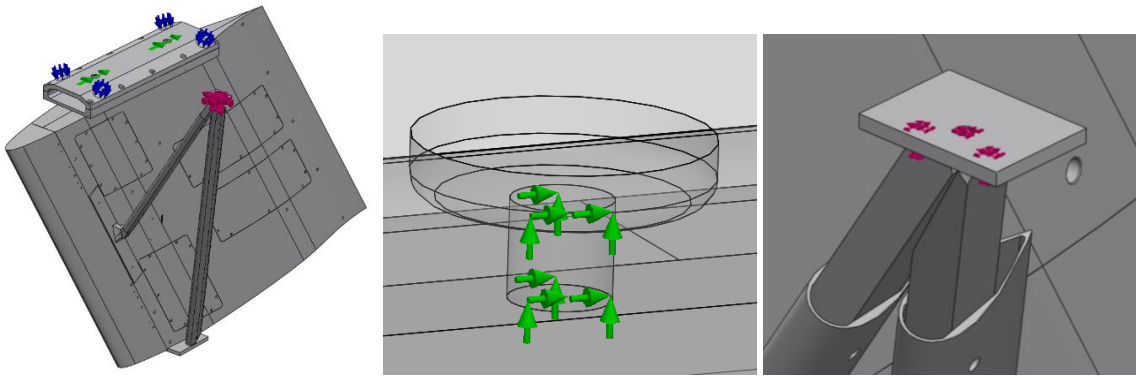

a) **b)** **c)**

Fig. 32 Fixture restraints: rocker arms (blue), eyebolt (green), strut screws (magenta), a) full model, b) eyebolt holes, c) strut tie down

Externally Applied Forces

The pressure distributions at 60% span were used for the externally applied forces, as this was shown to be conservative representation of the full-span pressure distribution. Due to the software not being capable of inputting the raw pressure distribution, sets of three to six linear regressions were used to represent the pressure on the test and non-test surfaces (TS and NTS, respectively). The linear regressions for the worst case, experimental, and buckling scenarios are shown in Fig. 33, Fig. 34, and Fig. 35, respectively. The pink set of points from x/c = 0.07 to 0.11 on the non-test side are non-physical pressure results from the CFD meshing scheme; this region is the meshing transition from a structured grid to an unstructured grid and is omitted from the load analysis. The sets of linear approximations have good agreement with the CFD pressure distributions at 60% span. Deviations from the CFD results are mainly conservative. The non-test surface asymptotic point at x/c = 0.15 is due to the midspan strut bracket.

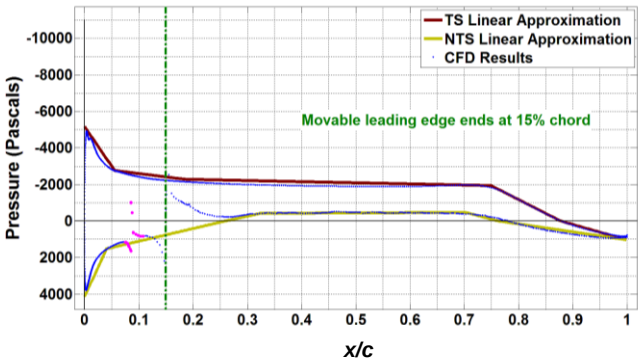

Fig. 33 Worst-case scenario linear regressions

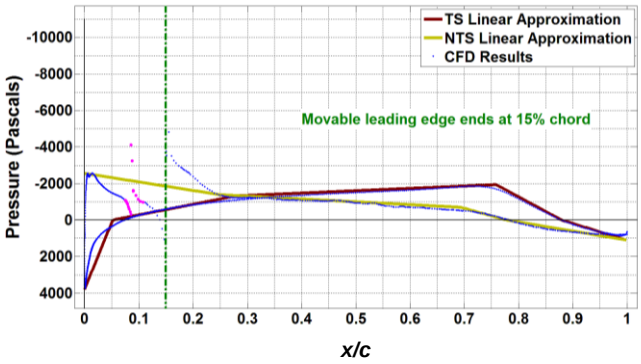

Fig. 34 Experimental scenario linear regressions

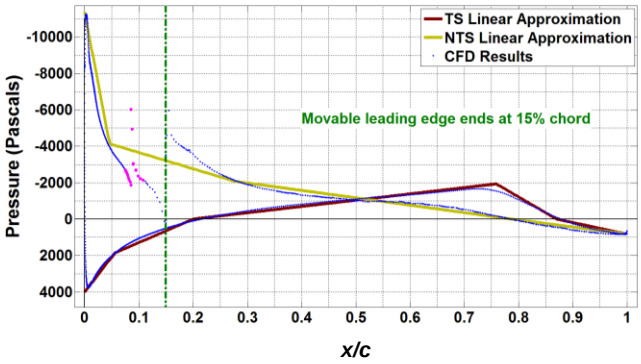

Fig. 35 Buckling scenario linear regressions

These sets of linear regressions are applied on the pressure and suctions sides, as shown in Fig. 36. The different colors represent each linear regression. The length of the arrows represent the change in pressure magnitude only within the same linear regression. Thus, a comparison of the magnitude based on arrow length cannot be made between different loading areas. A 2-g inertial load is shown with the black arrow; the applied direction is normal to the top face of SWIFTER. The minimal drag force was applied as a constant loading across the surface of the movable leading edge (not shown in Fig. 36).

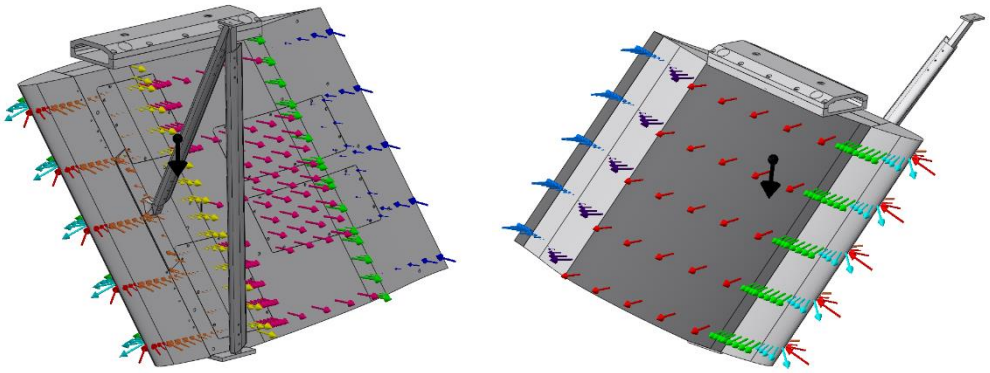

Fig. 36 Worst-case linear regression pressure inputs (colors), 2-g inertial load (black)

Mesh Information

The curvature based, solid mesh is used for the entire model; it automatically creates a finer mesh in high curvature areas. This allows the geometry to be better captured in high curvatures areas with a smaller grid compared to the standard mesher. This is important because of the relatively high number of curved surfaces in this simulation (e.g. airfoil of SWIFTER, airfoil struts, bolt holes). Local mesh controls were used on individual parts to capture detailed geometry without rapidly increasing the global mesh size. A focus was placed on the leading-edge assembly and channel assembly. A representative mesh can be seen qualitatively (mesh plot) and quantitatively (aspect ratio) in Fig. 37ab. The aspect ratio of the mesh is the amount that the tetrahedral element distorts from a perfect tetrahedron (aspect ratio = 1). A rule of thumb is to have the aspect ratio be less than 3 for the majority of the model for a structural analysis simulation (Ramamurty [51]). At least 66% of each of the three meshes have an aspect ratio of 3 or less, as shown in Fig. 37b and Fig. 38b (blue regions). Additional mesh information (e.g. number of elements and degrees of freedom) is summarized in Table 5. An important and necessary note is that the maximum stress and minimum factor of safety have converged with the meshes.

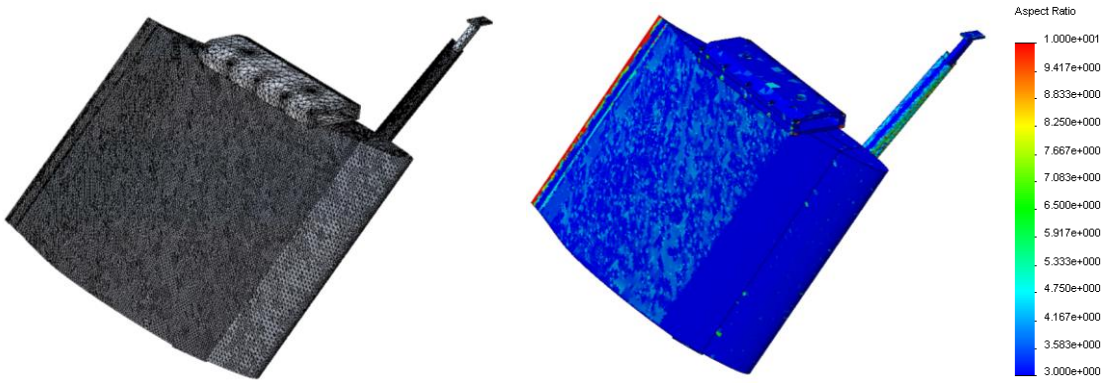

a) **b)**

Fig. 37 Meshing plots of test side, a) meshing grid, b) aspect ratio of mesh

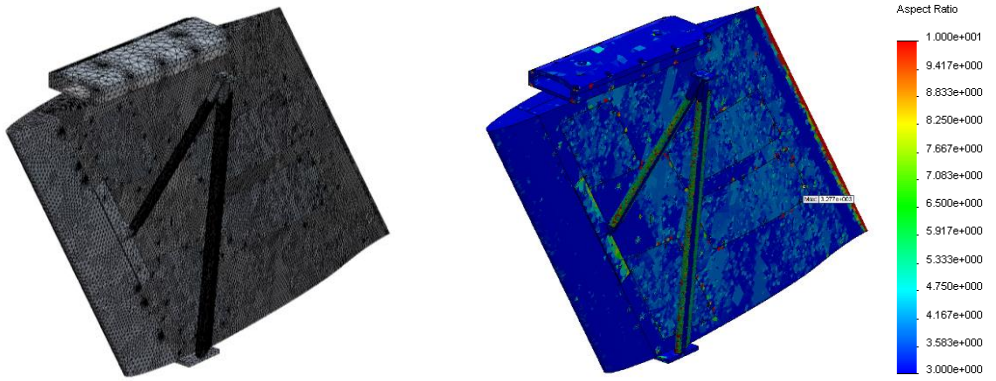

a) **b)**

Fig. 38 Meshing plots of non-test side, a) meshing grid, b) aspect ratio of mesh

Table 5 Mesh information summary

Mesh Information	Number of Elements	Degrees of Freedom	% of Aspect Ratio < 3
Worst Case	725,541	4,020,784	73.8
Experimental	574,601	3,177,172	66.0
Buckling	626,314	3,476,566	66.2

Additional Assumptions

The main modeling assumptions are included in this section.

The alignment shafts are simulated inside a 7075-T651 cylindrical housing with a no-penetration contact condition applied. However, in reality, the alignment shafts translate along frelon-lined bearings with a 6061-T6 shell. These bearings are press fit into the 7075-T651 cylindrical housing. The bearings were overdesigned with a radial load capacity of 2,700 N (600 lb) each and two of these bearings are used for each alignment shaft/cylindrical housing. Due to being overdesigned, they were not represented as separate parts inside the cylindrical housing in the simulation. However, the resultant forces from the final simulations were examined for radial forces that would be acting on the bearings. The minimum FOS_c of all simulations is 1.9; a reminder is provided that this is not the factor of safety to yield, FOS_y. Thus, the omission of the bearings in the simulation is a valid assumption.

The acme lead screws are simulated as smooth shafts with a diameter equal to the minor diameter of 4.77 mm (0.189”). The threads are not simulated due to unnecessary modeling complexity and computational processing time. The linear actuators are simulated as a 7075-T651 cylindrical housing, similarly to the alignment shaft housing. In reality, the acme lead screw interfaces with a bronze internal rotating nut inside the actuator. The lead screw interacts with the cylindrical housing as a bearing connector input, as described earlier in the Simulation Inputs section.

Each test-surface pylon is fastened to the test-surface part by a screw and prevented from rotating through the usage of two pins. Each pin has a shear strength of 1.03 GPa (150,000 psi). Initial simulations proved that simulating the pins were unnecessary and did not affect the overall stress values of the assembly. Thus, the pins were neglected for the simulation and the pylon face is bonded to the test surface.

A summary of the simulated parts and materials with associated yield strength is shown in Table 6. Ideally, the actual material would be the simulated material, but this was not possible with the material list in Solidworks Simulation. The carriages are simulated using plain carbon steel, but in reality it is made up of several different materials (e.g. frame, ball bearings, plastic covers). This is a valid assumption due to the FOS_c analysis shown earlier in Actuation System Analysis section. The remaining differences, in simulated

and actual materials, have conservative quantities for the yield strength, but more importantly, have similar stiffness values. These differences in the yield strength were taken into account during the FOS_y analysis.

Table 6 Parts list with materials simulated

Parts	Simulated Material	Yield Strength (psi)	Actual Material	Yield Strength (psi)
Carriages	Plain Carbon Steel	32,000	Various materials	n/a
Rail Guides	AISI 4340 Steel	103,000	52100 Steel	295,000
Step-Direction Lead Screws	AISI 4340 Steel	103,000	17-4 H925	210,000
Alignment Shafts	AISI 4340 Steel	103,000	17-4 H925	210,000
Gap-Direction Lead Screws	AISI 316 Steel	20,000	Same	Same
Electromagnet Steel Block	AISI 1020 Steel	51,000	Same	Same
All Other Parts	7075-T651 Aluminum	73,000	Same	Same

Results

The goal of the safety analysis is to achieve a factor of safety to yield (FOS_y) of greater than 1.5 for all parts. An important note is that the linear-actuator manufacturer does not provide the rated yield strength; thus, a factor of safety to proof (FOS_p) was used instead. In-house static-load tests were performed to have a proof strength for the actuators (see Static-Load Tests section). A reminder is given that the FOS_y of the linear actuator will be larger than the FOS_p. The gap-direction lead screws are omitted from the FOS_y plots; the inputted radial stiffness interfacing with the linear actuator was too stiff and resulted in unphysical moments on the lead screw. Independent simulations were performed for these lead screws and the minimum FOS_y was 4.2. However, this omission does not affect the results of the overall simulation.

Stress, displacement and FOS_y plots are shown below for the buckling scenario. The plots for the worst-case and experimental scenarios are included in APPENDIX A.

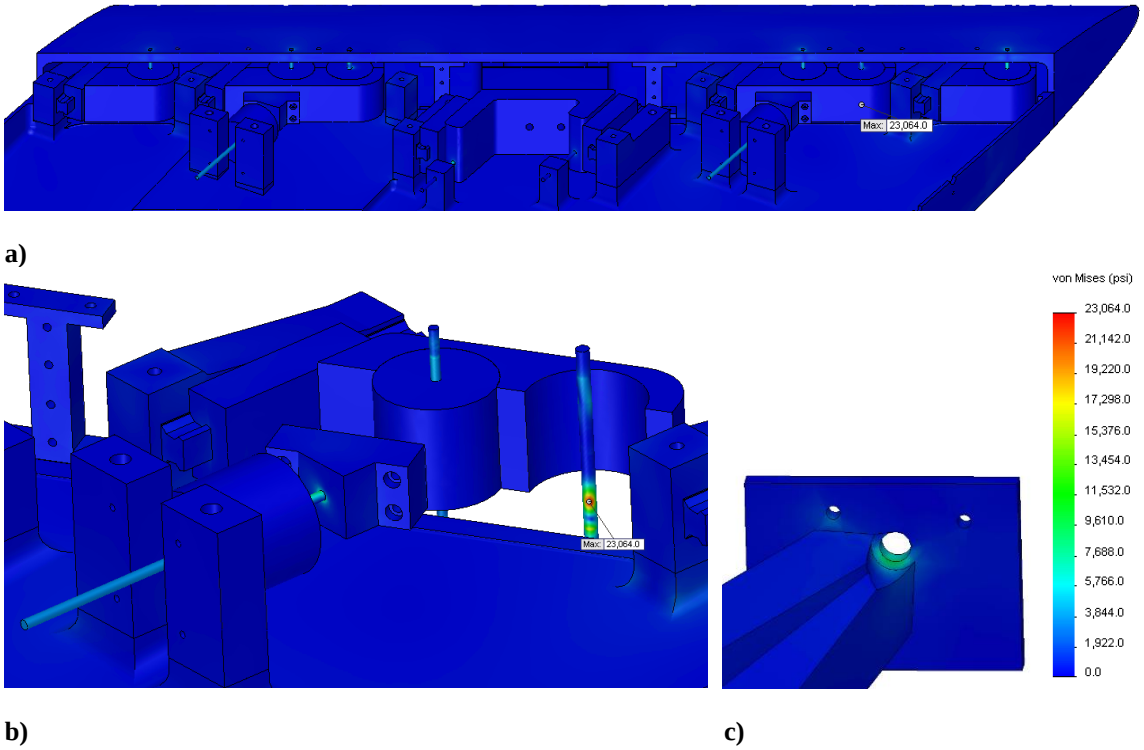

Fig. 39 Stress analysis for the buckling scenario (safety-of-flight simulations), a) full leading-edge assembly, b) root, linear-actuator assembly, c) strut tie-down part

The stress analysis for the buckling scenario is shown in Fig. 39. The majority of the model is below 20.7 MPa (3,000 psi) (blue color). Higher stress concentrations can be seen in all of the lead screws, smooth shafts and the strut tie-down part. The absolute maximum stress is 158.6 MPa (23,000 psi) located on the root smooth shaft. This is due to both the root and tip smooth shafts fully supporting the pitching movement of the movable leading edge. An annotation is included in Fig. 39b that points out the location of the maximum stress. The aluminum support block and linear-sleeve-bearing block are hidden to visualize the maximum stress.

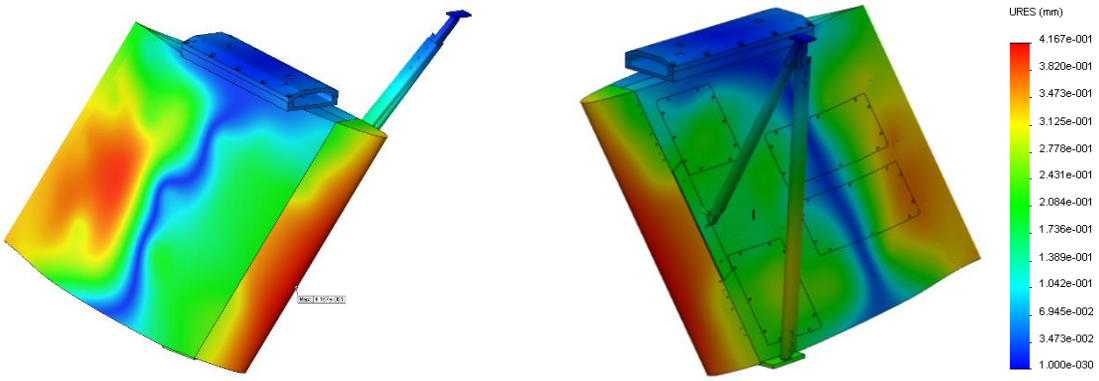

Fig. 40 Displacement analysis for the buckling scenario (safety-of-flight simulations)

The displacement analysis for the buckling scenario is shown in Fig. 40. A good check is that the pylon mount and strut tie-down part were inputted fixtures for the simulation and are outputted as negligible displacement. An important note is given to the absolute maximum displacement of 0.4 mm: the displacements shown are small deformations. The absolute maximum is indicated in Fig. 40 and is located midspan near the attachment line of the leading edge. Overall, the mid-chord region appears to have negligible deformation, while the leading edge and aft tip have higher displacements. A reminder is given to the reader that the electromagnet is not included in these safety-of-flight simulations; thus, the displacements in the test region (midspan) are much better than what are shown in these simulations.

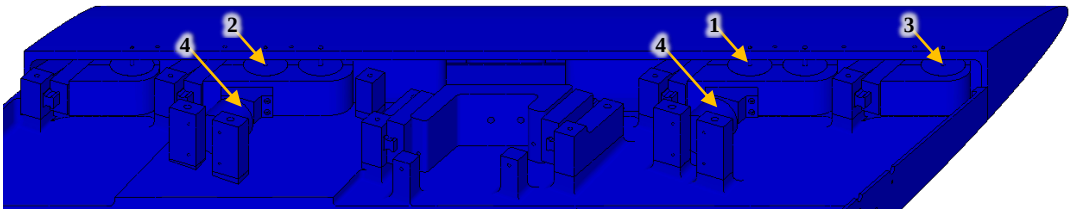

a)

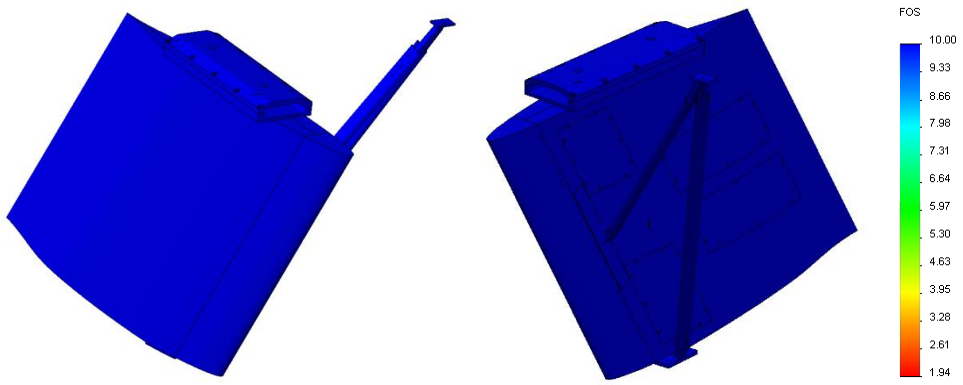

b) **c)**

Fig. 41 *FOS*$_y$ analysis for the buckling scenario (safety-of-flight simulations), a) leading-edge assembly (numbers indicate four lowest *FOS* (see Table 7), b) test side, c) non-test side

Table 7 Four smallest *FOS* for the buckling scenario (safety-of flight simulations)

Location	Minimum *FOS*	Material	Strength
(1) Root, outboard linear actuator	1.9 to proof	Component	200 lb proof
(2) Tip, inboard linear actuator	2.2 to proof	Component	200 lb proof
(3) Root, inboard linear actuator	2.7 to proof	Component	200 lb proof
(4) Gap-direction lead screws	4.2 to yield	AISI 316	20,000 psi yield

The *FOS*$_y$ analysis for the buckling scenario is shown in Fig. 41. The blue color corresponds to a *FOS*$_y$ greater than 10; thus, it is obvious that the majority of the model has a *FOS*$_y$ greater than 10. Fig. 41a has annotations for the four lowest *FOS* for the buckling scenario; these *FOS* details are summarized in Table 7. The material column describes the actual material of the part, or is described as 'component'. The 'component' material indicates that this commercial part either doesn't have a rated yield strength (e.g. the proof strength is used instead), or the commercial part is made up of several different materials (e.g. the

linear sleeve bearings have a rated radial yield strength and the calculated forces are compared against this radial yield strength). The linear actuators have the lowest *FOS*, but these are all factors of safety to proof load, FOS_p. The absolute minimum FOS_y or FOS_p for all scenarios (including worst-case and experimental, see APPENDIX A) is 1.9 (root, outboard linear actuator - Table 7 [Item 1]). Thus, the test article has met the safety-of-flight criteria ($FOS > 1.5$). A final reminder is that the electromagnet was not included in these safety-of-flight simulations. This allows the potential to modulate the step height during the high-speed dives; however, it was proved early in the flight-testing campaign that the relative displacement of the movable leading edge to the main body was too large using this technique. This actually proved beneficial for testing efficiency. The movement of the leading edge took slightly longer than holding constant model angle of attack and only modulating unit Reynolds number. Additional flight testing procedures are described in more detail in the Test Procedure section of the flight-test results chapter.

This structural analysis was approved by the Air Force Safety Review Board. The last step prior to the initial flight is to proof the model through ground static-load tests.

D. Static-Load Tests

The main objective of the static-load tests was to prove that the model was capable of supporting 1.5 times the maximum loading in the flight environment. Two important aspects are that the maximum overall force and the moment at the main mounting bolt (at $x/c = 0.52$) are both simulated as realistically as possible for the static-load tests. Ideally, a pressure distribution would be imposed on the model to achieve these two aspects. One possible method would be to install the model in a wind tunnel that was capable of producing a similar loading scenario. However, this method would be costly (time and money) due to additional CFD simulations in the new wind tunnel and additional design and manufacturing of test-section mounting brackets. A realistic solution is to apply external point or line loads to the model. External point loads were applied to the SWIFT test article to proof the model (McKnight [33]). It was decided that SWIFTER would not be static-load tested attached to the aircraft, since the O-2A's pylon and wing had been proofed through the SWIFT static-load tests. Also, at this time in 2012, over 700 SWIFT flights had been performed without a mishap. A reminder is given that SWIFTER and SWIFT are fastened to the O-2A's pylon in the same

fashion and they have the same maximum loading scenario. Lastly, an effort was made to avoid local deformations of the model shell due to a localized force; aft of x/c = 0.32, SWIFTER has 3.18 mm (0.125") wall thickness, while SWIFT has a minimum thickness of 4.78 mm (0.188"). Thus, a distributed line load was used in an attempt to avoid local deformations.

In order to achieve the main objective of the static-load tests, two loading configurations were performed. The maximum loading for the entire model is the worst-case scenario, while the maximum loading for the movable leading edge is the buckling scenario. It is especially important to test the maximum loading for the movable leading edge due to the results from the structural analysis portraying that the leading-edge assembly has the lowest *FOS*. Also, since the study of gap excrescences with this model is likely in the future, the movable leading edge was tested at 0 mm and 4.2 mm gap (measured normal to the leading edge). When the movable leading edge is gapped, the beneficial frictional force against the main body is removed; thus, it was important to test this configuration if any gap studies are to be performed for future flight testing. A total of four static-load tests were performed in order to incorporate all configurations (two loading configurations with two leading-edge gap configurations). Similarly to the structural analysis, the electromagnet was not engaged for all tests in order to provide the option of step modulation during high speed dives.

All tests have a 2-g inertial loading applied. This was achieved by adding 1,050 N (235 lb) of weight to the structure. The additional weight was spread throughout the model as much as possible by adding weights to the internal structure and physically hanging the weights from the bottom of the model. A 220 N (50 lb) weight was placed on the top face of the leading edge to simulate the leading-edge assembly weight. The drag force was not applied due to it being a relatively small force and the difficulty of applying this force to the swept-wing model. More importantly, this streamwise force was deemed unnecessary because it would only test the strongest parts of the SWIFTER model: the channel assembly and the strut assembly.

The experimental setup for the static-load tests is shown in Fig. 42. The model was hung from an I-beam structure, which was previously used for loading tests. Four bolts hold the channel of SWIFTER to the top surface of the I-beam structure. A fail-safe harness is attached to an additional steel plate on top of the channel; however, this harness is not supporting the model. A steel L-bracket was fastened to the top surface

of the I-beam structure to create a 'tie-down' location for the dual-strut assembly. The steel U-bracket on the right side of the I-beam structure in Fig. 42b was used as a fixture for the externally applied loads. A pipe clamp was used to apply the loads to the test article. A load cell was placed in-line with these loads to measure the applied force on the test article. The load cell is from Transducer Techniques and the model number is SW0-2K (8,900 N, 2,000 lb capacity). It had company-supplied calibration coefficients for compression loads only.

a) **b)**

Fig. 42 Static-load test setup, a) basic setup with internal and hanging weights, b) load applied with pipe clamp simulating worst-case scenario (see Table 8)

The total model lift was split up into two forces: movable leading-edge (LE) lift and main body (MB) lift. The location of the applied force for the LE lift was at the LE's streamwise center of pressure in order to simulate a similar pitching moment. The MB's lift force was applied at a location in which the total pitching moment of the model is similar to the actual condition. A summary of the static-load test conditions are included in Tables 8-9 (worst-case and buckling scenarios, respectively). Aircraft coordinates (*X*, *Y*, *Z*) are used, and the *Z* dimension is normalized by the span, *s*.

The total static-load test force (LE + MB) is 1.5 times the actual total force. The static-load's *X*-moment at the main bolt, τ_X, is roughly 1.5 times the actual moment, while the static-load's *Z*-moment at the main mounting bolt, τ_Z, is similar to the actual moment. The static-load test's τ_Z is not 1.5 times the actual τ_Z, but

the conditions shown in Tables 8-9 are the most realistic conditions that can be applied to the model using a two-force method. It is impossible to have 1.5 times the actual τ_Z because the MB force would need to be applied forward of the attachment line for the buckling case or the MB force would need to be significantly increased (i.e. this would make the total load applied much greater than 1.5 times the actual load). Also, it was not desired to overload the LE force to achieve this τ_Z due to the LE having the minimum overall *FOS*. Lastly, as portrayed earlier, a 2-g inertial load is simulated for both scenarios.

Table 8 Worst-case scenario, static-load test summary in comparison to the actual loads

Loads		**Force (lb)**	***x/c***	**τ_Z at main bolt (ft·lb)**	***Z/s***	**τ_X at main bolt (ft·lb)**
(1) Lift	Actual	Total = 527	0.35	139	0.47	861
	Static	LE = 321	0.07	128	0.50	1,384
		MB = 470	0.51		0.50	
(2) Weight	Actual	466	-	-	-	-
	Static	466	-	-	-	-

Table 9 Buckling scenario, static-load test summary in comparison to the actual loads

Loads		**Force (lb)**	***x/c***	**τ_Z at main bolt (ft·lb)**	***Z/s***	**τ_X at main bolt (ft·lb)**
(1) Lift	Actual	Total = -340	-0.06	503	0.47	-557
	Static	LE = -398	0.05	531	0.45	-805
		MB = -113	0.22		0.45	
(2) Weight	Actual	466	-	-	-	-
	Static	466	-	-	-	-

For all of the static-load tests, the loading was applied for approximately 2-3 minutes. Close examination of the structure was monitored during and after the loading. For all of the static-load tests, there were not any signs of local deformation around the applied force and failure never occurred. The gapped configurations lead to some compression of the LE relative to the MB on the opposite side of the loading (there is some slop in the LE). For example, the unloaded gap was 4.2 mm, but became approximately 3.6 mm after the loads for the worst-case scenario were applied (3 mm for the buckling scenario). If gap studies are performed in the future, this result is an important finding: the effective OML of the LE would change if a flexible, rubber gap insert was used. Thus, a rigid gap insert (e.g. plastic, metal) is recommended.

Linear-Actuator Static-Load Tests

As portrayed in the Structural and Displacement Analysis section earlier, the linear actuators did not have a company-rated yield strength. In-house static-load tests were performed to proof this component for the usage in the SWIFTER model. This was important for the assumptions made in the structural analysis.

One linear actuator was fastened vertically with the axis parallel with gravity. It was tested by hanging known weights from the lead screw. The unpowered test proved that the linear actuator was capable of supporting 890 N (200 lb) without yielding or failing. It was not necessary to prove a larger force. Powered tests proved that the actuator could support up to 530 N (120 lb) while traversing the lead screw without stalling. The company provided the traversing axial-load capability of 450 N (100 lb); this rating was used for the component force analysis in the Structural and Displacement Analysis section.

A secondary static-load test was to create a power optimization curve to find the best desired axial-force capability and actuator-speed combination. The dynamic axial force provided by the actuators generally decreases with increase of speed. The experimental setup is similar to the setup shown in Fig. 42b. Only one load was applied to the LE at x/c = 0.07. The LE was forced to compress the load cell until the actuators stalled; this provides the maximum force all four step-direction linear actuators could apply as an assembly. Six different actuator speeds were tested and the results are shown in Fig. 43.

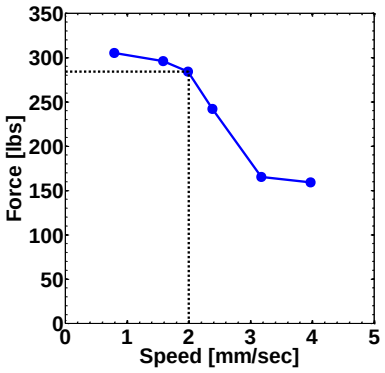

Fig. 43 Linear-actuator power optimization

The speed of 2 mm/sec and force of 1,260 N (284 lb) was selected for the best-desired speed and force combination. An important note is that these forces are slightly conservative because the loading in-flight will be more uniform across the span, instead of mainly centered around midspan. The maximum LE lift is 1,180 N (265 lb); consequently, these results portray that the LE can be moved in any flight condition, within the model angle of attack and aircraft speed limitations.

Conclusions

It was proven that SWIFTER's minimum FOS_y is greater than 1.9 for model angles of attack between -11° and 7° with aircraft speeds up to 175 KIAS during a 2-g, collision-avoidance maneuver. The model proved that it can withstand 1.5 times the maximum loading through a series of static-load tests. Special care was taken to ensure that the applied loads on the LE and MB simulated the actual total load and moment as realistically as possible. Lastly, it was shown in the static-load tests with a traversing actuator that the LE can translate in the step direction at any flight condition, within our aircraft limitations. After these static-load tests were complete, the Air Force granted permission to perform SWIFTER's clearance flight on the Cessna O-2A.

III. FLIGHT-TEST ANALYSIS AND CLEARANCE FLIGHT

After the Air Force approved the safety analysis and static-load tests of SWIFTER, the test article was mounted to the Cessna O-2A and prepped for the clearance flight tests. There are two main objectives for the clearance flights: (1) characterize the aircraft's handling qualities, and (2) test the aircraft for any flutter characteristics within the flight envelope. First, a flight-test analysis is presented to describe the main differences between SWIFTER and SWIFT: flight profiles, directional stability, high-speed flutter, and model mounting orientations are discussed. Then, the experimental configuration and operational test procedures for the clearance flight are documented, and lastly the clearance flight results are presented. The SWIFTER results are compared to the results obtained during a previous SWIFT clearance flight.

A. Flight-Test Analysis

The experience gained and lessons learned from the SWIFT flight program was helpful in planning the SWIFTER flight experiment. Since the two test articles are similar, this flight-test analysis section describes the new features of SWIFTER, relative to SWIFT, that influence each flight-test characteristic. Detailed flight-test analysis of SWIFT can be found in Ref [43-45].

Flight Profile

SWIFT's flight profile required a level flight at high altitude for approximately 20 minutes (i.e. cold soak) and then a high-speed dive until 3,000 ft (i.e. data collection). The cold soak and dive combination was necessary for the success of IR thermography with SWIFT: the cold surface would then be heated by the higher ambient temperature at the lower altitudes during the dive profile. In contrast, SWIFTER has an internal heating sheet to provide the necessary temperature differential. Therefore, the lengthy cold soak is eliminated, and IR thermography can be performed in all three phases of flight (climbout, level, and dive). A summary of the potential SWIFTER flight profiles is included in Table 10.

Table 10 SWIFTER potential flight profiles

	Altitude (ft)	KIAS	*Re´* (1/m)
Climbout	3,000 – 12,500	90 – 110	2.80 – 3.80 x 10^6
Level flight	12,500	90 – 130	2.80 – 4.00 x 10^6
	3,000	90 – 130	3.00 – 4.40 x 10^6
Dive	12,500 – 3,000	130 – 175	4.00 – 6.00 x 10^6

The lower limit on the altitude band is implemented for safety concerns: the highest obstacle in the test area is approximately 2,000 ft. The higher limit is the highest altitude one can fly at without supplemental oxygen provided to the flight crew for extended periods of time. The indicated airspeed shown in Table 10 is the approximate speed of each maneuver (based on experience with the O-2A). The *Re´* listed is an approximate minimum and maximum for each configuration based on standard atmospheric quantities. It is important to note that all results shown in this dissertation are using only the dive profile. The effective leading-edge sweep, Λ, that SWIFTER experiences is dependent on the pitch angle of the aircraft. A near-zero aircraft pitch angle (measured from the 5HP) is desired for this experiment to make the assumption that Λ is nominally 30°. This can only be achieved during a dive profile with the O-2A, which is beneficial to achieve the larger *Re´* applicable to the transport class of aircraft. The O-2A and SWIFTER have the capability to test combinations of lower Λ and lower *Re´* without any modifications, which is left to future experimenters. If SWIFTER was altered to explore a different Λ, the pylon-mount part could be modified to include a sloped (forward to aft) interface to the channel part, in order to change the nominal Λ of SWIFTER.

Center of Gravity Movement

In an effort to establish SWIFTER as a candidate for flutter clearance through similarity, the center of gravity (CG) of SWIFTER is required to be at the same aircraft station number, 3.71 m (146 in, datum in front of propeller along X-axis with positive direction pointing towards tail), as all previously flown ordnances by the US Air Force ([43]). SWIFTER's CG moved approximately $\Delta X \approx 150$ mm (5.9 in, forward) and $\Delta Z \approx 48$ mm (1.9 in, towards floor of cabin) referenced from SWIFT's CG, due to the additional weight for the movable leading-edge assembly. The airfoil structure was moved aft, relative to the mounting structure (channel and pylon-mount parts), approximately by the same amount of $\Delta X \approx 150$ mm (5.9 in).

Thus, SWIFTER's CG location in the *X*-axis is the same as all of the previously flown US Air Force ordnances (and SWIFT), and SWIFTER is a candidate for flutter clearance through similarity.

A CFD analysis was performed to examine the effect of SWIFTER's airfoil structure moving aft relative to the aircraft. A concern was that the influence of the O-2A's wing would become more apparent in the pressure distribution near the test region of SWIFTER. A pressure distribution comparison and SWIFTER's streamlines are shown in Fig. 44.

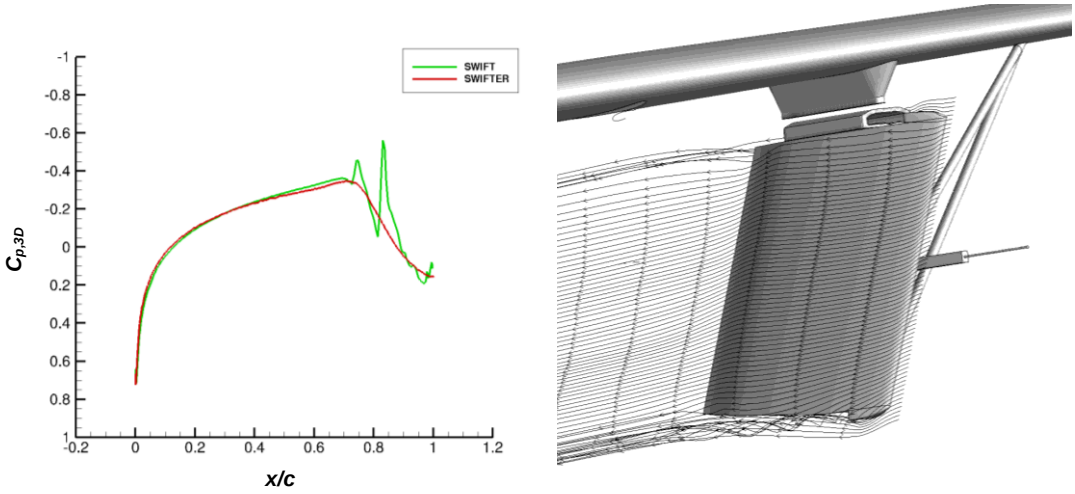

a) **b)**

Fig. 44 CG movement analysis (graphics by Matthew Tufts and used with permission), a) midspan $C_{p,3D}$ cut comparison between SWIFT and SWIFTER, both at α = -4.50° and Re' = 5.50 x 10^6/m, b) SWIFTER streamlines

SWIFTER's test-surface pressure distribution is essentially the same as SWIFT's pressure distribution, as shown in Fig. 44a. Also, the O-2A's influence on the streamlines over SWIFTER's test surface can be seen qualitatively in Fig. 44b. It appears that the shift of SWIFTER's airfoil structure aft relative to the aircraft is not a significant effect.

Directional Stability

Directional stability at low speeds was deemed acceptable during the flying-quality flights with SWIFT installed onto the O-2A ([52]). Since SWIFTER is nearly identical to SWIFT, a significant change in

directional stability characteristics at low speeds was not expected. As a conservative flight-testing measure, a buildup approach is used during the low-speed, flying-quality maneuvers of the clearance flight with both the landing gear extended and retracted.

The takeoff and landing crosswind limitations were modified and approved by the Air Force for the usage of SWIFTER. Fig. 45 portrays how the crosswind limits are modified due to different asymmetric loading scenarios for both the inboard and outboard pylons ([53]).

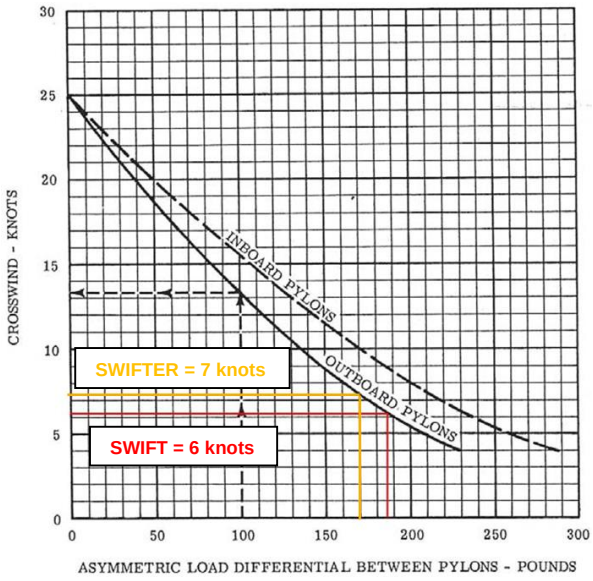

Fig. 45 Crosswind/asymmetric load limitations (modified from [53])

SWIFT's crosswind limit was 6 knots due to an asymmetric weight of approximately 185 lb. This asymmetric loading is caused by SWIFT on the port wing, but counterbalanced by the weight of the hotwire sting mount (32 lb) and additional fuel (36 lb) on the starboard wing. SWIFTER's crosswind limit is slightly improved to 7 knots due to an asymmetric weight of approximately 170 lb. This is caused by the 15 lb reduction in SWIFTER relative to SWIFT. This 1 knot improvement was rarely needed due to typically having three runways at Easterwood airport for takeoff and landing. However, any go/no-go improvements are always desired for a flight test program.

The go/no-go decision matrix was modified to include the crosswind amendment and the full matrix is included in APPENDIX B. Another amendment was the maximum and minimum beta angle: -11° to +7° are the SWIFTER beta limits. All other items in the go/no-go matrix are kept the same as the SWIFT flight experimentation.

An examination on the changes of the flare attitude and bank-angle limitations during takeoff and landing are necessary due to the changes in SWIFTER relative to SWIFT. A graphical schematic indicating the two angles examined are shown in Fig. 46.

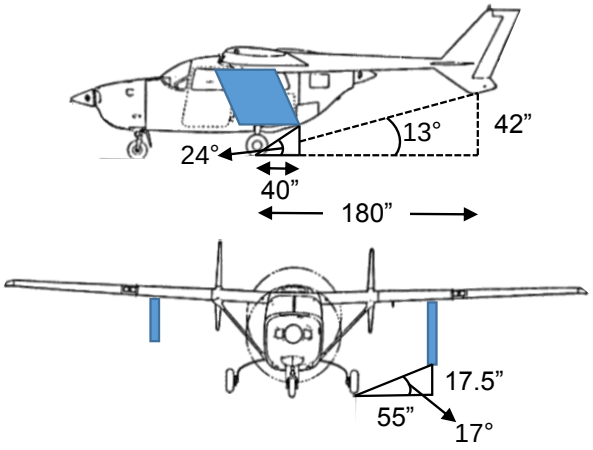

Fig. 46 SWIFTER flare attitude (top) and bank-angle (bottom) limitations during takeoff/landing

The flare angle decreases from 27° to 24° for SWIFTER, due to SWIFTER's airfoil structure moving approximately 150 mm (5.9 in) aft relative to the aircraft (described in Center of Gravity Movement section). However, this is not an issue because the maximum flare angle is still 13° due to the O-2A's tail: the tail will always hit the ground first before SWIFTER's aft tip hits the ground. The bank-angle limitation is calculated by simulating a 4° flare during landing. Both SWIFTER and SWIFT have the same vertical ground clearance: approximately 521 mm (20.5 in) without 4° simulated flare. Consequently, the bank-angle limitation of 17° is identical for both test articles.

Flutter at High Speeds

There were two types of flutter that could be experienced with SWIFTER fastened to the O-2A: the model could flutter and/or the aircraft could flutter. It was highly unlikely that the model would flutter, due to its stiff airfoil structure. Also, it was highly unlikely that the O-2A would flutter with SWIFTER attached because of the results of the previous ordnance tests performed by the Cessna Aircraft Company ([54]). Several ground-vibration and flutter-analysis tests were performed with different ordnances attached to the aircraft. It was shown that the critical mode for failure is a hump mode at 155 KIAS. The critical mode is a symmetric empennage bending mode, which is shown to be insensitive to wing store configuration. Similarly to SWIFT, SWIFTER attempted to receive clearance through similarity based on the ordnances already flown by Cessna. This was achieved by placing the model's CG at the same location as the previously flown ordnances (Station 146). Another requirement for clearance through similarity is that the pitch moment of inertia of SWIFTER needed to be lower than the previously flown ordnances.

Table 11 Pitch moment of inertia comparison

Ordnance	**Weight (lb)**	**CG location (Station Number)**	**CG location below rivet pattern (in)**	**I_{yy} about CG ($lb \cdot in^2$)**	**I_{yy} about rivet pattern ($lb \cdot in^2$)**
SUU-11A/A minigun	325	146	11.0	180,500	219,600
SUU-14/A bomblet dispenser	250	146	~8.7	139,200	158,100
SUU-14 – 350 modified bomblet dispenser with 100 lb ballast	350	146	~8.7	195,400	221,900
2 SUU-14/A bomblet dispenser (inboard and outboard) w/o ballast	500	146	~8.7	278,400	316,200
SWIFT with strut and 12 lb insert	226	146	25.0	116,200	257,500
SWIFT with strut and without 12 lb insert	214	146	26.0	104,500	249,400
SWIFTER	233	146	28.0	123,000	305,600

A major contributor to an aircraft's flutter characteristics is the pitch moment of inertia of the ordnance attached to the aircraft. A comparison of the pitch moment of inertias, I_{yy}, of previously flown ordnances and SWIFT/SWIFTER is shown in Table 11 ([43]).

SWIFTER and SWIFT's I_{yy} about the CG is lower than all of the previously flown ordnances. However, a common datum is needed to compare all of the pitch moment of inertias. The rivet pattern on the O-2A is the datum and the parallel axis theorem is used to calculate the I_{yy} about the rivet pattern. SWIFTER clearly has a larger I_{yy} about the rivet pattern than SWIFT: this is due to both having a larger weight and a CG 51 mm (2.0 in) farther below than SWIFT's CG. The values shown for SWIFT are directly from [43]. This represents an early design of SWIFT which had the option of inserting a 12 lb ballast inside SWIFT to shift the CG (this weight insert was not used). The final SWIFT weight is actually 247 lb, which adds approximately 13,000 lb·in^2 to the values shown in Table 11 (this only accounts for the weight difference - the final CG is unknown). This weight difference is pointed out to the reader to not confuse the correct weight of SWIFT (247 lb) and that SWIFTER's I_{yy} increase from SWIFT is smaller than what is shown. Nonetheless, the major point of Table 11 is that SWIFTER has a lower I_{yy} about the rivet pattern than the previously-cleared ordnance setup of two bomblet dispensers. Therefore, SWIFTER falls within the ordnance envelope already tested and is cleared through similarity.

As a conservative flight-testing measure, accelerometers were placed on the vertical tail in order to examine the potential critical flutter mode. The empennage vibration characteristics were monitored in real time during the clearance flights.

Electrical Analysis

SWIFTER has a large addition in its electrical needs compared to SWIFT; thus, a detailed electrical analysis is necessary to provide sufficient total power and to avoid the potential for electrical fire. The power inverter onboard the O-2A provides a potential 1,100 W for all electrical systems and instrumentation. The electrical components are split up into three groups: 12 VDC, 24 VDC and 110 VAC. Also, the power budget is split up into three sources: SWIFTER control box (Table 12), pressure-transducer box (Table 13), and the total SWIFTER power budget (Table 14).

Table 12 SWIFTER control box power budget

	Load		Qty	Current Draw		Fuse Rating	Total Wattage
				Each	Total		
24 VDC	Electromagnet		1	1.3 A	1.3 A	2 A	31 W
	Root stepper motors		3	0.7 A	2.1 A	3 A	50 W
	Tip stepper motors		3	0.7 A	2.1 A	3 A	50 W
	Heater PID controller		1	0.8 A	0.8 A	2 A	20 W
	Sensor power supply		1	125 mA	125 mA	250 mA	3 W
				Total	6.5 A	8 A	155 W
				Available	8.3 A		200 W
110 VAC	24 VDC power supply	max	1	2.2 A	2.2 A	2.5 A	242 W
		typical	1	1.7 A	1.7 A		189 W
	Forward heater		1	1.8 A	1.8 A	2 A	200 W
	Aft heater		1	2.7 A	2.7 A	3 A	300 W
	DAQ		1	0.8 A	0.7 A | 0.8 A	2 A	78 W | 88 W
				Total	7.0 A | 7.1 A	8 A	767 W | 777 W

Table 13 Pressure-transducer box power budget

	Load		Qty	Current Draw		Fuse Rating	Total Wattage
				Each	Total		
12 VDC	Heat sink fan		2	0.8 A	1.5 A	-	18 W
				Total	1.5 A	-	18 W
				Available	1.6 A	-	19 W
24 VDC	Pressure transducers		4	15 mA	60 mA	1 A	1 W
	Circulation fans		2	0.1 A	0.2 A		6 W
	12 VDC power supply	max	1	0.9 A	0.9 A		21 W
		typical	1	0.8 A	0.8 A		20 W
	TEC		1	6.0 A	3.3 A | 6.0 A	-	80 W | 144 W
				Total	4.5 A | 7.1 A	-	107 W | 171 W
				Available	8.8 A	-	211 W
110 VAC	24 VDC power supply	max	1	2.2 A	2.2 A	-	243 W
		typical	1	1.7 A	0.9 A | 1.7 A		123 W | 214 W
	Temperature display		1	40 mA	40 mA	-	4 W
	Transducer box PID temperature controller		1	40 mA	40 mA	-	4 W
				Total	1.2 A | 2.0 A	2.5 A	131 W | 222 W

Table 14 Total SWIFTER power budget

	Load	Current Draw	Total Wattage
110 VAC	SWIFTER box	7.0 A | 7.1 A	767 W | 777 W
	Pressure transducer box	1.2 A | 2.0 A	131 W | 222 W
	IR camera	0.3 A | 0.5 A	34 W | 62 W
	Laptop	0.6 A	70 W
	Pilot display	0.1 A	14 W
	Two DAQ boards	0.2 A | 0.4 A	20 W | 40 W
	Carbon monoxide monitor	35 mA	4 W
	Pressure scanner	0.2 A	17 W
	Total	9.6 A | 11.0 A	1,057 W | 1,206 W
	Available	10 A	1,100 W

Some of the cells for the current draw and total wattage columns are split into two cells: the left cell is the typical requirement and the right cell is the absolute maximum power. For example in Table 12, the DAQ boards can require an absolute maximum of 88 W (if all inputs and outputs are used), but all of the outputs are not needed. Thus, typically only 78 W is used during SWIFTER experimentation. For example in Table 14, the IR camera requires 62 W while the camera initially cools itself, and then 34 W after the cooling process is complete. It is important to note that a power efficiency is applied to each power supply. For example in Table 13, the 24 VDC power supply typically requires 107 W at 24 VDC, but the power efficiency of 87% results in 123 W needed at 110 VAC. Each power supply has the rated maximum power available, and also it has the typical power required by each system (split into two rows for each table). The main point is that the absolute maximum power required by each system is lower than the rated maximum power available provided by the power supply.

The temperature-controlled pressure-transducer box is a new addition for the SWIFTER experiment. In previous SWIFT experiments, the pressure transducers previously received 28 VDC power supply directly from the aircraft battery; a power switch, to control the pressure transducers, was next to the inverter switch on the O-2A's instrumentation panel. The two power switches allowed the AC and DC components to be shut down separately by the test pilot in the event of an emergency. However, this option did not prove to be operationally useful. In an effort to minimize the error due to temperature drift, the pressure transducers were placed inside an in-house-built, temperature-controlled box. A thermoelectric cooler (TEC), with heat

sinks inside and outside the box, is used to cool and heat the insulated pressure-transducer box. A PID controller adjusts the duty cycle of the TEC based on the temperature measurement by a RTD placed in the middle of the box. The transducers need approximately 1 hour of warm-up time (temperature controlled); thus, this led to changing the power source from the aircraft battery to a 24 VDC power supply that is installed on the instrumentation rack. This 24 VDC power supply can still be turned off in an emergency, along with all other SWIFTER electronics, by the test pilot through the inverter switch on the O-2A's instrumentation panel.

Table 14 portrays that 1,057 W is typically required, while the maximum available power is 1,100 W. Most of the power requirements shown are the rated absolute maximum power needed for each component; thus, this is a conservative power budget. Also, the laptop power requirement varies based on the computer's current computations (i.e. the power required can be much lower than 70 W). Lastly, the TEC power is typically negligible by the beginning of the flight. The pressure-transducer box (pressure transducers and TEC) are turned on for approximately an hour before the beginning of the flight. Typically by flight time, the temperature inside the box has reached steady state and the power required by the TEC is minimal.

All components inside the SWIFTER control box have a separate fuse for each component. Each component has an indicator light on the outside of the box, as shown in Fig. 20. Also, most other electrical systems either have fuses or internal fail-safe mechanisms. Shielded twisted pair/triple wiring is used for all sensor lines. All wiring (including sensor lines) use aircraft grade wiring with Tefzel insulation (rated to 150 °C). All harnesses are sheathed with flame retardant sheathing, and all wiring is secured to the frame of the SWIFTER control box, O-2A instrumentation rack, or the internal pylons of SWIFTER.

In terms of electrical safety for the heating sheet, a ground-fault circuit interrupter is used; if a short circuit is detected in the resistive heating wire, the interrupter will shut off the electrical circuit. Also, a foam-rubber insulation covers the entire heating sheet with a rating for flame and smoke (ASTM E84 25/50). Since SWIFTER is heated, it is important to note that all electronics or components inside the model have a temperature rating greater than 85 °C (Velcro has the smallest temperature rating). A ground test of the heating sheet, without surface convection, resulted in a maximum internal-cavity temperature differential of approximately 12 °C above the ambient temperature. On a summer afternoon, the maximum ambient

temperature could be up to 40 °C; thus, the internal temperature could reach 52 °C. In conclusion, all components are rated for the temperature range that is expected for the flight and wind tunnel experiments.

SWIFTER and SWIFT Comparison

In an effort to reduce the aircraft sideslip needed to achieve experimental model angles of attack, SWIFTER's β_{offset} was changed to 4°, instead of the 1° used for SWIFT. Fig. 47 is a schematic that portrays the model offset with the freestream velocity vector, U_∞. This mounting angle adjustment is made in SWIFTER's channel part: the channel's bolt holes that interface with the airfoil structure are 4° off the pylon's centerline. SWIFT has an angle adjustment through a lead-screw mechanism inside the pylon mounting assembly. It was decided that an angle adjustment was not necessary for SWIFTER due to the added complexity and the fact that the β_{offset} was never changed from the 1° during the SWIFT campaign.

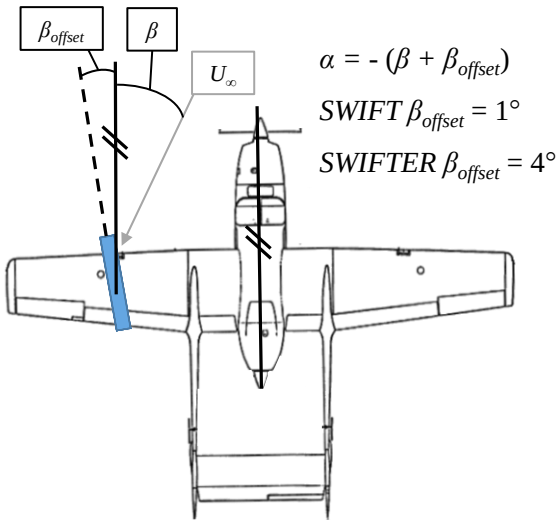

Fig. 47 SWIFTER and SWIFT β_{offset} schematic (angles are exaggerated for visualization purposes)

At the high-speed configuration, the lift force produced by SWIFTER with zero aircraft sideslip is minimal (80 N, 18 lb, α = -4.00° at 175 KIAS). During the design stage of SWIFTER, this was predicted to be the nominal experimental configuration. The goal was to help the test pilots with holding conditions and not sustaining large aircraft sideslip for the experiment. Once experimentation began, the nominal

experimental configuration changed and the β angles used were 2.50° and 3.50° (α = -6.50° and -7.50°, respectively). In contrast, the aircraft sideslip with SWIFT would need to be 5.50° and 6.50° to achieve the same angles of attack. This beta-offset modification from SWIFT to SWIFTER proved to be beneficial and the goal of assisting the test pilots was achieved.

B. Clearance Flight: Experimental Configuration and Planning

During the clearance flight, SWIFTER's movable leading edge was kept locked at zero step and zero gap with the electromagnet engaged. A new five-hole probe was used for the first time during these clearance flights. It is the same functional design as the five-hole probe used with SWIFT. Fig. 48 shows SWIFTER attached to the aircraft with the dual-strut assembly and the new five-hole probe.

Fig. 48 Preflight preparations for SWIFTER clearance flight, left – Lt. Col. Aaron Tucker (test pilot), right – Glen Duncan (FTE)

PCB Piezotronics accelerometers were mounted to the aircraft's port wingtip and vertical tail, and the tip of SWIFTER (Fig. 49). Two triaxial (Model 356A32) and three uniaxial (Model 302A) accelerometers were used. The triaxial accelerometers have a sensitivity of 100 mV/g and the uniaxial accelerometers have a sensitivity of 10 mV/g. The triaxial accelerometers can measure a frequency range of 1 to 4,000 Hz (±5%), and the uniaxial accelerometers can measure a frequency range of 1 to 5,000 Hz (±5%). All accelerometer traces were sampled at 1,000 Hz; thus, the maximum frequency that could be resolved is 500 Hz. The structural vibrations are expected to be below 100 Hz.

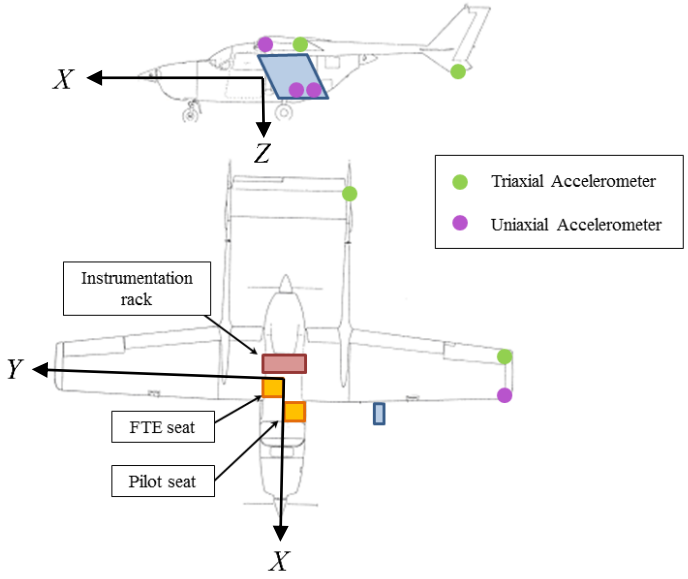

Fig. 49 O-2A and SWIFTER accelerometer locations and cabin configuration

The wingtip's uniaxial accelerometer monitored acceleration along the aircraft *Z*-axis, and the uniaxial accelerometers mounted inside SWIFTER monitored acceleration along the aircraft *X*- and *Y*-axes. The triaxial accelerometers are aligned with the aircraft coordinate system in Fig. 49. Tefzel-insulated, shielded twisted pair is used for wiring and is fastened internally throughout the port wing and empennage. Fig. 50 portrays pictures of the accelerometers for each of the three different locations. The vertical tail (Fig. 50b) shows a circular plastic connector with the shielded wiring behind it. The triaxial accelerometer is fastened inside the vertical tail and is hidden behind the shielded wiring.

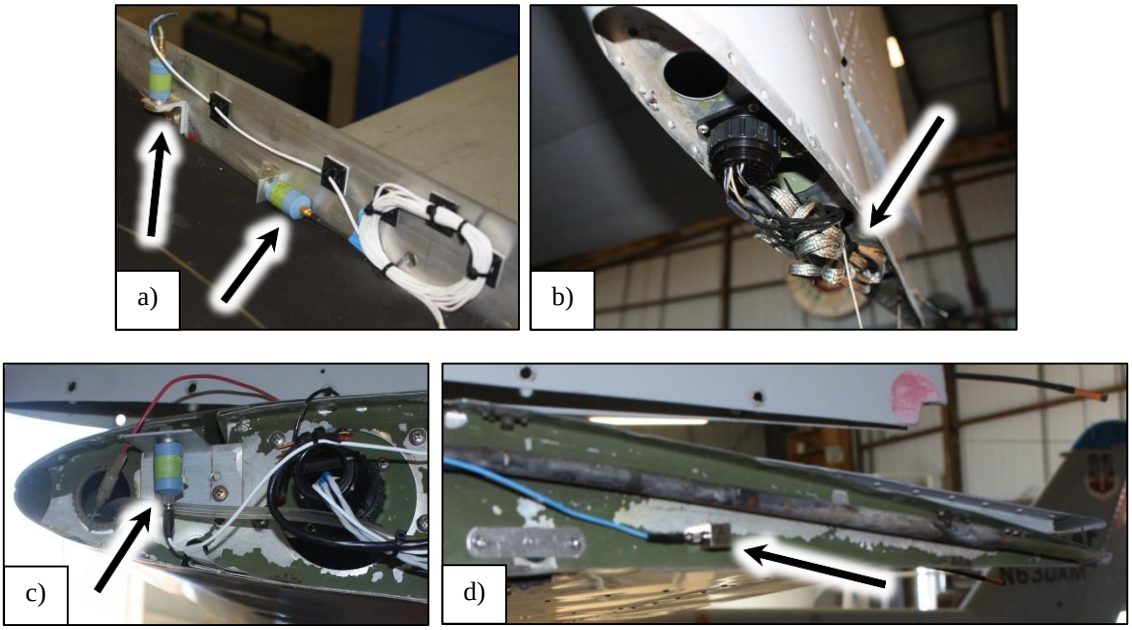

Fig. 50 Accelerometers, a) two uniaxial, SWIFTER, b) triaxial, vertical tail, c) uniaxial, wingtip leading edge, d) triaxial, wingtip trailing edge

Based on a review of the O-2A bailout procedures and several egress practice sessions, the copilot seat was removed from the aircraft for the SWIFTER clearance flight. This facilitated ground and in-flight egress for the test pilot and FTE.

Both crew members wore parachutes and flight suits for the initial SWIFTER flights. The pilot also wore a flight helmet with boom microphone. Smoke hoods and supplemental oxygen were also accessible for both crew members. Emergency parachutes were borrowed and inspected by a certified rigger. A 2-hour parachute training session was conducted with the owner of the parachutes and augmented by the test pilot's US Air Force training experience. A parachute training briefing was created which detailed:

1. Parachute preflight inspection procedures
2. Scenarios requiring bailout
3. Communications plan
4. Bailout procedures including a discussion of the parachute landing fall
5. Parachute malfunction procedures

The parachute training briefing was presented by the test pilot during the test card review and during the preflight briefing.

Weight and balance calculations showed that the final test configuration center of gravity was just forward (3.573 m, 140.7 in) of the aft limit (3.581 m, 141.0 in) with 44 gallons of fuel in the right main tank and 38 gallons of fuel in the left main tank. The center of gravity moved slightly forward with fuel burn. The lateral imbalance was 170 lb (port-wing heavy) and resulted in a 7-kt crosswind limit on landing. The test team elected to clear the forward center-of-gravity configuration by similarity with the SWIFT envelope clearance results ([44]).

Fig. 51 shows the setup of the instrumentation rack for the clearance flight. The SWIFTER control box was fastened to the bottom of the instrumentation rack. The internal heating sheet, linear actuators, temperature and displacement sensors, and electromagnet are all controlled by this box. The signal conditioners for the accelerometers were fastened on the top of the instrumentation rack. The triaxial signal conditioners are the two larger boxes on the left and the uniaxial signal conditioners are the three smaller boxes on the right.

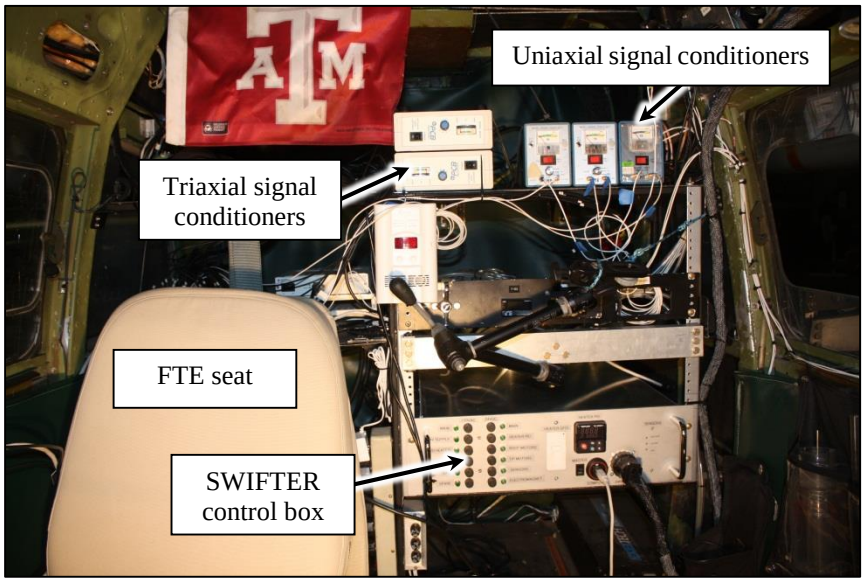

Fig. 51 Instrumentation rack (looking aft in the O-2A cabin)

C. Clearance Flight: Test Procedure

The test procedure for SWIFTER was modeled after the SWIFT clearance flights ([44]). The revision to the SWIFT test procedures was developed by Lt. Col. Aaron Tucker. Test cards were created to guide the execution of all handling quality and flutter test points during the clearance flight. The test plan is summarized below in Fig. 52, and all test cards are represented in APPENDIX C.

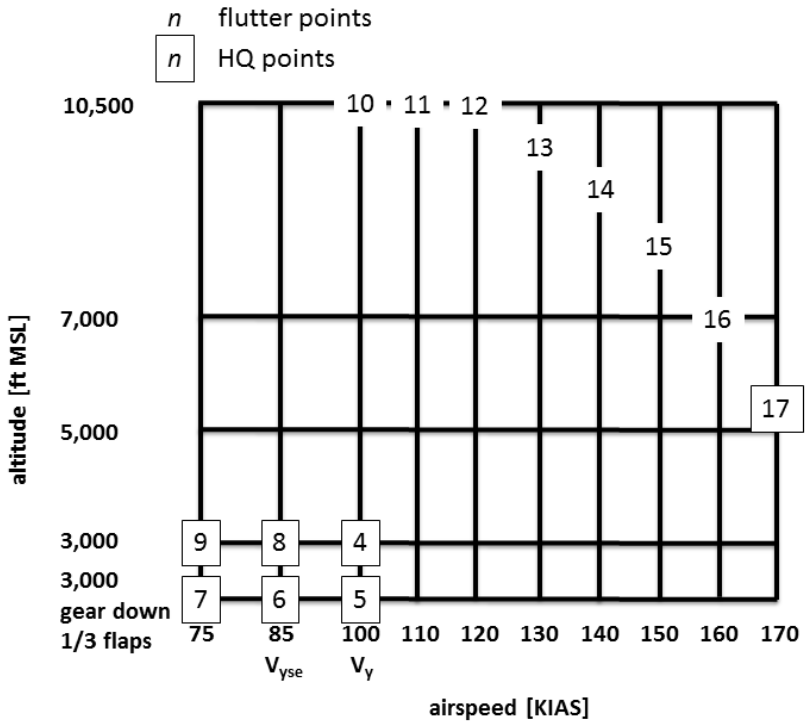

Fig. 52 Test plan for the SWIFTER clearance flight (test cards 4-17 shown) (graphic by Lt. Col. Aaron Tucker, USAF)

Test cards 1 through 3, not shown in Fig. 52, included a ground vibration check, electromagnetic interference check, and takeoff, respectively. Test cards 4 through 9 are low-speed handling quality checks including the landing configuration. Half of the maneuvers are performed with the landing gear and flaps up, and the other half are performed with the landing gear down and flaps deployed to $^1/_3$ deflection in the order shown in Fig. 52.

Test cards 10 through 16 are flutter test points within the altitude data band of 3,000 ft to 10,500 ft MSL. Indicated airspeeds of 100, 110, and 120 KIAS were achieved in level flight, while airspeeds ranging from 130 to 170 KIAS require an aircraft descent, as shown in Fig. 52. The last test card, 17, is both a handling quality and flutter check at the highest indicated airspeed of 170 KIAS. All speeds have a tolerance of ±5 KIAS; thus, the maximum allowable speed is 175 KIAS.

The complete description of the aircraft handling quality maneuvers is included in APPENDIX D. Each flutter test card followed a procedure including a trim shot, pitch rap, roll rap, pitch doublet, and rudder doublet. Each handling-quality test card included all maneuvers from the flutter test cards and also included a 30° to 30° bank roll, steady-heading sideslip, and wind-up turn. All raps and doublets used a buildup approach to clear each flight condition. The flight-control deflection incremented from ¼ to ½ to ¾. Rudder and aileron inputs also included a full throw input. The bank roll and steady-heading sideslip included maneuvers both to the left and right. The aircraft sideslip limits for SWIFTER of +7° to -11° were observed. Also, a bank angle limit of 45° was imposed on the steady-heading sideslip and wind-up turn.

The FTE conducted the test and directed the progression of the specific maneuvers with the test pilot, as portrayed in the communications plan in APPENDIX C. The main responsibility of the FTE is to monitor all of the accelerometer readings during each control input. If the accelerometer readings were within limits, the FTE would direct the pilot to the next increment of control deflection or next maneuver, as appropriate. A three-fold amplitude increase or signal phase lock in response to the pilot's input for any accelerometer reading could indicate structural resonance; thus, if occurred, the maneuver is immediately aborted and the aircraft is returned to a stabilized flight condition. Other general test limits and the go/no-go table are included in APPENDIX B.

In order to monitor the accelerometer data, the FTE monitored the raw accelerometer output voltages with a high-pass filter of 0.5 Hz (AC coupling). This removed the DC component of the voltages and simplified the task of monitoring multiple, simultaneous accelerometer signals in the time domain. Also, the voltage scales were adjusted to portray three times the baseline acceleration amplitude at each flight condition. Therefore, a three-fold amplitude increase could be observed as a full-scale deflection of the accelerometer signal after the aircraft responded to the test pilot's input. It is important to note that each

flight condition had different baseline acceleration, and the scales had to be adjusted accordingly as the aircraft speed increased.

The FTE recorded accelerometer and five-hole probe readings for each test card on the flight computer. It was the FTE's responsibility to record aircraft overshoots (i.e. number of times the aircraft oscillated past the neutral point) and settling times (i.e. how long it took the aircraft to stop oscillating) on the test cards. The test pilot would count out loud the number of overshoots, while the FTE used the stopwatch to measure the settling time. Any comments about specific maneuvers or overall aircraft handling qualities were documented on the test cards by the FTE.

D. Clearance Flight: Results

The clearance flights were performed on 29 Dec 2012; two successive sorties were executed totaling 2.2 flight hours. A conservative buildup approach in airspeed and flight-control deflection was used during the clearance flight. Before the SWIFTER clearance flight, the test pilot and flight test engineer (FTE) practiced the entire procedure using the existing test article, SWIFT, mounted to the Cessna O-2A on 12 and 13 Dec 2012. This practice flight enabled the FTE to gain experience with monitoring accelerometer flight data, and it exercised the in-flight communication and coordination between the test pilot and FTE. Additionally, the practice flights provided the crew a baseline to compare the aircraft's handling qualities directly between SWIFT and SWIFTER.

The notable results from each test card will be discussed. Approximate damping ratios from the recorded number of overshoots will be documented and compared to aircraft performance standards. Lastly, a comparison of the aircraft's accelerometer readings of the port wingtip and empennage with SWIFT and SWIFTER attached is shown.

Ground Tests Results

The first test was the ground vibration check accomplished on 20 Dec 2012. Both engines were started and advanced to a maximum RPM of 2,600 separately first, and then in unison. No three-fold amplitude increase or phase lock was observed. The engines were then shut down and the model was inspected. There were no signs of cracks, deformation, or loosening of any hardware.

The team proceeded to the next test of electromagnet interference (EMI) with the aircraft's avionics and flight instruments on 20 Dec 2012 caused by the additional SWIFTER electronics. All communication checks included radio transmissions to the flight lab's handheld radio (ground crew's responsibility) and Easterwood airport's ground frequency. A ground source was initially used to power all the SWIFTER electronics while the communication check commenced using the aircraft battery power for the avionics. All of the SWIFTER electronics, including the heating sheet, were power cycled to detect any EMI. The first EMI test showed no interference caused by SWIFTER's electronics. After completing the EMI testing using a ground source, the SWIFTER electronics were plugged into the aircraft's power inverter for another EMI test. A communication check was completed with the front engine at idle and the rear engine at 1,800 RPM to provide sufficient power to the inverter with the heating sheet operating. There were no indications of EMI with the aircraft's avionics or flight instruments. After the ground tests were complete, the aircraft was cleared for takeoff (card 3) and the crew continued with the rest of the clearance flight.

In-Flight-Recorded, Aircraft-Handling Qualities

The first flight was on 26 Dec 2012 for 1.0 flight hour. A sign reversal on the pilot's aircraft sideslip gage forced an abort during the first handling-qualities test card. This sideslip calibration error was corrected and the next flight was on 29 Dec 2012. All test points were completed in two, successive sorties of 1.0 and 1.2 flight hours.

There was a minimal difference in handling qualities between SWIFT and SWIFTER during pitch raps, roll raps, and pitch doublets for all flight conditions, and no objectionable handling qualities or flutter characteristics were noted. After the pilot applied the above flight-control inputs, the aircraft quickly returned to the steady-state flying condition without oscillating. During the SWIFTER clearance flight, it was noticed that the minimum g limit (+0.5 g loading) was observed during the pitch rap and doublet maneuver with ¾ elevator deflection at 140 KIAS. The remaining higher speeds were limited to ½ elevator deflection to stay within g limits. The g limits (+0.5 to +2.0) represent an operationally-relevant traffic-avoidance maneuver, and the elevator deflections used during the flutter and handling-qualities test points are reasonable to complete such a maneuver. The handling qualities throughout the flight envelope were acceptable.

The FTE recorded the aircraft's response to the rudder doublets by recording the number of overshoots and settling times. The number of overshoots was examined instead of the number of oscillations because it was easier to monitor. The number of oscillations is simply half the number of overshoots.

Based on the number of oscillations, an approximate damping ratio can be calculated using Eq. (6). This equation is based on the settling time to get within 2% of the steady-state value, as shown Eq. (3) from [55], and it assumes the system is underdamped. The settling time and natural frequency can be defined as shown in Eq. (4)-(5) from [56], respectively.

$$T_s \approx \frac{4}{\zeta \omega_n} \tag{3}$$

$$T_s = \frac{2\pi n}{\omega_d} \tag{4}$$

$$\omega_n = \frac{\omega_d}{\sqrt{1-\zeta^2}} \tag{5}$$

$$\zeta \approx \sqrt{\frac{1}{\frac{n^2\pi^2}{4}+1}} \tag{6}$$

ζ is the damping ratio, n is the number of oscillations, T_s is the settling time, ω_d is the damped (observed) frequency and ω_n is the natural frequency of the system. The damping ratio for the short period and Dutch roll were examined for different levels of aircraft handling performance (MIL-F-8785C, [57]).Table 15 portrays the minimum damping ratio for three different handling levels for a Class I aircraft (small, light aircraft). Also, an approximate number of oscillations, computed from Eq. (6), is included for reference in Table 15.

An aircraft handling performance level 1 was expected for SWIFTER for the entire test envelope, based on experience with the O-2A with and without the SWIFT model. All pitch doublets for SWIFT and SWIFTER had zero overshoots. This confirms that both test articles meet the criterion for level 1 aircraft

handling performance for the short period mode (Table 15). The pitch handling-qualities were evaluated as acceptable.

Table 15 Minimum damping ratio for different aircraft handling performance levels

	Short Period		Dutch Roll	
Performance Level	*n*	**ζ**	*n*	**ζ**
1	< 2	> 0.30	< 8	> 0.08
2	< 3	> 0.20	< 32	> 0.02
3	< 4	> 0.15	Neutral	> 0.00

A quick reference to the aircraft configurations for each test card is shown in Table 16. In an effort to be more efficient during the SWIFTER clearance flight, test card 10 was performed on the climb out to 10,500 ft. This does not influence the results of this handling quality test.

Table 16 Aircraft configuration summary

Test Card	KIAS	Gear	Flaps	Trajectory
4	100	Up	Up	Level
5	100	Down	1/3	Level
6	85	Down	1/3	Level
7	75	Down	1/3	Level
8	85	Up	Up	Level
9	75	Up	Up	Level
10	100	Up	Up	Climb
11	110	Up	Up	Level
12	120	Up	Up	Level
13	130	Up	Up	Descent
14	140	Up	Up	Descent
15	150	Up	Up	Descent
16	160	Up	Up	Descent
17	170	Up	Up	Descent

The rudder-doublet number of overshoots varied depending on the flight configuration for both SWIFT and SWIFTER. A comparison between the SWIFT and SWIFTER rudder-doublet data is presented in Table 17.

Table 17 Rudder-doublet comparison between SWIFT and SWIFTER

Test Card	Rudder Doublet														
	SWIFTER												SWIFT		
	1/4 Deflection			1/2 Deflection			3/4 Deflection			Full Deflection			Full Deflection		
	T_s	OS	ζ	T_s	OS	ζ	T_s	OS	ζ	T_s	OS	ζ	T_s	OS	ζ
4	0	0	1.00	0	0	1.00	0	0	1.00	5	4	0.30	7	3	0.39
5	0	0	1.00	6	3	0.39	8	4	0.30	10	5	0.25	7	3	0.39
6	0	0	1.00	4	2	0.54	7	3	0.39	8	3	0.39	0	0	1.00
7	0	0	1.00	0	0	1.00	5	1	0.79	6	1	0.79	7	2	0.54
8	0	0	1.00	0	0	1.00	0	0	1.00	7	3	0.39	0	0	1.00
9	0	0	1.00	0	0	1.00	0	0	1.00	0	0	1.00	8	2	0.54
10	0	0	1.00	7	2	0.54	6	3	0.39	7	3	0.39	5	3	0.39
11	5	2	0.54	6	3	0.39	7	4	0.30	9	4	0.30	8	4	0.30
12	6	3	0.39	6	3	0.39	7	4	0.30	9	5	0.25	9	3	0.39
13	5	2	0.54	7	4	0.30	7	4	0.30	10	6	0.21	8	4	0.30
14	3	2	0.54	9	5	0.25	9	5	0.25	9	5	0.25	9	5	0.25
15	5	2	0.54	8	4	0.30	9	5	0.25	9	5	0.25	7	3	0.39
16	8	4	0.30	11	5	0.25	X	X	X	X	X	X	5	4	0.30
17	5	2	0.54	7	5	0.25	X	X	X	X	X	X	8	4	0.30

OS is the number of overshoots ($n = OS/2$). Due to time constraints, full-rudder deflection data were only collected for the practice clearance flights with SWIFT. Details about the original clearance flights in 2006 can be found in [44]. Also, when the number of overshoots is zero in Table 17, the approximate damping ratio is shown as 1. In reality, the aircraft could be overdamped. The 'X's' indicate that the flight maneuver was not performed due to the previous rudder-deflection magnitude causing an aircraft response that approached the aircraft sideslip limits. During the SWIFTER clearance flight, it was noticed that the positive aircraft sideslip limit was achieved with ½ rudder deflection starting at 150 KIAS. Therefore, the ¾ and full rudder deflection was not performed for 160 or 170 KIAS.

The estimated accuracy for the number of overshoots is ±1 overshoot and the accuracy for the settling time is ±1 second due to the analysis of hand-recorded data. The possible error in number of overshoots is due to the faintness of the last overshoot and the fact that only integer overshoots may be counted. The settling time was recorded in whole seconds.

Both SWIFT and SWIFTER had similar handling characteristics with a rudder-doublet input. SWIFT had an overshoot range from zero to five, while SWIFTER had an overshoot range from zero to six. The two biggest differences occur at 85 KIAS in the clean and landing configurations. At full-rudder deflection,

SWIFTER had three overshoots for both configurations, while SWIFT had zero overshoots. At the higher speeds of 120, 130 and 150 KIAS, the overshoot difference is two. Additionally, the approximate minimum damping ratio with SWIFTER was 0.21, while SWIFT was 0.25. This confirms that both test articles comply with the criterion for level 1 aircraft handling performance for the Dutch roll mode (Table 15).

As the amount of rudder deflection increased, the number of overshoots increased monotonically. The settling time did increase monotonically, as expected, for all flight conditions except at 100 KIAS. The settling time decreased from 7 to 6 seconds between ½ and ¾ deflection. This is likely due to the accuracy of the settling-time measurement made by the FTE.

The 30° to 30° bank roll had similar handling qualities for all flight conditions for both SWIFT and SWIFTER. After the roll input was initiated, the aircraft roll rate slowly increased until 10° of bank then decreased as the aircraft attitude passed through wings level. The roll rate increased again after 10° of bank on the opposite direction and accelerated until the maneuver was terminated at 30° of bank. This behavior was approximately symmetric and did not depend on the direction of roll. As expected, the magnitude of the roll rate increased with aircraft speed, but the observation persisted. This behavior was never deemed to be objectionable.

The steady-heading sideslip maneuvers were performed in both directions to the prescribed limits of +7° and -11° for SWIFTER and +6° and -8° for SWIFT. The results of the steady-heading sideslip maneuver are shown in Table 18.

Table 18 Steady-heading sideslip comparison between SWIFT and SWIFTER

Test Card	Flight Conditions				Steady-Heading Sideslip							
					SWIFTER				SWIFT			
					β = +7°		β = −11°		β = +6°		β = −8°	
	KIAS	Gear	Flaps	Trajectory	φ	*RD*	φ	*RD*	φ	*RD*	φ	*RD*
4	100	Up	Up	Level	2°	1/4	7°	1/2	—	—	—	—
5	100	Down	1/3	Level	4°	1/4	11°	1/2	10°	1/2	—	—
6	85	Down	1/3	Level	2°	—	9°	—	—	—	—	—
7	75	Down	1/3	Level	—	~0	5°	1/2	—	~0	—	—
8	85	Up	Up	Level	—	~0	5°	1/3	—	—	—	—
9	75	Up	Up	Level	—	Zero	3°	—	—	1/4	—	~0
17	170	Up	Up	Descent	11°	—	X	2/3	9°	—	X	2/3

φ is the aircraft bank angle, β is the aircraft sideslip angle measured by the five-hole probe, and *RD* is the amount of rudder deflection inputted by the test pilot. "—" indicates that the test point was not recorded during the flight. Also, "~0" indicates that a small rudder deflection was used to achieve the specified aircraft sideslip limit. Lastly, "X" indicates that the aircraft sideslip limit was never achieved with full rudder deflection.

The bank angle and rudder deflection data were only sporadically recorded. Therefore, a complete comparison of the sideslip data cannot be made. However, the highest speed tested, 170 KIAS, will be compared since it results in the highest structural loading on the test articles and aircraft. The positive sideslip limit resulted in approximately the same aircraft bank angle required to counteract the sideslip force due to sideslip angle. The negative sideslip limit could not be achieved for either SWIFT or SWIFTER. Approximately $^{2}/_{3}$ rudder deflection was applied at 170 KIAS, and approximately 670 N (150 lb) of rudder force was required. The test pilot elected to not increase the rudder force to achieve higher angles of sideslip because it wasn't a reasonable flight-control input for the flight-research mission.

At 170 KIAS, the maximum negative aircraft sideslip angle was $\beta = -2.0°$ for SWIFT and $\beta = -2.5°$ for SWIFTER. The limiting flight condition was a result of the balance of the moments generated by the rudders and the SWIFT/SWIFTER airfoil lift and drag. As the aircraft sideslip decreases, the angle of attack on the test articles increase. This causes a larger lift force along the aircraft *Y* axis produced by the test articles. The center of pressure of the test articles are aft of the aircraft center of gravity and are counteracting the rudder input by the pilot. At $\beta = -2.0°$, SWIFTER has a drag force of 89 N (20 lb), but has a large moment arm of 2.637 m (103.8") (aircraft centerline to outboard pylon). The lift force is about 430 N (97 lb) with a moment arm of about 150 mm (6.0") (aircraft center of gravity to the center of pressure of SWIFTER). The lift and drag force contribution to the yawing torque is approximately -5,200 N·m (-580 in·lb) and -18,400 N·m (-2,080 in·lb), respectively. As observed on the test flights, the maximum loading case of $\beta = -11°$ (minimum aircraft sideslip limit) cannot be achieved for either test article at the maximum test speed without excessive rudder forces. Therefore, this worst-case scenario (see Structural and Displacement Analysis section) is self-limiting during flight-research operations.

Post-Processed, Accelerometer-Signal Comparison

A comparison of the SWIFT and SWIFTER acceleration signals was made at the 170±5 KIAS flight condition. This condition was selected because it represents the maximum speed in the research envelope and results in the largest loads on the model and airplane. A fourth-order, infinite impulse response, lowpass, Butterworth filter at 10 Hz was applied to all the signals. The filtered, time-domain signals are plotted together for each flight maneuver, except the steady-heading sideslip and wind up turn: neither of these maneuvers generated signals of interest. A reminder is given that the accelerometer traces were not lowpassed while performing the clearance flight; thus, the baseline acceleration amplitude shown in the plots within this section are lower than what was observed during the clearance flight. This is an important distinction when the abort criterion is a three-fold amplitude increase in response to the input: a three-fold amplitude increase was never observed during the clearance flights.

The test pilot's flight-control input begins near the beginning of each trace. The wingtip and vertical tail accelerations are plotted for all maneuvers of interest. It is important to note that the maneuver input dictates which accelerometer will have the dominant signal. The pitch and yaw maneuvers significantly influence the vertical tail accelerometer while the roll maneuver significantly influences the wingtip accelerometer.

Fig. 53 shows the pitch-rap buildup approach with ¼ to ½ elevator deflection for SWIFTER. The vertical-tail, *Z*-axis accelerometer has the dominant signal. The input occurs approximately at 0.5 seconds and the signal exponentially decays. The amplitude of the ¼ deflection is clearly smaller than the ½ deflection for both the SWIFT and SWIFTER signals. The ½ deflection signals are nearly identical in the decay rate and vibrational frequency. No objectionable handling qualities were noted in this maneuver.

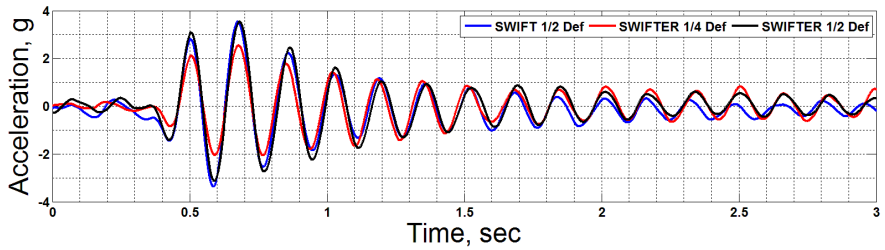

Fig. 53 Pitch-rap buildup: *Z*-axis, vertical-tail accelerometer

Fig. 54 shows the roll-rap buildup approach with ¼ to ½ to ¾ and full deflection for SWIFTER. The dominant signal is the wingtip, *Z*-axis accelerometer. The signal rapidly increases with the abrupt aileron input from the test pilot approximately at 0.3 seconds. SWIFT and SWIFTER with full aileron deflection have similar double peaks and then a fast decay to steady state. The initial amplitude after the aileron input grows with the increasing deflection input for the SWIFTER signals, except the ¾ deflection case. This could be due to a slight difference in the way the test pilot applied the rap maneuver. No objectionable handling qualities were noted in this maneuver.

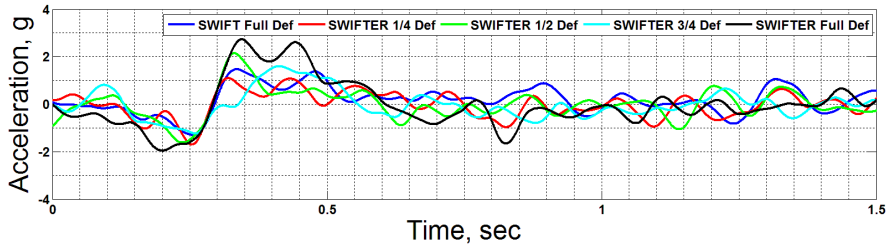

Fig. 54 Roll-rap buildup: *Z*-axis, wingtip accelerometer

Fig. 55 shows the pitch-doublet buildup approach with ¼ to ½ elevator deflection for SWIFTER. The dominant signal is the vertical tail, *Z*-axis accelerometer. The elevator input is approximately at 0.3 seconds. After the input, the average of the signal slowly decreases, increases, and then decays to steady state, all while vibrating at approximately 6 Hz. The ¼ deflection, initial amplitude is clearly smaller than the ½ deflection, initial amplitude, but the response amplitude is larger from 0.6 to 1.0 seconds. The decay rate

and vibrational frequency match well for all deflections. No objectionable handling qualities were noted in this maneuver.

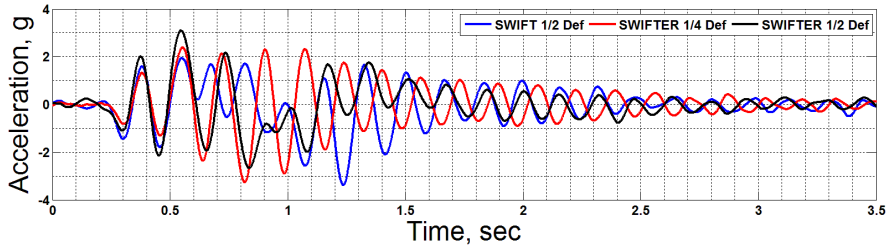

Fig. 55 Pitch-doublet buildup: *Z*-axis, vertical-tail accelerometer

Fig. 56 shows the rudder-doublet buildup approach with ¼ to ½ elevator deflection for SWIFTER. The dominant signal is the vertical tail, *Y*-axis accelerometer. The rudder input is approximately at 1 second. The ¼ deflection input is smaller in amplitude than the ½ deflection inputs. The decay rate and the low-frequency oscillations (< 1 Hz) match well for all deflections. The time scale for these charts was increased to 8 seconds to account for the longer settling time for the rudder doublet. No objectionable handling qualities were noted in this maneuver.

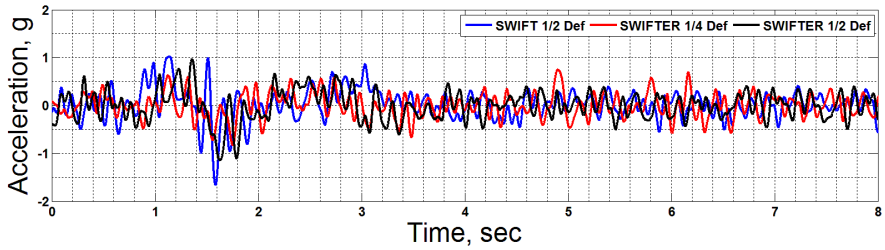

Fig. 56 Rudder-doublet buildup: *Y*-axis, vertical-tail accelerometer

The rolls left and right maneuvers do not have any interesting content within each time trace; thus, the figures are not included. Both maneuvers portrayed a spike in the wingtip, *Z* direction accelerometer with a rapid decay to the background vibration. The response after the input does not have an identifiable response like the rest of the maneuvers. No objectionable handling qualities were noted in both of these maneuvers.

Overall, SWIFT and SWIFTER showed similar effects on the aircraft based on the accelerometer data. After the SWIFTER clearance flight, all four panels were removed from the non-test side to investigate the internal structure. There were no signs of loosening of hardware, or any cracks or deformation in the structure inside or outside of the test article.

E. Clearance Flight: Conclusions

SWIFTER successfully cleared the entire flight envelope through aircraft handling-quality and flutter tests. There were no signs of the SWIFTER electronics causing electromagnetic interference with the aircraft's avionics and flight instruments. The short period and Dutch roll modes examined resulted in an aircraft performance handling level of 1 for a class I aircraft. The number of overshoots and settling times were documented at several aircraft configurations, and these details will be helpful for future clearance flights using the Cessna O-2A. Based on the test pilot's comments about the clearance flight, SWIFTER handled similarly to SWIFT. There were no noticeable differences in the handling qualities between the two test articles. The FTE never observed a rapid, three-fold amplitude increase or phase lock of the background acceleration signals in response to the test pilot's input during the clearance flights. Finally, SWIFT and SWIFTER's post-processed, acceleration signals at 170 KIAS had similar aircraft responses, decay rates, and vibrational frequencies for all flight maneuvers.

IV. EXPERIMENTAL METHODS

An extensive instrumentation suite is essential for this flight and wind tunnel experiment. An accurate instrumentation package is required to properly characterize the freestream orientation of the test article and the freestream properties. The surface pressures are also needed to compare and validate with the CFD results. A transition detection technique is vital to formulate critical step height values. Lastly, boundary-layer profiles in the wind tunnel provide additional detailed validation with CFD.

Summaries of the instrumentation for freestream characterization in each facility are presented. The five-hole probe used at the FRL has its own section to describe the complex calibration and model design implementations. Then, the instrumentation for the surface-pressure measurements are documented. To conclude, experimental setup and post-processing techniques for both the infrared thermography and hotwire anemometry are detailed.

A. FRL Instrumentation for Freestream Characterization

Fig. 57 portrays the experimental layout for the characterization of the freestream environment at the FRL. The 5HP, temperature probe, internal pressure-transducer box, and aircraft Pitot tube are indicated. The aircraft's Pitot tube displays the aircraft's indicated airspeed to the pilot, and it is not acquired during the experiment. It is needed so that the aircraft does not exceed the rated maximum airspeed during the experiment. The 5HP attached to SWIFTER acquires the freestream orientation, total pressure and static pressure. There is less than two meters of pneumatic-line travel from the tip of the 5HP to the pressure transducers inside the model; this length was kept to a minimum due to its negative influence on the 5HP's frequency response. Two electrical harnesses can be seen connecting to the underside of the O-2A's wing: one harness is strictly for SWIFTER hardware, while the other is for the pressure transducers connected to the 5HP (the pressure transducers can then be used with another test article, if necessary). The electrical harnesses travel through the wing into the cabin, and then to the instrumentation rack behind the FTE.

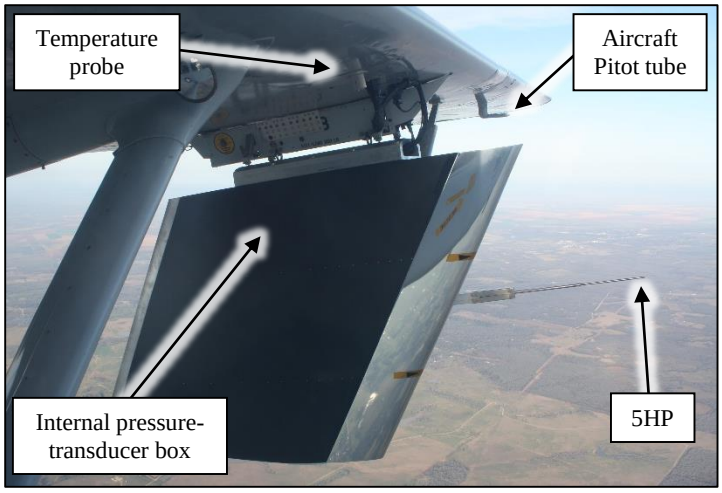

Fig. 57 FRL instrumentation setup for freestream characterization

A static-temperature probe from SpaceAge Control is mounted on the port, inboard hardpoint of the Cessna O-2A, as shown in Fig. 57. With a second-order polynomial curve fit, the accuracy of the internal 500 Ohm RTD is ±0.5 K. The small acceleration of the flow under the O-2A's wing is assumed to have a negligible effect of the temperature measurement.

a) **b)**

Fig. 58 Temperature-controlled pressure-transducer box, a) inside box, b) outside box

Four Honeywell Sensotech FP2000 pressure transducers are used for the 5HP measurements, and they can be seen in Fig. 58. Three transducers are differential sensors for the model angle of attack (α), pitch angle of the aircraft (θ_{AC}), and dynamic pressure (q) measurements with a range of ±14 kPa and accuracy of ±14 Pa. The remaining transducer is an absolute sensor for the freestream static pressure (p_s) measurements with a range of 103 kPa and accuracy of ±103 Pa. It is important to note that the transducer accuracies listed assume a 1 hour warm-up time; thus, the pressure transducers are turned on at the beginning of preflight of the aircraft to reach this threshold by engine startup. These accuracies (±0.1% full scale) are based on maintaining the constant calibration temperature; if the temperature varies, a temperature error of ±0.5% full scale has to be added to the accuracy of the sensors. It is obvious that the temperature changes drastically in the flight environment. Thus, a temperature-controlled box was created in house to contain the four transducers internally to the model and it is shown in Fig. 58. A thermoelectric cooler was placed inside the aluminum box with heat sinks placed on either side of this cooler (one inside the box and one outside the box). The thermoelectric cooler can provide up to 230 W of heating and 110 W of cooling for the box. A 100 Ohm RTD from Omega was placed inside the box to constantly monitor the internal temperature. To maintain a constant temperature, a PID controller was then used to automatically switch the thermoelectric cooler on and off during the flight. Also, 12 mm thick extruded polystyrene foam insulation was adhered to the walls of the aluminum box. The box can maintain the constant transducer calibration temperature throughout the entire flight to within 1 K. Two electrical connectors and one pneumatic connector provide a quick removal and installation, and they can be seen on the exterior of the box in Fig. 58b.

A thorough description of the 5HP with its unique calibration is included in the next Five-Hole Probe section.

B. Five-Hole Probe

A five-hole probe (5HP) is used to measure the α, θ_{AC}, q, and p_s. Aeroprobe manufactured the conical-tip 5HP (Fig. 59c) and calibrated the probe at Mach numbers of 0.2 and 0.3. A custom calibration grid consisting of 966 different calibration points was performed five times at each Mach number, so that

repeatability and hysteresis could be quantified. An α and θ_{AC} sweep from -16.20° to 16.20° was executed. The resolution of the calibration grid points becomes finer as zero is approached for both angles (Fig. 59a).

Model Angle of Attack (α) and Aircraft Pitch Angle (θ_{AC}) Calibration

A schematic of the main five ports of the probe is shown in Fig. 59b (pressure measurements, $p_{1\text{-}5}$), and additionally the 5HP has a static pressure ring of 8 ports 101 mm aft of the tip of the probe (p_6 is this static pressure measurement). Differential measurements between ports 2 and 3 are used for the model angle of attack, while differential measurements between ports 4 and 5 are used for the aircraft pitch angle. The total-pressure measurement is acquired through port 1. Calibration coefficients were used to perform an in-house calibration for α and θ_{AC}, as shown in Eq. (7)-(8).

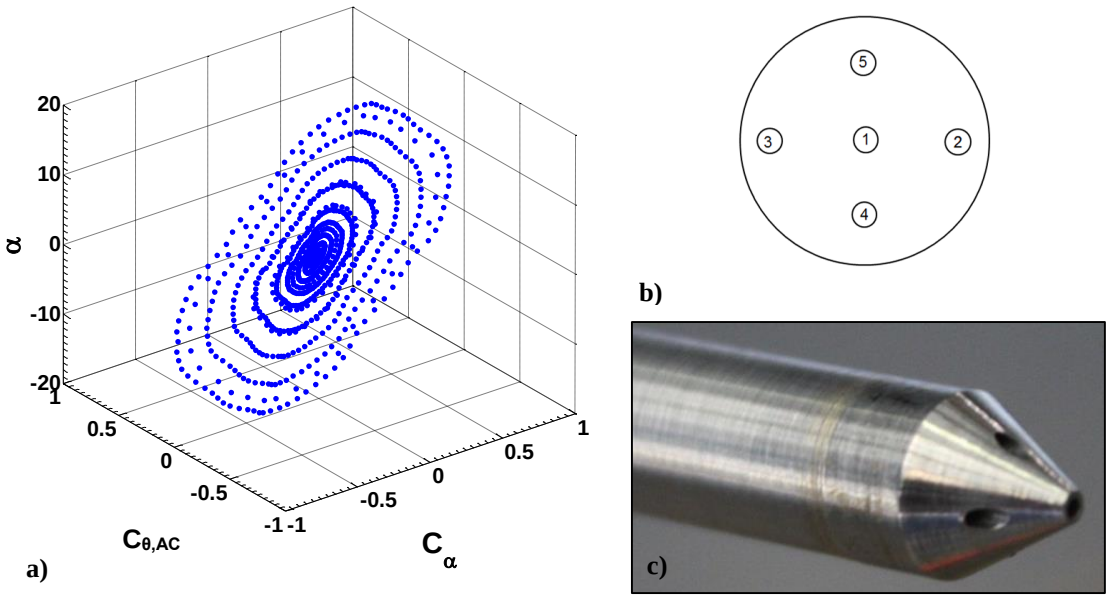

Fig. 59 5HP details, a) 5HP calibration grid for α, b) 5HP schematic, c) conical tip

$$C_{\theta,AC} = \frac{p_4 - p_5}{p_1 - p_6} \tag{7}$$

$$C_{\alpha} = \frac{p_2 - p_3}{p_1 - p_6} \tag{8}$$

The dependence on the measured dynamic pressure is removed through these calibration coefficients. Once the calibration coefficients were calculated, a significant nonlinear effect was observed as the orientation deviates from the 0° and 45° cross configurations. One 0° cross configuration is an α sweep with θ_{AC} = 0°. 45° cross configurations are simple rotations from the 0° cross configurations. Errors can be up to 3° if this effect is not accounted for in the calibration.

Based on the previous SWIFT experiments, it was known that the experimental regime for crossflow testing has a narrow α and θ_{AC} band (-8° < α < 2° and -1° < θ_{AC} < 2°). The accuracy of the calibration must be excellent in these bands. However, due to safety-of-flight concerns, reasonable accuracy is needed in a much larger band (-15° < α < 11° and -1° < θ_{AC} < 16°). Calibration coefficients were examined against both a Cartesian frame (α, θ_{AC}) and a polar reference frame (inclination of the probe axis and probe-axis rotation). Several calibration methods were examined: look-up tables, surface fits, and curve fits with a quasi-constant coordinate. Surface fits up to the 9th order polynomial were globally inaccurate; accuracy could be gained by splitting the global domain into smaller sectors. The smaller sectors would then have to be meshed together. However, the accuracy could not become as low as desired. Look-up tables up to 1,024x1,024 were created using linear and cubic interpolation schemes. Excellent accuracy could be obtained near the origin, but was less accurate elsewhere. The curve fits with a quasi-constant coordinate proved to have the best accuracy in the range of interest of the methods tested.

The α calibration involved dividing the $C_{\theta,AC}$ into a certain number of bins and then creating a polynomial curve from 3rd up to the 9th order based on the data in each bin. Exponential, natural log, and sinusoidal expansions of the $C_{\theta,AC}$ domain were explored due to the higher grid resolution near the origin; this distributed the number of data points more evenly. Gaussian and rectangular windows were also examined to see the effect of overlapping data among the different $C_{\theta,AC}$ bins. The same method was performed for the θ_{AC} calibration with splitting up C_{α}. An extensive trade study was performed varying the order of the polynomial, the expansions around the origin, and the windowing techniques. The primary requirements for the fit are that it does not exhibit any non-physical phenomena (such as oscillations between data points), and that it has a low residual (both maximum and RMSE). A close examination of the α calibration curves

at Mach = 0.3 is shown in Fig. 60. The fits were verified to not exhibit any non-physical ripples due to the nature of the higher order fit. The typical α range of interest from -11° to 7° is shown by dashed black lines.

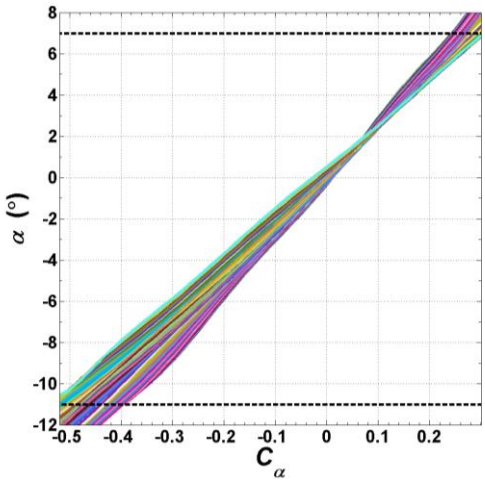

Fig. 60 All α calibration curves overlaid at Mach = 0.3

The exponential expansions of the calibration coefficients and the Gaussian windowing were selected during the calibration scheme trade study as the best parameters. The α calibration resulted in 61 9th-order polynomial fits and the θ_{AC} calibration resulted in 97 3rd-order polynomial fits, both over the larger bands of interest noted above.

The α residuals of the selected calibration scheme in the α range from -11° to 7° are shown in Fig. 61. The green dashed line is the desired residual range of ±0.1°. The large scatter in the residuals near zero was evident in all calibration schemes (data less than θ_{AC} = 1° are omitted in figure due to this large scatter). Thus, it was decided that the probe would be canted 2° upwards to avoid this region, and experimental measurements would only be in the regime from θ_{AC} = 1° to 16°. Flight experience with the O-2A with the SWIFT model (Carpenter *et al.* [6], Carpenter [7]) proved that the measured aircraft pitch angle referenced to the test article generally will not be below -1° (now θ_{AC} = 1° with 2° inclination).

The Mach = 0.25 case was created by combing the calibration data of both Mach = 0.20 and 0.30. Linear interpolation is then used between either the 0.20 and 0.25 cases or the 0.25 and 0.30 cases. This is the cause of the larger residuals for the Mach = 0.25 case.

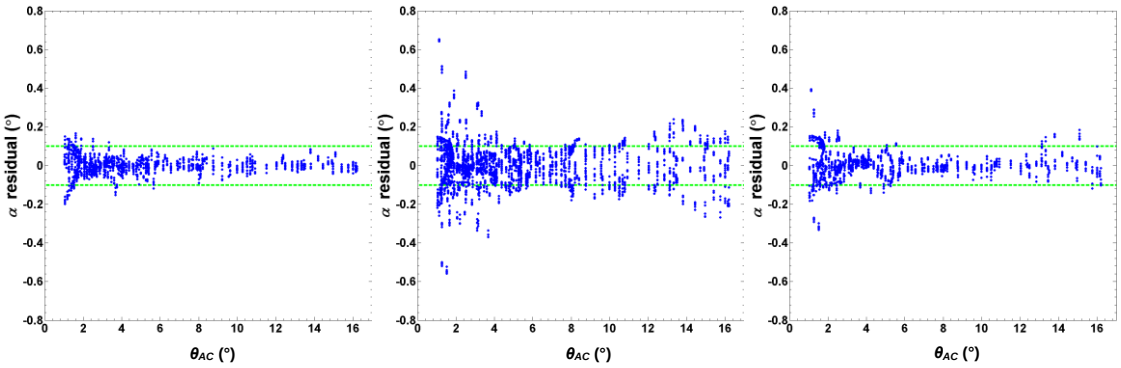

a) **b)** **c)**

Fig. 61 α residuals in α range from -11° to 7°, a) Mach = 0.20, b) Mach = 0.25, c) Mach = 0.30

Table 19 RMSE and Pk-Pk values of the 5HP calibration

	θ_{AC} Calibration		α Calibration	
Mach	RMSE (°)	Pk-Pk (°)	RMSE (°)	Pk-Pk (°)
0.20	0.12	0.85	0.03	0.35
0.25	0.18	1.12	0.07	1.21
0.30	0.13	0.70	0.06	0.69

A summary of the root-mean-square errors (RMSE) and peak-to-peak (Pk-Pk) values is shown in Table 19. The experimental band of θ_{AC} = 1° to 3° and α = -7° to 7° was used for this summary. As a conservative measure in the total uncertainty calculations of α and θ_{AC}, the values of the RMSE of the Mach = 0.25 case are used: RMSE = 0.07° and RMSE = 0.18° for α and θ_{AC}, respectively. It is important to note that the effective leading-edge sweep, Λ, of SWIFTER while in-flight is related to θ_{AC} in the manner shown in Eq. (1).

Dynamic Pressure (q) and Static Pressure (p_s) Calibration

The variance of the measured dynamic pressure and static pressure was examined as the 5HP was swept through a range of α and θ_{AC}. The calibration coefficients $C_{p,s}$ and C_q were created to examine this variance, as shown in Eq. (9)-(10). Like C_α and $C_{\theta,AC}$, the measured dynamic pressure dependence is removed. Since the total pressure port, p_1, is highly sensitive to the attitude of the 5HP relative to the freestream, the actual dynamic pressure from the calibration process, q_{actual}, is used to calibrate the measured dynamic pressure.

$$C_{p,s} = \frac{p_6}{p_1 - p_6} \tag{9}$$

$$C_q = \frac{q_{actual}}{p_1 - p_6} \tag{10}$$

There was minimal variance of the $C_{p,s}$ compared against C_α and $C_{\theta,AC}$, and a calibration was not necessary; the 8-hole static ring acts as an averaging medium at any 5HP attitude. However, in an effort to further reduce the uncertainty of the static pressure measurement in the experimental regime, a constant coefficient of $C_{p,s}$ = 0.02 was multiplied with the measured dynamic pressure and then added to the p_6 measurement. This results in a maximum calibration uncertainty of ±43 Pa for the static pressure measurement.

The calibration surface fit for C_q is shown in Fig. 62. The severe effect of the 5HP's attitude on the dynamic pressure measurement can be easily seen. A sixth-order polynomial in both C_α and $C_{\theta,AC}$ is used, without any nonlinear terms. This results in a maximum calibration uncertainty of ±17 Pa.

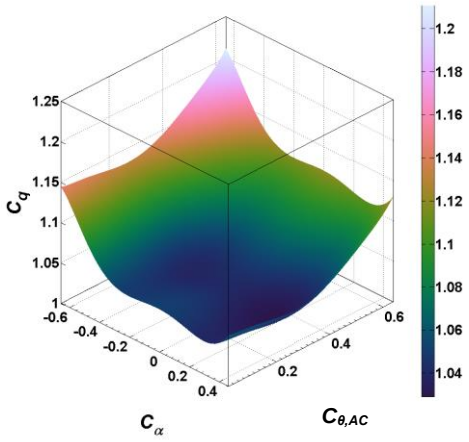

Fig. 62 Dynamic pressure calibration

5HP-Model Alignment Measurements

Attitude measurements of the 5HP tip relative to the model are necessary to calculate the total uncertainty of the model angle of attack and effective leading-edge sweep. Repeatability tests were performed for three removals and reinstallations of the 5HP mount. The mounting blocks used fit the exact contour of the non-test surface in only one fashion and are described in detail in the Five-Hole Probe Mount section. Angularity of the box channel up to the tip of the probe was measured using a laser displacement sensor on the bench. This measurement was added to the attitude of the box channel relative to the model. With the 5HP installed on the model, the α angle measurement was performed with a digital caliper, while the θ_{AC} measurement was performed with a digital level. The average α_{offset} was -0.051° ± 0.008° with a peak-to-peak of 0.005° (within the total measurement uncertainty). The $\theta_{AC,offset}$ was 2.02° ± 0.10° all three times, due to the limitations of the accuracy of the digital level (±0.10°). The digital-level measurement is quick and reliable, and additional accuracy is not necessary for θ_{AC}. The total alignment uncertainty, for both α and θ_{AC}, includes errors due to standard deviations of the measurements and the sensor accuracy of the laser, caliper, and level. The total angle uncertainties presented in the results section include this alignment uncertainty.

Frequency Response

The dynamic response of a pneumatic system is driven by the fluid inertial and viscous forces. The smaller inner diameters and longer lengths of tubing cause the viscous forces to dominate and attenuate the frequency response. In contrast, larger inner diameters are dominated by the inertial forces and can lead to an underdamped system that causes amplification of high frequency components. Also, time delay (i.e. phase lag) can be introduced in this dynamic system and can have a negative effect on the experiment by causing pilot-induced oscillations (PIO). A time delay less than 0.12 sec is recommended to avoid PIO ([58]). It is imperative to understand the cutoff frequency and time delay of any pneumatic system. Thus, the frequency response of the 5HP system was examined prior to experimentation. Bergh & Tijdeman's model, shown in [59], was used to compute the frequency response of this system using Aeroprobe's *Acoustic Transfer Function* software.

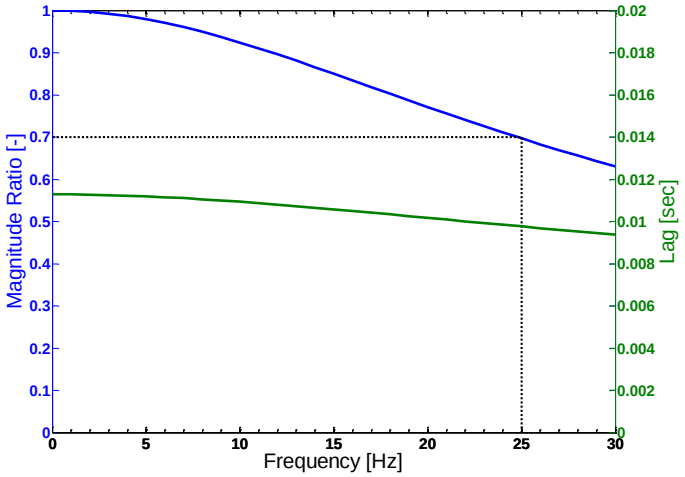

Fig. 63 Transfer function of total-pressure pneumatic line at 6,500 ft

The length of the pneumatic lines was kept to a minimum from the 5HP to the transducer cavity. The pneumatic travel from the 5HP tip to the exit of the 5HP base is 622 mm at 0.9 mm inner diameter (ID), and the pneumatic travel from the 5HP base to the transducer is 880 mm at 0.8 mm ID (1502 mm total travel). A tubing ID of 0.8 mm ($^{1}/_{32}$ in) was the closest ID to the 5HP's ID. An initial trade study proved that larger

IDs after the small 5HP ID caused poor frequency response. This is in agreement with Williams [40] showing that a smaller 5HP ID followed by a larger ID to the transducers caused a "disastrous effect" on the frequency response. The ID of 0.8 mm was kept constant with Tygon tubing from the base of the 5HP to the transducers; this includes the pneumatic connectors that were fabricated in-house.

A representative magnitude ratio and time lag of the pneumatic system is shown in Fig. 63. This analysis was performed at 6,500 ft on the total-pressure line at 175 KIAS. The higher altitude (compared to 3,000 ft) provides a conservative estimate on the frequency response. Ports 2-6 (angular and static measurement) are expected to have a slightly degraded frequency response, due to the lower pressure in the line. The cutoff frequency is determined by the point at which the curve falls below a magnitude ratio of 0.707 (3 dB), as shown by the dotted black line. The cutoff frequency is approximately 25 Hz and the total time lag is less than 0.012 sec. In conclusion, the 5HP measurements were acquired at 25 Hz, and the time lag is sufficiently low to not cause PIO.

C. KSWT Instrumentation for Freestream Characterization

A Pitot-static probe and temperature probe are used to characterize the freestream environment in the KSWT. The experimental setup of the test section is shown in Fig. 64. Both probes are mounted on the non-test side wall 230 mm downstream from the entrance of the test section and are separated apart by 76 mm.

The model number for the Pitot-static probe is PAE-12-M-W from United Sensor. An absolute pressure transducer is used to measure the static pressure; the MKS Baratron 1,000-torr (model 390HA-01000SP05) is used. A differential pressure transducer is used to measure the dynamic pressure; the MKS Baratron 10-torr (model 698A11TRA) is used. Both transducers have an accuracy of ±0.05% of the reading. The $C_{p,3D}$ profiles require a reference static pressure. A pneumatic line connects the static tube of the freestream Pitot-static probe to the reference port on the pressure scanner inside of SWIFTER. More details about the pressure scanner are included in the Surface Pressure Instrumentation section.

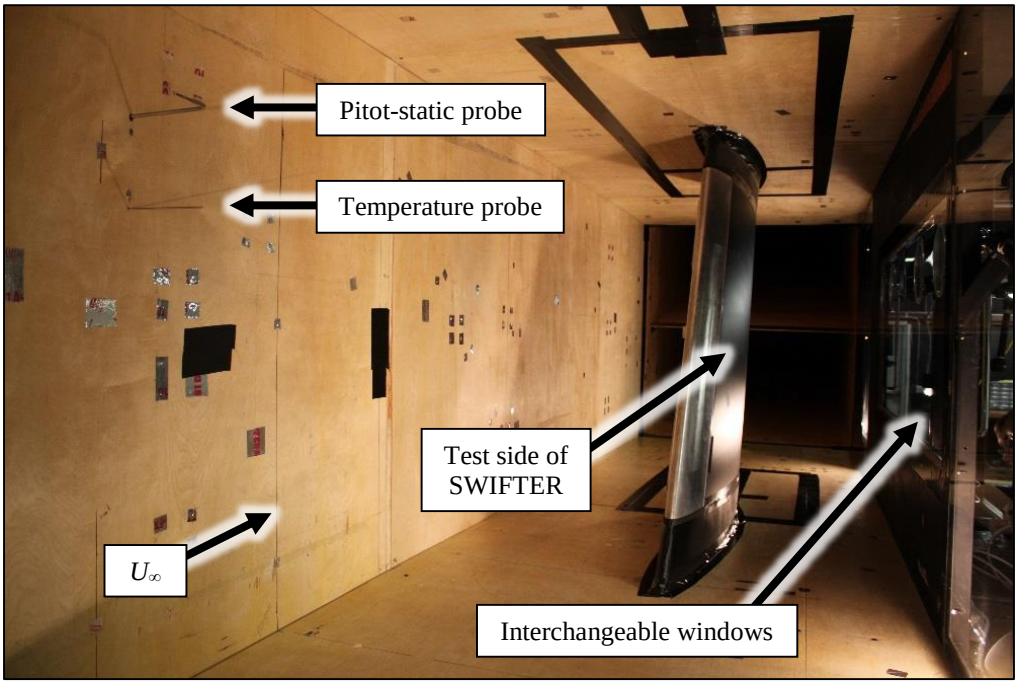

Fig. 64 KSWT test-section experimental setup

An Omega RTD probe (model PR-11-2-100-1/8-9-E) is used to measure the freestream static temperature. The accuracy of the temperature measurement is ±0.15 K.

The control of the freestream conditions in the test section is fully automated. For the current experiment, the user inputs the desired unit Reynolds number, and the control algorithm consistently maintains that constant unit Reynolds number. The standard deviation percentage of the Re' is less than ±0.2% for the current range of interest. Throughout a typical experiment, the freestream velocity is increased to compensate for the increased freestream temperature. The freestream temperature increases due to the frictional heating of the air.

The orientation of the test article relative to the test-section walls are determined with a tape measure and digital inclinometer. The spanwise-uniform model angle of attack is set to nominally -1.73° referenced to the test-section walls (reference frame preferable for experimentalist). In other words, the model angle of attack is -2.00° referenced normal to the leading edge (reference frame preferable for computationalist). This distinction is important to ensure that the experiments and computations are studying the same problem.

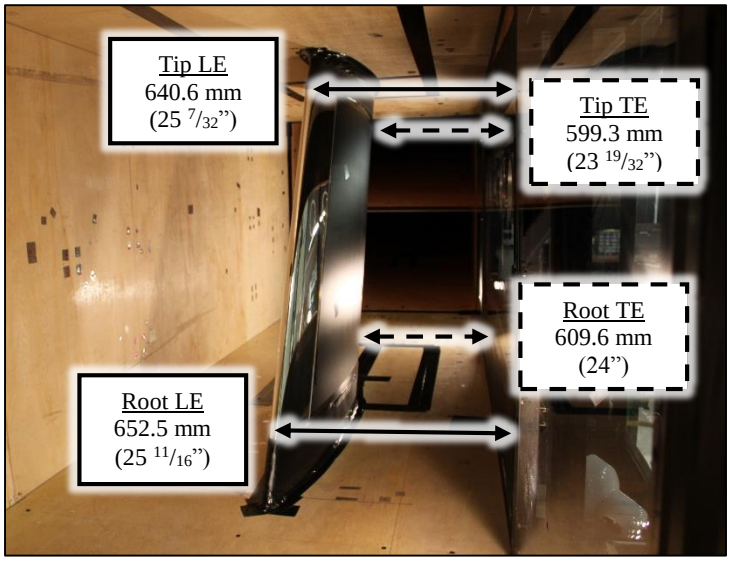

Fig. 65 SWIFTER/test-section mounting measurements referenced to test-side wall

The normal distance between the leading/trailing edges (LE and TE, respectively) and test-side walls are measured on the root and tip of the model, as shown in Fig. 65. Using the tape measure, the model angle of attack measurement has an uncertainty of ±0.1°. The effective leading-edge sweep was set to 30° by measuring the inclination difference of the ceiling and leading-edge interface at x/c = 0.15. The floor was not used due to being slightly angled to account for boundary-layer growth. The leading-edge interface location was used due to the ease of the measurement with the inclinometer. The leading-edge sweep measurement uncertainty is ±0.1° due to the inclinometer's accuracy.

The model's streamwise location in the test section is characterized by the distance from the entrance of the test section to the root LE: 1,513.7 mm (59 19/32"). The distance from the center of the shaft to the test-side wall is approximately 618.3 mm (24 11/32"), which is 45% the width of the test section (1,370 mm total width). This offset from the center of the test section is to evade nodes of potential large-scale vortical motion caused by the contraction cone, and this percentage meets the recommendation provided in Saric [60].

D. Surface Pressure Instrumentation

A pressure scanner with temperature compensation from Measurement Specialties was used to measure the pressure differential between the surface pressure ($p_{surface}$) and the freestream static pressure (p_s). This compact unit has an independent piezoresistive pressure sensor for each measurement. The p_s is acquired by connecting the scanner's reference port to the 5HP's static pneumatic line. The dynamic pressure measurement (q) from the 5HP is used to calculate the pressure coefficient, $C_{p,3D}$, as shown in Eq. (11). The subscript '3D' is added to clearly differentiate itself from the $C_{p,2D}$ ($C_{p,2D}$ will be described below).

$$C_{p,3D} = \frac{p_{surface} - p_s}{q} \tag{11}$$

SWIFTER has 64 static pressure ports (0.635 mm inner-diameter) that are split evenly between two rows at constant span, as shown in Fig. 66. The highest concentration of ports are located near the attachment line on the movable leading edge, as shown in Fig. 67; 32 out of 64 ports are located on the movable leading-edge part (x/c < 0.15). Several ports up to x/c = 0.60 are also placed on the pressure side for validation of simulated loads on the test article.

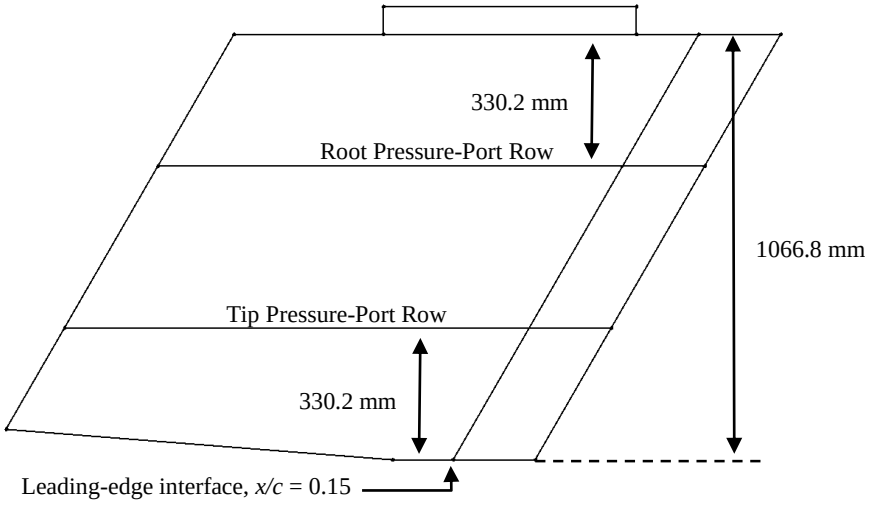

Fig. 66 Test-side static pressure ports on SWIFTER

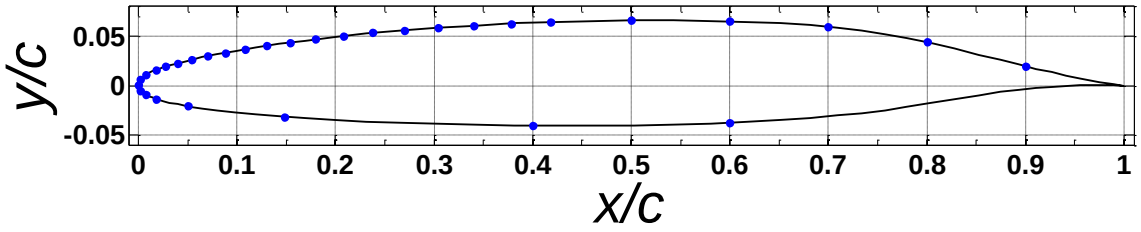

Fig. 67 Schematic of pressure-tap locations

In order to compare directly to unswept data, the 2-D C_p (normal to the leading edge) needed to be calculated and compared to the dimensional streamwise location. This is a simple transformation shown in Eq. (12).

$$C_{p,2D} = \frac{C_{p,3D}}{\cos^2 \Lambda} \tag{12}$$

The ESP-64HD (64-port scanner) with digital temperature compensation (DTC) was initially used during flight testing. It has a pressure range of ±35 kPa with a total uncertainty of ±17 Pa (static accuracy and total thermal stability errors). However, during the initial flight tests, the internal calibration of the scanner appeared to be significantly off (believed to be mainly offset error). It was determined based on the project's time schedule that surface pressure measurements will continue to be debugged during the infrared thermography campaign with the polished leading-edge part; thus, only measurements aft of x/c = 0.15 could be acquired and compared to CFD results.

A recently-calibrated pressure scanner (ESP-32HD, 32-port scanner) was used for the remainder of the flight experiments and all of the wind tunnel experiments. It has a pressure range of ±2.5 kPa with a total uncertainty of ±5 Pa (static accuracy and total thermal stability errors). It is important to note that this 32-port scanner could not be used in flight with the pressure-tap leading edge, due to the limited pressure range. The ESP-32HD with DTC was only used in flight for the pressure taps aft of x/c = 0.15. In the wind tunnel, measurements using the pressure-tap leading edge were capable due to the lower dynamic pressures. Due to

only having a 32-port scanner, the surface measurements had to be acquired separately for each row of pressure taps in the wind tunnel.

The measurements from the pressure scanner are acquired at 25 Hz, identically to the 5HP's sampling frequency. It is important to note that the scanner's uncertainties listed above assume a 1 hour warm-up time; thus, the pressure scanner is turned on at the beginning of preflight of the aircraft and wind tunnel setup for each experiment.

E. Infrared Thermography

When the boundary layer over a surface transitions from laminar to turbulence, a sharp rise in shear stress causes a distinct change in convection coefficient. An experimentalist can capitalize on this sharp gradient and identify the transition location through several measurement techniques, such as infrared thermography, naphthalene flow visualization, and temperature sensitive paint. In the present experiment, the global boundary-layer transition location is quantified via infrared (IR) thermography. Advantages to IR thermography include, but not limited to, measurements that are high fidelity, operationally efficient, real-time, and non-intrusive to the surface. Non-intrusiveness is especially valuable in the flight environment with its larger Reynolds numbers and higher sensitivity to 3-D roughness. Comparisons with other experimental techniques for boundary-layer transition detection are included in Mavris *et al.* [61], Vavra *et al.* [62], and Crawford *et al.* [63-64].

Infrared thermography requires a temperature differential between the test surface and the ambient freestream in order to visualize the surface temperature gradient between the laminar and turbulent regions. This necessary temperature differential can be obtained through a cold-soaked model or heated model; the present experiment utilizes a heated model via an internal heating sheet inside of SWIFTER. This allows efficient IR thermography without regard to the freestream conditions. A schematic of the temperature distribution of the surface is shown in Fig. 68b (red indicates higher temperatures, blue indicates lower temperatures): the laminar region remains warm, while the turbulent region's temperature decreases due to the higher convection coefficient.

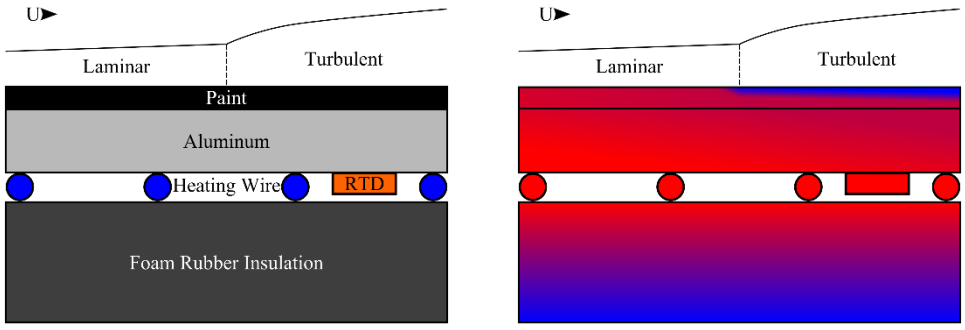

a) **b)**

Fig. 68 Infrared thermography schematics (Crawford *et al.* [64]), a) experimental setup of heated model, b) temperature distribution of heated model

The experimental setup of the heated model is shown in Fig. 68a. Resistive heating wire is bonded directly to the aluminum surface inside the model. An insulated foam layer is installed over the heating wire to direct the heat towards the test surface. Maximum power output is approximately 500 W. A temperature differential between the freestream and test surface of 2-4 K is maintained through the use of a PID controller. Three internal RTDs are strategically placed to monitor the temperature of the model. This setup has been used successfully in both the flight and wind tunnel environment. Additional details regarding the heating sheet can be found in the Heating Sheet section and Electrical Analysis section.

A high-emissivity, insulating black paint is implemented on the SWIFTER model in order to minimize spurious reflections, and allow for sharper thermal gradients, respectively. Previous experiments without this paint resulted in strong IR reflections of the bottom of the O-2A fuselage and exhaust pipes (Carpenter *et al.* [6], Carpenter [7]). The removal of these non-boundary-layer features made the computer-automated post-processing easier and more accurate. The movable leading-edge interface with the static main body was match sanded together; this reduced some of the high-emissivity properties in this region and can be seen at $x/c \approx 0.15$ to 0.17 in Fig. 69ab.

The FLIR SC8100 IR camera is used for the present experiment; a 17 mm lens is used in the wind tunnel, and a 50 mm lens is used in the flight environment. The camera has a resolution of 1,024x1,024, which allows the measurement of fine flow features. A sampling frequency of 20 Hz was selected for the present

experiment; this frequency is the maximum frequency allowable to obtain all frames during the experimental dives without any dropped frames. Each pixel is approximately 900 μm wide and has a sensitivity of 25 mK. In the Cessna O-2A, the IR camera is mounted to the instrumentation rack next the FTE, and there is hole cutout of the window for an unobstructed view of the model. In the KSWT, the IR camera is fixed to the viewing window directed through the third open port. In both environments, the camera is tilted to its side so that the edge of the field of view is parallel with the leading edge; this orientation acquires the largest area on the test surface.

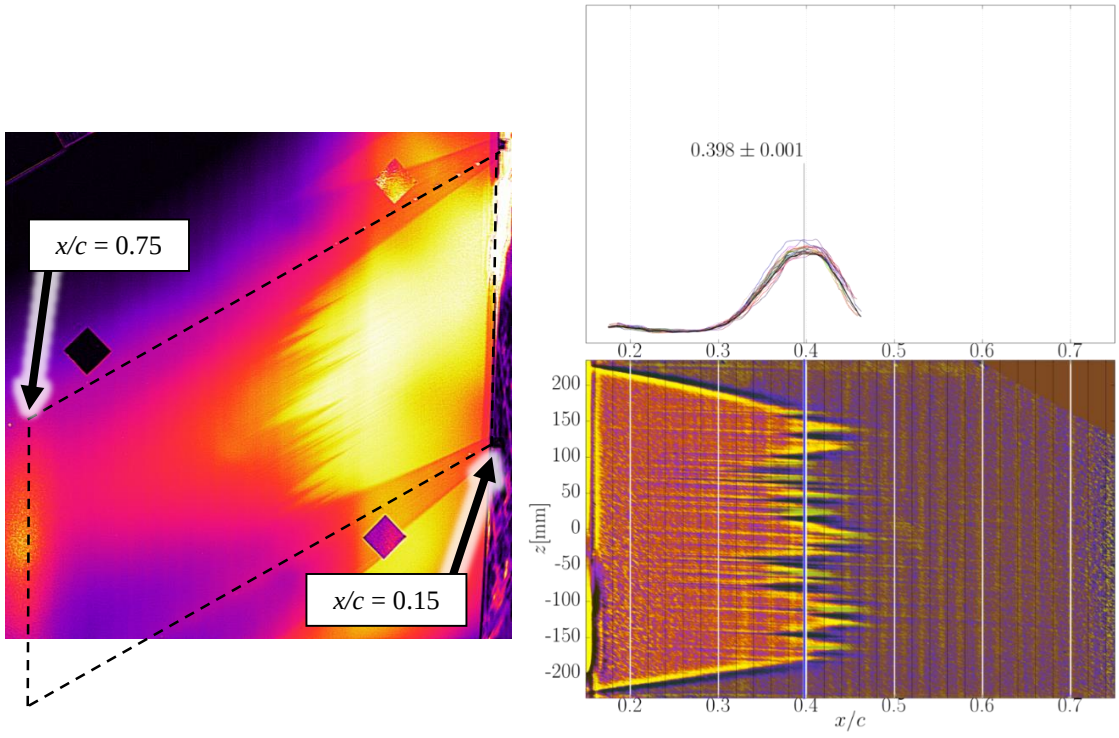

a) **b)**

Fig. 69 IR thermography in flight (Crawford *et al.* [63]), a) ExaminIR image with test area indicated by black dashed lines, b) post-processed image (bottom) with respective PDF distribution (top)

Computer Post-Processing Details

A computer, post-processing code was created by Brian Crawford (Crawford *et al.* [63]) to obtain quantitative transition information. This is important due to the fact that by eye, the transition location can only be determined with an uncertainty of approximately $x/c = \pm 0.05$ and, most importantly, is subject to biasing error by the interpreter. An example of the IR image provided by the FLIR *ExaminIR* software is shown in Fig. 69a. Automated post-processing, however, is capable of transition detection uncertainty on the order of $x/c = \pm 0.001$. This uncertainty is primarily due to the variation of the detected transition front from frame to frame; it does not include the systematic errors of the freestream conditions (α and Re'). It is calculated by the Standard Error of the Mean (SEM) of the transition location for a set of images taken in a data set, in order to characterize the error of aggregate transition location. The code can reliably fix the position of the model to within ±0.3 pixels (approximately 300 μm or $x/c = 0.0002$) using a set of three fiducials.

The basic steps of the post-processing code include: track the location of the model, transform the image into span and chord coordinates, filter the image to enhance features, and detect the transition front. More specifically, three 50.8 mm square fiducials are placed at known locations on the model; these fiducials can be seen in Fig. 69a. Silver Mylar tape was chosen for the fiducials. It is highly IR reflective and typically reflects the cooler ambient temperature. This provides a high temperature gradient between itself and the higher surface temperature surrounding the fiducial. Once the fiducials have been tracked, the model is transformed such that the flow is left-to-right as per convention, and that the spanwise direction is vertical and the chordwise direction is horizontal. Additionally, any effects due to model curvature and IR camera lens distortion are removed. This results in a one-to-one correspondence between pixel location and chord/span location.

The transition front is then detected by calculating the gradient vector at every pixel and projecting it to the vector perpendicular to the characteristic lines along which turbulent wedges propagate. This gradient is then used to calculate the most likely transition front. Once the transition front has been acquired, these data are then sorted to create a cumulative distribution function. The derivative of this function is the probability density function (PDF). An example IR plot (Fig. 69b, bottom) with the corresponding PDF (Fig. 69b, top)

is shown. The colored lines are the individual PDFs of the 20 images analyzed (1 second centered around being "on condition"). Holding the target α and Re' within certain tolerances for 3 seconds was deemed "on condition"; an example of being "on condition" is provided in the Five-Hole Probe section below. The black line is the PDF generated from the cumulation of the transition locations from all 20 images processed in the sample shown. This was performed to remove any outliers where the local transition location may have been detected incorrectly, as well as to compensate for small variations in the detected front. The abscissa of the local maxima of the PDF corresponds to the dominant transition location. Turbulent wedges can cause local maxima due to the fact that they are essentially very narrow transition fronts (i.e. bug-strikes). However, the amplitude is very small for these maxima. As such, a threshold is set on the amplitude to squelch any such detected fronts. In general, the strongest peak is the transition front of interest. As noted before, the uncertainty shown in Fig. 69b is the SEM of the dominant transition location. Additional details on all of the post-processing techniques can be found in Crawford *et al.* [63].

F. Hotwire Anemometry

In order to compare directly with CFD results and enhance the understanding of the physics within a boundary layer, a measurement technique is needed to spatially resolve the boundary layer with the ability to detect high-frequency components. Also, the technique needs to have minimal intrusiveness into the flow in order to have robust measurements. An obvious solution is to use optical techniques, such as particle image velocimetry or laser Doppler velocimetry. However, resolving the boundary layer is problematic due to an inadequate number of seeded particles captured within the boundary layer. For the present experiment, hotwire anemometry is used in the wind tunnel in addition to the global transition measurements using IR thermography. The present experiment utilizes constant temperature anemometry with an overheat ratio of 1.8.

Two channels from an AA Labs AN-1003 anemometer are used with Dantec Dynamics' miniature hotwire probes. One boundary-layer probe (Model Number 55P15) and one straight wire-probe (Model Number 55P11) are used together, as shown in Fig. 70a. The platinum-plated tungsten wire sensors are 5 μm in diameter and 1.25 mm long. The full length of the wire is active (from prong to prong). The hotwire

probe supports are mounted to a hotwire sting which protrudes through the test-side wall, connecting to the hotwire traverse system inside the pressure-box (shown in Fig. 70b). The freestream hotwire is placed 175 mm away (wall-normal direction) from the boundary-layer probe. The pressure-box is necessary to minimize the mass flow from outside the test-section to inside the test section. The 3-D hotwire traverse has a resolution of 11.9 μm, 0.6 μm, and 1.3 μm (streamwise, test-side wall normal, vertical, respectively). The traverse is capable of acquiring measurements from x/c = 0 to 0.75, and 180 mm in the spanwise direction (z = -96 to 84 mm, z = 0 is SWIFTER's midspan).

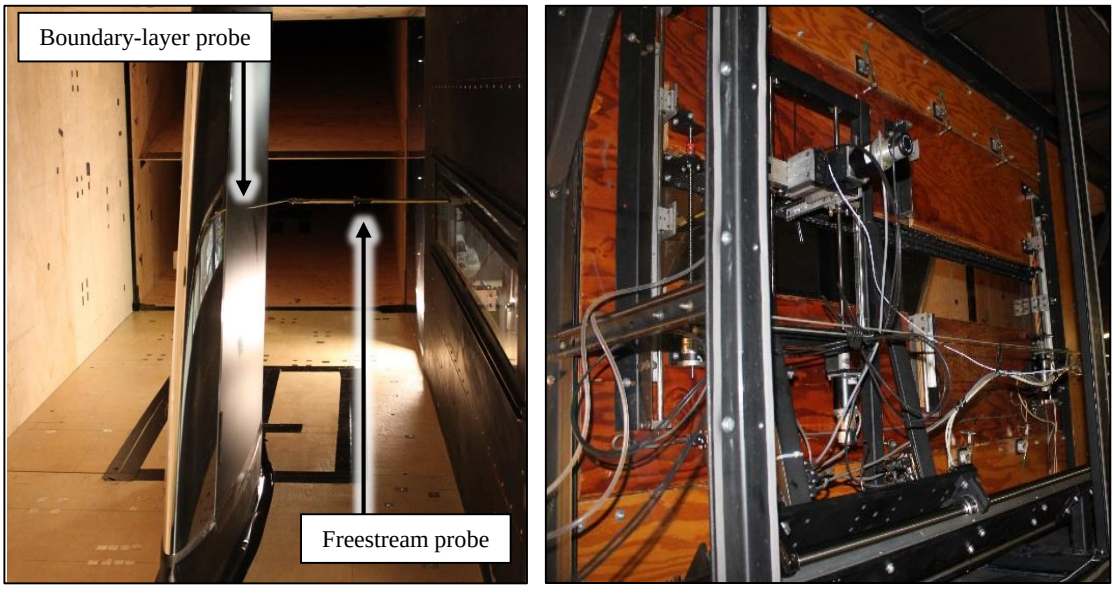

a) **b)**

Fig. 70 Hotwire anemometry experimental setup, a) hotwire sting with boundary-layer and freestream probes (view of inside test section), b) 3-D hotwire traverse inside pressure box (view of outside test section)

Hotwire Calibration and Measurement Details

The hotwires are calibrated at the beginning of each day. The hotwires are placed at the same calibration location each time. A velocity ratio between each hotwire calibration location to the freestream Pitot-static measurement was performed by placing a temporary Pitot-static probe at each hotwire calibration location. These velocity ratios are used throughout the automated calibration program to always apply this ratio to

the freestream velocity measurement. Before the calibration begins, the tunnel is started to 100 RPM and the temperature is allowed to reach steady-state. Once this is achieved, the fan is incremented from 50 to 1,000 RPM in 13 steps. Raw voltages are acquired at each step to form the cold calibration. Then, the fan maintains 1,000 RPM for 20 minutes or a 6 K rise in freestream static temperature (whichever occurs first). Raw voltages are then acquired as the fan increments from high speed to low speed in 13 steps, matching the velocities achieved on the cold calibration, to form the hot calibration. A thermal compensation coefficient is then created to adjust the raw voltages acquired during the scans. The temperature can vary up to 4 K over the course of a spanwise scan (at $Re' = 1.00 \times 10^6$/m tested). A fitted form of King's Law is used for the hotwire calibration with the added temperature compensation step. Additional details regarding the hotwire calibration and temperature compensation are included in White [65], Hunt [66], and Downs [67].

Hotwire measurements enable the characterization of both the steady, $u\,(x, y, z)$, and unsteady, $u'\,(x, y, z, t)$, velocity components that combine to give the total velocity, $U\,(x, y, z, t)$, as shown in Eq. (13). Model fixed coordinates (x, y, z) are used, as shown in Fig. 71; x is leading-edge normal, y is wall-normal, and z is leading-edge-parallel root to tip.

$$U\,(x, y, z, t) = u\,(x, y, z) + u'(x, y, z, t) \tag{13}$$

The DC component of the hotwire signal is averaged over a 2-second sampling time and results in the steady velocity, $u\,(x, y, z)$. The AC component of the hotwire signal represents the temporally unsteady velocity, $u'\,(x, y, z, t)$, and this fluctuating component can be quantified through the usage of the temporal root-mean-square, $u'_{rms}\,(x, y, z)$. A Kemo VBF44 filter and amplifier is used; the AC components are measured with a passband filter from 1 to 5 kHz with a 30 dB gain. Both DC and AC components are sampled at 10 kHz in order to avoid aliasing. In order to minimize crosstalk, the AC components are acquired on a separate DAQ board. Both the DC and AC components are acquired for the boundary-layer hotwire, while the DC is only acquired for the freestream hotwire.

Boundary-Layer Scans

A dual-hotwire configuration is necessary because the freestream velocity is not maintained throughout the boundary-layer scans. The freestream maintains a constant Re'. Since the wind tunnel is not temperature controlled, the velocity has to be modulated. Thus, the boundary-layer hotwire is always referenced to the freestream hotwire. An automated program performs the spanwise boundary-layer scans. The boundary-layer hotwire is initially placed a few mm away from the boundary-layer edge. An initial, velocity ratio between the boundary-layer hotwire, u, and freestream hotwire, u_{FS}, is used to compute the boundary-layer-edge velocity, U_{edge}, throughout each boundary-layer scan. This compensates for the local acceleration of the air around the model relative to the freestream. In conclusion, the steady and unsteady boundary-layer measurements take the form of $u\,(x, y, z)/U_{edge}$ and $u'_{rms}\,(x, y, z)/U_{edge}$.

The hotwires march towards the wall with smaller increments used as the wall of the model is approached. The automated scan is completed once $u\,(x, y, z)/U_{edge}$ is less than 0.20. This avoids any measurement contamination by conduction to the wall surface, due to the small distance between the probe and the wall. It also keeps the fragile hotwire further away from the surface. Once the boundary-layer scan reaches this threshold, the hotwires are pulled away from the surface and moved to the next (x, y, z) location. Model midspan is at $z = 0$ mm, as shown in Fig. 71.

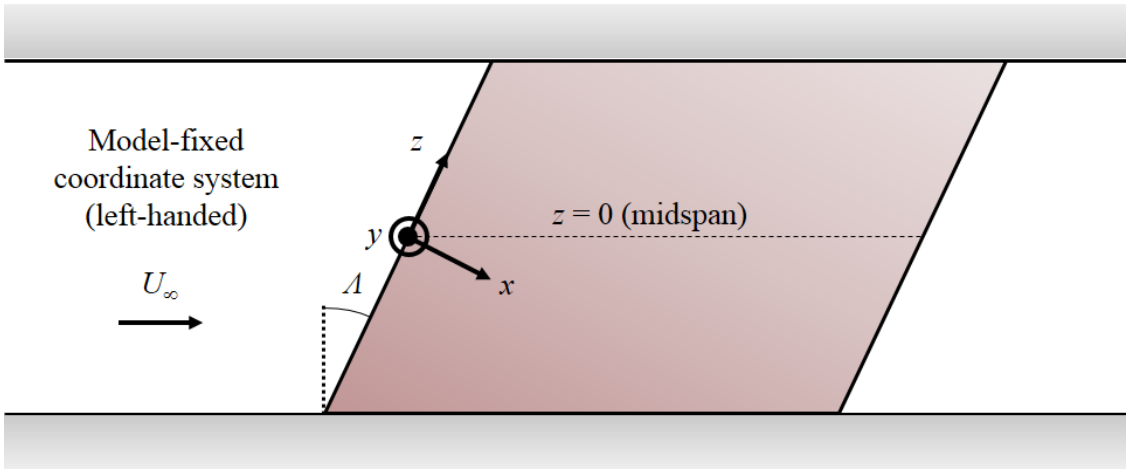

Fig. 71 Model-fixed coordinate system (x, y, z)

Approximately 40 points are measured for each boundary-layer profile. One representative, boundary-layer profile is shown in Fig. 72. A 2nd order polynomial fit, from $0.20 < u\,(x, y, z)/U_{edge} < 0.50$, is used to extrapolate from the last acquired point to the wall (White [65]). It is important to note that the location of the wall is found experimentally: the wall location is not known a priori.

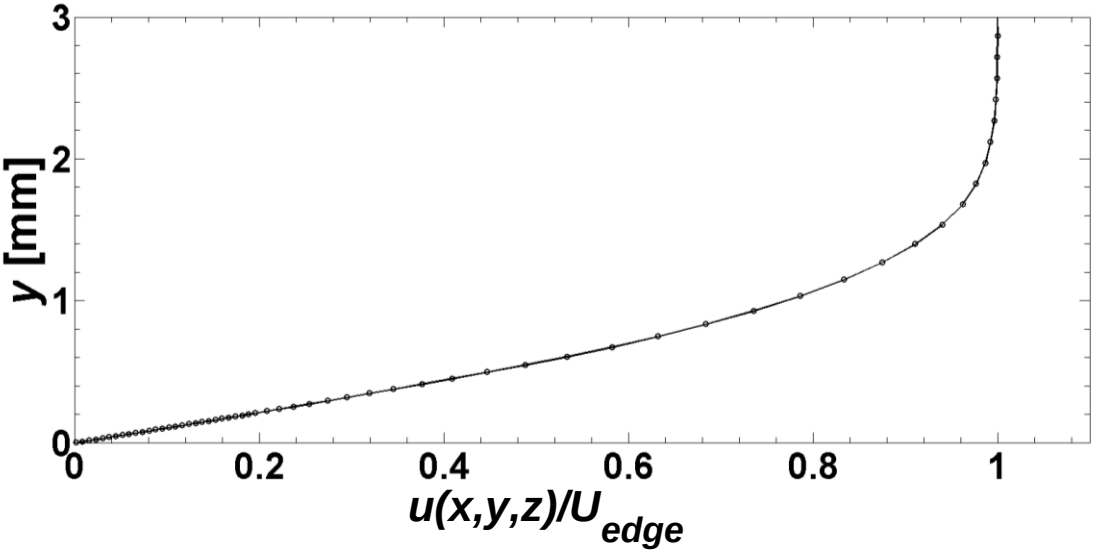

Fig. 72 Representative baseline, boundary-layer profile with extrapolated region $u\,(x, y, z)/U_{edge} < 0.20$, $k = 0$ µm, $x/c = 0.18$, $Re' = 1.00 \times 10^6$/m

The u'_{rms} is calculated by taking the square root of the integration of the PSD in the frequency domain. Spanwise-differential, hotwire vibration was noticed during the spanwise measurements. The first indication of the problem was observed when the maximum z values (+z) had noticeably higher u'_{rms} within the boundary layer than the minimum z values (-z) during a baseline ($k = 0$ µm) case. After several rap tests with wind-on, and with the probe inside the boundary layer, it was observed that this vibrational frequency band was from 20 to 24 Hz. A notch filter from 20 to 24 Hz is applied to the u'_{rms} calculations for all presented results: this equates to a linear interpolation from 20 to 24 Hz for the PSD integration scheme. The hotwire vibration slowly gets worse starting near midspan ($z \approx 0$ to +z). It is believed that the hotwire sting tends to vibrate more as it gets farther away from the traverse carriage. Previous experiments at Texas A&M

exclusively focused on the lower-half of the traverse travel (-z to $z \approx 0$); thus, spanwise-differential, hotwire vibration was not an issue.

V. FLIGHT-TEST RESULTS AT TRANSPORT UNIT REYNOLDS NUMBERS

The results from the flight experiment will be documented in this section. First, the flight-test procedure will be described. Then, the 5HP measurements will describe the steady conditions for this stability experiment. The measurements of the surface pressures will be shown with a CFD comparison. Finally, the infrared thermography campaign will show the effect of steps on boundary-layer transition.

A. Test Procedure

Directly after takeoff, the heating sheet is turned on; full aircraft power is required for the power draw of the heating sheet. A test flight begins with a climbout to approximately 6,500 to 7,500 ft; the maximum altitude depends on the atmospheric conditions for that flight. If possible, temperature inversions and substantial wind shears are avoided; these conditions typically lead to unsteady conditions during the experimental dives. Once the maximum altitude has been achieved, a step-height check and pre-dive checklist are commenced. It is the FTE's responsibility to check if the step height is correct or if a step-height configuration change is required. Typically, the first step-height configuration is set on the ground before takeoff. If the step height needs to be adjusted in flight, the aircraft's speed is reduced to 80 KIAS; this is the slowest the test pilot is comfortable repetitiously flying near stall. Also, the test pilot holds a constant α = -2.00°; this configuration imposes a minimal loading on the movable leading-edge. Then, the FTE adjusts the step height of the movable leading-edge. Finally, the test pilot returns the aircraft to normal cruise operating conditions.

The pre-dive checks ensure that the pilot inputs maximum throttle and fuel mixture for the aircraft, and the FTE ensures that all instrumentation are properly acquiring. After the pre-dive checklist is completed, the experimental dive is started. The test pilot holds constant α throughout the dive while increasing Re' in 0.10 x 10^6/m increments. In real time, the LabVIEW program on the FTE's laptop informs the FTE when each α and Re' test point has been maintained within certain tolerances. The FTE is the test conductor and initiates the changes to the next Re' condition to the test pilot. The co-pilot is the safety observer during the experimental dive because the test pilot is focused on the instrumentation in order to hold steady conditions. The experimental dive is completed once the aircraft's altitude is approximately 3,000 ft for safety concerns;

this altitude is approximately 1,000 ft above any obstacle in the experimental test areas. The climbout and dive procedures are repeated until there is not enough fuel for additional dives. Typical duration of a flight test is about 1-2 hours and includes about 50-100 test points.

B. Five-Hole Probe

The steadiness of the Re' and α traces are greatly affected by the atmospheric conditions, pilot control stability, and the method for maneuvering the control surfaces of the aircraft. It has been found at the FRL that early morning flights are the best times to fly. The air is steady in the morning as air thermals later on in the afternoon typically create an unstable freestream environment. The ability of the test pilot to hold steady conditions is obviously greatly influenced by the steadiness of the atmosphere. Also, frequent flying helps our test pilots practice and get better at holding conditions. Pilot-induced oscillations (PIO) are normally apparent, but they have a low frequency and amplitude.

It has been proven that the rudder trim produces much steadier α traces compared to using the rudder pedals. The rudder trim allows the test pilot to have a finer resolution of stable control on the α; it is also much easier on the test pilot to use the rudder trim. The standard deviation of the α measurement can be greater than two times larger using the rudder pedals. However, the rudder trim only has a certain range of rudder authority. This range had to be manually set at the beginning of these flight experiments. All of the results shown are using the rudder trim. The elevator trim, instead of the yoke, is used to finely control the Re', for the same reason as the rudder trim. Controlling the Re' is much more forgiving than the α.

In an effort to help the pilot hold steady conditions, an exponentially-weighted-moving-average filter is applied to the traces provided to the pilot on the display attached to the yoke. The filter has a low cutoff frequency of approximately 1.4 Hz; this cutoff frequency was determined experimentally in flight. The cutoff frequency was adjusted based on the pilot's comments until the pilot was satisfied with the output. It is important to note that this filter is only applied to the pilot's display: the acquired data is not filtered.

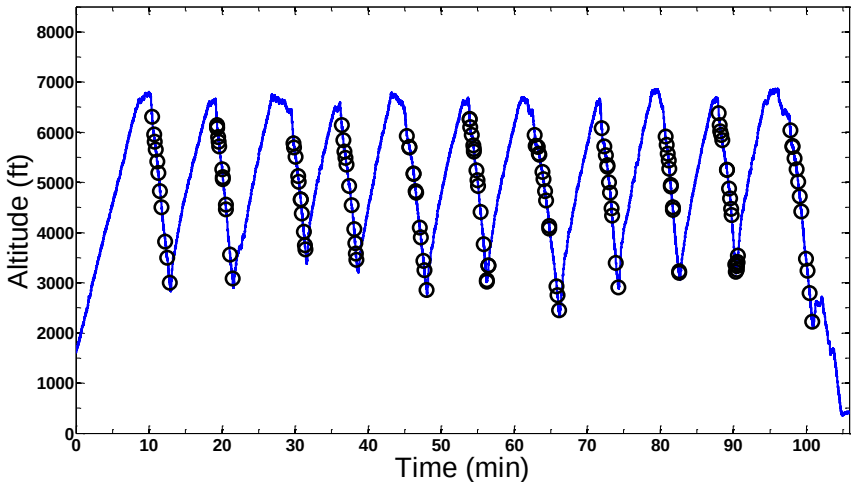

Fig. 73 Flight profile with "on condition" points (black circles)

An example flight profile is shown in Fig. 73. The blue trace is the altitude measurement by the 5HP and the black circles are the "on condition" points for holding constant *Re´* and α. This flight performed 11 experimental dives and acquired 142 data points. It takes about 10-20 minutes to climb to the maximum altitude to start the experimental dives. Each experimental dive lasts approximately 2-4 minutes and it takes about 5-8 minutes to climb back to the maximum altitude.

The associated traces of the *Re´* and α of the 1st dive of the flight profile in Fig. 73 are shown in Fig. 74. The vertical dashed black lines represent the "on condition" data points. During the first 1,000 ft of the dive, the test pilot slowly increases the airspeed until the first *Re´* is achieved (*Re´* = 4.70 x 10^6/m), while inputting the correct aircraft yaw angle to obtain the desired α = -7.50°. It typically takes the pilot 1,000 to 1,500 ft to get "on condition". The pilot then slowly increases the *Re´* in 0.10 x 10^6/m increments while holding the α constant. PIO is evident in both the α and *Re´* number traces, but it has a low frequency. A closer examination into the "on condition" data points is shown below.

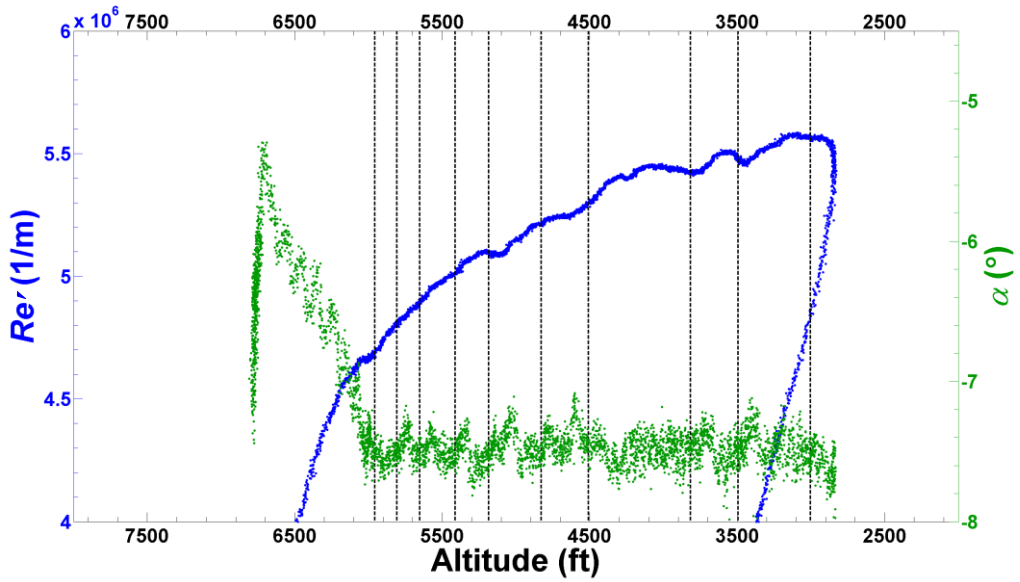

Fig. 74 α and Re' traces from 1st dive of the flight profile in Fig. 73

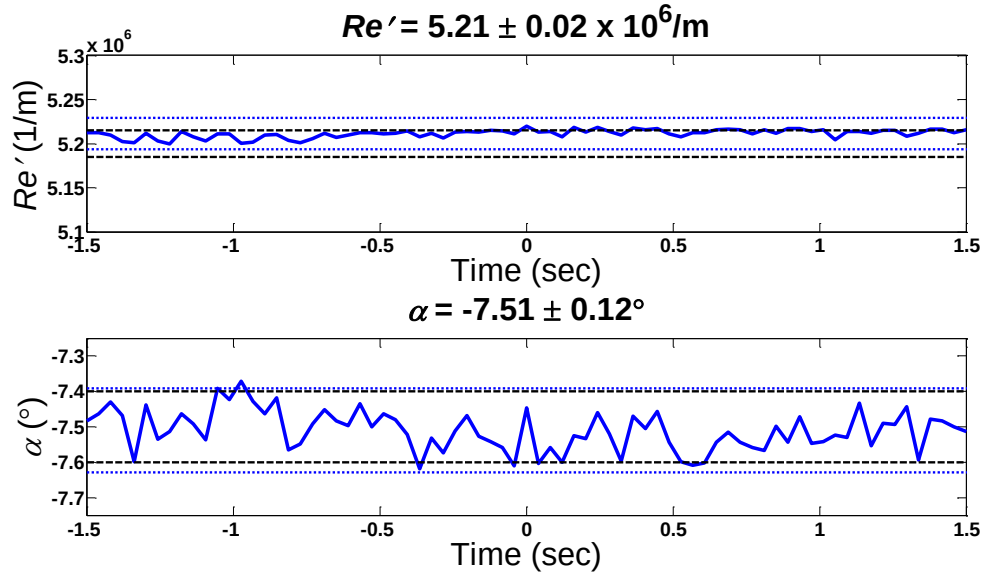

Fig. 75 "On condition" example, *Re'* and α traces for 3 seconds

A 3-second sample of being "on condition" is shown in Fig. 75. The total uncertainty (represented by the dashed blue lines) of each measurement for the full sample is provided for each condition in the plot's title; this includes sensor error, calibration error, probe-alignment error, and the standard deviation of the

measurement. The typical systematic uncertainty (all errors except the standard deviation) is represented by the black dashed lines; these lines essentially represent the lowest possible total uncertainty.

Total uncertainty in α typically is 0.12-0.14°, but can be as low as the systematic uncertainty: 0.10°. Re' total uncertainty typically is 0.02-0.03 x 10^6/m, but can be as low as the systematic uncertainty: 0.015 x 10^6/m. The θ_{AC}, or Λ as shown in Eq. (1), total uncertainty typically is 0.23-0.25°, but can be as low as the systematic uncertainty: 0.22°. The Λ range tested during this experiment is 28° to 31° (dictated by the Re') and is assumed to be nominally constant for the presented results at 30°. The total uncertainty formulations for α, θ_{AC}, and Re' are included in APPENDIX E.

A post-processing code finds the best "on condition" points (i.e. lowest standard deviation) throughout the entire flight for each desired test point. If certain tolerance requirements are not met for a certain desired test point, then the test point is not examined. The code outputs the timestamps of each "on condition" point to match up with the timestamps of the measurements of the pressure scanner and IR camera.

C. Pressure Distribution

The CFD model used for comparison with the flight results is shown in Fig. 76. The "clean" geometry represents SWIFTER without the non-test side struts, lead-screw plates and the 5HP assembly. This is in contrast to the safety-of-flight CFD model, as shown in Fig. 26. A simplified O-2A model was utilized (identical to the safety-of-flight model); the fuselage, wings, port empennage, port wing strut, and port outboard pylon were modeled. Previous experience with the SWIFT project enabled the confident usage of this simplified aircraft model, the exclusion of the propeller wash, and the usage of the three-tier gridding method (Rhodes [50]). The grids were created using ANSYS ICEM and the CFD solution was computed using ANSYS Fluent. The CFD solution methods are second order, incompressible and pressure based. The flow was set to be turbulent after the pressure minimum to prevent separation; thus, this method provides a 'clean' pressure distribution. Additional details of the CFD analysis can be found in Tufts *et al.* [1].

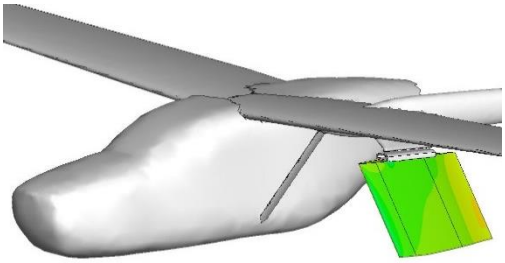

Fig. 76 CFD model with 'clean' SWIFTER geometry (from Tufts *et al.* [1])

The measured $C_{p,3D}$ data were compared directly to CFD calculations by Tufts *et al.* [1], as shown in Fig. 77. Both profiles are at $Re' = 5.50 \times 10^6$/m and $\alpha = -6.50°$. The excrescence is located at $x/c = 0.15$ and the pressure minimum is near $x/c = 0.70$. It is also important to note that the CFD solution is set to turbulent near the pressure minimum ($x/c = 0.70$) which causes the noticeable dip in the pressure distribution. Total uncertainty bars are added to the experimental measurement. Uncertainty due to the static and dynamic pressure, the α uncertainty sensitivity, and the standard deviation of $C_{p,3D}$ are used in the total uncertainty calculation. The root row has good agreement between experiment and computations. However, the tip row does not match as well as the root row. This is believed to be due to the wing tip vortex at the tip of the model not being fully captured by the CFD solution. A comparable behavior was noticed in the $C_{p,3D}$ analysis of the similar test article, SWIFT, which has the same airfoil, chord, and span (Carpenter *et al.* [6], Carpenter [7]).

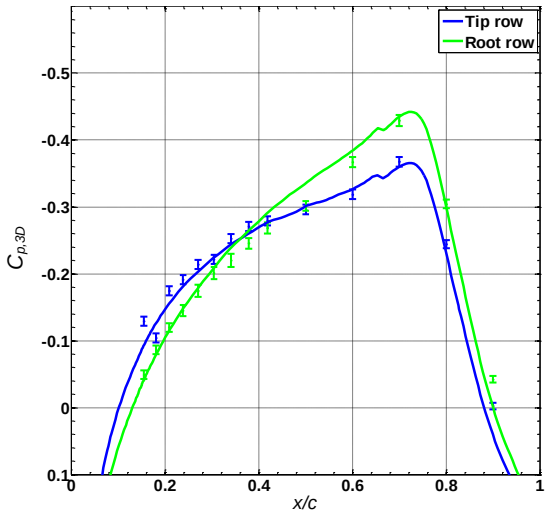

Fig. 77 $C_{p,3D}$ baseline comparison with CFD, Re' = 5.50 x 10^6/m, α = -6.50°

In an effort to compare directly with unswept results, SWIFTER's $C_{p,2D}$ profiles are shown with NGC's unswept Grad A model in Fig. 78. A reminder is given that the dimensional streamwise length is used rather than the percentage of the model's chord. Only the region of interest of SWIFTER is shown for comparison (x/c = 0.15 to 0.70).

As shown in Fig. 77 and by comparing the root and tip profiles (Fig. 78a and Fig. 78b), it is clear that SWIFTER has a slightly varying pressure across the span of the model. The root row has a more negative pressure-coefficient gradient, $C_{p,x}$, than the tip row (i.e. more favorable). It is evident that NGC's wedge shape produces a linear pressure distribution, as shown in Fig. 78: NGC's $C_{p,x}$ is equal to -0.6 1/m. Also, SWIFTER's airfoil shape creates a slightly curved pressure distribution. There is a more favorable pressure gradient directly aft of the excrescence.

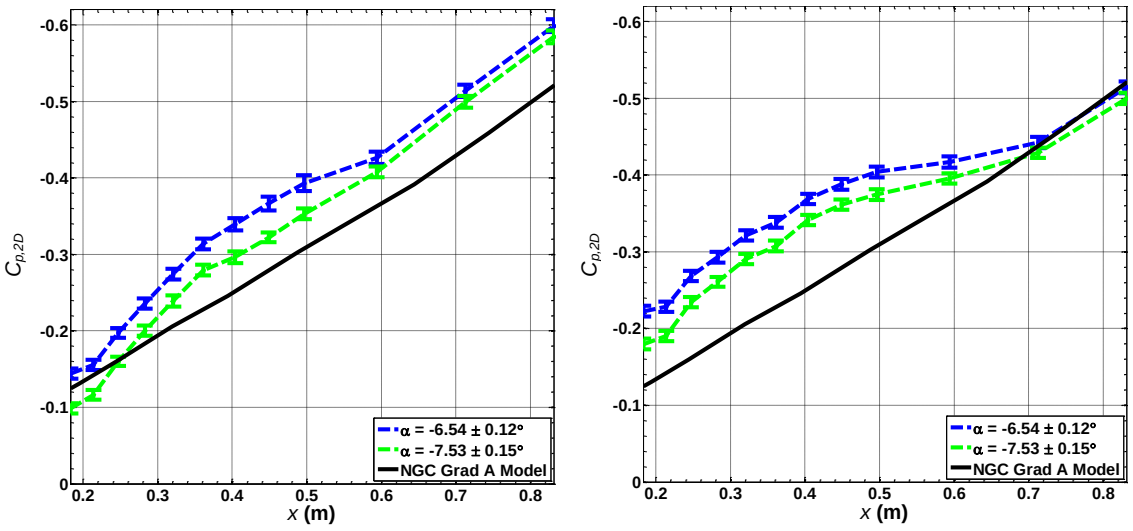

Fig. 78 $C_{p,2D}$ comparison with NGC Grad A model, SWIFTER x/c = 0.15 to 0.70 shown, a) root row, b) tip row

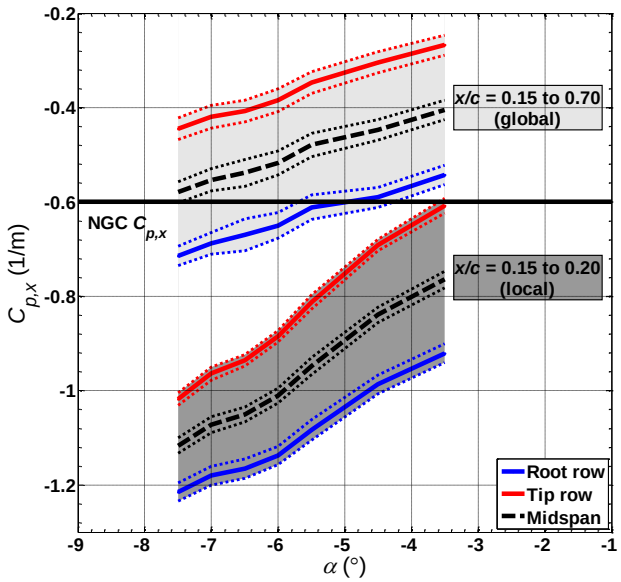

Fig. 79 Pressure-coefficient gradient, $C_{p,x}$, comparison with NGC Grad A model

A linear least-squares analysis was performed on the $C_{p,2D}$ profiles to get a quantitative value for the slope of the $C_{p,2D}$ profiles (i.e. pressure-coefficient gradient, $C_{p,x}$), and this is shown in Fig. 79. Two different

streamwise regions were analyzed for SWIFTER: a global pressure gradient (x/c = 0.15 to 0.70) and a local pressure gradient near the excrescence (x/c = 0.15 to 0.20). These calculations were performed with the experimental results of the root and tip pressure tap rows. The midspan gradient is estimated by performing a linear interpolation between the root and tip rows. Uncertainty regions are shown with dotted lines; the $C_{p,x}$ uncertainty formulation is included in APPENDIX E.

It is clear that the local pressure gradient is more favorable than the global pressure gradient (i.e. more negative $C_{p,x}$). The NGC Grad A pressure gradient intersects the global pressure gradient region of SWIFTER α from -5.00° to -7.50°. In order for the baseline transition front to occur within the global test region (x/c = 0.15 to 0.70) using a polished leading-edge part, the more negative α needs to be used; additional details are included in the Baseline Transition Location section. Also, the rudder-trim authority of the O-2A limits the most negative α to -7.50°. Thus, it was decided that the target α would be -6.50° and -7.50° for the current excrescence experiment.

D. Infrared Thermography

Non-Dimensional Parameters

Non-dimensional parameters were calculated to compare to previous excrescence experiments. $Re_{k\infty}$ references the freestream conditions (Re'), while Re_{kk} references the undisturbed boundary-layer conditions at step height k, as shown in Eq. (14)-(15). u_k is the velocity normal to the leading edge at step height k, and v_k is the kinematic viscosity at step height k. The forward-facing steps correspond to positive values and aft-facing steps correspond to negative values.

$$Re_{k\infty} = Re'k \tag{14}$$

$$Re_{kk} = \frac{u_k k}{v_k} \tag{15}$$

The use of Re_{kk} is not used everywhere and some authors choose to call Eq. (15) Re_k. However, using the notation Re_{kk} clearly shows that the *roughness Reynolds number* is $O(k^2)$. Moreover, using u_k as the velocity normal to the leading edge is the only velocity component that makes sense in the case of 2-D roughness.

The undisturbed boundary-layer conditions in Re_{kk} were calculated using computations from Tufts *et al.* [1] at α = -6.50 and -7.50: u/U_{edge} vs. $y(Re')^{1/2}$ and θ_T vs. $y(Re')^{1/2}$. These boundary-layer properties were examined at midspan of SWIFTER. The non-dimensional temperature variable θ_T, relates the temperature T, boundary-layer edge temperature T_{edge}, and the adiabatic wall temperature T_{aw}, as described in Eq. (16). The steps that lead to the formulation of the Re_{kk} calculation are shown in Eq. (16)-(22).

$$\theta_T = \frac{T - T_{aw}}{T_{edge} - T_{aw}} \tag{16}$$

$$U_{edge} = U_\infty \cos(\Lambda) \sqrt{1 - C_{p,3D}} \tag{17}$$

$$p_{edge} = C_{p,3D} q + p_s \tag{18}$$

$$T_{edge} = T_\infty \left(\frac{p_{edge}}{p_s}\right)^{\frac{\gamma-1}{\gamma}} \tag{19}$$

$$T_{aw} = T_{edge} \left[1 + 0.72^{0.5} \left(\frac{\gamma - 1}{2}\right) M^2\right] \tag{20}$$

$$\mu_k = 0.00001827 \frac{411.15}{T_k + 120} \left(\frac{T_k}{291.15}\right)^{1.5} \tag{21}$$

$$\rho_k = \frac{p_{edge}}{R T_k} \tag{22}$$

An assumption in this formulation is that the $C_{p,3D}$ at the excrescence (x/c = 0.15) is equal to the $C_{p,3D}$ at x/c = 0.0154. This is due to the fact that the nearest static pressure port is at x/c = 0.0154. This pressure difference is considered negligible. The incompressible Bernoulli's equation is used to calculate the edge

velocity that is normal to the leading edge, U_{edge}. The edge pressure, p_{edge}, is calculated via definition of the pressure coefficient; q and p_s are both known. Isentropic relations for an ideal gas are used to calculate T_{edge}. The adiabatic wall temperature, T_{aw} has an assumed recovery factor of the square root of the Prandtl number, ($0.72^{1/2}$). Sutherland's law is used to calculate the viscosity at the step height, μ_k. Lastly, the ideal gas law is used to calculate the density at the step height, ρ_k. All of the calculated variables can then be used to calculate Re_{kk}.

Propagation of each variable's total uncertainty through Eq. (16)-(22) leads to the total uncertainty of Re_{kk}. The dominant term in the Re_{kk} is the uncertainty of k, which is effectively squared since it used both for the u_k calculation and the obvious k term. The total uncertainty is much more straightforward for $Re_{k\infty}$ with two primary variables: k and Re'. The uncertainty of k is ±25 μm for all step configurations, while the Re' and variables in Eq. (16)-(22) vary depending on the conditions. Similarly to Re_{kk}, the dominant term is the step height k.

Three other non-dimensional parameters were computed; the step height was referenced to the boundary-layer height δ_{99} ($0.99U_{edge}$), displacement thickness δ^*, and momentum thickness θ. Similarly to the boundary-layer properties computed above, these boundary-layer scales were computed from the same computational similarly profiles. The complete formulation of every variable's total uncertainty is shown in APPENDIX E.

Baseline Transition Location

A surface fit was created for the baseline transition location ($x_{tr,baseline}$) as a linear function of Re' and α, as shown in Fig. 80. This was important for the usage of the laminar-fraction analysis (shown below) in order to account for small variations in Re' and α between the baseline and experimental test points. A Re' range of 4.50 to 5.50 x 10^6/m and α = -6.50 and -7.50° were used for the surface fit. The α tolerance accepted as being "on condition" was ±0.05°. The surface fit's RMSE is x/c = 0.015.

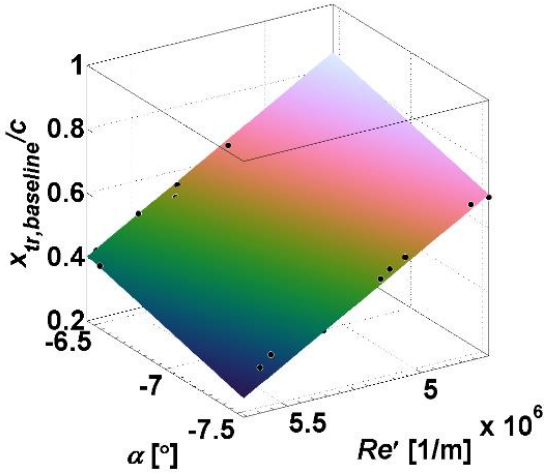

Fig. 80 Baseline-transition surface fit from flight experiment,
$x_{tr,baseline}/c = 4.005 + (0.13*\alpha) + (-4.9e^{-7}*Re')$

A total uncertainty of the baseline transition front can be computed from the above surface fit. The average baseline-transition location uncertainty is $x/c = \pm 0.025$ with a maximum uncertainty of $x/c = \pm 0.058$. This total uncertainty includes the total uncertainty of the Re' and α and the surface fit's RMSE, as shown in APPENDIX E.

At the beginning of the flight-test experiment, several baseline test points were repeated on separate flights and matched within this uncertainty.

A reminder is provided that this is the total uncertainty of the baseline cases; once excrescences are added, the total uncertainty is complicated by the added uncertainty of the step height *k*. There is not a reasonable method to add this uncertainty into the total uncertainty equation. However, the average and maximum total uncertainty of the baseline-transition location will be used as representative uncertainties with the excrescence results.

Transition-Front Analysis

Fig. 81-82 include IR thermography plots of the transition front for three forward-facing steps and three aft-facing steps compared with a baseline case with similar initial conditions. Each IR plot has the computer post-processed transition location at the top of the plot alongside the computed transition uncertainty. The total uncertainty of the transition location includes the total uncertainty of the Re' and α and the baseline

surface fit's RMSE. Turbulent trips were placed just forward of the excrescence to showcase the usable test area of undisturbed flow by the pressure taps; turbulent wedges can be seen propagating from the top left and bottom left corners. It is important to note that this is not a phenomena related to the excrescence or test article; the computer post-processing code neglects the area created by these turbulent wedges in the transition location calculation.

Each IR plot and transition-location calculation was inspected to ensure correctness. Some test points needed to be discarded due to large deviations of the conditions. Also, the code sometimes computes 2-3 potential transition locations. Typically, the transition location with the largest amplitude in the PDF was selected; otherwise, the transition location that is most laminar was selected. Due to transition to turbulence being sensitive, turbulence can be caused easily while laminar flow cannot.

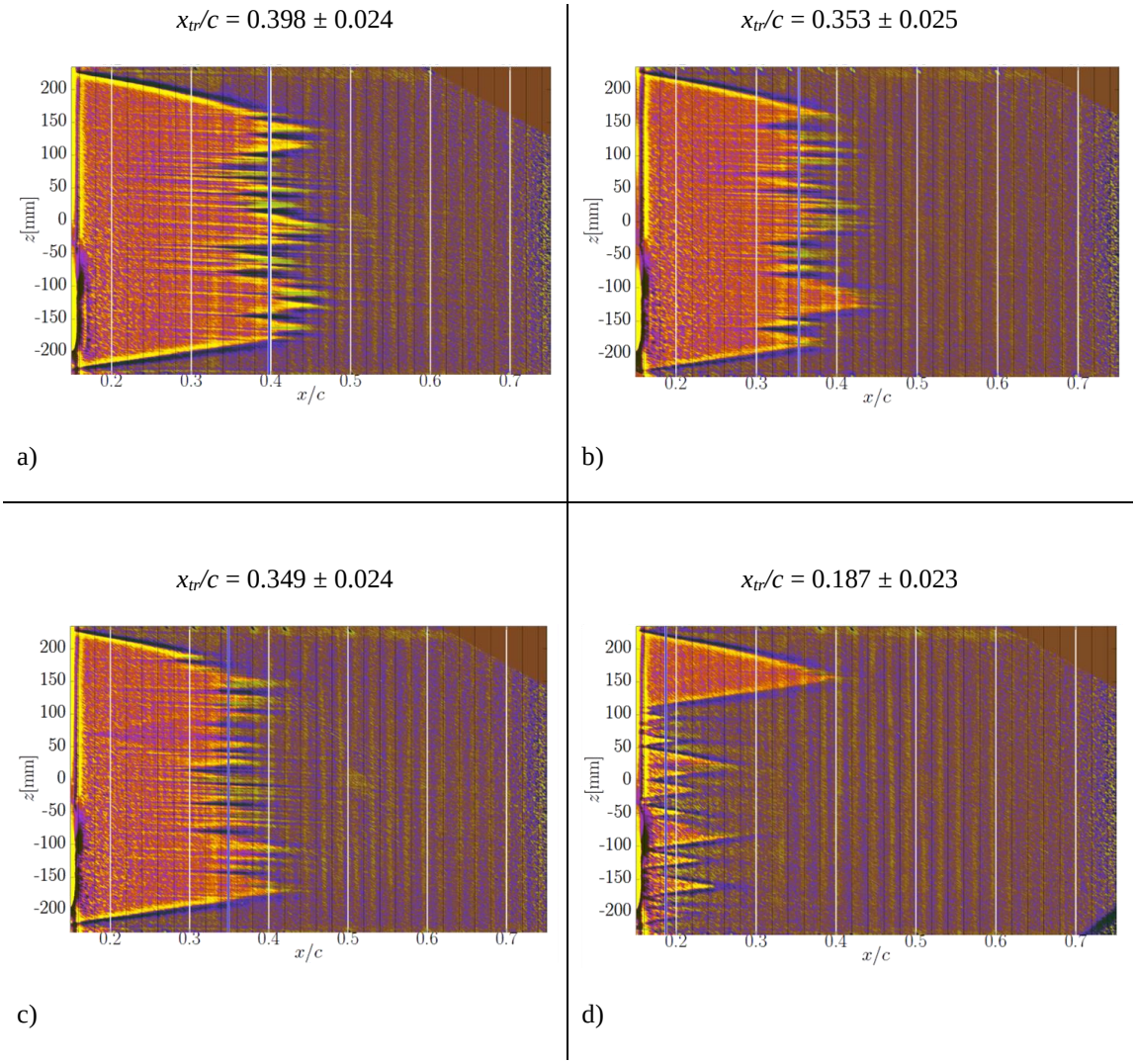

	α [°]	Re' [x 10^6/m]	k [µm]	Re_{kk} [-]	$Re_{k\infty}$ [-]	k/δ_{99} [-]	k/δ^* [-]
a)	-7.52 ± 0.12	5.35 ± 0.02	0 ± 25	0 ± 0	0 ± 134	0 ± 0	0 ± 0
b)	-7.47 ± 0.13	5.25 ± 0.02	200 ± 25	446 ± 73	1048 ± 131	0.26 ± 0.03	0.8 ± 0.1
c)	-7.45 ± 0.12	5.30 ± 0.02	350 ± 25	1212 ± 102	1857 ± 133	0.45 ± 0.03	1.5 ± 0.1
d)	-7.51 ± 0.11	5.26 ± 0.02	450 ± 25	1771 ± 110	2362 ± 132	0.58 ± 0.03	1.8 ± 0.1

Fig. 81 IR thermography: forward-facing steps, α = -7.50°, Re' = 5.30 x 10^6/m

x_{tr}/c = 0.398 ± 0.024

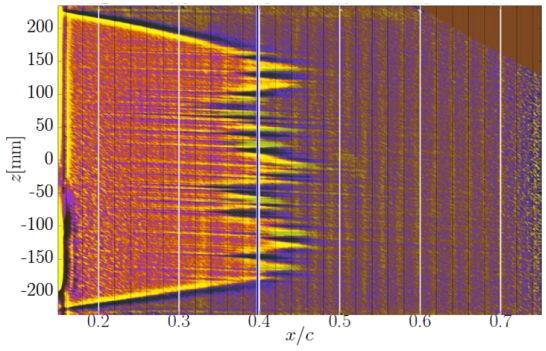

a)

x_{tr}/c = 0.369 ± 0.024

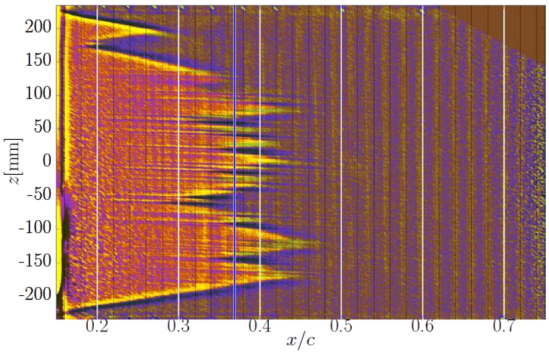

b)

x_{tr}/c = 0.406 ± 0.025

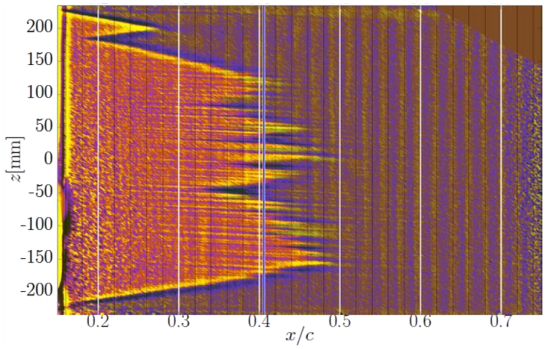

c)

x_{tr}/c = 0.195 ± 0.024

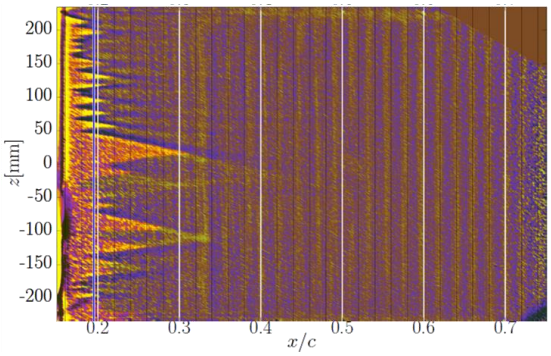

d)

	α [°]	Re' [x 10^6/m]	k [µm]	Re_{kk} [-]	$Re_{k\infty}$ [-]	k/δ_{99} [-]	k/δ^* [-]
a)	-7.52 ± 0.12	5.35 ± 0.02	0 ± 25	0 ± 0	0 ± 134	0 ± 0	0 ± 0
b)	-7.45 ± 0.12	5.29 ± 0.02	-75 ± 25	-71 ± 32	-401 ± 132	-0.10 ± 0.03	-0.3 ± 0.1
c)	-7.45 ± 0.13	5.27 ± 0.02	-125 ± 25	-186 ± 50	-657 ± 132	-0.16 ± 0.03	-0.5 ± 0.1
d)	-7.51 ± 0.12	5.27 ± 0.02	-200 ± 25	-449 ± 73	-1052 ± 132	-0.26 ± 0.03	-0.8 ± 0.1

Fig. 82 IR thermography: aft-facing steps, α = -7.50°, Re' = 5.30 x 10^6/m

The first notable of the transition fronts is that they all display a “saw-tooth” pattern. This type of nonuniform transition front is a signature of crossflow-dominated transition (Saric *et al.* [25]). Secondly, crossflow streaking can be resolved using the FLIR SC8100. This is indicative of stationary crossflow vortices with the spanwise periodic shear stress. It is interesting to note that both fully turbulent cases (“d” plots) show minimal signs of crossflow streaking in the laminar regions; this is believed to be due to the shorter streamwise length of the laminar region for the vortices to grow in strength for them to be detected with this experimental setup. However, if this is physical, it could imply that the transition process is dominated by the shear layer rather than stationary crossflow. Lastly, there does not appear to be a dependence of the varying spanwise pressure distribution on the transition front; the tip of the turbulent wedges appear to begin near the same streamwise location.

The first three transition locations (Fig. 81abc) of the forward-facing steps of k = 0, 200 and 300 μm are all barely within their experimental uncertainty bars. An argument could be made that the two cases with small forward-facing steps have slightly moved forward of the baseline. The only notable difference is that there is a faint turbulent wedge that can be seen in Fig. 81c at z = +70 mm starting at $x/c \approx 0.17$; this is believed to be due to a small nick in the polished leading-edge part upstream of this spanwise location. This turbulent wedge does not affect the detection of the main transition location. Lastly, once the forward-facing step is increased to 450 ± 25 μm, the transition front is essentially fully turbulent.

Unlike the forward-facing steps, the first three transition locations (Fig. 82abc) of the aft-facing steps are all confidently within the experimental uncertainty bars. An aft-facing step of -125 ± 25 μm is shown to have the same transition location as the baseline case. Fig. 82bc both have turbulent wedges appearing in the spanwise region from z = +150 to 200 mm starting near $x/c \approx 0.18$; this is believed to be due to slightly larger Pk-Pk roughness on the polished leading-edge part upstream of this spanwise location. These wedges do not affect the detection of the main transition location. Lastly, once the aft-facing step is increased to -200 ± 25 μm, the transition front is essentially fully turbulent.

The transition fronts for every step configuration acquired at nominal initial conditions of α = -7.50° and Re' = 5.30 x 10^6/m are shown in Fig. 83 for forward-facing steps and Fig. 84 for aft-facing steps. The color legend is increasing magnitude of step height with colors varying from light to dark. These plots of the

transition location are directly from the output of the computer post-processing code. Sometimes the code incorrectly detects the transition front; this usually takes the form of a nearly horizontal streak across the streamwise direction. One example is the -250 ± 25 μm case in Fig. 84. However, this does not affect the ability to accurately detect the transition location.

All of the reduced transition fronts in the flight environment are shown in APPENDIX F and grouped together by similar initial conditions, like Fig. 83 and Fig. 84. This method for archiving the transition results is used in lieu of attaching 500+ IR plots.

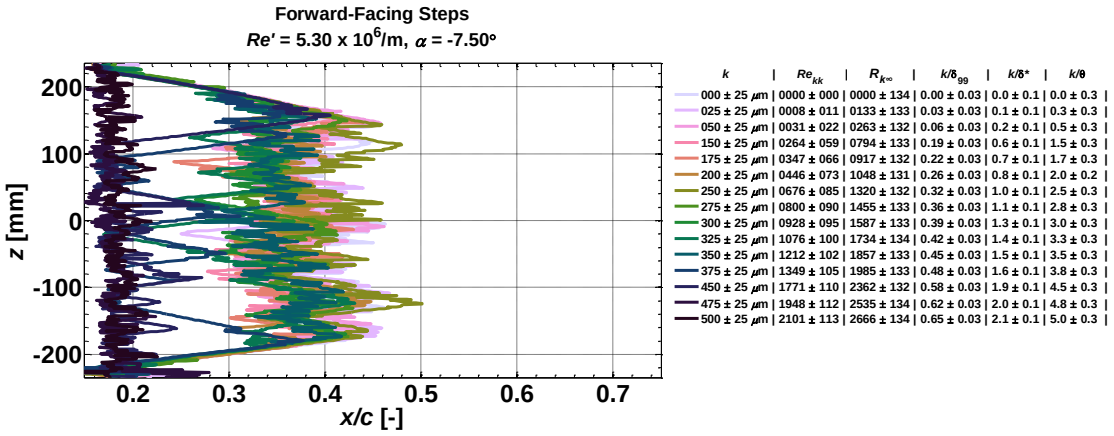

Fig. 83 Transition-front analysis of forward-facing steps, α = -7.50°, Re' = 5.30 x 10^6/m

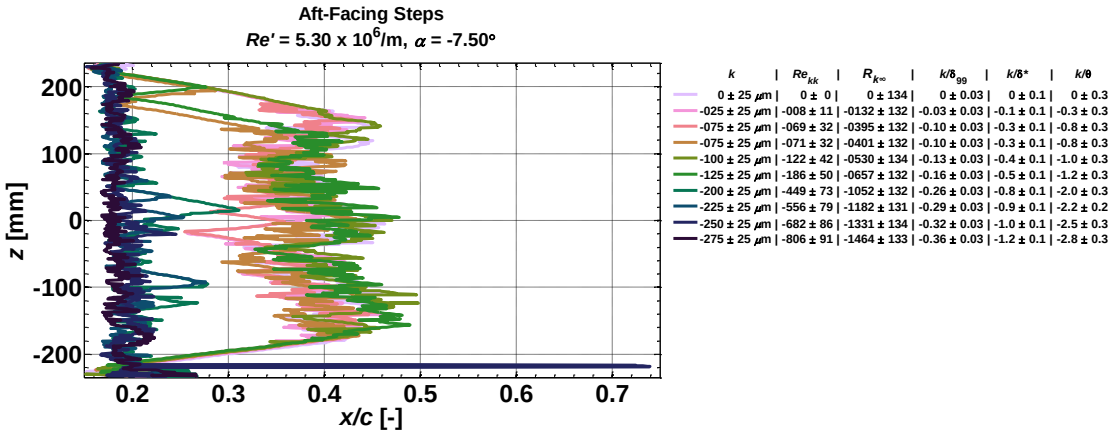

Fig. 84 Transition-front analysis of aft-facing steps, α = -7.50°, Re' = 5.30 x 10^6/m

It is clear that aft-facing steps are more precarious than the forward-facing steps; at these initial conditions, a forward-facing step can be at least twice as large as an aft-facing step. It is also apparent for both the forward- and aft-facing steps that there are two distinct transition locations: a laminar case and a fully turbulent case. Most of the smaller step heights have the same nominal transition location within experimental uncertainty (laminar case). As the larger step heights are increased, the laminar region rapidly decreases as the turbulent wedges begin to appear starting at $x/c \approx 0.16$-0.18; the full span then becomes fully turbulent with the tip of the wedges closely spaced together across the full span (fully turbulent case).

Also, it is important to note that the initial conditions presented in Fig. 81-84 are nominally $\alpha = -7.50°$ and $Re' = 5.30 \times 10^6$/m. The tolerance of the "on condition" mean value for α is ±0.05° and Re' is ±0.05 x 10^6/m. This is fitting for α due to the higher uncertainty of 0.13°; however, the Re' uncertainty of ±0.02 x 10^6/m is slightly lower than this tolerance. This distinction is made to remind the reader that it is difficult to compare transition fronts of one specific initial condition. In an effort to alleviate this issue, the baseline-transition surface fit is used to compute a laminar-fraction quantity and a global analysis is performed of all data points, as described below.

Laminar-Fraction Analysis

In an effort to compare the amount of laminar flow for each initial condition (i.e. Re' and α), the laminar fraction was computed. The transition location of the test point of interest, x_{tr}, is compared to the baseline transition location; the baseline transition curve fit is used for the specific initial conditions. The streamwise location of the excrescence (x_k) is removed in order to compare directly with other excrescence experiments. A value of "1" is fully laminar, while a value of "0" is fully turbulent at the excrescence. The laminar-fraction formulation is shown in Eq. (23).

$$\text{Laminar fraction} = \frac{x_{tr} - x_k}{x_{tr,baseline} - x_k} \tag{23}$$

All α = -6.50° and -7.50° data collected during the flight experiment are shown as a colored representation of the laminar fraction in Fig. 85-87, except Fig. 85c which is a representation of the leading-

edge sweep. Fig. 85 portrays how the laminar fraction or Λ varies as a function of the Re' and step height. Fig. 86-87 portrays how the laminar fraction varies as a function of Re' and non-dimensional Reynolds parameters, Re_{kk} and $Re_{k\infty}$, and boundary layer parameters δ_{99}, δ^*, and θ, respectively. The black dots are the acquired data points, and the plotted quantity is interpolated between these points to create a surface plot.

For the two pressure gradients tested in the flight environment, pressure gradient does not appear to be a major contributor to the critical step height; this is the reason for combining both α in Fig. 85-87. The main effect is that α = -7.50° has a baseline transition located farther upstream than α = -6.50°; however, the shown trends appear to be similar.

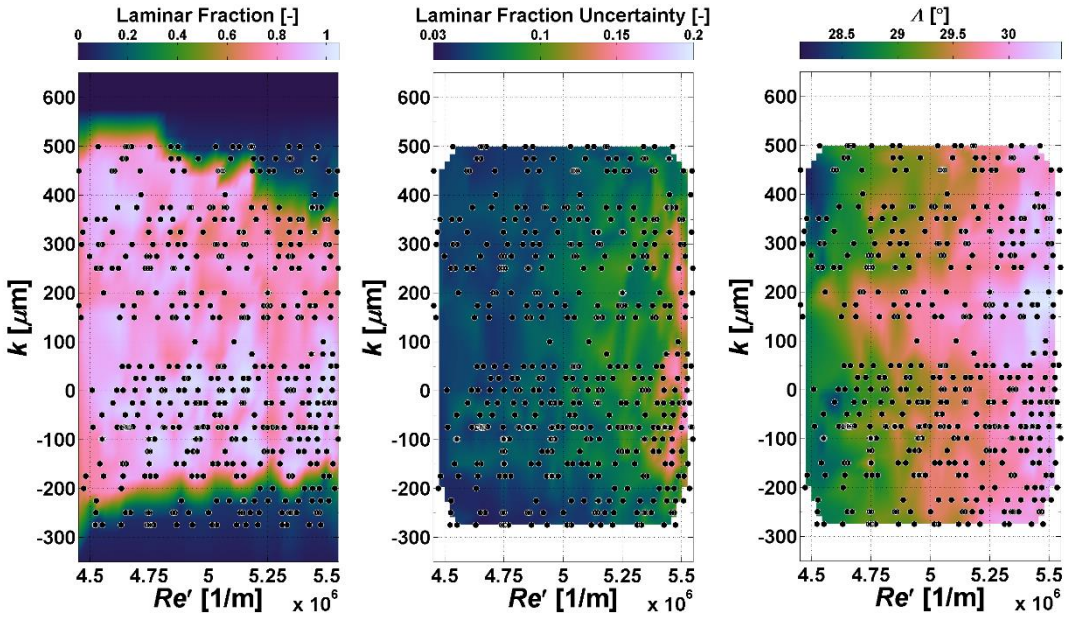

Fig. 85 Transition analysis, a) laminar fraction, b) laminar-fraction total uncertainty, c) leading-edge sweep, (+) = forward-facing steps, (-) = aft-facing steps

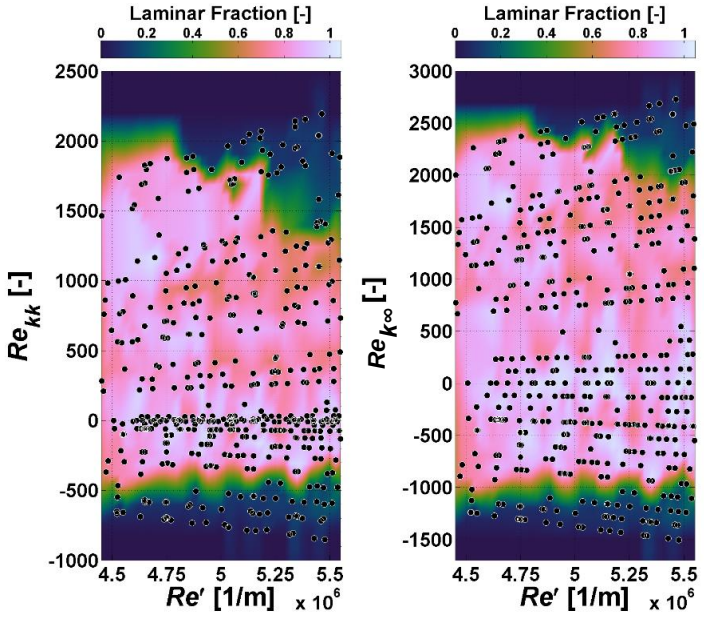

Fig. 86 Laminar-fraction analysis with non-dimensional Reynolds parameters, (+) = forward-facing steps, (-) = aft-facing steps

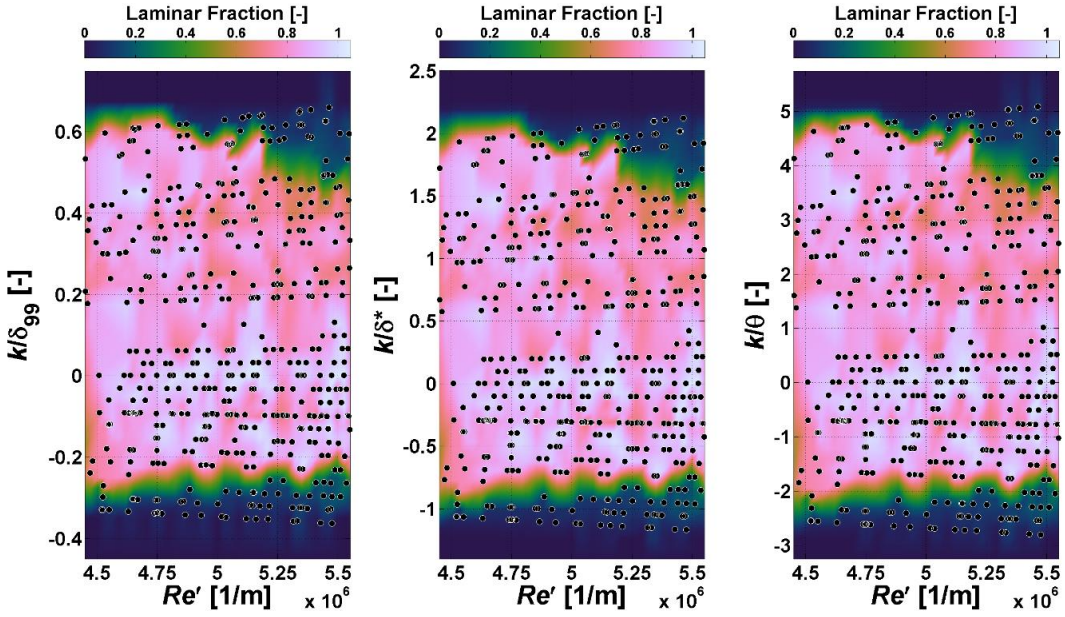

Fig. 87 Laminar-fraction analysis with boundary-layer relationships, (+) = forward-facing steps, (-) = aft-facing steps

It is evident that there are two separate laminar-fraction regions: [0 to ~0.30] and [~0.60 to 1]. It is believed that the latter region is dominated by the crossflow instability, while the former is dominated by the shear-layer instability caused by the step. As the step height is increased from the baseline, the transition front remains mainly laminar and breakdown is due to the crossflow instability. Then, the step height reaches a 'critical' height and the front snaps forward; breakdown is due to shear-layer instability. Immediately prior to this distinct gradient in the laminar-flow fraction is the defined as the 'critical' step threshold. This is in agreement with the crossflow streaking disappearing in the IR plot for the critical cases in Fig. 81d and Fig. 82d. Also, this type of phenomenon is in agreement with the description provided in Klebanoff & Tidstrom [15] of the stability-governed breakdown with smaller steps to a shear-layer breakdown with larger steps.

There are two important observations for the laminar-fraction analysis. (1) Within the critical step envelope as the forward-facing step height is increased, it appears that a slight reduction from the baseline laminar fraction occurs, just outside the experimental uncertainty. However, generally, within the critical step envelope for the aft-facing steps, the laminar fraction is equal to 1 within the experimental uncertainty. (2) As the Re' is increased, the critical step height becomes smaller in magnitude for both forward- and aft-facing steps. The slope is more severe for the forward-facing steps. Both of these observations could be due to the modulation of the precarious separated region aft of the forward-facing step as a function of Re', as this separated region is the dominant factor in the shear-layer instability. The aft-facing steps only have one separated region.

The primary variation in the laminar fraction within the critical step envelope is due to the experimental error, as shown in Fig. 85b; as the Re' increases, the baseline transition location moves forward, and essentially the laminar-fraction signal-to-noise ratio gets worse. The minimum laminar-fraction uncertainty is 0.03 at low Re', while the maximum is 0.20 at high Re'. Also, there is a secondary weak correlation with Λ, as shown in Fig. 85b; when the Λ is higher, the transition fraction tends to be slightly lower than its neighbors.

A summary of the critical step height values for $Re' = 5.50 \times 10^6$/m derived from Fig. 85-87 is shown in Table 20. These values are the maximum steps with a laminar fraction in the laminar region. The critical

step height for forward-facing is more than 2 times larger than the aft-facing. The step height can be up to $^1/_5$ of the boundary-layer height for aft-facing steps, but can be up to about $^1/_2$ for forward-facing.

Table 20 Critical step height values at $Re' = 5.50 \times 10^6$/m, derived from Fig. 85 and Fig. 86

	Aft-facing	Forward-facing
k	-150 ± 25 μm	350 ± 25 μm
Re_{kk}	-280 ± 60	1290 ± 110
$Re_{k\infty}$	-830 ± 140	1930 ± 140
k/δ_{99}	-0.20 ± 0.03	0.47 ± 0.03
k/δ^*	-0.6 ± 0.1	1.5 ± 0.1
k/θ	-1.5 ± 0.3	3.6 ± 0.3

VI. WIND-TUNNEL RESULTS AT SUB-TRANSPORT UNIT REYNOLDS NUMBERS

This section describes the results obtained during the wind-tunnel campaign. The surface pressure measurements are then compared and validated with two CFD solutions. Also, the pressure gradient obtained in the wind tunnel is compared with the pressure gradient in the flight environment. Finally, the notables of the infrared thermography and hotwire anemometry campaigns will be documented.

A. Pressure Distribution

During the surface pressure measurements, the step height was kept constant while the Re' was modulated from 0.50 to 1.50 x 10^6/m in 0.50 x 10^6/m increments. Forward- and aft-facing step heights of 1, 3 and 5 mm were tested at these unit Reynolds numbers. Additional unit Reynolds numbers were acquired for the baseline measurements from 0.50 to 1.50 x 10^6/m in 0.25 x 10^6/m increments.

Experimental and CFD comparisons of the baseline $C_{p,3D}$ profiles are shown in Fig. 88. All cases shown are at Re' = 1.50 x 10^6/m and k = 0 μm. During $C_{p,3D}$ measurements, IR thermography was used to detect transition. All baseline cases are fully laminar up to the pressure minimum. Two types of computations, by Matthew Tufts and Kristin Ehrhardt, were performed: (1) The infinite-span calculation is a 2.5-D calculation, meaning all three velocity components are computed, but there is no variation of properties in the spanwise direction. This modeling technique allows for higher resolution compared to other methods. The infinite-span results lie in between those from the experimental root and tip pressure port rows with the majority being in the experimental uncertainty. (2) The finite-span calculation is a 3-D calculation using a Navier-Stokes flow solver. The KSWT test section is directly modeled with all four test-section walls with fully viscous boundaries. All turbulence in the simulation was modeled using a k-omega SST turbulence model. Only the test side of the model was assumed to be laminar, up to the pressure minimum (x/c = 0.70). The finite-span calculation has good agreement with the experimental results. The differences between the root and tip rows are captured in the computation. From x/c = 0.16 to 0.70, the finite-span results lie within the experimental uncertainty, while the remaining chord results are near the uncertainty bars.

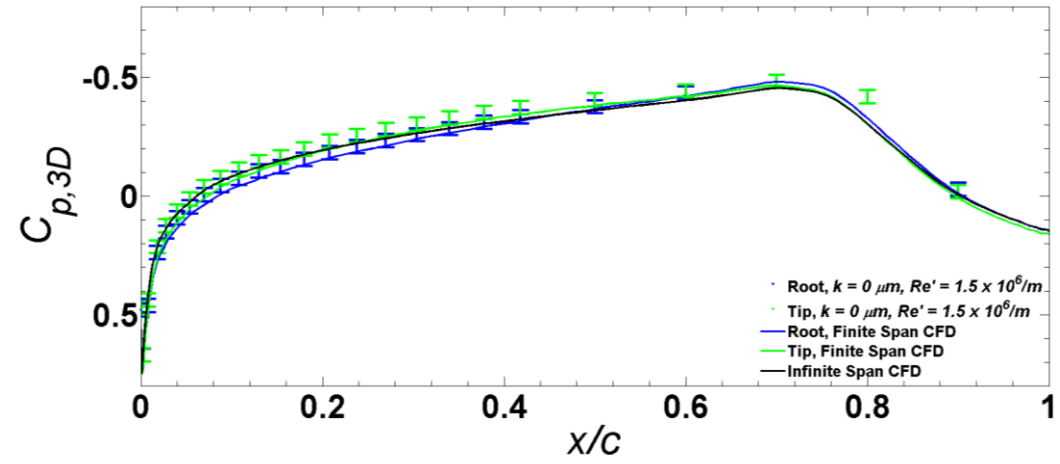

Fig. 88 Experimental baseline comparison with CFD (finite and infinite span), k = 0 μm, Re' = 1.50 x 10^6/m

The effect of step height on the pressure distribution is shown in Fig. 89. Forward- and aft-facing steps of height k = (±) 1, 3, and 5 mm are shown at Re' = 1.0 x 10^6/m. A baseline case is also shown for comparison. For the step cases shown, the boundary layer is either fully laminar to the pressure minimum or turbulent directly aft of the excrescence. The boundary layer in the presence of an excrescence of 1 mm height is fully laminar for both forward- and aft-facing, while those for k = 3 and 5 mm are fully turbulent aft of the excrescence. Thus, there should not be any localized $C_{p,3D}$ spikes due to transition-induced variation in the displacement thickness.

A zoomed-in plot around the excrescence is shown in Fig. 90. The upstream influence of the aft-facing steps is less pronounced than that for the forward-facing steps. Around x/c = 0.12, the flow starts to accelerate with an aft-facing step relative to the baseline. Around x/c = 0.02, the flow starts to decelerate with a forward-facing step relative to the baseline. A reminder is provided that the experimental data is at discrete points; thus, the character of the profile, especially around x/c = 0.15 (excrescence location), might be misleading. These data will be used to validate specific points on a finely-meshed computation to capture the character of the profile around the excrescence. The aft-facing steps have more influence on the $C_{p,3D}$ downstream of the step than the forward-facing steps. By x/c = 0.25, all of the step cases have collapsed to the baseline case within measurement uncertainty. The $\Delta C_{p,3D}$ at x/c = 0.154 (immediately after step) is much

more pronounced for the forward-facing steps. For 5 mm, $\Delta C_{p,3D}$ = -0.5 from the baseline, while for -5 mm, $\Delta C_{p,3D}$ = -0.15 from the baseline.

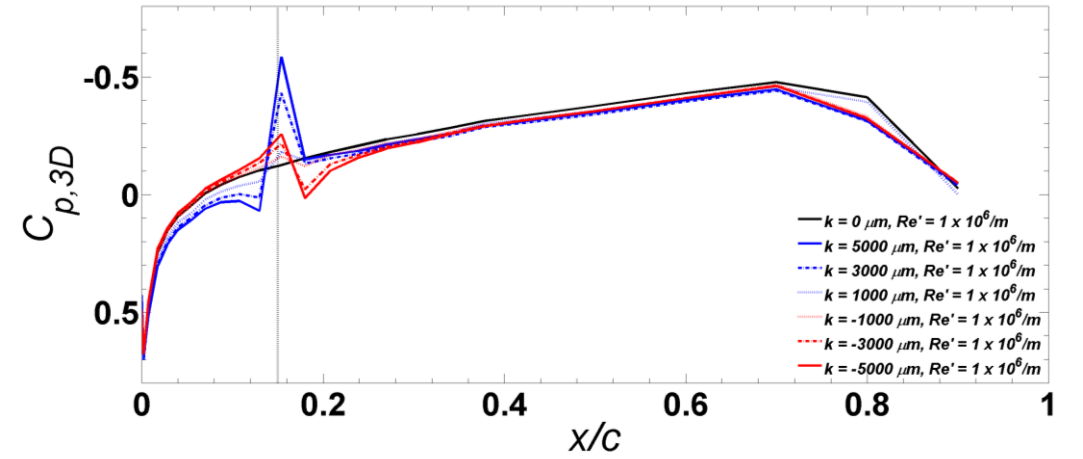

Fig. 89 Experimental step-sweep comparison to baseline, *Re´* = 1.00 x 10^6/m

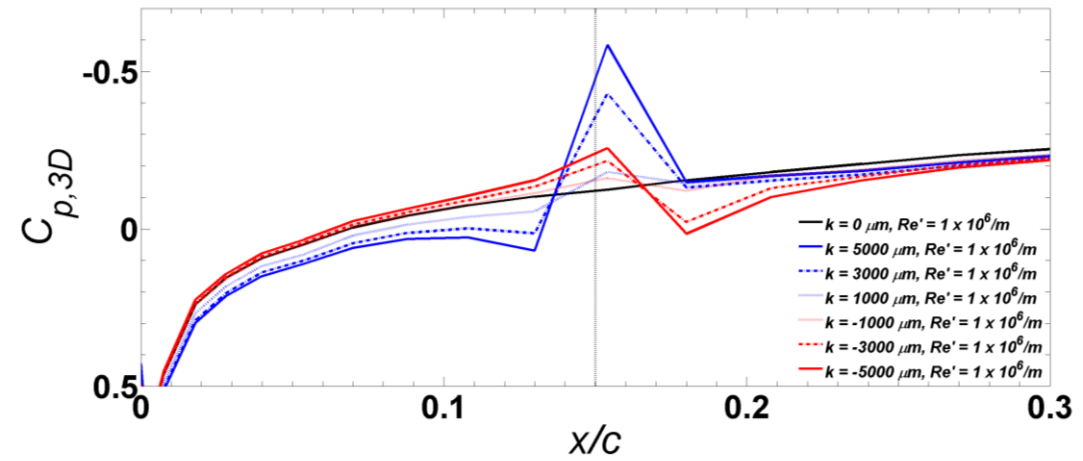

Fig. 90 Experimental step-sweep comparison to baseline, *Re´* = 1.00 x 10^6/m (zoomed-in of previous figure)

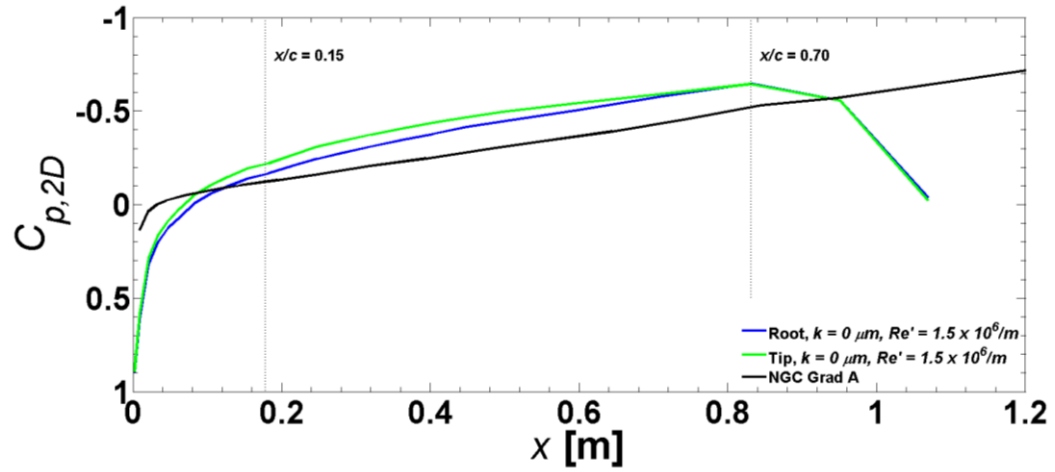

Fig. 91 Experimental data $C_{p,2D}$ comparison with NGC's Grad A model

Table 21 $C_{p,x}$ comparison between flight and wind tunnel environment

$C_{p,x}$	Flight (α = -7.50°)	Wind Tunnel (α = -1.70°)
Root Local (x/c = 0.15 to 0.20)	-1.22 ± 0.02	-1.21 ± 0.01
Tip Local (x/c = 0.15 to 0.20)	-1.02 ± 0.01	-1.38 ± 0.01
Root Global (x/c = 0.15 to 0.70)	-0.71 ± 0.02	-0.73 ± 0.02
Tip Global (x/c = 0.15 to 0.70)	-0.44 ± 0.02	-0.63 ± 0.03

The α tested in the wind tunnel was determined through matching the pressure gradient normal to the leading edge of the unswept work of NGC's Grad A model. Before the wind tunnel experiment, a CFD analysis was performed by calculating the pressure gradient at several α. It was decided that α = -1.70° (experimental reference frame) matched NGC's Grad A model the best and the experiment could commence. A baseline experimental comparison of the $C_{p,2D}$ profiles at α = -1.70° is shown in Fig. 91. The excrescence location and pressure minimum are displayed for reference.

Similarly to the flight profiles, the local (x/c = 0.15 to 0.20) pressure gradient is more favorable than the global (x/c = 0.15 to 0.70) pressure gradient. A comparison of the flight and wind tunnel $C_{p,x}$ calculations are summarized in Table 21. The root values are essentially identical, while there is a slight variance in the tip values; the tip profiles in the wind tunnel are slightly more favorable. Comparable to the flight environment, the wind-tunnel pressure gradient is similar to NGC's Grad A model; thus, the unswept work and swept work can be compared directly.

B. Infrared Thermography

The test matrix for the IR thermography campaign consisted of *Re´* from 0.50 to 1.50 x 10^6/m in 0.10 x 10^6/m increments. The step-height range was adjusted for each *Re´* for efficiency purposes. Approximately 900 unique configurations (*Re´* and *k*) were tested. The first mentionable is that the transition front was never spanwise uniform, similar to what is seen in the flight environment (except when fully laminar or fully turbulent). As the step height was increased, turbulent wedges would start to appear aft of the separated region. More wedges would appear until the entire test surface is turbulent. There is consistent spanwise character to all of the aft-facing steps and all of the forward-facing steps. However, the spanwise character is different between the forward- and aft-facing steps.

Three IR images are shown in Fig. 92-94. Fig. 92 portrays a fully laminar case. The post-processing code will attempt to find a transition front, even if it is a fully laminar case. Thus, it shows false positives as the darker transition front. The brown region in the upper-right corner of each IR figure is the area that was not captured in the field-of-view of the IR camera. Also, there are not any turbulent trips forward of the excrescence at the pressure tap rows, like the IR thermography campaign in the flight environment. The blue vertical line(s) in each of the IR plots represents the calculated transition location(s).

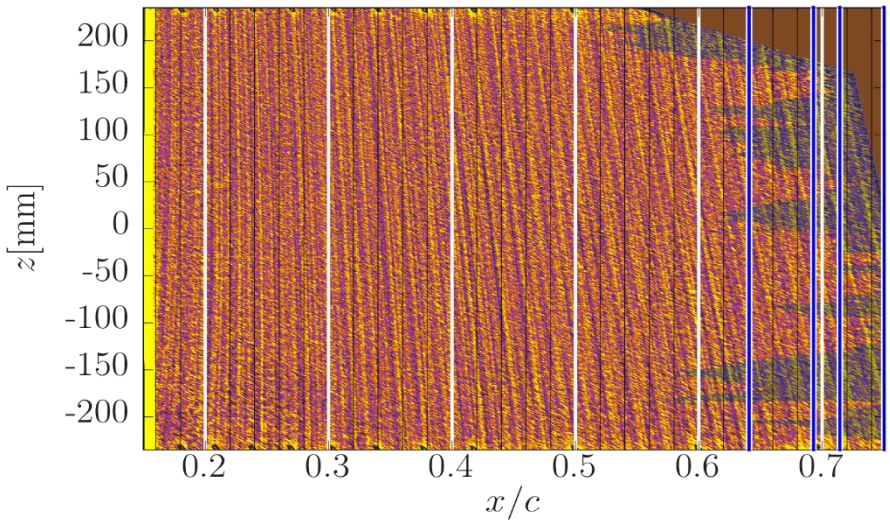

Fig. 92 Fully laminar, *k* = 1,500 µm, *Re´* = 1.00 x 10^6/m

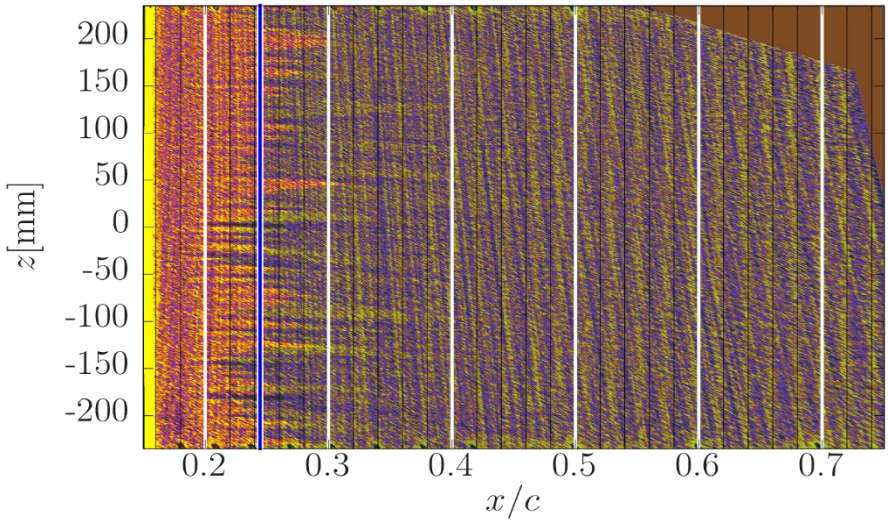

Fig. 93 Nonuniform transition front, k = -1,525 µm, Re' = 1.00 x 10^6/m

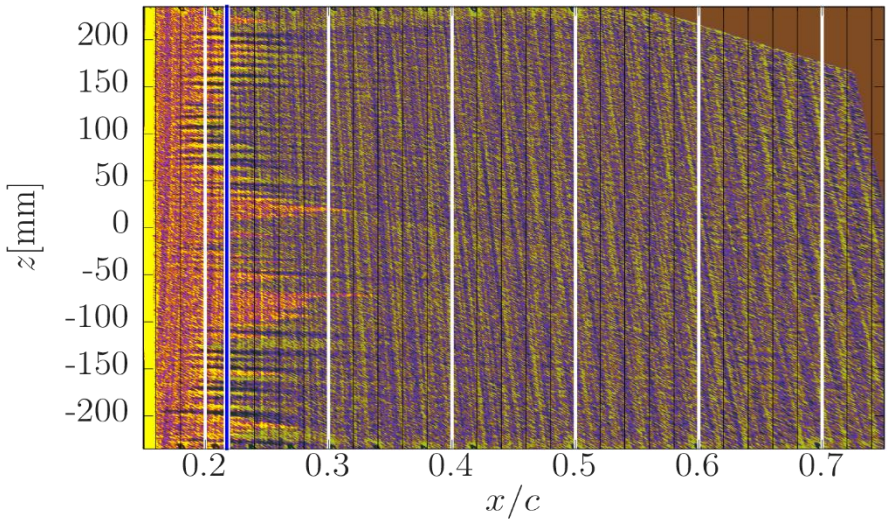

Fig. 94 Nonuniform transition front, k = 1,775 µm, Re' = 1.00 x 10^6/m

Fig. 93 portrays a spanwise nonuniform transition front created by an aft-facing step. The darker, purple bands are turbulent streaks from x/c = 0.20-0.30 at these z locations: [0 to -50] mm and [-100 to -170] mm. The majority of the lighter purple regions are intermittent laminar areas. A few laminar regions extend to x/c = 0.50 for this configuration. The intermittency of the transition front is believed to be due to unsteadiness in the separated region caused by the steps.

Fig. 94 portrays a spanwise nonuniform transition front created by a forward-facing step. The forward-facing steps consistently had regions of turbulence at these *z* locations: [220 to 50] mm and [-110 to -230] mm. The most negative region correlates with the aft-facing steps turbulent region, but the positive *z* region did not have any correlation. The main difference between the flight and wind tunnel IR plots is that the transition front in the wind tunnel appears to be more streaky, compared to the large-scale array of turbulent wedges in flight. Also, the flight IR plots are clearer due to the higher shear stress.

In the wind tunnel, the basic state of the flow is very stable. As such, when the flow first starts to transition visibly, it has likely already passed the critical threshold. Because of this, the largest step that is still fully laminar, without any intermittent wedges, is deemed the critical step threshold for the wind tunnel results. Since the results shown in Fig. 93 and Fig. 94 are already past the critical value, it is not surprising that the front is nonuniform.

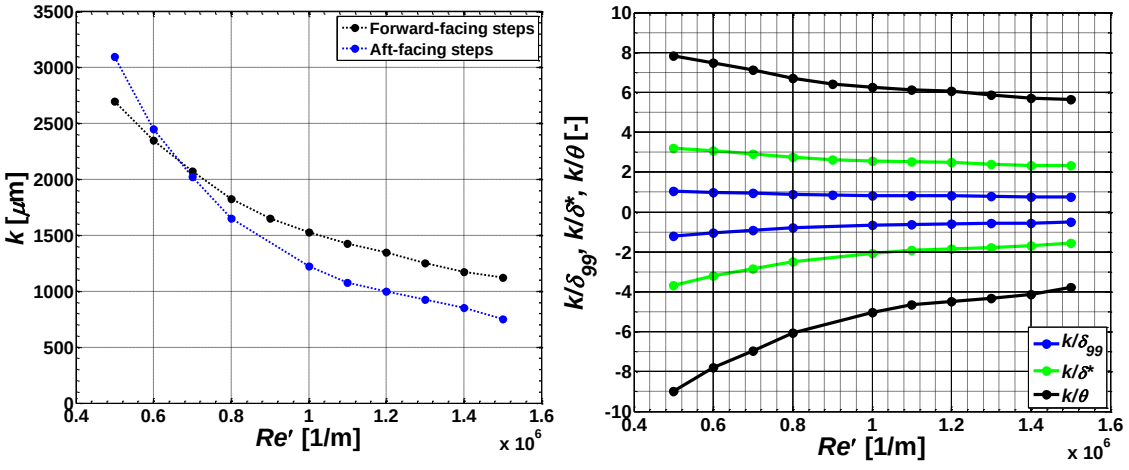

a) **b)**

Fig. 95 Critical step height analysis, a) step height, b) boundary-layer relationships

The critical step height as a function of *Re´* is shown in Fig. 95a, and the boundary-layer relationships are shown in Fig. 95b. It is important to note that the uncertainty of the step height is smaller than the dot height (±25 μm). The critical aft-facing steps at *Re´* = 0.50-0.60 x 10^6/m are larger than the forward-facing steps; this is attributed to a low Reynolds number effect. At low Reynolds numbers, the critical step height

is larger than the boundary-layer height, but becomes 0.75 and 0.50 of the boundary-layer height at 1.50 x 10^6/m for forward- and aft-facing, respectively. Also, the slope of the forward-facing steps is more gradual than the aft-facing steps. For reference in the hotwire measurements at Re' = 1.00 x 10^6/m, the aft- and forward-facing critical step heights are -1,225 ± 25 and 1,525 ± 25 μm, respectively.

Spanwise Nonuniformity

Several tests were conducted to attempt to resolve the cause of the spanwise nonuniformity in the wind tunnel. The first obvious suspect was a differential step height. The step height is measured in real time by two internal displacement sensors. Sensor error and calibration error lead to a conservative uncertainty of ±25 μm. Also, as an additional measurement, a camera with a macro lens (4 μm/pixel) was used several times to measure the step-height variation across the span. The standard deviation of the measurement was 6 μm with a peak-to-peak of 12 μm. There was not any correlation with the deviations from the nominal with the transition front. Another suspect was the gasket not properly sealing at the excrescence. A piece of Kapton tape (64 μm thick, 13 mm wide) was placed over the excrescence and re-tested. There was no change in the transition front, even with influence of the tape. Differential surface roughness could be a suspect. However, the advantage to having a polished surface is that any major imperfections are easily seen by eye. After several examinations of the leading-edge part, differential surface roughness is not likely. A potential source of nonuniformity could be the surface waviness in the leading-edge part. A one meter-long, laser profilometer built in-house was used to measure the outer mean line of the leading-edge part. Measurements were performed in 0.1% chord increments and the peak-to-peak was ±50 μm across the entire meter long travel. Also, there was not any correlation with the transition front and outer mean line deviations. Attachment-line contamination from the relatively large step from the interface of the root spacer to the root of the model could be problematic. The root spacer was removed and saw no effect on the transition front. Attachment-line contamination was not expected to be an issue because of the low attachment-line, momentum thickness Reynolds number ($Re_\theta << 100$).

A potential culprit was freestream acoustics interacting with the 2-D step and exciting T-S waves, travelling crossflow, or shear-layer instability. A speaker wall installed in the KSWT, capable of producing controlled acoustical disturbances, was driven to 110 dB and incremented through frequencies of 10 to 650

Hz. There was no effect on transition, which confirms that none of the instabilities present on this model are sensitive to freestream acoustics in this frequency range (similarly to Radeztsky *et al.* [8]). The inclusion of a large (k = 1,400 μm) forward-facing step does not change these results.

Lastly, an examination into possible spanwise-varying freestream conditions was performed. Using the IR camera and the unheated model as the reference, the variation in freestream temperature was measured to be less than 0.5 K and did not correlate with the transition front. The freestream steady and unsteady velocity were measured with a hotwire. A vertical scan (not swept) was performed approximately 400 mm ($x/c \approx$ -0.30) in front of SWIFTER. The y-location was approximately 50 mm wall-normal from the attachment-line (farthest the traverse could travel). The steady and unsteady velocity did not correlate with the transition front. Also, the transition front did not change character as the unit Reynolds number was modulated, even though the freestream turbulence varies through the full velocity range of the tunnel. However, once the unsteady velocity was transformed into the frequency domain, a nonuniform measurement was noticed, as shown in Fig. 96. Five seconds of data were acquired at each spanwise location. Welch's method was used to calculate the PSD: nine hamming windows were averaged with 50% overlap. The most noticeable non-spanwise frequency was 56 Hz. 52 Hz had similar character to 56 Hz, but had lower spanwise power variation. There were also spikes in 82 Hz sporadically across the spanwise direction. The 56 Hz PSD has a strong correlation with the forward-facing step transition front (Fig. 97). The high PSD corresponds to turbulent regions, while the lower and moderate PSD corresponds to intermittent laminar extension. Linear stability theory predicts elevated N-factors at travelling crossflow frequencies up to 70 Hz at $Re' = 1.00 \times 10^6$/m, as compared to the stationary mode. Travelling crossflow coupled with this freestream-frequency nonuniformity may be contributing to the nonuniform transition front.

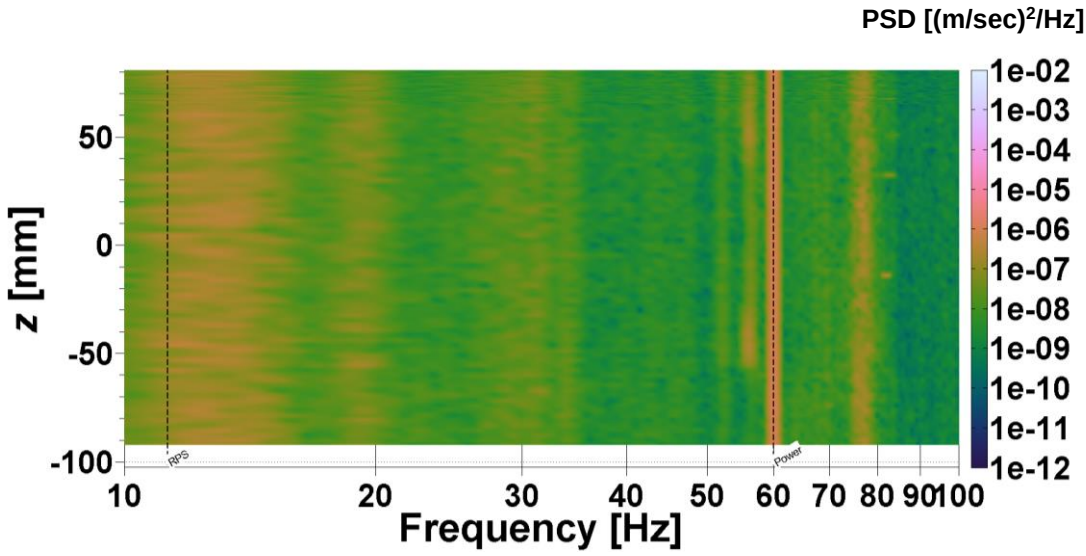

Fig. 96 Freestream PSD spectrogram, RPS = revolutions per second, Power = 60 Hz AC

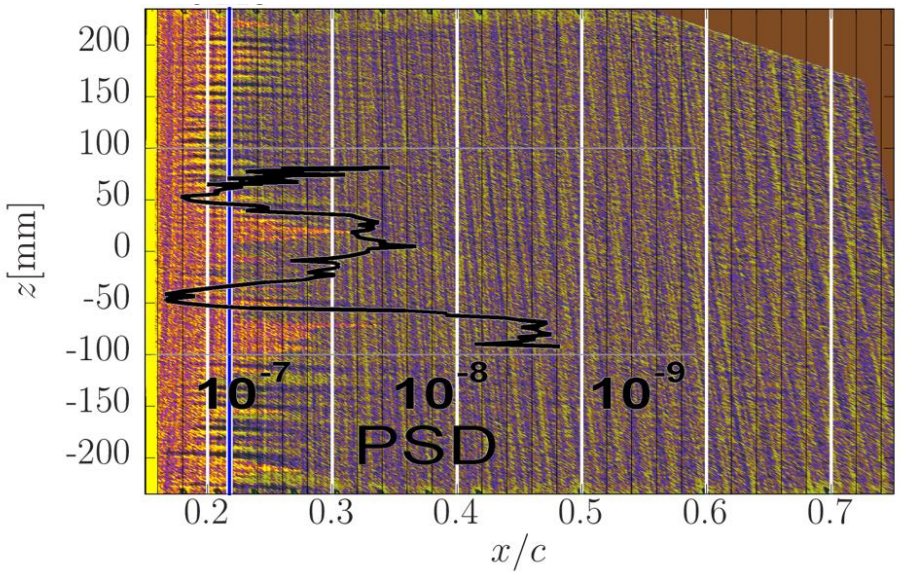

Fig. 97 Infrared measurement with overlaid freestream hotwire PSD of 56 Hz
***Re´* = 1.00 x 10^6 1/m, *k* = 1,775 µm**

Critical Step Height Comparisons

A transition analysis of the critical step-height relationship with unit Reynolds number is shown in Fig. 98. The wind tunnel results are the lower *Re´* from 0.50 to 1.50 x 10^6/m, while the flight results are from 4.45 to 5.55 x 10^6/m.

The shown trends have good agreement for including this large *Re´* range. A conservative effort was applied to ensure that the shown trend does not include data points that are in the turbulent region. However, the forward-facing steps have some slight disagreement from 4.45 to 5.25 x 10^6/m (the lighter colors above the trend line). This could be attributed to a secondary effect with the second separated region aft of the forward-facing step (first separated region is forward of the forward-facing step). The aft-facing steps only have one separated region (aft of the step) and do not have any significant disagreement with the presented trends. It is believed that the crossflow instability is the primary breakdown mechanism for the area between the two critical curves. The primary breakdown mechanism outside of these curves is believed to be the shear layer created by the step.

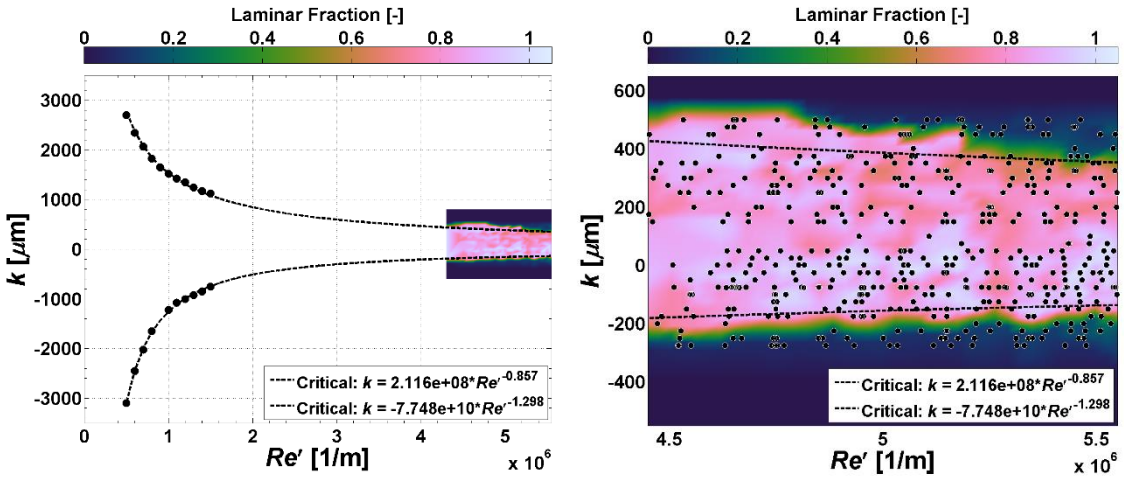

Fig. 98 Critical step height analysis (+*k* = forward-facing steps, -*k* = aft-facing steps), a) wind tunnel and flight work combined, b) flight work only

In an effort to study the influence of wing sweep, the unswept work of NGC is included in Fig. 99 ([20-24]). The TAMU team computed the laminar fraction for the unswept NGC work. The laminar-fraction amplitudes are the best estimates based on the provided information, but the relative values can be compared to find the critical step.

Fig. 99a compares the swept and unswept cases with similar 2-D pressure gradient, while Fig. 99b has an additional comparison: the slightly favorable pressure gradient, Grad Z (i.e. $C_{p,x}$ = -0.1 1/m, less favorable than Grad A). The horizontal, dashed lines of the unswept work are the reported $Re_{kk,crit}$ values from Drake *et al.* [24]; the line extends from the minimum to the maximum Re' tested for that configuration. A dependence on the Re' was not observed during their experiments; if additional data points were acquired, it is believed that it could have been observed. Based on examination of the results in Drake *et al.* [24], the $Re_{kk,crit}$ reported is the largest step height before the transition front begins to move forward; this is similar to the critical definition used in the wind tunnel with SWIFTER. Thus, these critical values can be compared with confidence. It is important to note that the swept-wing Re_{kk} values are based on the leading-edge normal velocity. Uncertainty dashed lines are also added to the swept-wing results in Fig. 99.

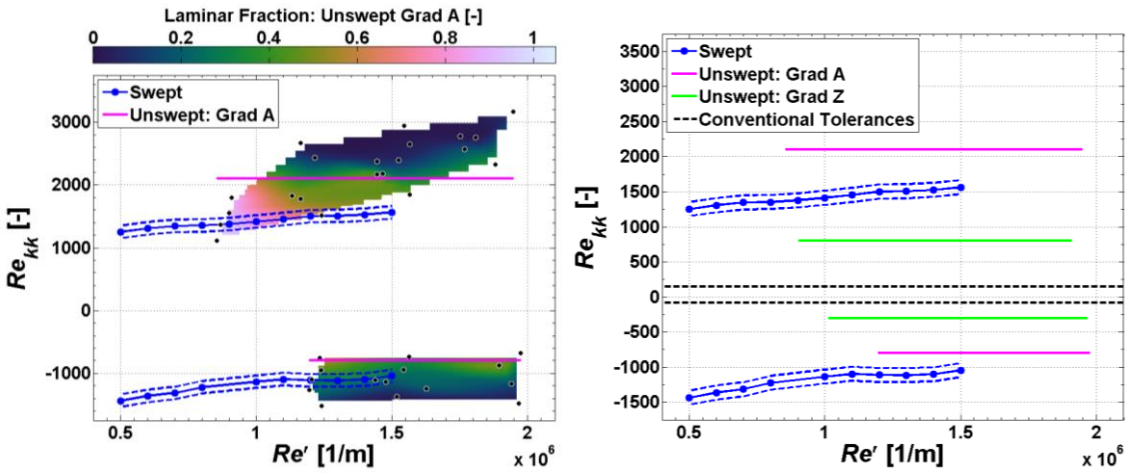

a) **b)**

Fig. 99 Critical Re_{kk} analysis with reported $Re_{kk,crit}$ from Drake *et al.* [24], a) swept, unswept Grad A (laminar fraction included), b) swept, unswept Grad A and Grad Z, conventional tolerances

It is evident that the addition of leading-edge sweep with similar 2-D pressure gradient lowers the $Re_{kk,crit}$ for the forward-facing steps by at least 500. However, the leading-edge sweep case has a larger $Re_{kk,crit}$ compared to the unswept Grad Z case by at least 400. It appears that the crossflow instability is a contributor in the critical step heights for forward-facing steps. In contrast, if similar uncertainty bars are added to the unswept work, the swept and unswept cases with similar 2-D pressure gradients have similar $Re_{kk,crit}$ for aft-facing steps. Thus, it appears that the crossflow instability is not a factor in the critical step heights for aft-facing steps.

Drake *et al.* [24] includes conventional laminar-flow tolerances used during airplane-wing design and manufacturing. Also, modifications to these tolerances were made with the testing and inclusion of pressure gradients of unswept wedges. These reported tolerances are compared with the swept-wing results of SWIFTER in Table 22 and Fig. 99b. It is important to note that the conventional tolerances do not have a listed *Re´* range; thus, dashed lines are used for reference in Fig. 99b.

Table 22 $Re_{kk,crit}$ comparison

	Re´ **[x 10^6/m]**	**Sweep**	**Pressure Gradient**	**Aft-facing** $Re_{kk,crit}$	**Forward-facing** $Re_{kk,crit}$
Conventional laminar-flow tolerances (Drake [24])	Not listed	0°	Zero	80	150
Unswept (Drake [24])	0.90-1.97	0°	Slightly favorable (Grad Z)	300	800
	0.80-1.97	0°	Favorable (Grad A)	800	2,100
Swept (Duncan 2014) SWIFTER	1.50	30°	Favorable	1,043 ± 100	1,564 ± 100
	5.50	30°	Favorable	280 ± 60	1,290 ± 110

Table 22 is included to provide quantitative values for the $Re_{kk,crit}$. It is clear that the *Re´* needs to be taken into account when using $Re_{kk,crit}$. The difference between the $Re_{kk,crit}$ for aft- and forward-facing steps at 1.50 and 5.50 x 10^6/m is 763 and 274, respectively. These are substantial differences, and if the lower *Re´* case is used for manufacturing tolerances for a transport-class aircraft, a loss of potential laminar flow would most likely occur. Thus, it appears that testing at transport unit Reynolds numbers are necessary for

application to transport-class aircraft. Also, it is evident that the conventional laminar-flow tolerances can be significantly relaxed if a favorable pressure gradient is implemented.

An interesting way to potentially relax the manufacturing tolerances is to create a rounded edge on the forward-facing step, compared to a sharp-edge step; it is believed that this reduces the extent of the separated region aft of the step. Holmes & Obara [16] reported flight-test results of unswept $Re_{k\infty,crit}$ values of 1,800 for sharp forward-facing steps and values of 2,700 for rounded forward-facing steps. The rounded-edge effect on aft-facing steps was not included; however, a $Re_{k\infty,crit}$ value of 900 was included for sharp aft-facing steps. It is interesting to note that the present swept-wing $Re_{k\infty,crit}$ results at $Re' = 5.50 \times 10^6$/m match these sharp-edge findings within the experimental uncertainty: 830 ± 140 and 1,930 ± 140 for aft- and forward-facing steps, respectively.

C. Hotwire Anemometry

Baseline Measurements

Baseline hotwire measurements were performed at six chord locations: x/c = 0.05, 0.10, 0.14, 0.16, 0.18, and 0.20. Fig. 100 shows the experimental spanwise-mean velocity profiles with the computational results of the normal-to-the-leading-edge velocity performed by Matthew Tufts; these computations are derived from the infinite-span results in the wind tunnel. The nearest streamwise location from the discrete data points of the CFD results are used to compare with the six chord locations from the experiments; the actual streamwise location is indicated in the legend. All streamwise locations have good agreement with the computations, except at x/c = 0.05. This could be attributed to a post-processed, wall-finding error from the experiment; most of the profile is slightly above the computational results.

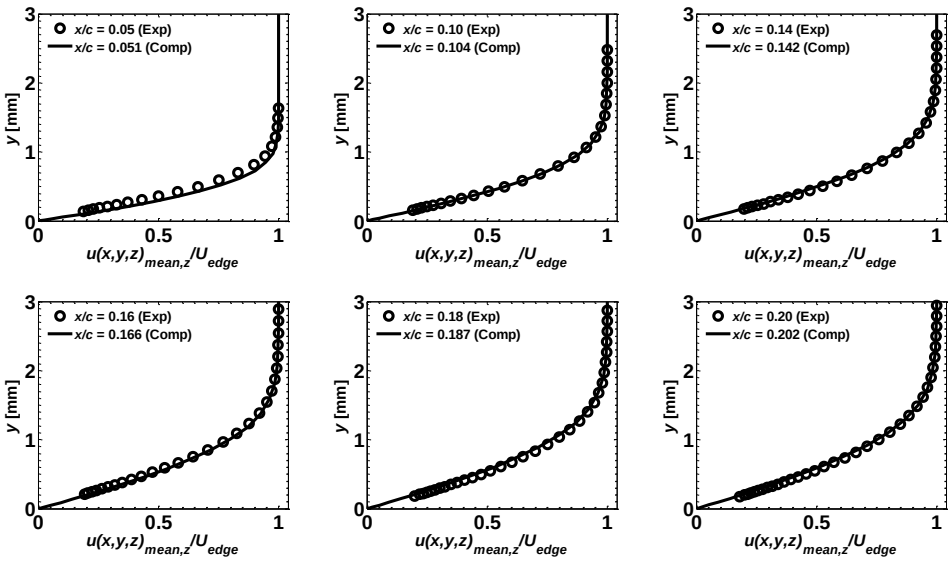

Fig. 100 Baseline experimental boundary-layer profiles compared to CFD at *Re´* = 1.00 x 10^6/m

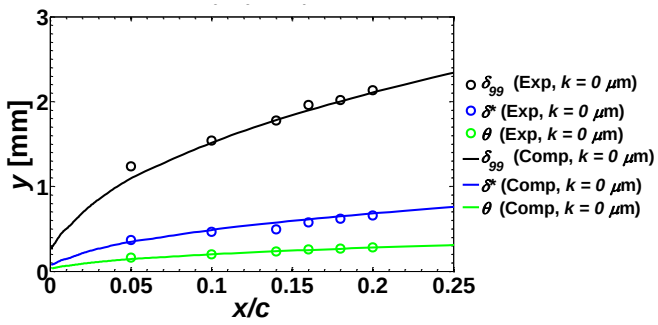

Fig. 101 Baseline experimental boundary-layer quantities compared to CFD at *Re´* = 1.00 x 10^6/m

Fig. 101 portrays the boundary-layer properties, δ_{99}, δ^*, and θ, for both the experimental and CFD results from the boundary-layer profiles shown in Fig. 100. This figure provides a quantitative insight into the differences between the experiment and computations. For reference, δ_{99}, δ^*, and θ at the excrescence location at *Re´* = 1.00 x 10^6/m equals 1.839, 0.594, and 0.244 mm, respectively. The good agreement found between the baseline experimental and CFD results provides confidence for the experiment results, especially with the addition of excrescences shown below.

Excrescence Measurements

Results of the hotwire campaign are shown in APPENDIX G. The step height configurations that were tested with hotwires were specifically selected in an attempt to provide insight to the intermittent, non-spanwise uniform transition front. The two main excrescences tested were k = -1,525 and 1,775 μm; both had regions of turbulence and as well as laminar flow in the full z travel of the 3-D hotwire traverse. Two smaller excrescences at x/c = 0.20 were also tested; k = -1,400 μm (still laminar/turbulent mix) and k = 1,500 μm (fully laminar). The z axis in the IR thermography (Fig. 93-94) and hotwire campaigns (Fig. 162-163) can be compared directly with a conservative uncertainty of ±1 mm; the dominant contributor is the hotwire placement relative to the model. All of the turbulent boundary layers measured have been removed from the presented analyses, except the unsteady-velocity contour plot; the large u'_{rms} regions can be compared with the turbulent regions in the IR figures.

Fig. 155-157 show the boundary-layer velocity profiles at x/c = 0.18. All of the measured profiles across the span are shown in black, while the spanwise mean profile is shown in blue. The spanwise deviation from the mean is clearly larger in the cases with the excrescences. In order to visualize the deviation from the mean, the steady disturbance profiles at x/c = 0.18 are shown in Fig. 158-160. The baseline case has a main lobe near y = 0.4 mm and secondary lobe near y = 0.9 mm. The aft-facing step has a slightly larger maximum disturbance than the baseline, but the profiles across the span seem to spread in the wall-normal direction within the boundary layer. The forward-facing step clearly has the largest maximum disturbance with most of the profiles reaching a maximum near y = 0.5 mm.

The unsteady velocity contours are shown in Fig. 161-163. Black contours are superimposed to indicate lines of constant velocity ratio every 10% up to 90% of the edge velocity; the last iso-velocity contour is 99% of the edge velocity. It is important to note that the unsteady velocity percentages have both the acoustic and vortical disturbances included in the measurement. Streamwise turbulence intensity measurements typically use only the fluctuations due to the vortical disturbances; thus, the unsteady velocity percentages are slightly higher than reported turbulence intensity values for the KSWT. The baseline case has an unsteady velocity of 0.06% in the freestream and reaches a maximum of 0.5% at y = 0.8 mm. Slightly higher percentages are seen at z = -83 and -20 mm; these are attributed to intermittent electronic noise of the

anemometer/filter system. The aft-facing step has an absolute maximum of 2.4%, while the majority is at 1.6%. Turbulent streaks are seen from z = -33 to 8 mm. This has excellent agreement with the IR image (Fig. 93). The forward-facing step reaches an absolute maximum of 4%, while the majority is at 1.5%. Turbulent streaks are seen from z = -42 to -24 mm and z = 28 to 84 mm. This has excellent agreement with the IR image (Fig. 94).

The remainder of the hotwire results are shown in sets of three figures for each streamwise location; (1) spanwise-mean velocity profiles, (2) spanwise-RMS steady disturbance profiles, and (3) spanwise-mean unsteady disturbances profiles. Fig. 164-166 portray the upstream influence of the steps at x/c = 0.10. Due to limited time in the wind tunnel, only one forward-facing step was tested at this streamwise location. The boundary-layer profiles lay directly on top of each other. The difference between the two profiles can be seen in the steady disturbance profile. The forward-facing step slightly reduces the magnitude of the steady disturbance profile from y = 0.3 to 1.2 mm. Similar magnitude reduction is seen in the unsteady disturbance profile from y = 0.3 to 0.8 mm.

Fig. 167-169 portray the upstream influence of the steps at x/c = 0.14. The aft-facing step is slightly accelerated relative to the baseline case, while the forward-facing step is thickened from the baseline case by approximately 300 μm. The aft-facing step reduces the magnitude of the steady disturbance profile with the character of the mode shape being similar. However, the forward-facing step has a similar absolute maximum, but changes from a bimodal shape to a unimodal shape. The unsteady disturbance profiles all have similar character and magnitude except the region from y = 0.2 to 0.8 mm. The forward-facing step reduces the unsteady content in this region, while the aft-facing step increases the unsteady content. This is believed to be due to the increased velocity for the aft-facing step and the decreased velocity for the forward-facing step.

Fig. 170-172 portray the downstream influence of the steps at x/c = 0.18. The boundary-layer profile comparison flips aft of the step; the aft-facing step is thickened from the baseline case approximately 300 μm (instead of the forward-facing), while the forward-facing step matches the baseline case. The steady disturbance profiles for both the aft- and forward-facing steps become unimodal, compared to the bimodal shape of the baseline. Both step configurations have a larger, absolute maximum of RMS amplitude than

the baseline case. The RMS magnitude is amplified to 1.3% for aft-facing and 3.6% for forward-facing, relative to 0.9% for the baseline. The forward- and aft-facing steps have similar character and magnitude for the unsteady disturbances profiles from y = 0.3 to 1.6 mm. However, the aft-facing step has an additional secondary lobe from y = 1.6 to 3 mm, while the forward-facing step does not. This is believed to be due to the shear layer shedding fluctuating components locally downstream.

Fig. 173-175 portray the downstream influence of the steps at x/c = 0.20. The boundary-layer profiles all appear to be similar at this streamwise location. The differences between each configuration can be seen in the steady disturbance profiles. All step configurations have a larger absolute maximum of RMS amplitude than the baseline case. The bimodal shape is seen in the baseline, k = 1,500 μm, and k = -1,525 μm. An interesting note for the aft-facing steps is that the mode shape transforms from a bimodal shape (baseline) to unimodal (k = -1,400 μm) and then back to bimodal (k = -1,525 μm) as step height is increased. The bimodal mode shape is maintained with the smaller forward-facing step (k = 1,500 μm), but then transforms to unimodal shape at the larger forward-facing step (k = 1,775 μm). Also, k = 1,775 μm has twice as large maximum RMS (3.3%) than the other configurations tested. The unsteady disturbance profiles are nearly identical for the baseline and smaller forward-facing step (k = 1,500 μm). The largest aft-facing step has a maximum unsteady mean disturbance amplitude of 1.9%.

In an effort to compare disturbance growth, the total disturbance amplitude, A, was calculated for each configuration. It is calculated by integrating the steady disturbance profiles up to the edge of the boundary layer, δ_{99}, as shown in Eq. (24). The total disturbance amplitude N factor is calculated by taking the natural log of the amplitude of interest referenced to the experimental baseline (k = 0 μm) amplitude at x/c = 0.05, A_o, as shown in Eq. (25). The penalty for the inclusion of a step can be represented through the usage of a ΔN factor metric. The ΔN is computed by subtracting the baseline N factor, $N_{baseline}$, from the configuration of interest, as shown in Eq. (26).

$$A = \frac{1}{\delta_{99}} \int_0^{\delta_{99}} \left[\frac{\left(u(x,y,z) - u(x,y,z)_{mean,z}\right)}{U_{edge}} \right]_{rms,z} dy \tag{24}$$

$$N = \ln(\frac{A}{A_o}) \quad ; A_o = \text{baseline amplitude at } x/c = 0.05 \tag{25}$$

$$\Delta N = N - N_{baseline} \tag{26}$$

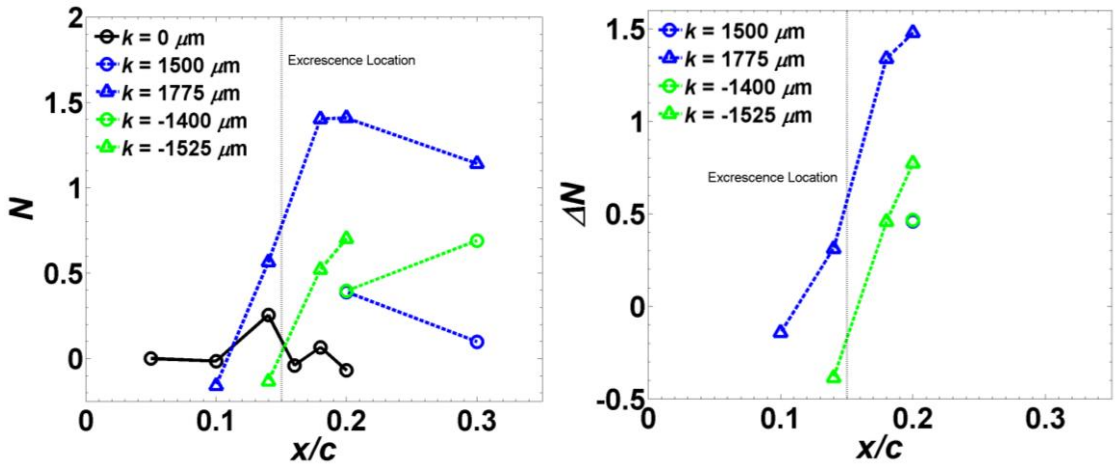

a) **b)**

Fig. 102 a) Total disturbance amplitude *N* factor, b) Δ*N* factor from the baseline *N* factor

The total disturbance amplitude *N* factor and Δ*N* are shown in Fig. 102. The baseline *N* factors are consistently small up to *x/c* = 0.20 (*x/c* = 0.20 is the farthest downstream baseline configuration tested); the largest amplification is an *N* factor of approximately 0.3 at *x/c* = 0.14. The variation in the baseline *N* factor is believed to be due to the low disturbance amplitude compared to the measurement uncertainty. The forward-facing case of *k* = 1,775 μm portrays disturbance growth upstream of the step at *x/c* = 0.14 and the largest overall *N* factor growth downstream of the step (*N* = 1.4). The aft-facing case of *k* = -1,525 μm has slightly less growth compared to the baseline (Δ*N* = -0.4) upstream of the step at *x/c* = 0.14. Also, it reaches a maximum *N* factor of 0.7 at *x/c* = 0.2. An important note is that *k* = 1500 μm is the only subcritical step tested; the critical step height at $Re' = 1.00 \times 10^6$/m is *k* = 1,525 μm and *k* = -1,225 μm. The *k* = 1,500 μm case has a small *N* factor of 0.4 at *x/c* = 0.20 and decreases to negligible at *x/c* = 0.30. An interesting note is

that the ΔN factor curves appear to be linear with similar slope including both upstream and downstream of the step.

D. Resonance Testing

In an effort to determine the cause of the spanwise frequency variation in the test section, resonance testing was performed in several locations around the wind tunnel circuit upstream of the test section to the fan. A focus was made on the surfaces in the center of the cross-sectional area of the circuit. Nine testing locations around the circuit are shown in the wind-tunnel schematic in Fig. 103.

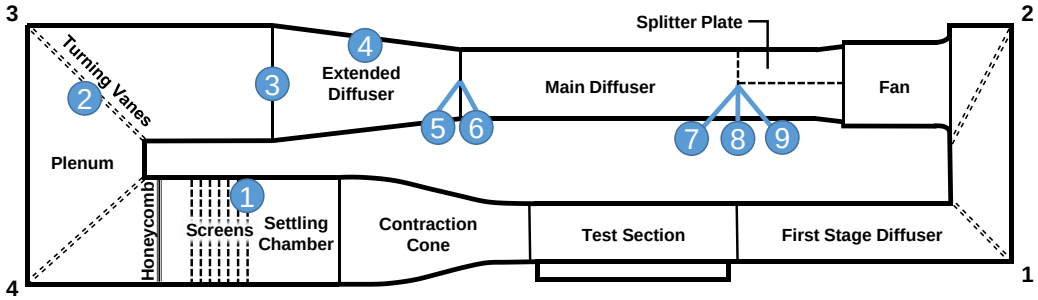

Fig. 103 Resonance testing locations

One PCB 356A32 tri-axial accelerometer was taped down to each surface using aluminum tape. Based on accelerometer model and mounting specifications, accelerations up to 4 kHz can be measured. However, due to only measuring lower structural frequencies, only a sampling frequency of 1 kHz was used (Nyquist of 500 Hz). Ten mallet-raps along the internal side wall of the circuit were performed at each location. Each response was normalized by the absolute-maximum amplitude of the 0.75 second time trace. The average PSD was then computed by averaging these 10 normalized amplitudes. This provides an opportunity to compare the PSD directly with other locations around the circuit. One representative average PSD plot is shown in Fig. 104. This response is for the eight, vertically-midspan struts at location 4. The global streamwise axis (*X*-axis) is shown for the struts. A torsional mode is believed to be excited, in contrast to a vertical oscillation. These struts stiffen the aluminum splitter plate that stands vertically in the extended diffuser (3.7 m). There are four struts on each side and the lengths of the struts are nearly symmetric. The

peaks, that are less than 100 Hz for the strut case, are listed in Table 23. The interesting frequency content in the freestream hotwire results was below 100 Hz (for the present experiment). The black highlighted cells in the table are peak frequencies in the freestream content (Fig. 96).

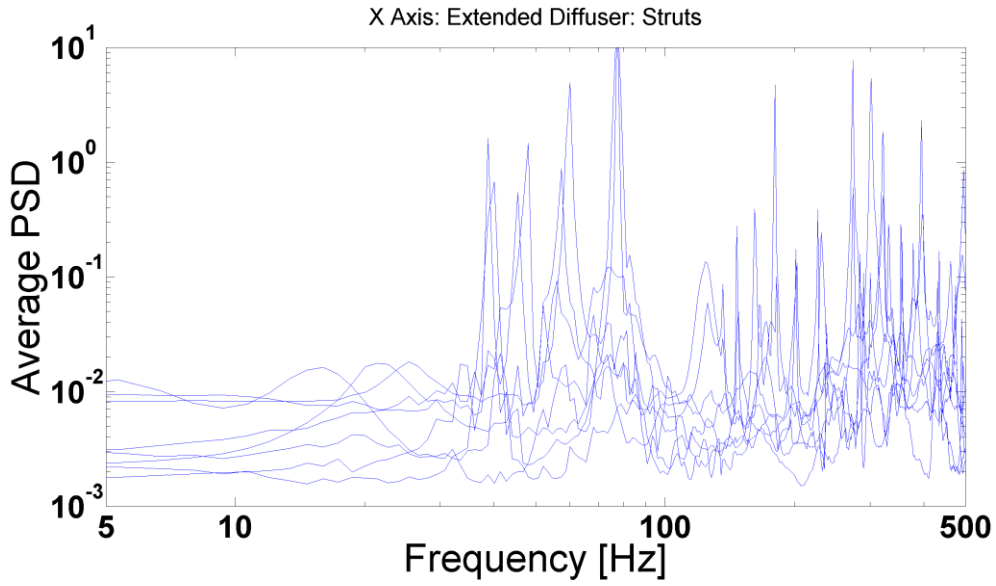

Fig. 104 Average PSD for vertically-midspan struts in extended diffuser (Location 4)

Table 23 Summary of PSD peak frequencies at each location number (Fig. 103), black highlighted cells are peak frequencies observed in freestream, hotwire measurements (Fig. 96)

#	Location	Resonant Frequencies [Hz]							
1	Screen	20	45	53	131	188	325		
2	Turning vane	67	91	238	310				
3	Vertical, aluminum plate	11	83	152	260				
4	Struts	38	40	45	48	57	60	77	77
5	Screen	23	97						
6	Horizontal, wooden plate, flap	12	27	84	108	186			
6	Horizontal, wooden plate	12	27	40	108	147			
7	Screen	27	66	76					
8	Horizontal, wooden plate	23	27	66	126	474			
9	Vertical, wooden plate	23	32	61	85	474			

An interesting note is given to the screens. The screens at location 1 have a much higher tension than the screens at locations 5 and 7. Thus, higher peak frequencies are being observed at location 1, than the locations 5 and 7. One potential outcome of these tests could be tailoring the screen's tension based on the

type of experiments being performed. If a T-S dominated boundary layer is being tested, the screens could be loosened to reduce the screen's peak frequencies to a stable regime for the T-S instability. If a crossflow dominated boundary layer is being tested, the screens could be tightened to increase the screen's peak frequencies to provide a more stable regime for travelling crossflow.

The spanwise varying frequency content seems to only affect the intermediary, spanwise-nonuniform transition fronts. The critical step height is dominated by the step height and surface roughness of the leading-edge part. The highlighted cells in Table 23 have potential to influence the freestream, unsteady content, but no conclusive arguments can be made at this time. Future cross-correlation testing (accelerometers and hotwire concurrently) will determine if these structural surfaces are the exact cause of the freestream, unsteady content.

VII. SUMMARY, CONCLUSIONS, AND RECOMMENDATIONS

A swept-wing experiment in the flight environment and low-disturbance wind tunnel studying the effects of 2-D steps on boundary-layer transition was presented. The design of a new swept-wing test article with an internal actuation system was documented; a comparison was made to a previous swept-wing test article used at the TAMU FRL. Forward- and aft-facing steps are creating via internal linear actuators that reliably translate the leading-edge assembly relative to the main body of the test article. Spanwise steps up to ±5 mm with an uncertainty of ±25 μm were tested.

Structural and displacement analyses were performed as part of the safety analysis for flight testing the test article mounted vertically to a hardpoint of a Cessna O-2A Skymaster. Static-load tests of the maximum loading conditions in flight provided confidence to the structural computations. The procedure and results from the flutter and handling-quality checks of the clearance flight were provided; no objectionable qualities were reported.

An extensive uncertainty analysis was performed for this flight and wind tunnel experiment, and details for each parameter can be found in APPENDIX E. Uncertainty values are occasionally missing in experimental publications, and this causes difficulty in validation. Also, laminar-flow aircraft designers are not provided with the level of confidence of the experimental results; thus, the results could be overlooked.

A. Flight-Test Summary

A new five-hole probe calibration was developed and shown to have a model angle of attack uncertainty as low as 0.10°. Also, uncertainty of the unit Reynolds number was shown to be as low as 0.015 x 10^6/m. Obtaining low uncertainties are especially important for the sensitivity of laminar-flow transition-detection experiments.

Measurements of the five-hole probe, surface pressure distribution, and infrared thermography were presented. The operational procedures for best flight-testing techniques were presented along with five-hole probe measurements. The experimental baseline pressure distribution of the test surface was compared to a CFD solution that incorporates the important geometries of the aircraft and model assembly. Good agreement was achieved for the root pressure port row, but had small deviation at the tip pressure port row.

This is believed to be due to a wing-tip vortex on the test article that is not being fully captured by the CFD solution.

The IR thermography campaign consisted of over 500+ step-height and unit Reynolds number configurations. A baseline transition-location surface fit was computed, as a linear function of both unit Reynolds number and model angle of attack. This fit was then used to compute the laminar fraction of each configuration: the amount of laminar flow achieved referenced to the baseline transition location. There were two distinct regions of laminar fraction: a laminar case and a turbulent case. Up to a certain step height, the transition front was still mainly laminar; however, once a certain critical step height was applied, the transition front snapped forward to fully turbulent. It is believed that the laminar case is dominated by the crossflow instability, while the turbulent case is dominated by the shear-layer instability. An observation was made that there appears to be a slight reduction from the baseline laminar fraction for the forward-facing steps within the critical envelope; however, the aft-facing steps within the critical envelope matched the baseline laminar fraction within the experimental uncertainty. It was also shown that as the unit Reynolds number is increased, the critical step height becomes smaller, with the slope being more severe for the forward-facing steps. This could be attributed to the modulation of the precarious separated region aft of the forward-facing step as a function of unit Reynolds number, since the separated region is a dominant factor in the shear-layer instability.

B. Wind-Tunnel Summary

$C_{p,3D}$ measurements were acquired and compared directly with infinite and finite span computations. Good agreement was found between the experiment and both computations. An experimental, step sweep examining the pressure profiles was performed. Both the upstream and downstream influences on the pressure distribution was cataloged.

An infrared thermography campaign was presented. The wind tunnel data were compared directly to the previous flight results. Good agreement was achieved with the usage of inverse power trends to map out both the transport and sub-transport unit Reynolds numbers from the flight and wind tunnel experiments, respectively. A second-order effect might need to be taken into account for the discrepancy in the forward-

facing step fit, potentially due to the separated regions both before and after the step. It also appears that pressure gradient might be a lower-order effect in this excrescence problem. A comparison was made to an unswept experiment with similar 2-D pressure gradient. The inclusion of leading-edge sweep lowers the $Re_{kk,crit}$ for forward-facing steps, while having similar $Re_{kk,crit}$ for aft-facing steps. It appears that the crossflow instability is a contributor in the critical step heights for the forward-facing steps. Even with the reduction of the $Re_{kk,crit}$ of the forward-facing steps, these results prove that the conventional laminar-flow tolerances are too restrictive for surfaces with favorable pressure gradients and can be significantly loosened.

In the wind tunnel, the intermediary transition fronts were spanwise nonuniform, in contrast to the spanwise uniform fronts observed in the flight environment. The spanwise varying frequency content seems to only affect the intermediary, spanwise-nonuniform transition fronts; the critical step height is dominated by the step height and surface roughness of the leading-edge part. Several suspects were investigated and cataloged. Acoustic disturbances are shown again to not have an effect on a typically crossflow-dominated swept-wing transition, even when a large 2-D forward-facing step is introduced. Spanwise-varying frequency content was measured with a hotwire in the freestream in front of the test article. The spanwise variation of the PSD of 56 Hz has a strong correlation with the transition front measured with the IR camera. This frequency is in the regime of elevated LST N factors of travelling crossflow for the unit Reynolds number tested. A preliminary theory regarding spanwise-varying travelling crossflow was introduced. However, additional tests are needed to conclusively determine the cause of the spanwise-varying transition front.

A hotwire campaign was presented. Excellent agreement was achieved with the IR transition fronts and the hotwire, unsteady-velocity contour plots. Comparisons of forward- and aft-facing steps to the baseline case was portrayed at several streamwise locations. Total disturbance amplitude N factors and ΔN factors were used to compare disturbance growth for the different step configurations. For the configurations tested, the inclusion of a 2-D step led to higher N factors immediately downstream of the step, as expected. The ΔN factor slope is similar for the forward- and aft-facing steps tested upstream and downstream of the step.

As a preliminary examination into the spanwise-varying frequency content measured in the freestream hotwire, a series of resonance tests were performed around the circuit of the wind tunnel upstream of the

test section to the fan. It was found that several peak frequencies measured with the accelerometer performing rap tests match peak frequencies measured with the hotwire in the freestream. No conclusive arguments can be made at this time, if the structural vibrations are causing the spanwise-varying frequencies in the freestream. Future cross-correlation experiments using hotwire and accelerometer traces will be used to examine this phenomenon.

C. Aircraft-Wing Design Recommendations

The obvious recommendations for maintaining the maximum amount of laminar flow for transport-class aircraft is to fly at high altitudes with lower aircraft speeds (i.e. lower Re'); larger step heights can then be used. Another recommendation is to design manufacturing tolerances that are within the critical step envelope as shown in the flight-test results section; it is important to obtain these tolerances at the planned cruising Re' for the aircraft, as it was shown to have a significant effect on the critical step height. If it is possible, an attempt to avoid sharp-edged steps could prove to be beneficial; a rounded edge could increase the critical step height. Lastly, if a forward-facing step is implemented, lessening the leading-edge sweep could allow a larger step height.

D. Future Research Recommendations

It would be interesting to see if the step-height trends still hold between the transport and sub-transport unit Reynolds number tested at the TAMU FRL and KSWT. Also, an examination into the effect of streamwise location of the step needs to be completed. Future testing at the TAMU FRL and KSWT will include performing steps at $x/c = 0.01$, in contrast to the results shown at $x/c = 0.15$. These experiments will also be able to examine the effect of higher curvature and more favorable pressure gradient near the step. A better grasp of the non-dimensional critical parameters will be obtained after these future experiments.

It seems like the separated region aft of the steps are the dominant factor for the shear-layer instability; a non-dimensional parameter based on the separated length and a representative rotational velocity could prove to be more universal. Also, CFD solutions around the step can provide additional insight into the problem. Computations are currently underway at TAMU FRL; hotwire measurements with excrescences will be compared directly with CFD solutions. Lastly, another remaining unexplored parameter is

compressibility. Computations and experiments at transport Mach numbers could indicate if there is a stabilizing effect on the critical step height.

REFERENCES

[1] Tufts, M. W., Duncan, Jr. G. T., Crawford, B. K., Reed, H. L., and Saric, W. S., "Computational Investigation of the Effects of Surface Imperfections and Excrescences on the Crossflow Instability," *AIAA Paper No. 2013-2415*, 2013.

[2] Tufts, M. W., Duncan, Jr. G. T., Crawford, B. K., Reed, H. L., and Saric, W. S., "Computational Design of a Test Article to Investigate 2-D Surface Excrescences on a Swept Laminar-Flow Wing," *Int. J. Engineering Systems Modelling and Simulation,* Vol. 6, Nos. 3/4, 2014, pp.181–190.

[3] Arnal, D., and Archambaud, J. P., "Laminar-Turbulent Transition Control: NLF, LFC, HLFC," *Advances in Laminar-Turbulent Transition Modeling*," VKI Lecture Series, Brussels, Belgium: Von Karman Institute for Fluid Dynamics, 2009.

[4] Kulfan, R. M., and Howard, W. M., "Application of Advanced Aerodynamic Concepts to Large Subsonic Transport Airplanes," *AFFDLTR-75.112*, 1975.

[5] Saric, W. S., Carrillo, Jr. R. B., and Reibert, M. S., "Nonlinear Stability and Transition in 3-D Boundary Layers," *Meccanica 33*, 1998, pp. 469–487.

[6] Carpenter, A. L., Saric, W. S., and Reed, H. L., "Roughness Receptivity in Swept-Wing Boundary Layers – Experiments," *International Journal of Engineering Systems Modelling and Simulation* Vol. 2, No. 1/2, 2010, pp. 128-138, doi: 10.1504/IJESMS.2010.031877.

[7] Carpenter, A. L., "In-Flight Receptivity Experiments on a 30-Degree Swept-Wing Using Micron-Sized Discrete Roughness Elements," Ph.D. Dissertation, Aerospace Engineering Department, Texas A&M University, College Station, TX, 2009.

[8] Radeztsky, Jr. R. H., Reibert, M. S., and Saric, W. S., "Effect of Isolated Micron-Sized Roughness on Transition in Swept-Wing Flows," *AIAA J.37*, No. 11, 1999, pp. 1370–1377.

[9] Drake, A., Westphal, R. V., Zuniga, F. A., Kennelly, R. A., and Koga, D. J., "Wing Leading Edge Joint Laminar Flow Tests," *NASA TM 4762*, 1996.

[10] Hood, M. J., "The Effects of Some Common Surface Irregularities," *NACA Technical Note,* No. 695, 1939.

[11] Tani, I., Hama, R., and Mituisi, S., "On the Permissible Roughness in the Laminar Boundary Layer," *NASA-TM-89802,* No. 199, 1940, pp. 419-428.

[12] Fage, A., "The Smallest Size of a Spanwise Surface Corrugation Which Affects Boundary Layer Transition on an Aerofoil," *British Aeronautical Research Council Report and Memoranda,* No. 2120, 1943.

[13] Loftin, Jr. L. K., "Effects of Specific Types of Surface Roughness on Boundary-Layer Transition," *NACA Wartime Report,* No. L5J29a, 1946.

[14] Smith, A. M. O., and Clutter, D. W., "The Smallest Height of Roughness Capable of Affecting Boundary-Layer Transition," *Journal of the Aerospace Sciences,* 1959, pp. 229-256.

[15] Klebanoff, P. S., and Tidstrom, K. D., "Mechanism by which a Two-Dimensional Roughness Element Induces Boundary-Layer Transition," *Phys. Fluids,* Vol. 15, 1972, pp. 1173-1188.

[16] Holmes, B. J., Obara, C. J., Martin, G. L., and Domack, C. S., "Manufacturing Tolerances for Natural Laminar Flow Airframe Surfaces," *Society of Automotive Engineers,* No. 850863, 1985, pp. 4.522 – 4.529.

[17] Zuniga, F. A., Drake, A., Kennelly, Jr. R. A., Koga, D. J., and Westphal, R. V., "Transonic Flight Test of a Laminar Flow Leading Edge with Surface Excrescences," *AIAA Paper No. 94-2142,* 1994.

[18] Wang, Y. X., and Gaster, M., "Effect of Surface Steps on Boundary Layer Transition," *Experiments in Fluids,* Vol. 39, 2005, pp. 679-686.

[19] Crouch, J. D., Kosorygin, V. S., and Ng, L. L., "Modeling the Effects of Steps on Boundary-Layer Transition," *IUTAM Symposium on Laminar-Turbulent Transition,* Springer Netherlands, ed. Govindarajan R., Vol. 78, 2006, pp. 37-44.

[20] Bender, A. M., Drake, A., McKay, V. S., Westphal, R. V., Yoshioka, S., and Kohama, Y., "An Approach to Measuring the Effects of Surface Steps on Transition Using a Propelled Model," *International Congress on Instrumentation in Aerospace Simulation Facilities*, Pacific Grove, CA, June 10-14, 2007.

[21] Bender, A. M., Harris, C., and Westphal, R. V., "The Effects of Favorable Pressure Gradient on Boundary Layer Transition with 2D Excrescences," Presentation at 3AF Conference, St. Louis, France, March 2013.

[22] Drake, A., and Bender, A. M., "Surface Excrescence Transition Study," *AFRL-RB-WP-TR-2009-3109*, 2009.

[23] Drake, A., Bender, A. M., and Westphal, R. V., "Transition Due to Surface Steps in the Presence of Favorable Pressure Gradients," *AIAA Paper No. 2008-7334*, 2008.

[24] Drake, A., Bender, A. M., Korntheuer, A. J., Westphal, R. V., McKeon, B. J., Gerashchenko, S., Rohe, W., and Dale, G., "Step Excrescence Effects for Manufacturing Tolerances on Laminar Flow Wings," *AIAA Paper No. 2010-375,* 2010.

[25] Saric, W. S., Reed, H. L., and White, E. B., "Stability and Transition of Three-Dimensional Boundary Layers," *Ann. Rev. Fluid Mech.,* 2003, 35:413-440.

[26] Saric, W. S., "Görtler Vortices," *Ann. Rev. Fluid Mech.,* 1994. 26:379-409.

[27] Reed, H. L., and Saric, W. S., "Stability of Three-Dimensional Boundary Layers," *Ann. Rev. Fluid Mech.,* 1989, 21:235-84.

[28] Gray, W. E., "The Effect of Wing Sweep on Laminar Flow," *Tech. Memo. Aero.,* 255, RAE, 1952.

[29] Roberts, M.W., "Computational Evaluation of a Transonic Laminar-Flow Wing Glove Design," M.S. Thesis, Aerospace Engineering Department, Texas A&M University, College Station, TX, 2012.

[30] Deyhle, H., and Bippes, H., "Disturbance Growth in an Unstable Three-Dimensional Boundary Layer and its Dependence on Environmental Conditions," *Journal of Fluid Mechanics,* Vol. 316, 1996, pp. 73-113.

[31] White, E. B., Saric, W. S., Gladden, R. D., and Gabet, P. M., "Stages of Swept-Wing Transition," *AIAA Paper No. 2001-0271*, 2001.

[32] Pfenninger, W., "Laminar flow control – Laminarization," *Special Course on Drag Reduction*, AGARD Rep. No. 654, von Karman Institute, Rhode St. Genèse, Belgium, 1977, pp. 3-1 – 3-75.

[33] McKnight, C. W., "Design and Safety Analysis of an In-Flight, Test Airfoil," M.S. Thesis, Aerospace Engineering Department, Texas A&M University, College Station, TX, 2006.

[34] Anaheim Automation, "23A - Hybrid Non-Captive Linear Actuators," 2011, Web, 25 July 2014, <http://www.anaheimautomation.com/products/stepper/stepper-linear-actuator-item.php?sID=25&pt=i&tID=80&cID=52>.

[35] Thomson, "500 Series Roller Linear Guide," 2014, Web, 25 July 2014, <http://www.thomsonlinear.com/website/com/eng/products/linear_guides/profilerail/500_series_roller_guide.php>.

[36] AEC Magnetics, "Rectangular Electromagnet," 2010, Web, 25 July 2014, <http://www.aecmagnetics.com/Sub-Category-Lobby.aspx?id=11>.

[37] UniMeasure, "ZX-PA SERIES - Analog Position Transducer," Web, 25 July 2014, <http://www.unimeasure.com/obj--pdf/zx-pa.pdf>.

[38] Freels, J. R., "An Examination of Configurations for Using Infrared to Measure Boundary Layer Transition," M.S. Thesis, Aerospace Engineering Department, Texas A&M University, College Station, TX, 2012.

[39] Fisher, D., Horstmann, K. H., and Riedel, H., "Flight Test Measurement Techniques for Laminar Flow," *RTO-AG-300*, Vol. 23, 2003.

[40] Williams, T. C., "Design of an Instrumentation System for a Boundary Layer Transition Wing Glove Experiment," M.S. Thesis, Aerospace Engineering Department, Texas A&M University, College Station, TX, 2012.

[41] Fanning, J. A., "In-Flight Measurements of Freestream Atmospheric Turbulence Intensities," M.S. Thesis, Aerospace Engineering Department, Texas A&M University, College Station, TX, 2012.

[42] Tucker, A. A., West, D. E., Crawford, B. K., and Saric, W. S., “Flexible Flight Research Platform at Texas A&M University Flight Research Laboratory,” *AIAA Paper No. 2013-2927*, 2013.

[43] Saric, W. S., Carpenter, A. L., Hunt, L. E., McKnight, C. W., and Schouten, S., "SWIFT Safety Analysis for Swept-Wing Experiments," Texas A&M University, *TAMUS-AE-TR-06-002*, revision B, College Station, Texas, 2007.

[44] Martin, M. L., Carpenter, A. L., and Saric, W. S., "Swept-Wing Laminar Flow Control Studies Using Cessna O-2A Test Aircraft," *AIAA Paper No. 2008-1636*. 2008.

[45] Saric, W. S., Carpenter, A. L., Hunt, L. E., and Kluzek, C., "SWIFT Flight-Test Plan for Swept-Wing Experiments," Texas A&M University, *TAMUS-AE-TR-06-001*, revision B, College Station, Texas, 2007.

[46] Hunt, L. E., Downs, R. S., Kuester, M. S., White, E. B., and Saric, W. S., “Flow Quality Measurements in the Klebanoff-Saric Wind Tunnel,” *AIAA Paper No. 2010-4538*, 2010.

[47] Hunt, L. E., and Saric, W. S., “Boundary-Layer Receptivity of Three-Dimensional Roughness Arrays on a Swept-Wing,” *AIAA Paper No. 2011-3881*, 2011.

[48] Reshotko, E., Saric, W. S, Nagib, H. M., “Flow Quality Issues for Large Wind Tunnels,” *AIAA Paper No. 97-0225*, 1997.

[49] Saric, W. S, Reshotko, E., “Review of Flow Quality Issues in Wind Tunnel Testing,” *AIAA Paper No. 98-2613*, 1998.

[50] Rhodes, R. G., Reed, H. L., Saric, W. S., Carpenter, A. L., and Neale, T. P., “Roughness Receptivity in Swept-Wing Boundary Layers – Computations,” *International Journal of Engineering Systems Modelling and Simulation* Vol. 2, No. 1/2, 2010, pp. 139-148, doi: 10.1504/IJESMS.2010.031878.

[51] Ramamurty G., *Finite Element Analysis*, 2nd ed., I.K. International Publishing House Pvt. Ltd., New Delhi, India, 2010.

[52] Martin, M. L., Carpenter, A. L., and Saric, W. S., “Swept-Wing Laminar Flow Control Studies Using Cessna O-2A Test Aircraft,” *AIAA Paper No. 2008-1636*, 2008.

[53] “Flight Manual USAF Series O-2A Aircraft,” *USAF T.O. 1L-2A-1*, 5 June 1985.

[54] Schultz, W., and Pate, C., *Report No. S-M337-26-2*, Cessna Aircraft Company, 30 October 1967.

[55] Nise, N. S., *Control Systems Engineering*, 6th ed., John Wiley & Sons, Inc., Hoboken, New Jersey, 2011.

[56] Nelson, R. C., *Flight Stability and Automatic Control*, 2nd ed., McGraw-Hill, Boston, 1998.

[57] U.S. Department of Defense, "Military Specification, Flying Qualities of Piloted Airplanes," *MIL-F-8785C*, Nov 1980.

[58] RTO NATO Task Group SCI-026, "Flight Control Design – Best Practices," *RTO-TR-029*, Canada Communication Group Inc., Hull, Canada, 2000.

[59] Bergh, H., Tijdeman, H., "Theoretical and Experimental Results for the Dynamic Response of Pressure Measuring Systems," *NLR-TR F.238*, National Lucht- en Ruimtevaartlaboratorium, Amsterdam, Netherlands, 1965.

[60] Saric, W. S., "Boundary-Layer Stability and Transition," *Springer Handbook of Experimental Fluid Mechanics*, ed. Tropea, C., Yarin, A., Foss, J. F., Berlin: Springer-Verlag, 2007, pp. 886-896.

[61] Mavris, D. N., Saric, W. S., Ran, H., Belisle, M. J., Woodruff, M. J., and Reed, H. L., "Investigation of a Health-Monitoring Methodology for Future Natural Laminar Flow Transport Aircraft," *ICAS Paper 1.9.3*, 2010.

[62] Vavra, A. J., Solomon, Jr. W. D., Drake, A., "Comparison of Boundary Layer Transition Measurement Techniques on a Laminar Flow Wing," *AIAA Paper No. 2005-1030*, 2005.

[63] Crawford, B. K., Duncan, Jr. G. T., West, D. E., and Saric, W. S., "Quantitative Boundary-Layer Transition Measurements Using IR Thermography," *AIAA Paper No. 2014-1411*, 2014.

[64] Crawford, B. K., Duncan, Jr. G. T., West, D. E., and Saric, W. S., "Laminar-Turbulent Boundary Layer Transition Imaging Using IR Thermography," *Optics and Photonics Journal*, Vol. 3, No. 3, 2013, pp. 233-239. doi: 10.4236/opj.2013.33038.

[65] White, E. B., "Breakdown of Crossflow Vortices," Ph.D. Dissertation, Aerospace Engineering Department, Arizona State University, Phoenix, AZ, 2000.

[66] Hunt, L. E., "Boundary-Layer Receptivity to Three-Dimensional Roughness Arrays on a Swept-Wing," Ph.D. Dissertation, Aerospace Engineering Department, Texas A&M University, College Station, TX, 2011.

[67] Downs, R. S., "Environmental Influences on Crossflow Instability," Ph.D. Dissertation, Aerospace Engineering Department, Texas A&M University, College Station, TX, 2012.

APPENDIX A

STRUCTURAL-ANALYSIS RESULTS

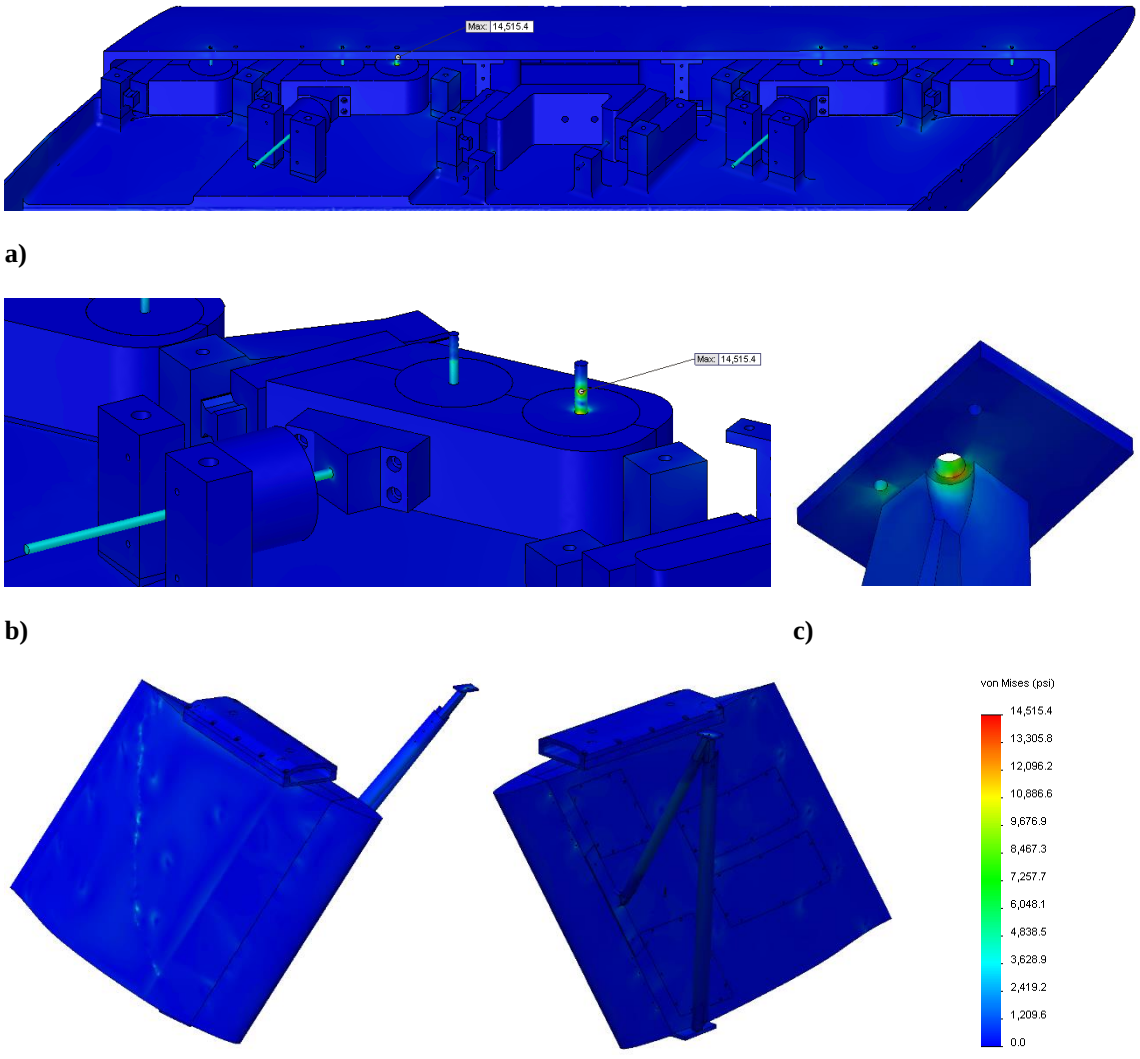

Fig. 105 Appendix: Stress analysis for the worst-case scenario, a) leading-edge assembly, b) root actuator assembly, c) strut tie-down part, d) test side, e) non-test side

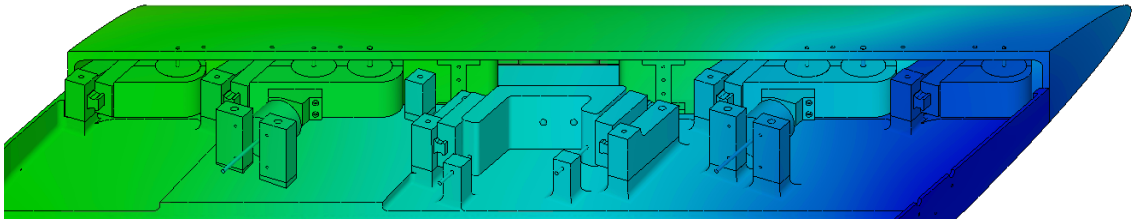

a)

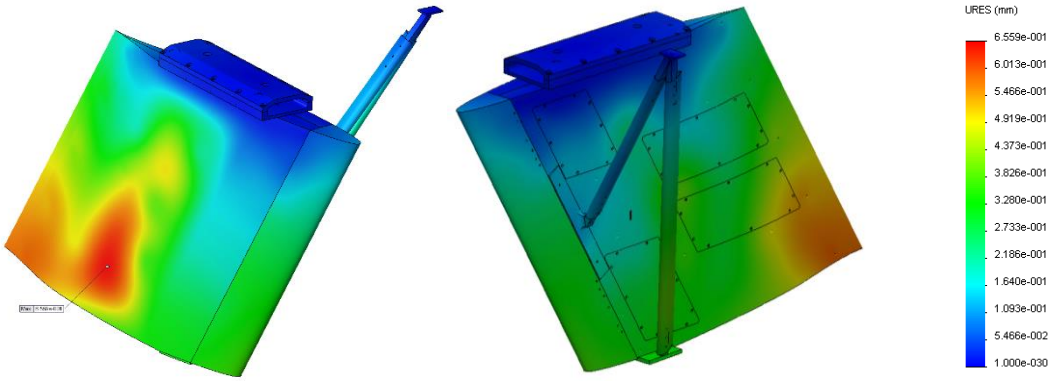

b) **c)**

Fig. 106 Appendix: Displacement analysis for the worst-case scenario, a) leading-edge assembly, b) test side, c) non-test side

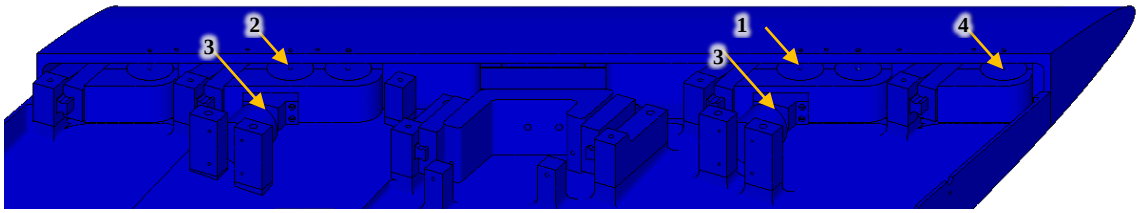

a)

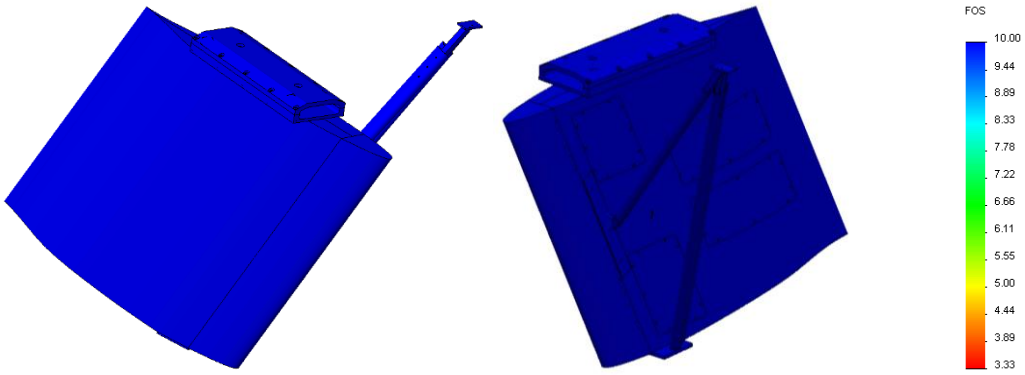

b) c)

Fig. 107 Appendix: Factor of safety analysis for the worst-case scenario, a) leading-edge assembly, b) test side, c) non-test side

Table 24 Appendix: Four smallest factors of safety for the worst-case scenario

Location	Minimum FOS	Material	Strength
(1) Root, outboard linear actuator	3.3 to proof	Component	200 lb proof
(2) Tip, inboard linear actuator	3.7 to proof	Component	200 lb proof
(3) Gap-direction lead screws	4.2 to yield	AISI 316	20,000 psi yield
(4) Root, inboard linear actuator	5.2 to proof	Component	200 lb proof

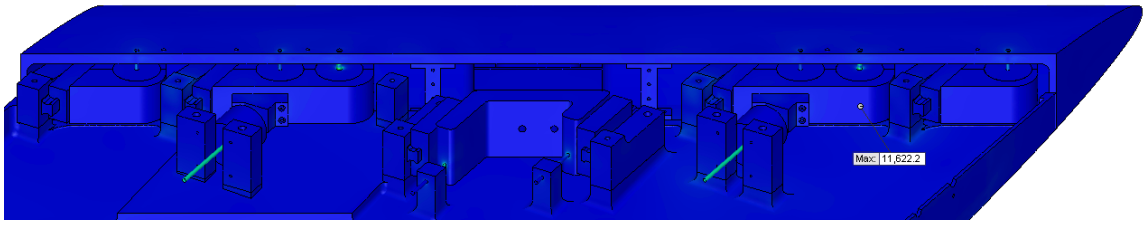

a)

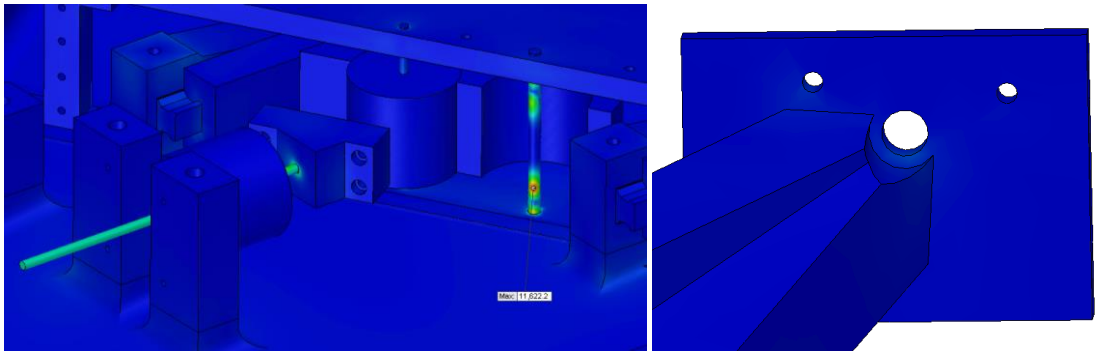

b) **c)**

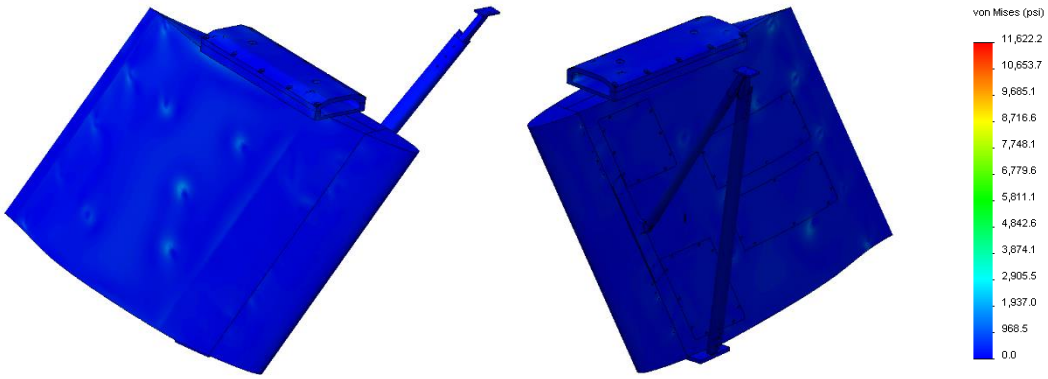

d) **e)**

Fig. 108 Appendix: Stress analysis for the experimental scenario, a) leading-edge assembly, b) root, actuator assembly, c) strut tie-down part, d) test side, e) non-test side

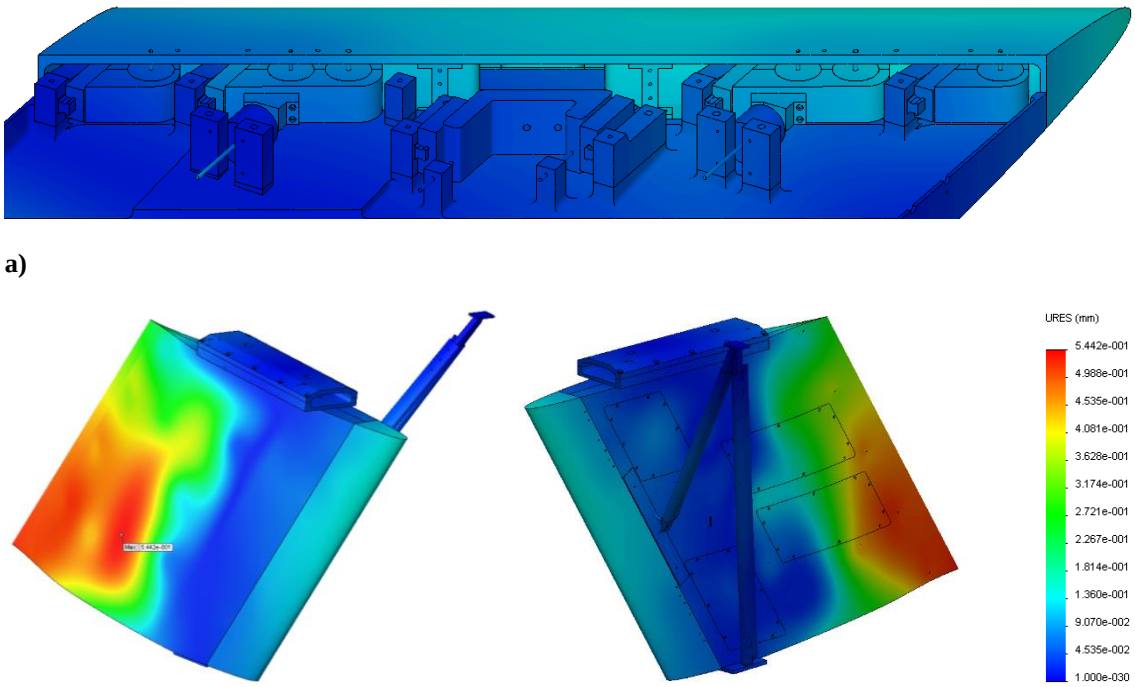

a)

b) **c)**

Fig. 109 Appendix: Displacement analysis for the experimental scenario, a) leading-edge assembly, b) test side, c) non-test side

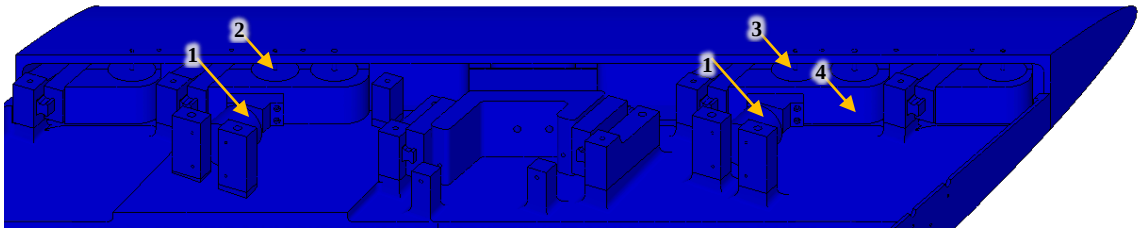

a)

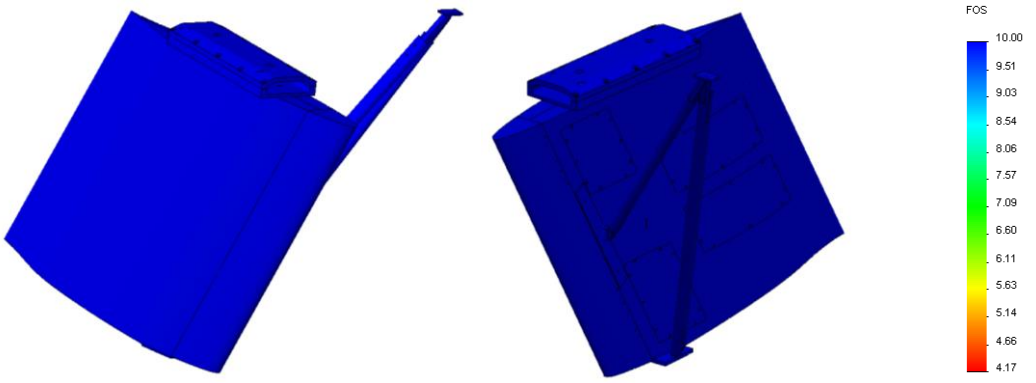

b) c)

Fig. 110 Appendix: Factor of safety analysis for the experimental scenario, a) leading-edge assembly, b) test side, c) non-test side

Table 25 Appendix: Four smallest factors of safety for the experimental scenario

Location	Minimum FOS	Material	Strength
(1) Gap-direction lead screws	4.2 to yield	AISI 316	20,000 psi yield
(2) Tip, inboard linear actuator	5.6 to proof	Component	200 lb proof
(3) Root, outboard linear actuator	5.9 to proof	Component	200 lb proof
(4) Linear sleeve bearing, root test side	6.9 to yield	Component	600 lb yield

APPENDIX B

GO/NO-GO MATRIX

Table 26 Appendix: Go/no-go, flight-critical issues, ground event

Flight-Critical Issues, Ground Event		
Problem	Decision	Reason
Ground winds greater than 15 knots	No Go	Wind speed exceeds FRL limitations
Ceiling less than that required for mission profile	No Go	Operating limitations state VFR flights only
Visibility less than 5 statute mile	No Go	Operating limitations state VFR flights only
Winds aloft exceed 20 knots AND a wind heading shift >90° occurs within a 3000’ band	No Go	Crosswind component may exceed design limitation set on airfoil support structure
>15 knots wind-speed inversion within a 6000’ band	No Go	Exceeds FRL limitations
Winds at any test altitude exceed 50 knots	No Go	Environment too unstable for testing
Crosswind component exceeds 7 knots	No Go	Crosswind component exceeds aircraft operating manual for an asymmetrical wing loading
Icing or rain condition at altitude	No Go	No-flight conditions

Table 27 Appendix: Go/no-go, in-flight event

In-flight Event		
Problem	Decision	Reason
Heading indicator malfunctions	Abort	Requirement FAR 91.205
Airspeed indicator malfunctions	Abort	Requirement FAR 91.205
g-meter malfunction	Abort	Required to limit load on aircraft
Loss of oil pressure	Abort	Safety risk for crew members
Loss of electrical power	Abort	Safety risk for crew members
Loss of radio communication	Abort	Could lead to other malfunctions
Hydraulic leak	Abort and lower landing gear	Gear only will come down manually if there is loss of hydraulic pressure
Loss of engine	Abort	Safety risk for crew members
Sideslip angle on aircraft exceeds -11°, +7° based on the pilot’s β display	Slow down and RTB	Crosswind component is exceeding design limitation set on airfoil support structure

Table 28 Appendix: Go/no-go, mission-critical issue

Mission-Critical Issue		
Problem	Decision	Reason
Loss of instrument electrical power	Abort	Flight is useless unless data are collected
Fuel gauge malfunction	Continue mission	Fuel estimates are based on visual inspection, calibrated fuel sticks, and time; not fuel gauges
Autopilot malfunction	Continue mission	Autopilot not necessary for experiment
GPS malfunction	Abort	GPS identifies areas of restricted airspace such as Dallas, TX
Test instrumentation malfunction	Continue or Abort	Flight Test Engineer decides the importance of the instrumentation for the mission and decides a course of action

APPENDIX C

CLEARANCE-FLIGHT TEST CARDS

The clearance-flight test cards were developed by Lt. Col. Aaron Tucker, USAF. Similar test cards are combined into one shown test card (e.g. handling-quality test cards 4-9); the aircraft configuration for each card is listed in order for the combined cards.

Communications Plan	SWIFTER
Pilot (P) **Flight Test Engineer (FTE)**	**HQ = handling quality**

1. Normal: "On Conditions" (P)

"Cleared to Maneuver" (FTE)

"Maneuver in 3, 2, 1, Hack" (P)

Record data/comments (FTE)

"Maneuver complete, next is ___" (FTE)

2. "Terminate (reason)" planned limit reached

Action: stop testing

3. "Knock-it-off (reason)" unplanned limit reached or unsafe situation developing

Action: stop testing, recover aircraft to stabilized flight condition

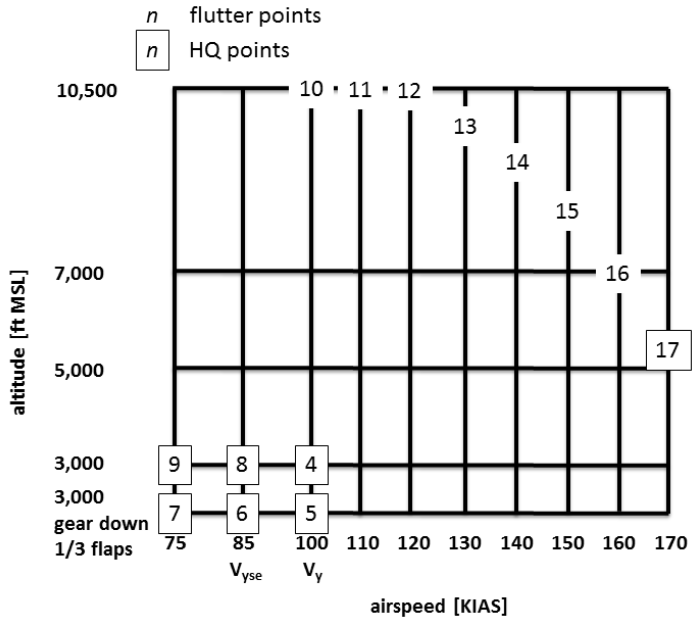

CARD 1	Ground Check	SWIFTER
Ground Crew 123.3 **Easterwood Ground 128.7** **main ramp parking spot**	**Test limits:** **2600 RPM ≤ 30 secs** **Avoid prop plane of rotation** **Vibration: 3-fold amp increase** **phase lock**	

Comm check

Start rear engine, 1000 RPM (IDLE)

Start front engine, 1000 RPM (IDLE)

Clear aft

Rear engine, slowly advance IDLE, 2600 RPM, IDLE

Oscilloscope ☐ _____ _____

Front engine, slowly advance IDLE, 2600 RPM

Oscilloscope ☐ _____ _____

Rear engine, slowly advance IDLE, 2600 RPM

Oscilloscope ☐ _____ _____

Both engines-IDLE

Engine shutdown check

Inspect model

Comments:

CARD 2	EMI/EMC Ground Test	SWIFTER
Ground Crew 123.3 **Easterwood Ground 128.7** **Main ramp parking spot**	**Test limits:** **Avoid prop plane of rotation**	

OK comments

Connect ground power

SWIFTER heater - OFF

Comm/instrument check ☐ _____

SWIFTER heater – ON

Comm/instrument check ☐ _____

SWIFTER heater – OFF

Disconnect ground power

Starting engines check

Rear engine, 1800 RPM

Comm/instrument check ☐ _____

SWIFTER heater – ON

Comm/instrument check ☐ _____

Comments:

CARD 3	Takeoff	SWIFTER
	Acft limits: 17° bank **Speed: 80 KIAS min** **Winds: 15 kts, 7-kt xwind** **Gear/Flaps: 122(ext), 139(op) KIAS** **Accel: 80 KIAS in 2000 ft**	
Before takeoff check **Advance throttles** **Liftoff no less than 80 KIAS** **Retract gear, flaps** **Climb check** **Climb 3000 ft MSL**		
Comments:		

CARD 4-9	Handling Qualities	SWIFTER
Speed: 100±5,100±5, 85±5, 85±5, 75±5, 75±5 KIAS **Altitude: 3000 -0/+50 ft MSL** **Gear: Up, Down, Down, Down, Up, Up** **Flaps: Up, 1/3, 1/3, 1/3, Up, Up**	**Test limits: β: -11° – +7°, 1-ball** **Speed: V_{stall} 64 KIAS - 175 KIAS** **Altitude: 3,000 – 12,500 ft MSL** **Gear/Flaps: 122(ext), 139(op) KIAS**	

time: _____ **OK time** **comments**
Trim shot

Pitch rap ☐ _____ _____

Roll rap ☐ _____ _____

Pitch doublet ☐ _____ _____

time _____s **o/s _____**

Rudder doublet ☐ _____ _____

time _____s **o/s _____**

Rolls (30°-30°) **L** ☐ _____ _____

R_____ ☐ _____

SHSS (ϕ_{max}=45°) **L** ☐ _____ _____

R_____ ☐ _____

WUT (ϕ_{max}=45°) ☐ _____ _____

Comments:

CARD 10-16	Flutter	SWIFTER
Speed: 100±5, 110±5, 120±5, 130±5, 140±5, 150±5, 160±5 KIAS **Altitude: 3000 - 10500 ft MSL** **Gear: test cards 10-16: Up** **Flaps: test cards 10-16: Up**	**Test limits: β: -11° – +7°, 1-ball** **Speed: V_{stall} 64 KIAS - 175 KIAS** **Altitude: 3,000 – 12,500 ft MSL** **Gear/Flaps: 122(ext), 139(op) KIAS** **Vibration: 3-fold amp increase** **phase lock**	

time: _____ OK time comments

HQ/Flutter

Trim shot

Pitch rap ☐/☐ _____ _____

Roll rap ☐/☐ _____ _____

Pitch doublet ☐/☐ _____ _____

time _____s o/s _____

Rudder doublet ☐/☐ _____ _____

time _____s o/s _____

Comments:

CARD 17	Flutter/Handling Qualities	SWIFTER
Speed: 170±5 KIAS **Altitude: 3000 - 10500 ft MSL** **Gear: Up** **Flaps: Up**	**Test limits: β: -11° – +7°, ¾-ball** **Speed: V_{stall} 64 KIAS - 175 KIAS** **Altitude: 3,000 – 12,500 ft MSL** **Gear/Flaps: 122(ext), 139(op) KIAS** **Vibration: 3-fold amp increase** **phase lock**	

time: _____ OK time comments

HQ/Flutter

Trim shot

Pitch rap ☐/☐ _____ _____

Roll rap ☐/☐ _____ _____

Pitch doublet ☐/☐ _____ _____

time _____s o/s _____

Rudder doublet ☐/☐ _____ _____

time _____s o/s _____

Rolls (30°-30°) R ☐/☐ _____ _____

L___ ☐/☐ _____

SHSS (ϕ_{max}=45°) R☐/☐_____ _____

L___ ☐/☐ _____

WUT (ϕ_{max}=45°) ☐/☐ _____ _____

Comments:

APPENDIX D

FLYING-QUALITY MANEUVER DESCRIPTIONS

All raps and doublets will build-up from ¼ to ½ and ¾ flight-control deflection. Rudder and aileron inputs will also include a full throw input.

Pitch rap (Pitch-impulse input): Starting from a trimmed flight condition, apply an abrupt pitch control yoke step impulse input, completing the input in approximately 0.5 seconds. Release control and observe aircraft response.

Roll rap (Roll-impulse input): Starting from a trimmed flight condition, apply an abrupt roll control yoke step impulse input, completing the maneuver in approximately 0.5 seconds. Release control and observe aircraft response.

Pitch doublet (Short-period mode): Trim the aircraft. Attitude indicator shows level flight attitude. Quickly pull the control yoke to a new location, then push to an equally opposite position and finally return it back to the original position. Observe the response of pitch attitude change as a function of time. The three-axis accelerometer records the oscillations from which the damping ratio and the frequency are determined. The flight engineer also records the number of pitch angle peaks, and time between each peak. Pilot input should take approximately one second.

Rudder doublet (Dutch-roll mode): Trim the aircraft. Kick the right rudder to ½ a ball width on the inclinometer and then immediately to the left, equal and opposite in direction. Then return the pedal to center. The three-axis accelerometer records the oscillations from which we can determine the damping ratio and the frequency. The flight engineer also records the time and peak heading (overshoots) for each oscillation. This enables calculation of the period and frequency of the oscillations. Pilot input should be less than 3 seconds.

30° to 30° bank roll: Trim the aircraft. Pilot enters a 30° bank. When established within 5° of the 30° mark on the attitude indicator, roll past neutral and then to a 30° bank on the opposite side. This is a qualitative

maneuver where the pilot comments on the observed roll rate, heading change (possible adverse or pro-verse yaw), heading control, bank-angle capture, stick force (bank-angle control), maneuverability (steady-state roll rate), stability of aircraft when in 30° bank (no over-banking tendency). Flight crew records comments. Note: actual bank angle may not reach 30° due to a 7° sideslip limitation.

Steady-heading side slip: (maximum of 3/4 ball width on the inclinometer - see recommended test limits). Trim the aircraft. Keep the wing within a 45° bank angle. Slowly input rudder and simultaneously apply opposite aileron as necessary to maintain heading or visual landmark. Increase the rudder input to a maximum of ¾ ball in the inclinometer. At the test point of 165 kts, a maximum ¾ ball width is imposed in order to restrict the model angle of attack to 7°. Pilot comments on aircraft handling of observed yaw and pitch forces as rudder is steadily increased. Flight crew records qualitative observations. Recover by smoothly releasing the rudder pedals while maintaining altitude. Do not sustain large sideslips to keep the fuel feed lines covered.

Wind-up turn: Trim the aircraft. Begin a gradual increase in bank angle (increase in g forces, not to exceed 2 g's) to 45° bank-angle limit while allowing nose to drop to keep airspeed constant. Upon reaching 45° bank-angle limit (or onset of airframe buffet), pilot smoothly recovers to level flight. During the maneuver, pilot comments on aircraft handling of observed pitch, roll and yaw forces.

APPENDIX E

UNCERTAINTY ANALYSIS

Uncertainty calculations are based on the square root of the sum squared of each contributing factor with no covariance between contributing factors. It is important to note that the standard deviation (std) term is included in each total uncertainty equation for completeness. The standard deviation of all the contributing factors that make up the variable of interest are to be omitted; the standard deviation of the variable of interest comprises all of the contributing factor's standard deviations. For instance, in the final formulation of Re_{kk}, the standard deviation of all three terms (u_k, k, and v_k) is included in the standard deviation of the Re_{kk} term. Thus, in each of the above three term's uncertainty formulations, the standard deviation term needs to be omitted; it is crucial to not double count the standard deviation terms.

Nomenclature for appendix

align	5HP alignment uncertainty relative to the model
cal	5HP calibration curve uncertainty
scanner	differential measurement by pressure scanner
std	standard deviation of the variable over 3 seconds of sampled data of being "on condition"
systematic	all errors included in the total uncertainty formulation, except the standard deviation term
LF	laminar fraction
trans	pressure-transducer uncertainty
$U_{edge,total}$	boundary-layer edge total velocity

Unit Reynolds number, Re´ [1/m]

Definition		
1	$Re' = 57249.6\left(\frac{T_\infty + 110.4}{{T_\infty}^2}\right)\sqrt{p_s q}$	
Total uncertainty equation		
2	$\partial Re' = \sqrt{\left[\left(\frac{\partial Re'}{\partial T_\infty}\right)(\sigma_{T_\infty})\right]^2 + \left[\left(\frac{\partial Re'}{\partial p_s}\right)(\sigma_{p_s})\right]^2 + \left[\left(\frac{\partial Re'}{\partial q}\right)(\sigma_q)\right]^2 + [Re'_{std}]^2}$	
Partial derivative formulation		
3	$\frac{\partial Re'}{\partial T_\infty} = 57249.6\sqrt{p_s q}\left[-{T_\infty}^{-2} - (110.4)(2){T_\infty}^{-3}\right]$	$\sigma_{T_\infty} = 0.5\ K$
4	$\frac{\partial Re'}{\partial p_s} = 57249.6\left[\frac{T_\infty + 110.4}{{T_\infty}^2}\right]\left[\frac{1}{2}(p_s q)^{-1/2}(q)\right]$	$\sigma_{p_s} = \sqrt{\left[\sigma_{p_s,trans}\right]^2 + \left[\sigma_{p_s,cal}\right]^2}$ $\sigma_{p_s,trans} = 103\ Pa\ (0.1\%\ full\ scale)$ $\sigma_{p_s,cal} = (0.00954)(q)$
5	$\frac{\partial Re'}{\partial q} = 57249.6\left[\frac{T_\infty + 110.4}{{T_\infty}^2}\right]\left[\frac{1}{2}(p_s q)^{-1/2}(p_s)\right]$	$\sigma_q = \sqrt{\left[\sigma_{q,trans}\right]^2 + \left[\sigma_{q,cal}\right]^2}$ $\sigma_{q,trans} = 14\ Pa\ (0.1\%\ full\ scale)$ $\sigma_{q,cal} = (0.00379)(q)$

Angular orientation, α and θ_{AC} angles [°]

Total uncertainty equation		
1	$\sigma_\alpha = \sqrt{\sigma_{\alpha,trans}^2 + \sigma_{\alpha,cal}^2 + \sigma_{\alpha,align}^2 + \alpha_{std}^2}$ $\sigma_{\theta_{AC}} = \sqrt{\sigma_{\theta_{AC},trans}^2 + \sigma_{\theta_{AC},cal}^2 + \sigma_{\theta_{AC},align}^2 + {\theta_{AC}}_{std}^2}$	
Transducer partial derivative formulation		
2	$\sigma_{\alpha,trans} = \sqrt{\left[\left(\frac{\partial\alpha}{\partial C_\alpha}\right)\left(\sigma_{C_\alpha}\right)\right]^2 + \left[\left(\frac{\partial\alpha}{\partial C_\theta}\right)\left(\sigma_{C_{\theta_{AC}}}\right)\right]^2}$ $\sigma_{\theta_{AC},trans} = \sqrt{\left[\left(\frac{\partial\theta_{AC}}{\partial C_\alpha}\right)\left(\sigma_{C_\alpha}\right)\right]^2 + \left[\left(\frac{\partial\theta_{AC}}{\partial C_{\theta_{AC}}}\right)\left(\sigma_{C_{\theta_{AC}}}\right)\right]^2}$	
3	$C_\alpha = \frac{p_2 - p_3}{p_1 - p_6} = \frac{P_\alpha}{q}$	$C_{\theta_{AC}} = \frac{p_4 - p_5}{p_1 - p_6} = \frac{P_{\theta_{AC}}}{q}$
4	$\sigma_{C_\alpha} = \sqrt{\left[\left(\frac{\partial C_\alpha}{\partial P_\alpha}\right)\left(\sigma_{P_{\alpha,trans}}\right)\right]^2 + \left[\left(\frac{\partial C_\alpha}{\partial q}\right)\left(\sigma_{q,trans}\right)\right]^2}$	$\sigma_{C_\theta} = \sqrt{\left[\left(\frac{\partial C_{\theta_{AC}}}{\partial P_{\theta_{AC}}}\right)\left(\sigma_{P_{\theta_{AC},trans}}\right)\right]^2 + \left[\left(\frac{\partial C_{\theta_{AC}}}{\partial q}\right)\left(\sigma_{q,trans}\right)\right]^2}$
5	$\frac{\partial C_\alpha}{\partial P_\alpha} = \frac{1}{q}$	$\frac{\partial C_{\theta_{AC}}}{\partial P_{\theta_{AC}}} = \frac{1}{q}$
6	$\frac{\partial C_\alpha}{\partial q} = \frac{-P_\alpha}{q^2} = \frac{-C_\alpha}{q}$	$\frac{\partial C_{\theta_{AC}}}{\partial q} = \frac{-P_{\theta_{AC}}}{q^2} = \frac{-C_{\theta_{AC}}}{q}$
7	$\sigma_{C_\alpha} = \sqrt{\left[\left(\frac{1}{q}\right)\left(\sigma_{P_\alpha,trans}\right)\right]^2 + \left[\left(\frac{-C_\alpha}{q}\right)\left(\sigma_{q,trans}\right)\right]^2}$	$\sigma_{C_{\theta_{AC}}} = \sqrt{\left[\left(\frac{1}{q}\right)\left(\sigma_{P_{\theta_{AC}}}\right)\right]^2 + \left[\left(\frac{-C_{\theta_{AC}}}{q}\right)\left(\sigma_q\right)\right]^2}$
8	$\sigma_{C_\alpha} = \frac{\sigma_{P_{\alpha,trans}}}{q}\sqrt{1 + C_\alpha^2}\ (\sigma_{P_{\alpha,trans}} = \sigma_{q,trans})$	$\sigma_{C_{\theta_{AC}}} = \frac{\sigma_{P_{\theta_{AC},trans}}}{q}\sqrt{1 + C_{\theta_{AC}}^2}\ (\sigma_{P_{\theta_{AC},trans}} = \sigma_{q,trans})$
10	Partial derivatives derived from 5HP calibration	
	$\frac{\partial\alpha}{\partial C_{\theta_{AC}}} = 1.33$ $\frac{\partial\alpha}{\partial C_\alpha} = 25$	$\frac{\partial\theta_{AC}}{\partial C_\alpha} = 1.33$ $\frac{\partial\theta_{AC}}{\partial C_\theta} = 25$
11	$\sigma_{P_{\alpha,trans}} = 14\ Pa\ (0.1\%\ full\ scale)$	$\sigma_{P_{\theta_{AC},trans}} = 14\ Pa\ (0.1\%\ full\ scale)$
Remaining uncertainty terms		
12	$\sigma_{\alpha,cal} = 0.07°$	$\sigma_{\theta_{AC},cal} = 0.18°$
13	$\sigma_{\alpha,align} = 0.008°$	$\sigma_{\theta_{AC},align} = 0.10°$

Pressure coefficient, $C_{p,3D}$ [-]

Definition		
1	$C_{p,3D} = \frac{p_{scanner}}{q}$	
Total uncertainty equation		
2	$\partial C_{p,3D} = \sqrt{\left[\left(\frac{\partial C_{p,3D}}{\partial p_{scanner}}\right)(\sigma_{p_{scanner}})\right]^2 + \left[\left(\frac{\partial C_{p,3D}}{\partial q}\right)(\sigma_q)\right]^2 + \left[\left(\frac{\partial C_{p,3D}}{\partial \alpha}\right)(\sigma_\alpha)\right]^2 + \left[C_{p,3D_{std}}\right]^2}$	
Partial derivative formulation		
3	$\frac{\partial C_{p,3D}}{\partial p_{scanner}} = \frac{1}{q}$	$\sigma_{p_{scanner}} = 5\ Pa$ Static accuracy = 0.12 % FS Thermal accuracy = 0.08 % FS (0.004 % FS/°C with 20° differential)
4	$\frac{\partial C_{p,3D}}{\partial q} = \frac{-p_{scanner}}{q^2}$	$\sigma_q = \sqrt{\left[\sigma_{q,trans}\right]^2 + \left[\sigma_{q,cal}\right]^2}$ $\sigma_{q,trans} = 14\ Pa\ (0.1\%\ full\ scale)$ $\sigma_{q,cal} = (0.00379)(q)$
5	$\frac{\partial C_{p,3D}}{\partial \alpha} = \frac{C_{p,3D}(\alpha=-6°) - C_{p,3D}(\alpha=-2°)}{-4}$ *experimentally found the partial derivative at every pressure tap from α = -6° to -2° (conservative measure)*	$\sigma_{\alpha,systematic} = calculated\ from\ \alpha\ table\ above$
6	$\partial C_{p,3D} = \sqrt{\left[\left(\frac{1}{q}\right)(\sigma_{p_{scanner}})\right]^2 + \left[\left(\frac{-p_{scanner}}{q^2}\right)(\sigma_q)\right]^2 + \left[\left(\frac{\partial C_{p,3D}}{\partial \alpha}\right)(\sigma_\alpha)\right]^2 + \left[C_{p,3D_{std}}\right]^2}$	

Pressure-coefficient gradient, $C_{p,x}$ [1/m]

Definition		
1	$C_{p,x} = \frac{\partial C_{p,2D}}{\partial x} = \frac{\partial}{\partial x}\left(\frac{p_{scanner}}{q(\cos 30°)^2}\right)$; Least-squares analysis of $C_{p,2D}$ profiles to calculate slope	
Total uncertainty equation		
2	$\sigma_{C_{p,x}} = \sqrt{\left[\left(\frac{\partial C_{p,x}}{\partial p_{scanner}}\right)(\sigma_{p_{scanner}})\right]^2 + \left[\left(\frac{\partial C_{p,x}}{\partial \alpha}\right)(\sigma_\alpha)\right]^2 + \left[RMSE_{curve\ fit}\right]^2 + \left[C_{p,x_{std}}\right]^2}$	
Partial derivative formulation		
3	$\frac{\partial C_{p,x}}{\partial p_{scanner}} = \frac{1}{q \cdot \Delta x \cdot (\cos 30°)^2}$ $\Delta x = 0.55 * 1.3716 * \cos(30°)\, m$	$\sigma_{p_{scanner}} = 5\ Pa$ Static accuracy = 0.12 % FS Thermal accuracy = 0.08 % FS (0.004 % FS/°C with 20° differential)
4	$\frac{\partial C_{p,x}}{\partial \alpha} = \frac{\partial}{\partial x}\left(\frac{\partial C_{p,3D}}{\partial \alpha}\right)$ $\frac{\partial C_{p,3D}}{\partial \alpha}\ from\ C_{p,3D}\ analysis\ above$ RMS $[central\ difference\ at\ every\ pressure\ tap]$	$\sigma_\alpha =\ total\ uncertainty\ from\ above\ table$
5	RMSE of the curve fit using least-squares analysis	
6	$C_{p,x_{std}} = RMS\left[central\ difference\ of C_{p,2D}\ at\ every\ pressure\ tap\right]$	
7	$\sigma_{C_{p,x}} = \sqrt{\left[\left(\frac{1}{q \cdot \Delta x \cdot (\cos 30°)^2}\right)(\sigma_{p_{scanner}})\right]^2 + \left[\left(\frac{\partial C_{p,x}}{\partial \alpha}\right)(\sigma_\alpha)\right]^2 + [RMSE\ of\ curve\ fit]^2 + \left[C_{p,x_{std}}\right]^2}$	

Mach number, M [-]

Definition	
1	$$M = \left[\left(\frac{q}{0.705 \cdot p_s}\right)\right]^{0.5}$$
Total uncertainty equation	
2	$$\sigma_M = \sqrt{\left[\left(\frac{\partial M}{\partial p_s}\right)(\sigma_{p_s})\right]^2 + \left[\left(\frac{\partial M}{\partial q}\right)(\sigma_q)\right]^2 + [M_{std}]^2}$$
Partial derivative formulation	
3	$$\frac{\partial M}{\partial p_s} = \frac{1}{2}\left(\frac{q}{0.705 \cdot p_s}\right)^{-0.5}\left(\frac{q}{0.705}\right)(-p^{-2})$$
4	$$\frac{\partial M}{\partial q} = \frac{1}{2}\left(\frac{q}{0.705 \cdot p_s}\right)^{-0.5}\left(\frac{1}{0.705 \cdot p_s}\right)$$

Freestream density, ρ_∞ [kg/m^3]

Definition	
1	$$\rho_\infty = \frac{p_s}{R \cdot T_\infty}$$
Total uncertainty equation	
2	$$\sigma_{\rho_\infty} = \sqrt{\left[\left(\frac{\partial \rho_\infty}{\partial p_s}\right)(\sigma_{p_s})\right]^2 + \left[\left(\frac{\partial \rho_\infty}{\partial T_\infty}\right)(\sigma_{T_\infty})\right]^2 + \left[\rho_{\infty_{std}}\right]^2}$$
Partial derivative formulation	
3	$$\frac{\partial \rho_\infty}{\partial p_s} = \frac{1}{R \cdot T_\infty}$$
4	$$\frac{\partial \rho_\infty}{\partial T_\infty} = \frac{p_s}{R}\left(-{T_\infty}^{-2}\right)$$

Freestream velocity, U_∞ [m/s]

Definition	
1	$$U_\infty = \left(\frac{2 \cdot q}{\rho_\infty}\right)^{0.5}$$
Total uncertainty equation	
2	$$\sigma_{U_\infty} = \sqrt{\left[\left(\frac{\partial U_\infty}{\partial q}\right)(\sigma_q)\right]^2 + \left[\left(\frac{\partial U_\infty}{\partial \rho_\infty}\right)(\sigma_{\rho_\infty})\right]^2 + \left[U_{\infty_{std}}\right]^2}$$
Partial derivative formulation	
3	$$\frac{\partial U_\infty}{\partial q} = \frac{1}{2}\left(\frac{2 \cdot q}{\rho_\infty}\right)^{-0.5}\left(\frac{2}{\rho_\infty}\right)$$
4	$$\frac{\partial U_\infty}{\partial \rho_\infty} = \frac{1}{2}\left(\frac{2 \cdot q}{\rho_\infty}\right)^{-0.5}\left(\frac{2 \cdot q}{{\rho_\infty}^2}\right)$$

Boundary-layer edge total velocity, $U_{edge,total}$ [m/s]

Definition	
1	$$U_{edge,total} = U_\infty\left(1 - C_{p,3D}\right)^{0.5}$$
Total uncertainty equation	
2	$$\sigma_{U_{edge,total}} = \sqrt{\left[\left(\frac{\partial U_{edge,total}}{\partial U_\infty}\right)\left(\sigma_{U_\infty}\right)\right]^2 + \left[\left(\frac{\partial U_{edge,total}}{\partial C_{p,3D}}\right)\left(\sigma_{C_{p,3D}}\right)\right]^2 + \left[U_{edge,total_{std}}\right]^2}$$
Partial derivative formulation	
3	$$\frac{\partial U_{edge,total}}{\partial U_\infty} = \left(1 - C_{p,3D}\right)^{0.5}$$
4	$$\frac{\partial U_{edge,total}}{\partial C_{p,3D}} = -0.5 \cdot U_\infty\left(1 - C_{p,3D}\right)^{-0.5}$$

Leading-edge-normal, boundary-layer edge velocity, $U_{edge,norm}$ [m/s]

Definition	
1	$U_{edge} = U_{edge,total} \cdot \cos(29.58° - \theta)$ 29.58° is the flow angle computed by CFD at *x/c* = 0.15
Total uncertainty equation	
2	$\sigma_{U_{edge}} = \sqrt{\left[\left(\frac{\partial U_{edge}}{\partial U_{edge,total}}\right)\left(\sigma_{U_{edge,total}}\right)\right]^2 + \left[\left(\frac{\partial U_{edge}}{\partial \theta}\right)(\sigma_\theta)\right]^2 + \left[U_{edge_{std}}\right]^2}$
Partial derivative formulation	
3	$\frac{\partial U_{edge}}{\partial U_{edge,total}} = \cos(29.58° - \theta)$
4	$\frac{\partial U_{edge}}{\partial \theta} = U_{edge,total} \cdot \sin(29.58° - \theta)$

Similarity parameter, η [$m^{0.5}$]

Definition	
1	$\eta = k\sqrt{Re'}$
Total uncertainty equation	
2	$\sigma_\eta = \sqrt{\left[\left(\frac{\partial \eta}{\partial k}\right)(\sigma_k)\right]^2 + \left[\left(\frac{\partial \eta}{\partial Re'}\right)(\sigma_{Re'})\right]^2 + [\eta_{std}]^2}$
Partial derivative formulation	
3	$\frac{\partial \eta}{\partial k} = \sqrt{Re'}$
4	$\frac{\partial \eta}{\partial Re'} = 0.5 \cdot k(Re')^{-0.5}$

Leading-edge-normal, undisturbed velocity at step height k, u_k [m/s]

Definition	
1	$u_k = U_{edge,norm}(a\eta^4 + b\eta^3 + c\eta^2 + d\eta + e)$ Curve fit from computational velocity similarity profile at *x/c* = 0.15
Total uncertainty equation	
2	$\sigma_{u_k} = \sqrt{\left[\left(\frac{\partial u_k}{\partial U_{edge,norm}}\right)\left(\sigma_{U_{edge,norm}}\right)\right]^2 + \left[\left(\frac{\partial u_k}{\partial \eta}\right)(\sigma_\eta)\right]^2 + \left[u_{k\,std}\right]^2}$
Partial derivative formulation	
3	$\frac{\partial u_k}{\partial U_{edge,norm}} = (a\eta^4 + b\eta^3 + c\eta^2 + d\eta + e)$
4	$\frac{\partial u_k}{\partial \eta} = U_{edge,norm}(4a\eta^3 + 3b\eta^2 + 2c\eta + d)$

Boundary-layer edge temperature, T_{edge} [K]

Definition	
1	$T_{edge} = T_\infty \left[\frac{C_{p,3D}q + p_s}{p_s}\right]^{\gamma-1/\gamma}$
Total uncertainty equation	
2	$\sigma_{T_{edge}} = \sqrt{\left[\left(\frac{\partial T_{edge}}{\partial T_\infty}\right)(\sigma_{T_\infty})\right]^2 + \left[\left(\frac{\partial T_{edge}}{\partial q}\right)(\sigma_q)\right]^2 + \left[\left(\frac{\partial T_{edge}}{\partial C_{p,3D}}\right)\left(\sigma_{C_{p,3D}}\right)\right]^2 + \left[\left(\frac{\partial T_{edge}}{\partial p_s}\right)(\sigma_{p_s})\right]^2 + \left[T_{edge_{std}}\right]^2}$
Partial derivative formulation	
3	$\frac{\partial T_{edge}}{\partial T_\infty} = \left[\frac{C_{p,3D}q + p_s}{p_s}\right]^{\gamma-1/\gamma}$
4	$\frac{\partial T_{edge}}{\partial q} = \left(\frac{\gamma-1}{\gamma}\right)T_\infty \left[\frac{C_{p,3D}q + p_s}{p_s}\right]^{(\gamma-1/\gamma)-1}\left(\frac{C_{p,3D}}{p_s}\right)$
5	$\frac{\partial T_{edge}}{\partial C_{p,3D}} = \left(\frac{\gamma-1}{\gamma}\right)T_\infty \left[\frac{C_{p,3D}q + p_s}{p_s}\right]^{(\gamma-1/\gamma)-1}\left(\frac{q}{p_s}\right)$
6	$\frac{\partial T_{edge}}{\partial p_s} = \left(\frac{\gamma-1}{\gamma}\right)T_\infty \left[\frac{C_{p,3D}q + p_s}{p_s}\right]^{(\gamma-1/\gamma)-1}\left(\frac{C_{p,3D}q}{{p_s}^2}\right)$

Adiabatic-wall temperature, T_{aw} [K]

Definition	
1	$T_{aw} = T_{edge}\left[1 + r\left(\frac{\gamma - 1}{2}\right)M^2\right]$
Total uncertainty equation	
2	$\sigma_{T_{aw}} = \sqrt{\left[\left(\frac{\partial T_{aw}}{\partial T_{edge}}\right)\left(\sigma_{T_{edge}}\right)\right]^2 + \left[\left(\frac{\partial T_{aw}}{\partial M}\right)(\sigma_M)\right]^2 + \left[T_{aw_{std}}\right]^2}$
Partial derivative formulation	
3	$\frac{\partial T_{aw}}{\partial T_{edge}} = 1 + r\left(\frac{\gamma - 1}{2}\right)M^2$
4	$\frac{\partial T_{aw}}{\partial M} = T_{edge} r(\gamma - 1)M$

Temperature at step height k, T_k [K]

Definition	
1	$T_k = T_{aw} + \left(T_{edge} - T_{aw}\right)(A\eta^4 + B\eta^3 + C\eta^2 + D\eta + E)$ Curve fit from computational temperature similarity profile at *x/c* = 0.15
Total uncertainty equation	
2	$\sigma_{T_k} = \sqrt{\left[\left(\frac{\partial T_k}{\partial T_{aw}}\right)(\sigma_{T_{aw}})\right]^2 + \left[\left(\frac{\partial T_k}{\partial \eta}\right)(\sigma_\eta)\right]^2 + \left[\left(\frac{\partial T_k}{\partial T_{edge}}\right)\left(\sigma_{T_{edge}}\right)\right]^2 + \left[T_{k\,std}\right]^2}$
Partial derivative formulation	
3	$\frac{\partial T_k}{\partial T_{aw}} = 1 - (A\eta^4 + B\eta^3 + C\eta^2 + D\eta + E)$
4	$\frac{\partial T_k}{\partial \eta} = \left(T_{edge} - T_{aw}\right)(4A\eta^3 + 3B\eta^2 + 2C\eta + D)$
5	$\frac{\partial T_k}{\partial T_{edge}} = (A\eta^4 + B\eta^3 + C\eta^2 + D\eta + E)$

Dynamic viscosity at step height k, μ_k [Pa·sec]

Definition	
1	$$\mu_k = 0.00001827\left(\frac{411.15}{T_k + 120}\right)\left(\frac{T_k}{291.15}\right)^{1.5}$$
Total uncertainty equation	
2	$$\sigma_{\mu_k} = \sqrt{\left[\left(\frac{\partial \mu_k}{\partial T_k}\right)(\sigma_{T_k})\right]^2 + \left[\mu_{k_{std}}\right]^2}$$
Partial derivative formulation	
3	$$\frac{\partial \mu_k}{\partial T_k} = 0.00001827\frac{\left[411.15 \cdot 1.5(T_k + 120)\left(\frac{T_k}{291.15}\right)^{0.5}\left(\frac{1}{291.15}\right)\right] - 411.15\left(\frac{T_k}{291.15}\right)^{1.5}}{(T_k + 120)^2}$$

Density at step height k, ρ_k [kg/m^3]

Definition	
1	$$\rho_k = \frac{p_{edge}}{RT_k} = \frac{C_{p,3D}q + p_s}{RT_k}$$
Total uncertainty equation	
2	$$\sigma_{\rho_k} = \sqrt{\left[\left(\frac{\partial \rho_k}{\partial C_{p,3D}}\right)\left(\sigma_{C_{p,3D}}\right)\right]^2 + \left[\left(\frac{\partial \rho_k}{\partial q}\right)(\sigma_q)\right]^2 + \left[\left(\frac{\partial \rho_k}{\partial p_s}\right)(\sigma_{p_s})\right]^2 + \left[\left(\frac{\partial \rho_k}{\partial T_k}\right)(\sigma_{T_k})\right]^2 + \left[\rho_{k_{std}}\right]^2}$$
Partial derivative formulation	
3	$$\frac{\partial \rho_k}{\partial C_{p,3D}} = \frac{q}{RT_k}$$
4	$$\frac{\partial \rho_k}{\partial q} = \frac{C_{p,3D}}{RT_k}$$
5	$$\frac{\partial \rho_k}{\partial p_s} = \frac{1}{RT_k}$$
6	$$\frac{\partial \rho_k}{\partial T_k} = \frac{C_{p,3D}q + p_s}{RT_k{}^2}$$

Kinematic viscosity at step height k, ν_k [$m^2 \cdot sec^{-1}$]

Definition	
1	$$\nu_k = \frac{\mu_k}{\rho_k}$$
Total uncertainty equation	
2	$$\sigma_{\nu_k} = \sqrt{\left[\left(\frac{\partial \nu_k}{\partial \mu_k}\right)(\sigma_{\mu_k})\right]^2 + \left[\left(\frac{\partial \nu_k}{\partial \rho_k}\right)(\sigma_{\rho_k})\right]^2 + \left[\nu_{k_{std}}\right]^2}$$
Partial derivative formulation	
3	$$\frac{\partial \nu_k}{\partial \mu_k} = \frac{1}{\rho_k}$$
4	$$\frac{\partial \nu_k}{\partial \rho_k} = \mu_k {\rho_k}^{-2}$$

Step-height Reynolds number, based on undisturbed boundary-layer quantities, Re_{kk} [-]

Definition	
1	$$Re_{kk} = \frac{u_k k}{\nu_k}$$
Total uncertainty equation	
2	$$\sigma_{Re_{kk}} = \sqrt{\left[\left(\frac{\partial Re_{kk}}{\partial u_k}\right)(\sigma_{u_k})\right]^2 + \left[\left(\frac{\partial Re_{kk}}{\partial k}\right)(\sigma_k)\right]^2 + \left[\left(\frac{\partial Re_{kk}}{\partial \nu_k}\right)(\sigma_{\nu_k})\right]^2 + \left[Re_{kk_{std}}\right]^2}$$
Partial derivative formulation	
3	$$\frac{\partial Re_{kk}}{\partial u_k} = \frac{k}{\nu_k}$$
4	$$\frac{\partial Re_{kk}}{\partial k} = \frac{u_k}{\nu_k}$$
5	$$\frac{\partial Re_{kk}}{\partial \nu_k} = \frac{-u_k k}{{\nu_k}^2}$$

Step-height Reynolds number, based on freestream quantities, $Re_{k\infty}$ [-]

Definition	
1	$Re_{k\infty} = Re' \cdot k$
Total uncertainty equation	
2	$\sigma_{Re_{k\infty}} = \sqrt{\left[\left(\frac{\partial Re_{k\infty}}{\partial Re'}\right)(\sigma_{Re'})\right]^2 + \left[\left(\frac{\partial Re_{k\infty}}{\partial k}\right)(\sigma_k)\right]^2 + \left[Re_{k\infty_{std}}\right]^2}$
Partial derivative formulation	
3	$\frac{\partial Re_{k\infty}}{\partial Re'} = k$
4	$\frac{\partial Re_{k\infty}}{\partial k} = Re'$

Baseline transition location, $x_{tr,baseline}/c$ [-]

Definition		
1	$\left(\frac{x_{tr,baseline}}{c}\right) = 4.005 + (0.13\alpha) + (-4.9e^{-7}Re')$ Baseline transition curve fit from flight experiment	
Total uncertainty equation		
2	$\sigma_{\left(\frac{x_{tr,baseline}}{c}\right)} = \sqrt{\left[\left(\frac{\partial\left(\frac{x_{tr,baseline}}{c}\right)}{\partial Re'}\right)(\sigma_{Re'})\right]^2 + \left[\left(\frac{\partial\left(\frac{x_{tr,baseline}}{c}\right)}{\partial \alpha}\right)(\sigma_\alpha)\right]^2 + \left[RMSE_{curve\ fit}\right]^2}$	
Partial derivative formulation		
3	$\frac{\partial\left(\frac{x_{tr,baseline}}{c}\right)}{\partial Re'} = -4.9e^{-7}$	$\sigma_{Re',avg} = 0.023e^6$ (average of all points collected) $\sigma_{Re',max} = 0.084e^6$ (max of all points collected)
4	$\frac{\partial\left(\frac{x_{tr,baseline}}{c}\right)}{\partial \alpha} = 0.13$	$\sigma_{\alpha,avg}$ = 0.13° (average of all points collected) $\sigma_{\alpha,max}$ = 0.17° (max of all points collected)
6	$\left(RMSE_{curve\ fit}\right) = 0.015$	
Average and maximum total uncertainty		
7	$\sigma_{\left(\frac{x_{tr,baseline}}{c}\right)average}$ = 0.025; $\sigma_{\left(\frac{x_{tr,baseline}}{c}\right)max}$ = 0.049	

Laminar fraction, LF [-]

Definition	
1	$$LF = \frac{x_{tr} - x_k}{x_{tr,baseline} - x_k}$$
Total uncertainty equation	
2	$$\sigma_{LF} = \sqrt{\left[\left(\frac{\partial LF}{\partial x_{tr}}\right)\left(\sigma_{x_{tr}}\right)\right]^2 + \left[\left(\frac{\partial LF}{\partial x_{tr,baseline}}\right)\left(\sigma_{x_{tr,baseline}}\right)\right]^2 + [LF_{std}]^2}$$ This is a conservative estimate to the total uncertainty; no covariance terms are included.
Partial derivative formulation	
3	$$\frac{\partial LF}{\partial x_{tr}} = \left(\frac{1}{x_{tr,baseline} - x_k}\right)$$
4	$$\frac{\partial LF}{\partial x_{tr,baseline}} = \left(\frac{-(x_{tr} - x_k)}{\left(x_{tr,baseline} - x_k\right)^2}\right)$$
5	$$\frac{\sigma_{x_{tr}}}{c} = \frac{\sigma_{x_{tr,baseline}}}{c} = 0.025\ (average)$$
Minimum and maximum total uncertainty	
6	$\sigma_{LF,min}$ = 0.03 (low Re'); $\sigma_{LF,max}$ = 0.20 (high Re')

Boundary-layer thickness at x/c = 0.15, δ_{99} [μm]

Definition		
1	$\eta(u/U_{edge} = 0.99) = \delta_{99}\sqrt{Re'}$ (from computational velocity similarity profile at *x/c* = 0.15) $$\delta_{99} = \frac{\eta(u/U_{edge} = 0.99)}{\sqrt{Re'}}$$	
Total uncertainty equation		
2	$$\sigma_{\delta_{99}} = \sqrt{\left[\left(\frac{\partial \delta_{99}}{\partial Re'}\right)\left(\sigma_{Re'}\right)\right]^2 + \left[\left(\frac{\partial \delta_{99}}{\partial \eta}\right)\left(\sigma_{\eta}\right)\right]^2 + \left[\delta_{99_{std}}\right]^2}$$	
Partial derivative formulation		
3	$$\frac{\partial \delta_{99}}{\partial Re'} = -0.5 \cdot \eta \cdot Re'^{-1.5}$$	
4	$$\frac{\partial \delta_{99}}{\partial \eta} = Re'^{-0.5}$$	$\sigma_\eta = 0.02$ This accounts for potential CFD errors, α error, and curve fit errors

Displacement thickness at x/c = 0.15, δ [μm]*

Definition	
1	$$\delta^* = \int_0^{\delta_{99}} \left(1 - {}^{u}/_{U_{edge}}\right) dy$$ $$\delta^* = \delta_{99} - \frac{a}{5} Re'^{2} {\delta_{99}}^{5} - \frac{b}{4} Re'^{1.5} {\delta_{99}}^{4} - \frac{c}{3} Re' {\delta_{99}}^{3} - \frac{d}{2} Re'^{0.5} {\delta_{99}}^{2} - e\,\delta_{99}$$ Coefficients from curve fit from computational velocity similarity profile at *x/c* = 0.15
Total uncertainty equation	
2	$$\sigma_{\delta^*} = \sqrt{\left[\left(\frac{\partial \delta^*}{\partial Re'}\right)(\sigma_{Re'})\right]^2 + \left[\left(\frac{\partial \delta^*}{\partial \delta_{99}}\right)(\sigma_{\delta_{99}})\right]^2 + [\delta^*_{std}]^2}$$
Partial derivative formulation	
3	$$\frac{\partial \delta^*}{\partial Re'} = -\frac{2a}{5} Re' {\delta_{99}}^{5} - \frac{3b}{8} Re'^{0.5} {\delta_{99}}^{4} - \frac{c}{3} {\delta_{99}}^{3} - \frac{d}{4} Re'^{-0.5} {\delta_{99}}^{2}$$
4	$$\frac{\partial \delta^*}{\partial \delta_{99}} = 1 - a\, Re'^{2} {\delta_{99}}^{4} - b\, Re'^{1.5} {\delta_{99}}^{3} - c\, Re' {\delta_{99}}^{2} - d\, Re'^{0.5} \delta_{99} - e$$

Momentum thickness at x/c = 0.15, θ [μm]

Definition	
1	$$\theta = \int_0^{\delta_{99}} {}^{u}/_{U_{edge}} \left(1 - {}^{u}/_{U_{edge}}\right) dy$$ $$\theta = -\frac{(a^2)}{9} Re'^{4} {\delta_{99}}^{9} - \frac{(2ab)}{8} Re'^{3.5} {\delta_{99}}^{8} - \frac{(2ac+b^2)}{7} Re'^{3} {\delta_{99}}^{7} - \frac{(2ad+2bc)}{6} Re'^{2.5} {\delta_{99}}^{6} + \frac{(a-2ae-2bd-c^2)}{5} Re'^{2} {\delta_{99}}^{5}$$ $$+ \frac{(b-2be-2cd)}{4} Re'^{1.5} {\delta_{99}}^{4} + \frac{(c-2ce-d^2)}{3} Re' {\delta_{99}}^{3} + \frac{(d-2de)}{2} Re'^{0.5} {\delta_{99}}^{2} + (e - e^2)\delta_{99}$$ Coefficients from curve fit from computational velocity similarity profile at *x/c* = 0.15
Total uncertainty equation	
2	$$\sigma_\theta = \sqrt{\left[\left(\frac{\partial \theta}{\partial Re'}\right)(\sigma_{Re'})\right]^2 + \left[\left(\frac{\partial \theta}{\partial \delta_{99}}\right)(\sigma_{\delta_{99}})\right]^2 + [\theta_{std}]^2}$$
Partial derivative formulation	
3	$$\frac{\partial \theta}{\partial Re'} = -\frac{(4a^2)}{9} Re'^{3} {\delta_{99}}^{9} - \frac{(7ab)}{8} Re'^{2.5} {\delta_{99}}^{8} - \frac{(6ac+3b^2)}{7} Re'^{2} {\delta_{99}}^{7} - \frac{(5ad+5bc)}{6} Re'^{1.5} {\delta_{99}}^{6} +$$ $$\frac{(2a-4ae-4bd-2c^2)}{5} Re' {\delta_{99}}^{5} + \frac{(3b-6be-6cd)}{8} Re'^{0.5} {\delta_{99}}^{4} + \frac{(c-2ce-d^2)}{3} {\delta_{99}}^{3} + \frac{(d-2de)}{4} Re'^{-0.5} {\delta_{99}}^{2}$$
4	$$\frac{\partial \theta}{\partial \delta_{99}} = -(a^2) Re'^{4} {\delta_{99}}^{8} - (2ab) Re'^{3.5} {\delta_{99}}^{7} - (2ac + b^2) Re'^{3} {\delta_{99}}^{6} - (2ad + 2bc) Re'^{2.5} {\delta_{99}}^{5} +$$ $$(a - 2ae - 2bd - c^2) Re'^{2} {\delta_{99}}^{4} + (b - 2be - 2cd) Re'^{1.5} {\delta_{99}}^{3} + (c - 2ce - d^2) Re' {\delta_{99}}^{2} + (d -$$ $$2de) Re'^{0.5} {\delta_{99}} + (e - e^2)$$

Boundary-layer relationships, k/δ_{99}, k/δ^*, k/θ [-]

Definition		
1	$BL\ Relation\ 1 = k/\delta_{99}$ $BL\ Relation\ 2 = k/\delta^*$ $BL\ Relation\ 3 = k/\theta$	
Total uncertainty equation		
2	$\sigma_{BL\ Relation\ 1} = \sqrt{\left[\left(\frac{\partial BL\ Relation\ 1}{\partial \delta_{99}}\right)(\sigma_{\delta_{99}})\right]^2 + \left[\left(\frac{\partial BL\ Relation\ 1}{\partial k}\right)(\sigma_k)\right]^2 + [BL\ Relation\ 1_{std}]^2}$ $\sigma_{BL\ Relation\ 2} = \sqrt{\left[\left(\frac{\partial BL\ Relation\ 2}{\partial \delta^*}\right)(\sigma_{\delta^*})\right]^2 + \left[\left(\frac{\partial BL\ Relation\ 2}{\partial k}\right)(\sigma_k)\right]^2 + [BL\ Relation\ 2_{std}]^2}$ $\sigma_{BL\ Relation\ 3} = \sqrt{\left[\left(\frac{\partial BL\ Relation\ 3}{\partial \theta}\right)(\sigma_\theta)\right]^2 + \left[\left(\frac{\partial BL\ Relation\ 3}{\partial k}\right)(\sigma_k)\right]^2 + [BL\ Relation\ 3_{std}]^2}$	
Partial derivative formulation		
3	$\frac{\partial BL\ Relation\ 1}{\partial \delta_{99}} = -k{\delta_{99}}^{-2}$ $\frac{\partial BL\ Relation\ 2}{\partial \delta^*} = -k\delta^{*-2}$ $\frac{\partial BL\ Relation\ 3}{\partial \theta} = -k\theta^{-2}$	
4	$\frac{\partial BL\ Relation\ 1}{\partial k} = {\delta_{99}}^{-1}$ $\frac{\partial BL\ Relation\ 2}{\partial k} = \delta^{*-1}$ $\frac{\partial BL\ Relation\ 1}{\partial k} = \theta^{-1}$	$\sigma_k = 25\ \mu\text{m}$

APPENDIX F

FLIGHT-TESTING TRANSITION-FRONT RESULTS

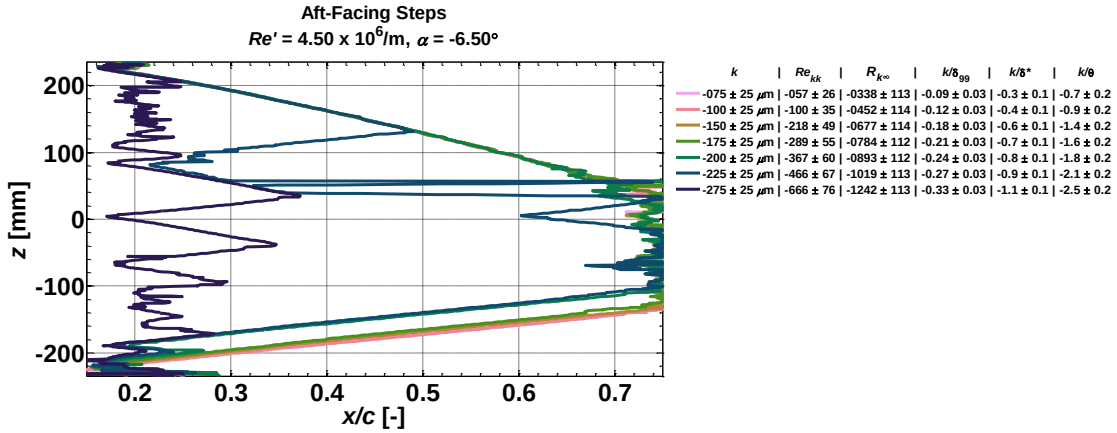

Fig. 111 Appendix: Aft-facing step, *Re´* = 4.50 x 10^6/m, α = -6.50°

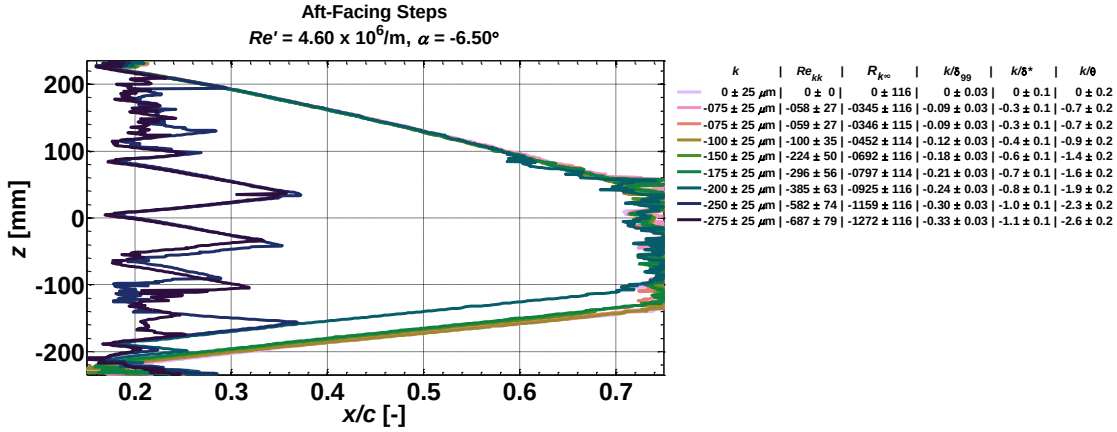

Fig. 112 Appendix: Aft-facing step, *Re´* = 4.60 x 10^6/m, α = -6.50°

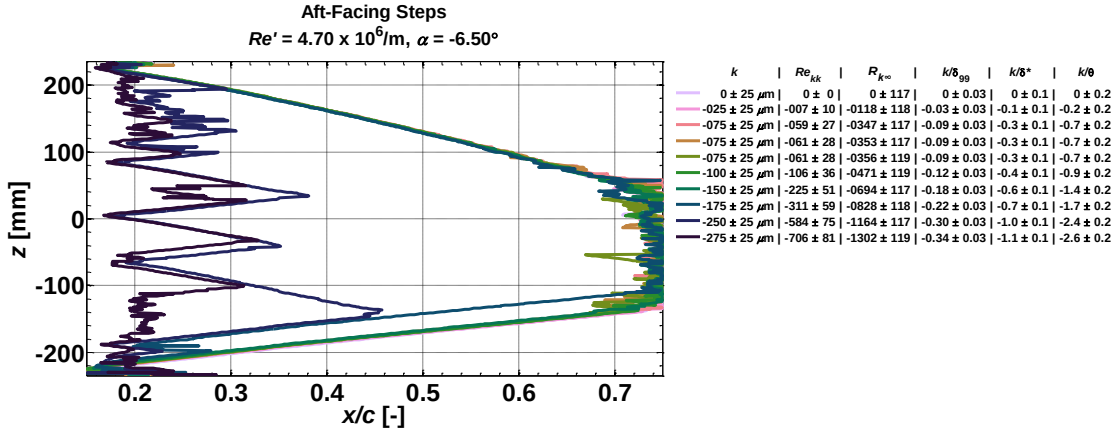

Fig. 113 Appendix: Aft-facing step, *Re´* = 4.70 x 10^6/m, α = -6.50°

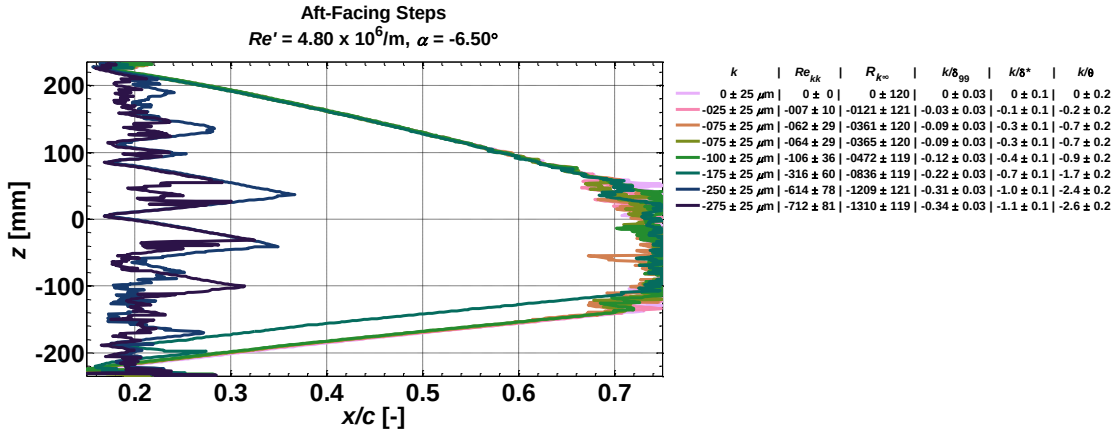

Fig. 114 Appendix: Aft-facing step, *Re´* = 4.80 x 10^6/m, α = -6.50°

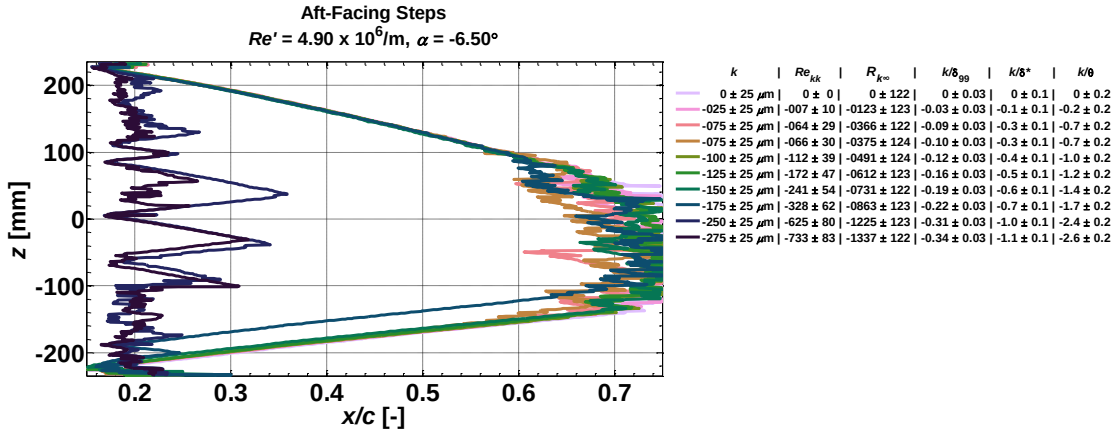

Fig. 115 Appendix: Aft-facing step, *Re´* = 4.90 x 10^6/m, α = -6.50°

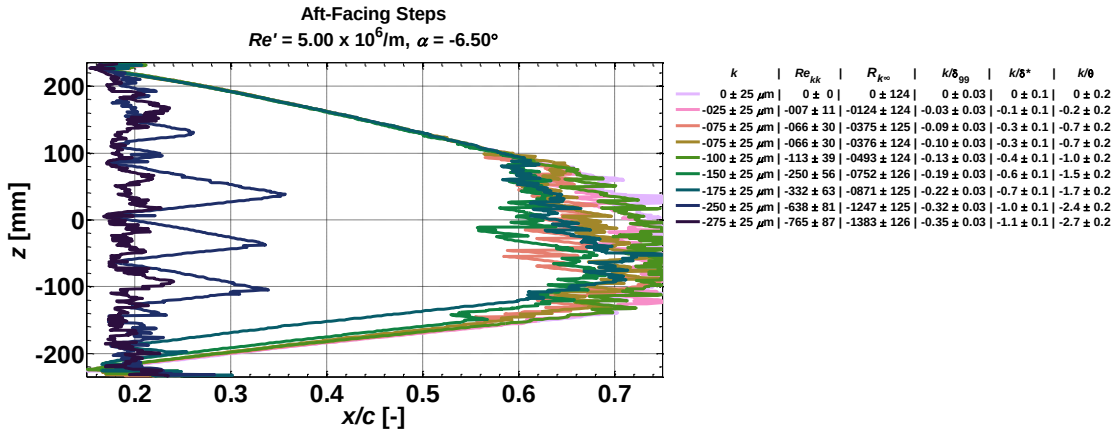

Fig. 116 Appendix: Aft-facing step, *Re´* = 5.00 x 10^6/m, α = -6.50°

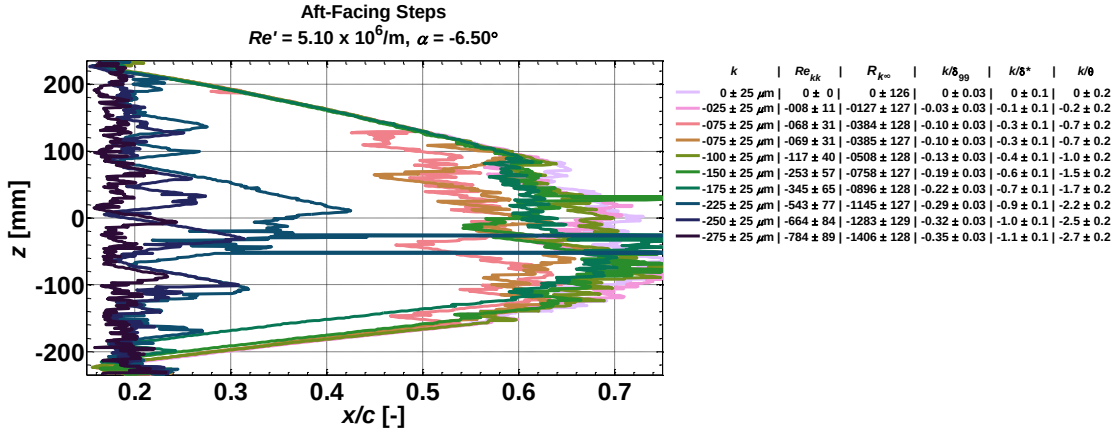

Fig. 117 Appendix: Aft-facing step, *Re´* = 5.10 x 10^6/m, α = -6.50°

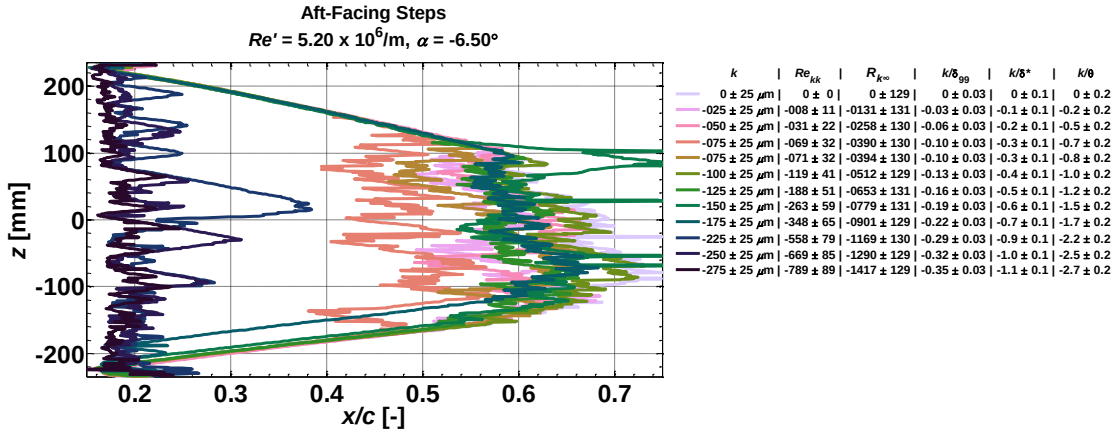

Fig. 118 Appendix: Aft-facing step, *Re´* = 5.20 x 10^6/m, α = -6.50°

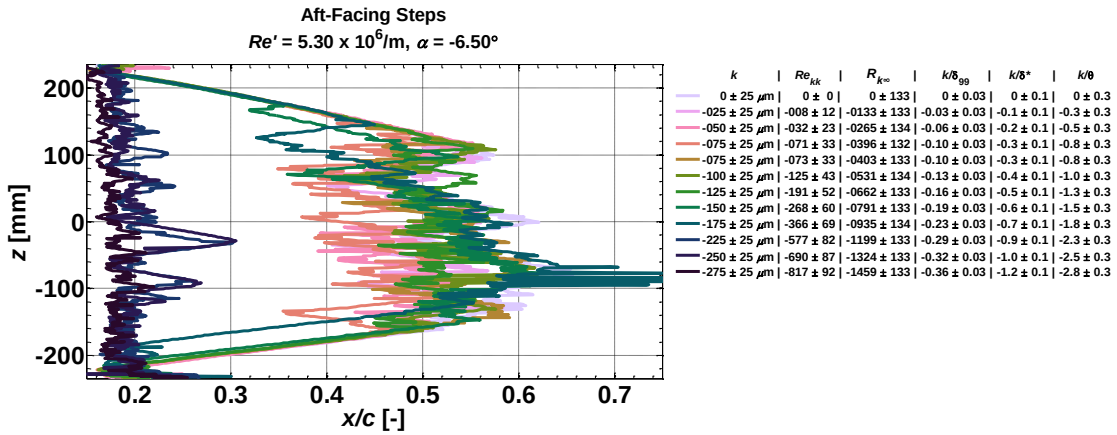

Fig. 119 Appendix: Aft-facing step, *Re´* = 5.30 x 10^6/m, α = -6.50°

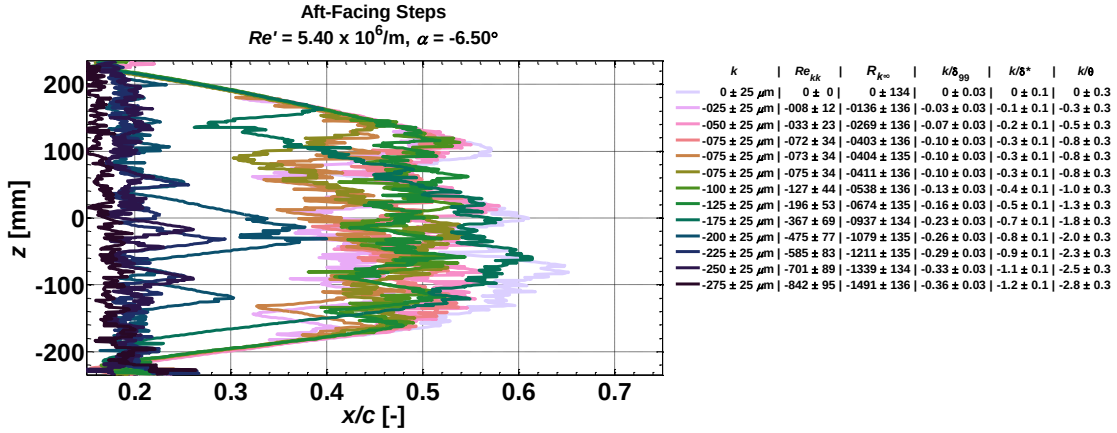

Fig. 120 Appendix: Aft-facing step, *Re´* = 5.40 x 10^6/m, α = -6.50°

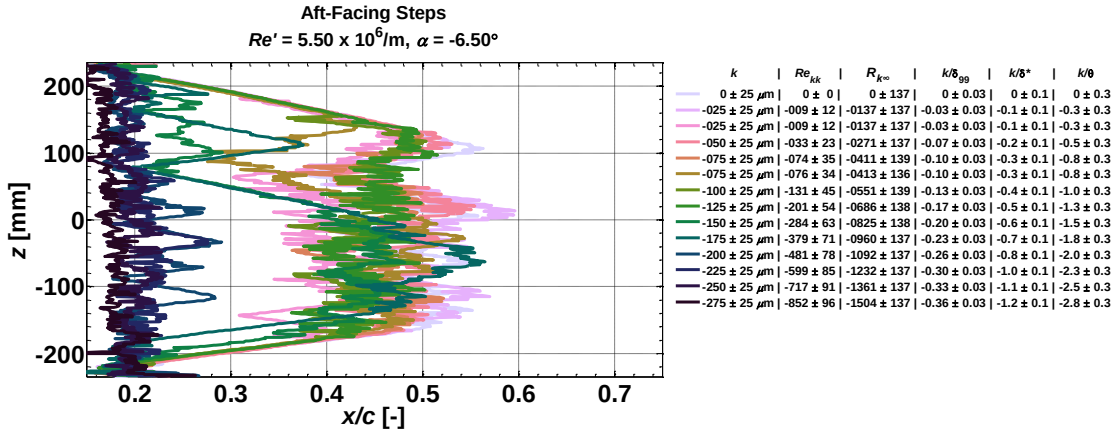

Fig. 121 Appendix: Aft-facing step, *Re´* = 5.50 x 10^6/m, α = -6.50°

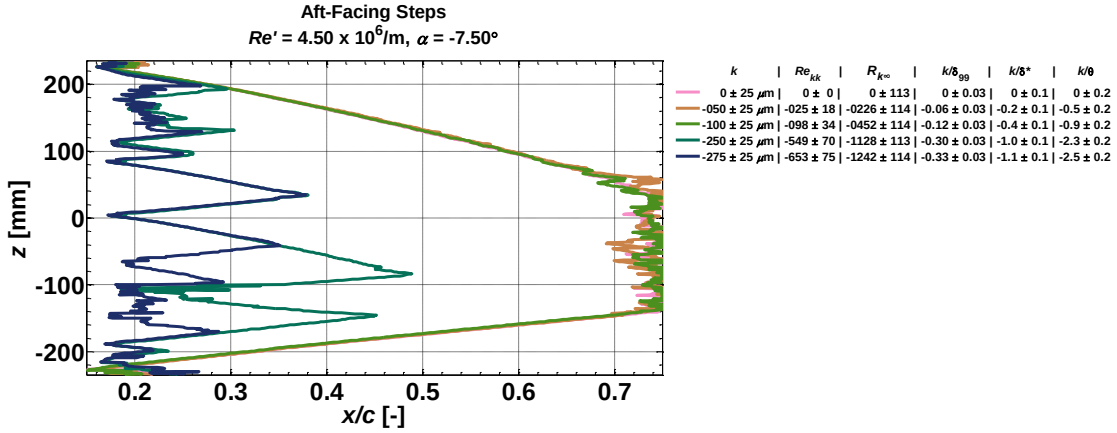

Fig. 122 Appendix: Aft-facing step, *Re´* = 4.50 x 10^6/m, α = -7.50°

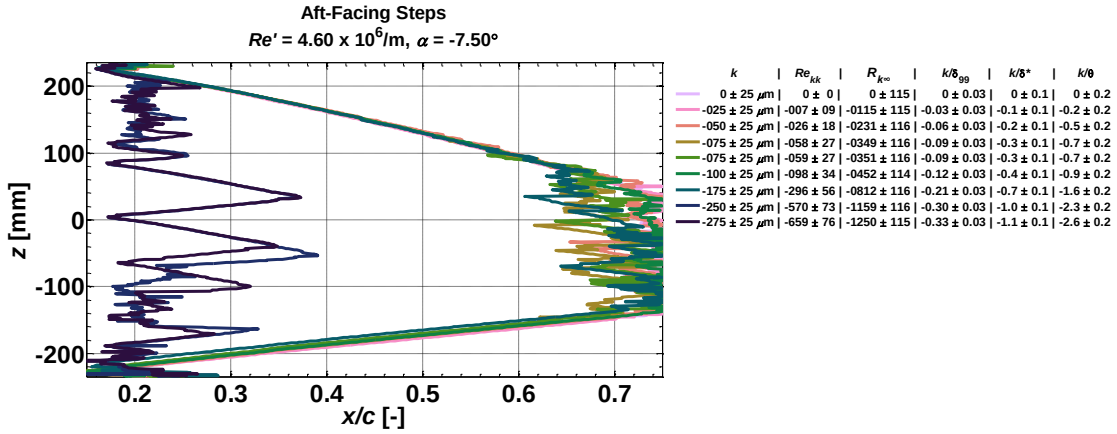

Fig. 123 Appendix: Aft-facing step, *Re´* = 4.60 x 10^6/m, α = -7.50°

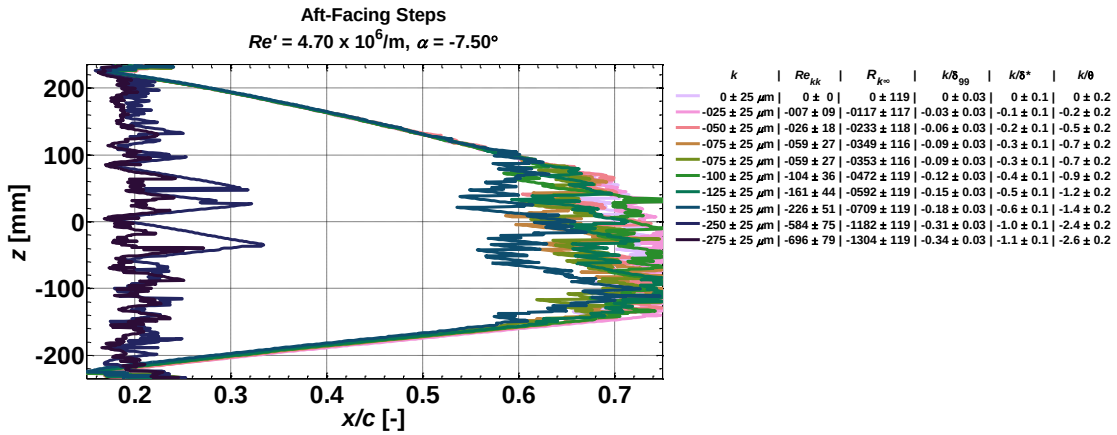

Fig. 124 Appendix: Aft-facing step, *Re´* = 4.70 x 10^6/m, α = -7.50°

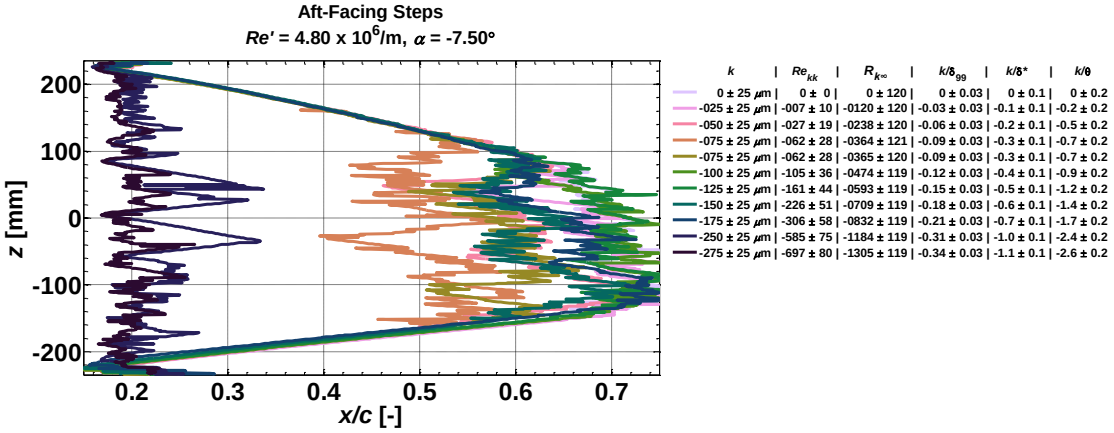

Fig. 125 Appendix: Aft-facing step, *Re´* = 4.80 x 10^6/m, α = -7.50°

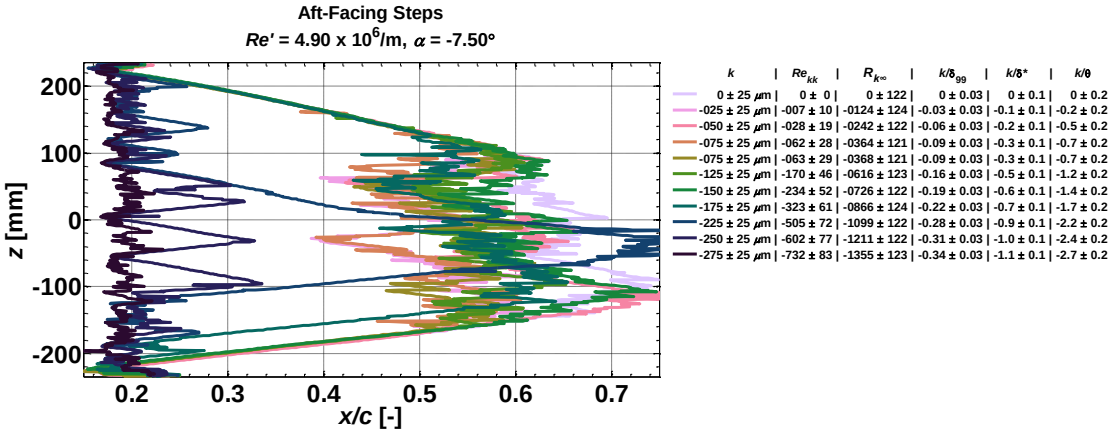

Fig. 126 Appendix: Aft-facing step, *Re´* = 4.90 x 10^6/m, α = -7.50°

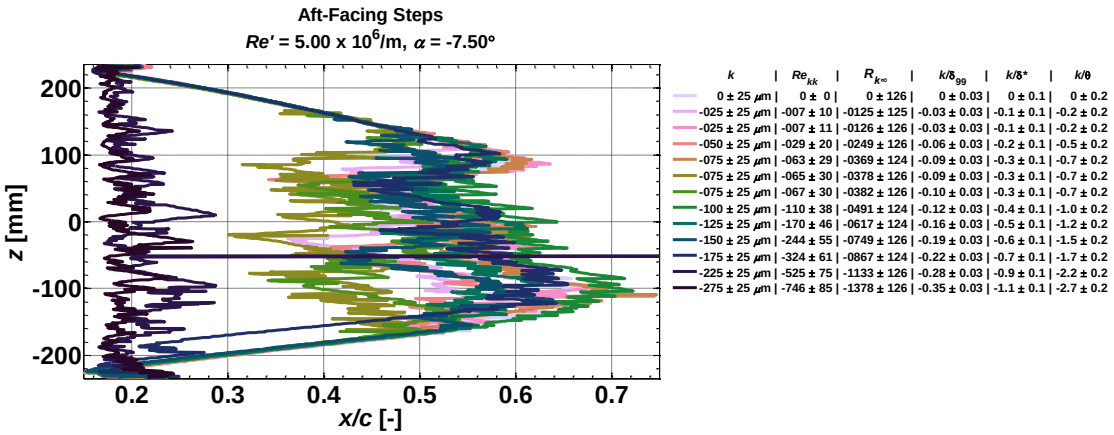

Fig. 127 Appendix: Aft-facing step, *Re´* = 5.00 x 10^6/m, α = -7.50°

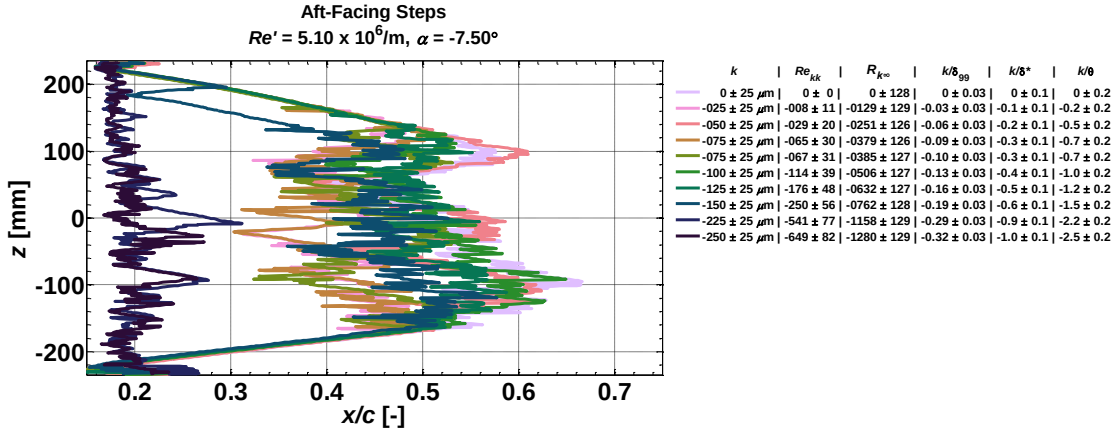

Fig. 128 Appendix: Aft-facing step, *Re´* = 5.10 x 10^6/m, α = -7.50°

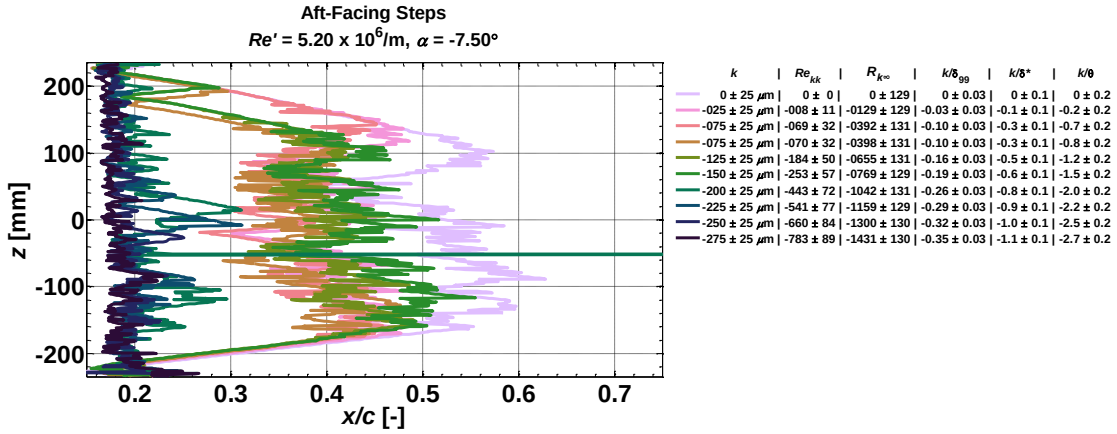

Fig. 129 Appendix: Aft-facing step, *Re´* = 5.20 x 10^6/m, α = -7.50°

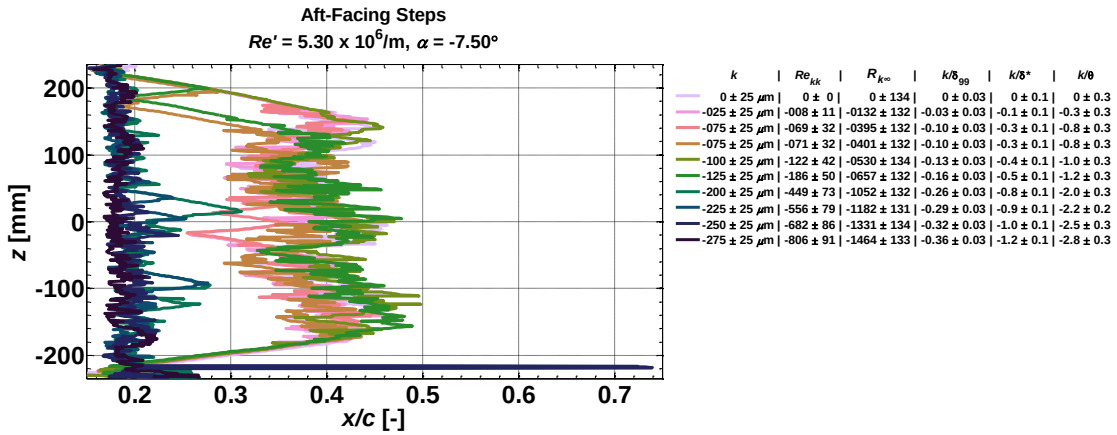

Fig. 130 Appendix: Aft-facing step, *Re´* = 5.30 x 10^6/m, α = -7.50°

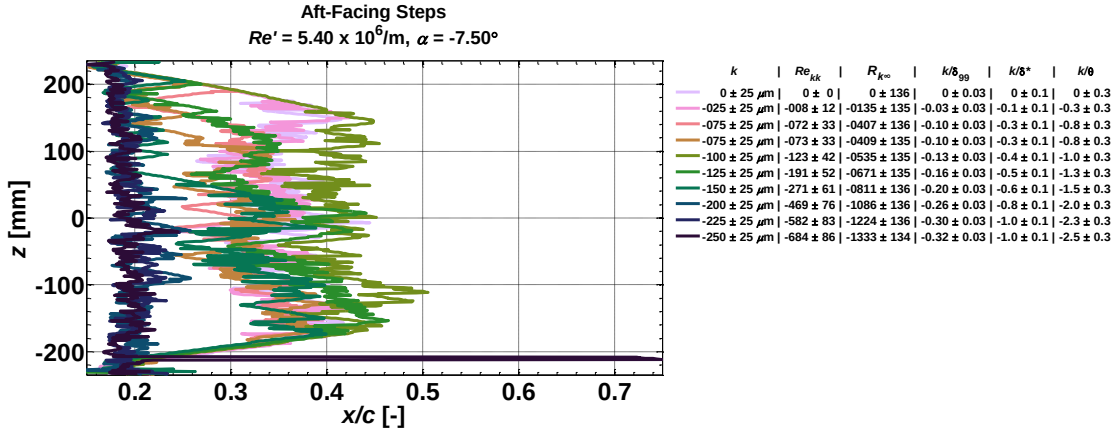

Fig. 131 Appendix: Aft-facing step, *Re´* = 5.40 x 10^6/m, α = -7.50°

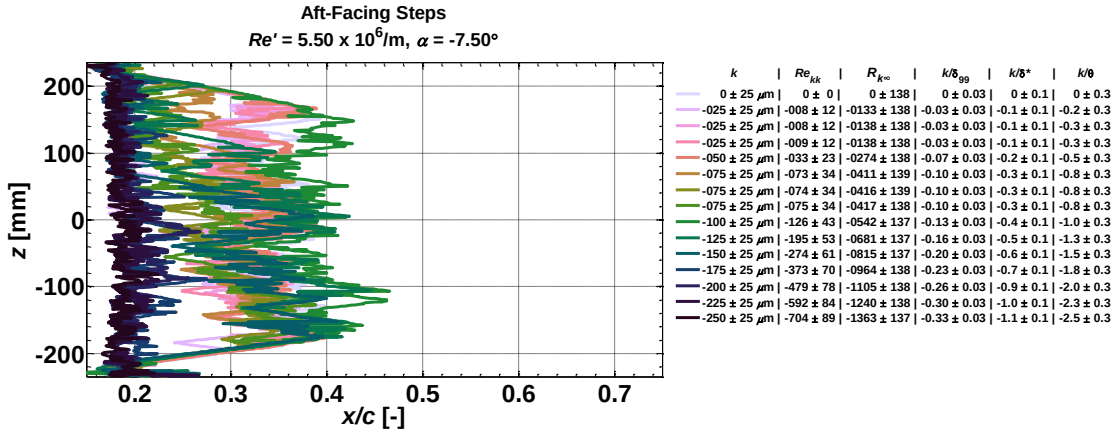

Fig. 132 Appendix: Aft-facing step, *Re´* = 5.50 x 10^6/m, α = -7.50°

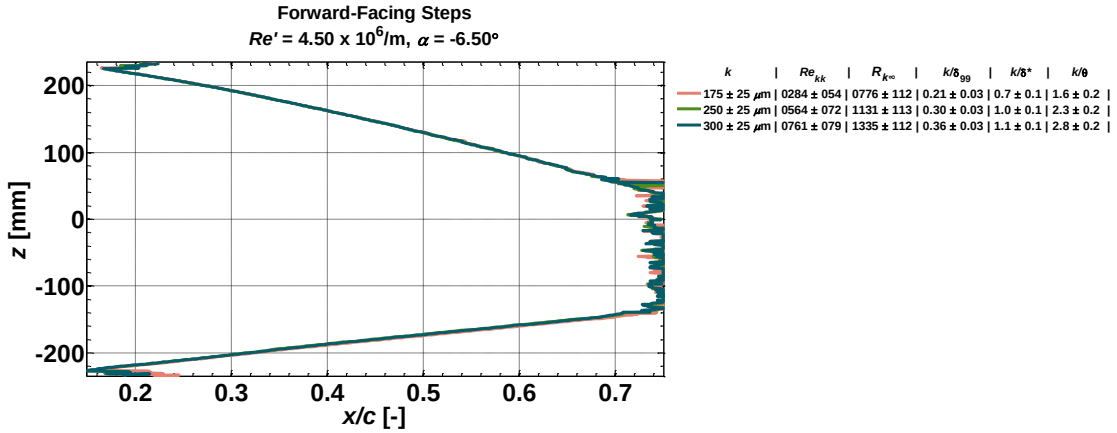

Fig. 133 Appendix: Forward-facing step, *Re´* = 4.50 x 10^6/m, α = -6.50°

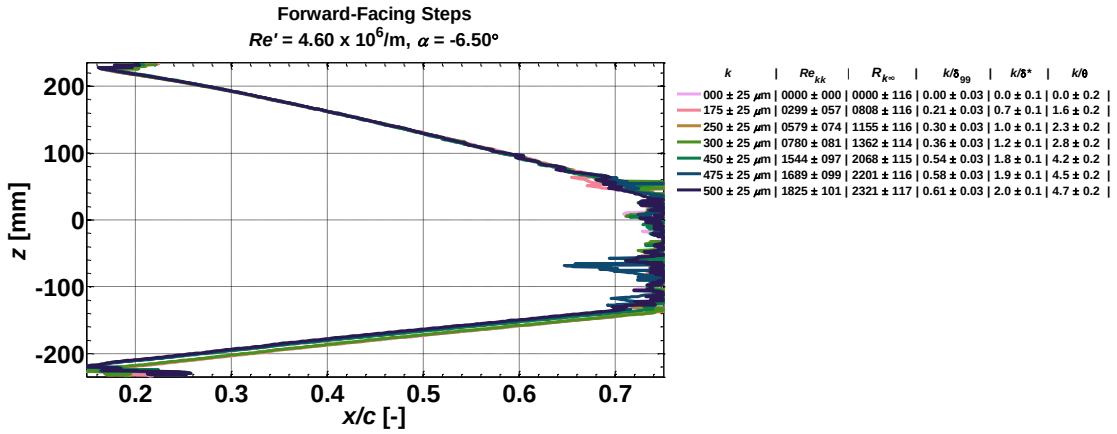

Fig. 134 Appendix: Forward-facing step, *Re´* = 4.60 x 10^6/m, α = -6.50°

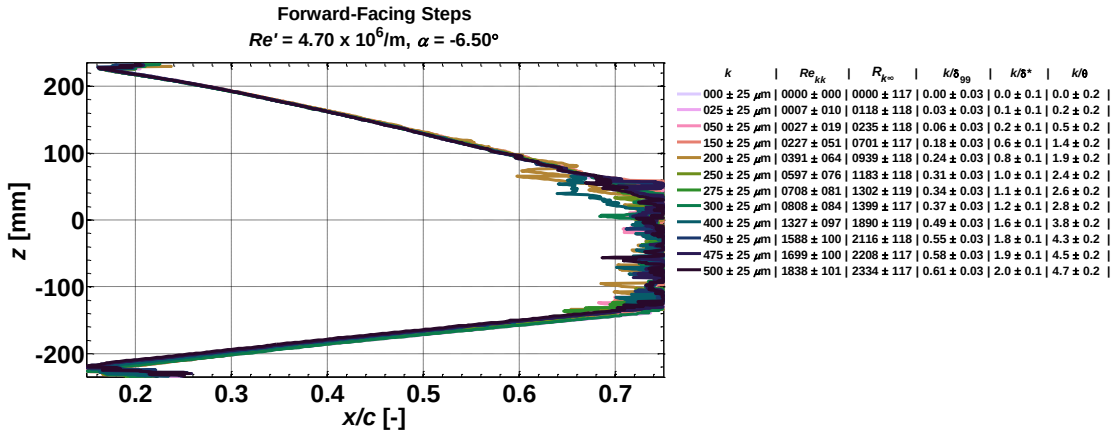

Fig. 135 Appendix: Forward-facing step, *Re´* = 4.70 x 10^6/m, α = -6.50°

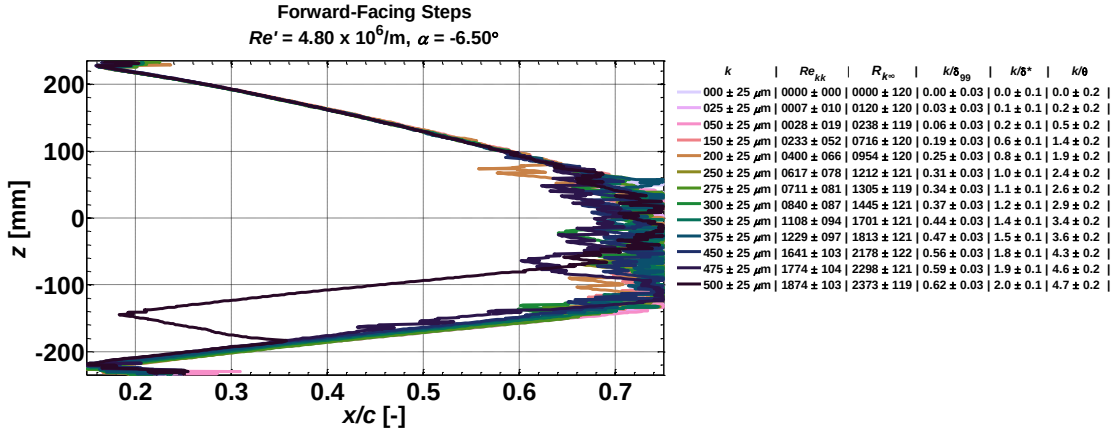

Fig. 136 Appendix: Forward-facing step, *Re´* = 4.80 x 10^6/m, α = -6.50°

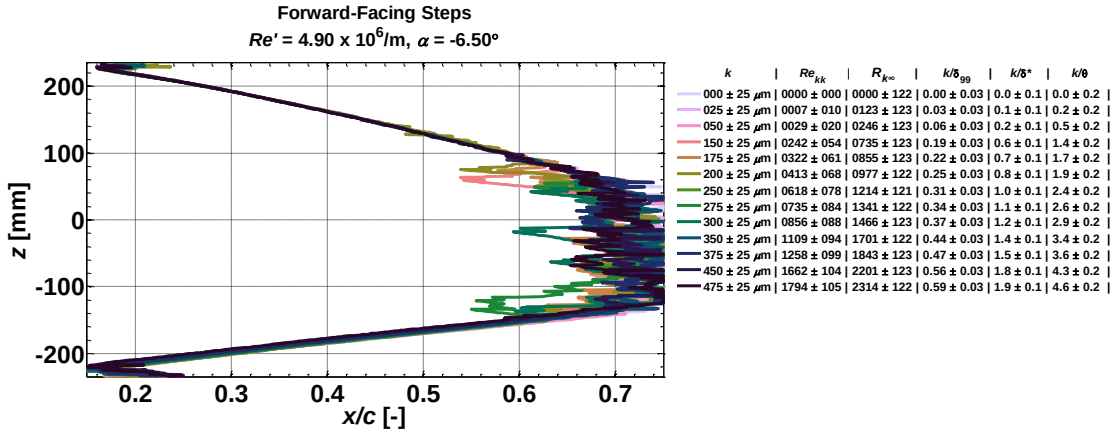

Fig. 137 Appendix: Forward-facing step, *Re´* = 4.90 x 10^6/m, α = -6.50°

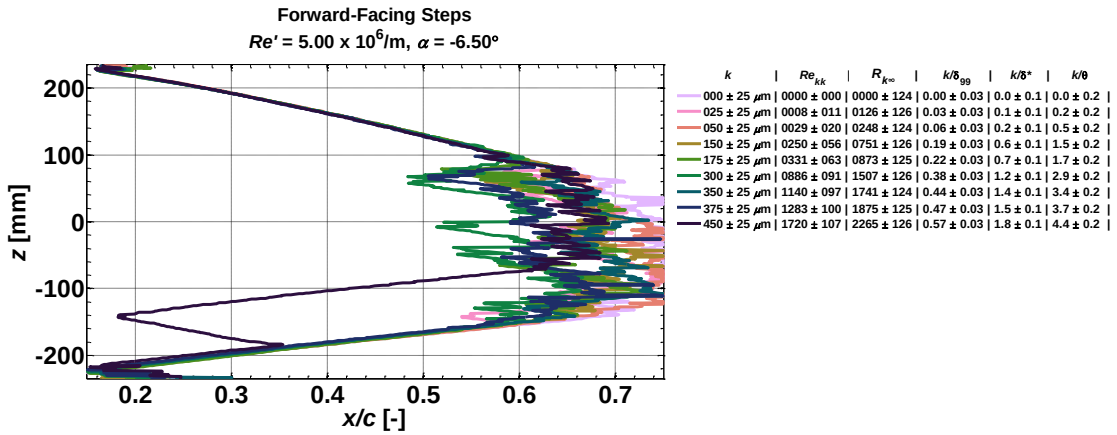

Fig. 138 Appendix: Forward-facing step, *Re´* = 5.00 x 10^6/m, α = -6.50°

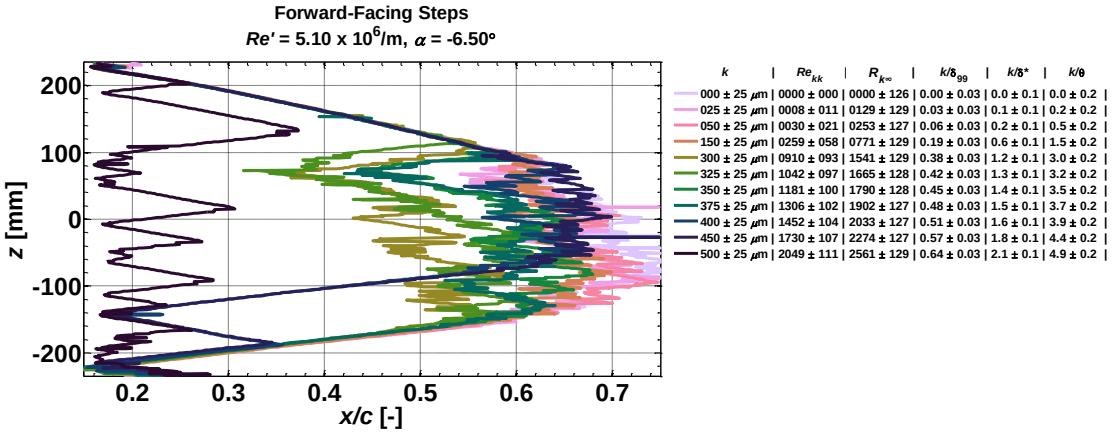

Fig. 139 Appendix: Forward-facing step, *Re´* = 5.10 x 10^6/m, α = -6.50°

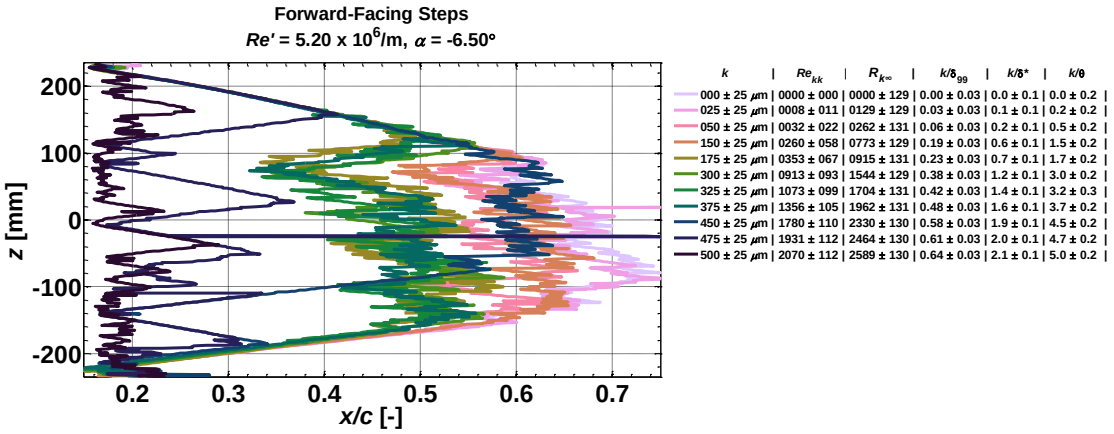

Fig. 140 Appendix: Forward-facing step, *Re´* = 5.20 x 10^6/m, α = -6.50°

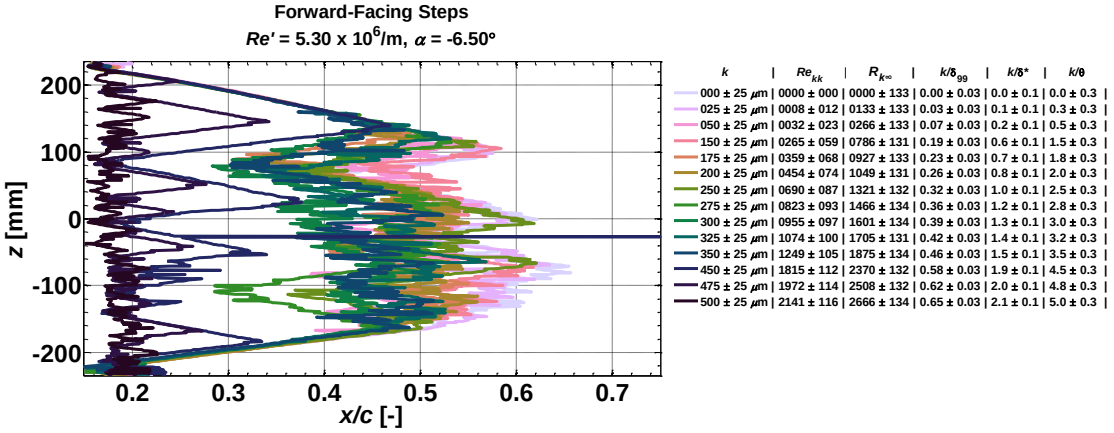

Fig. 141 Appendix: Forward-facing step, *Re´* = 5.30 x 10^6/m, α = -6.50°

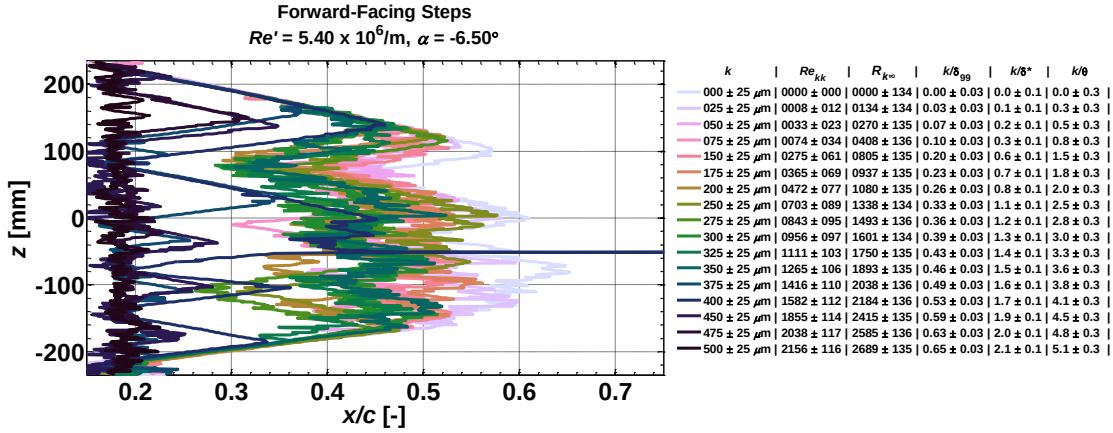

Fig. 142 Appendix: Forward-facing step, Re' = 5.40 x 10^6/m, α = -6.50°

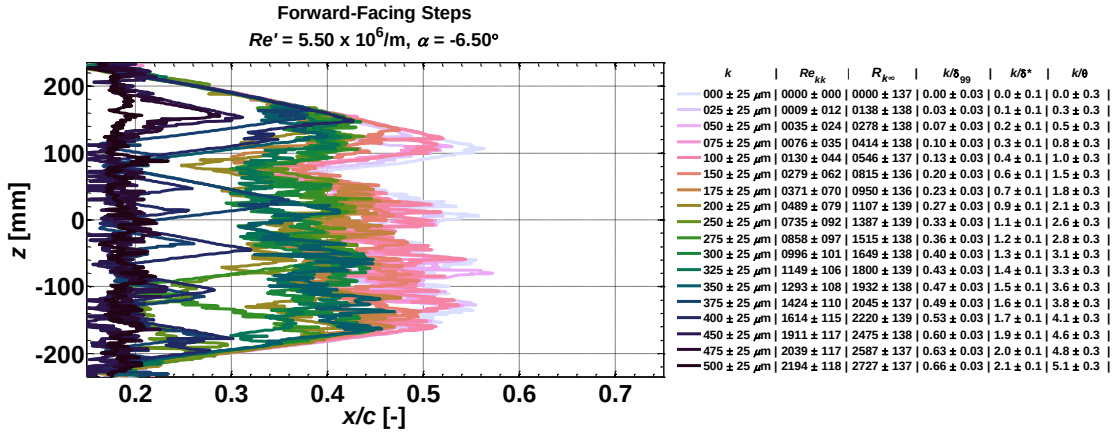

Fig. 143 Appendix: Forward-facing step, Re' = 5.50 x 10^6/m, α = -6.50°

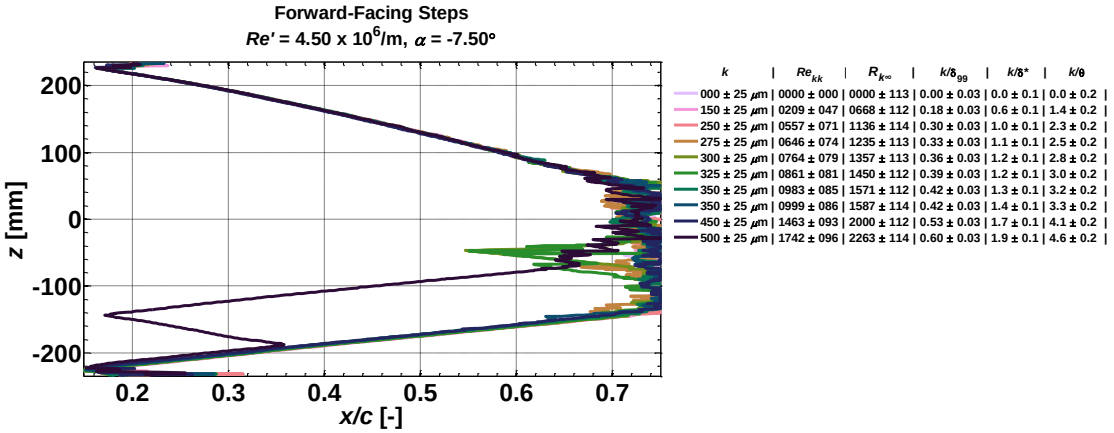

Fig. 144 Appendix: Forward-facing step, *Re´* = 4.50 x 10^6/m, α = -7.50°

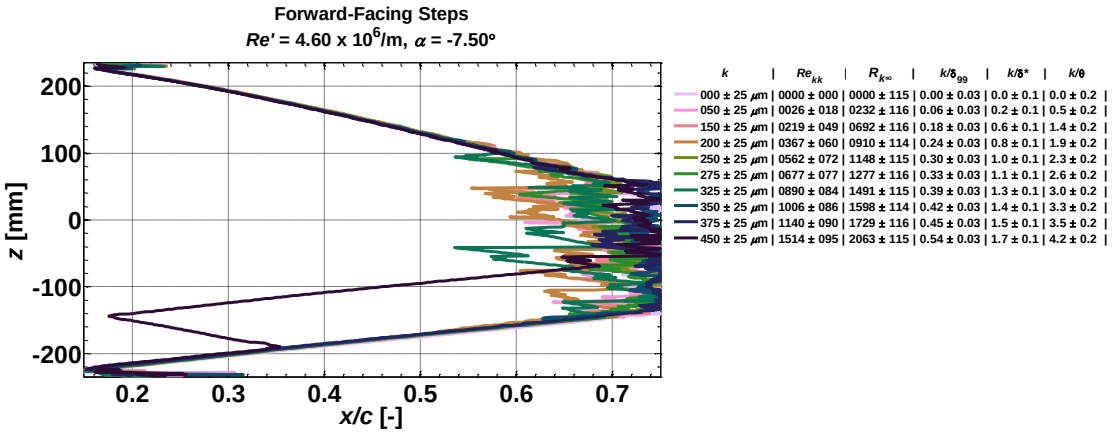

Fig. 145 Appendix: Forward-facing step, *Re´* = 4.60 x 10^6/m, α = -7.50°

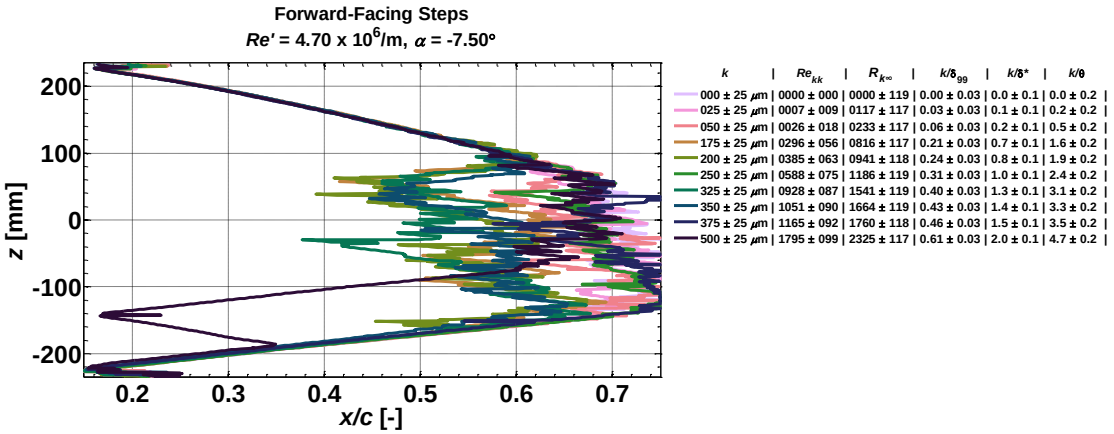

Fig. 146 Appendix: Forward-facing step, *Re´* = 4.70 x 10^6/m, α = -7.50°

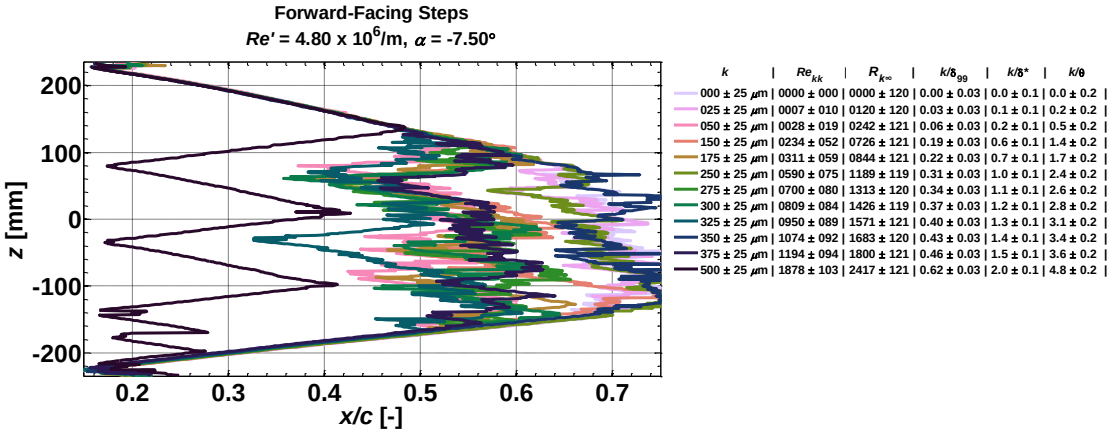

Fig. 147 Appendix: Forward-facing step, *Re´* = 4.80 x 10^6/m, α = -7.50°

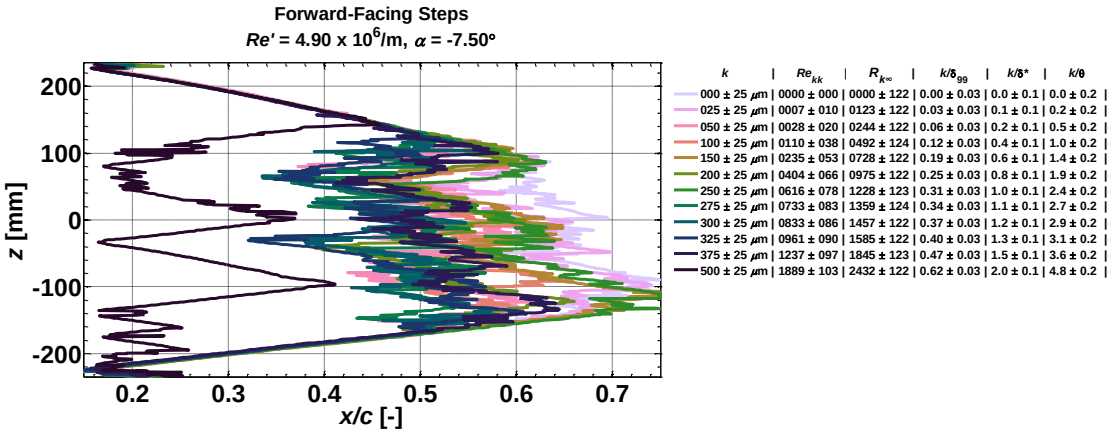

Fig. 148 Appendix: Forward-facing step, *Re´* = 4.90 x 10^6/m, α = -7.50°

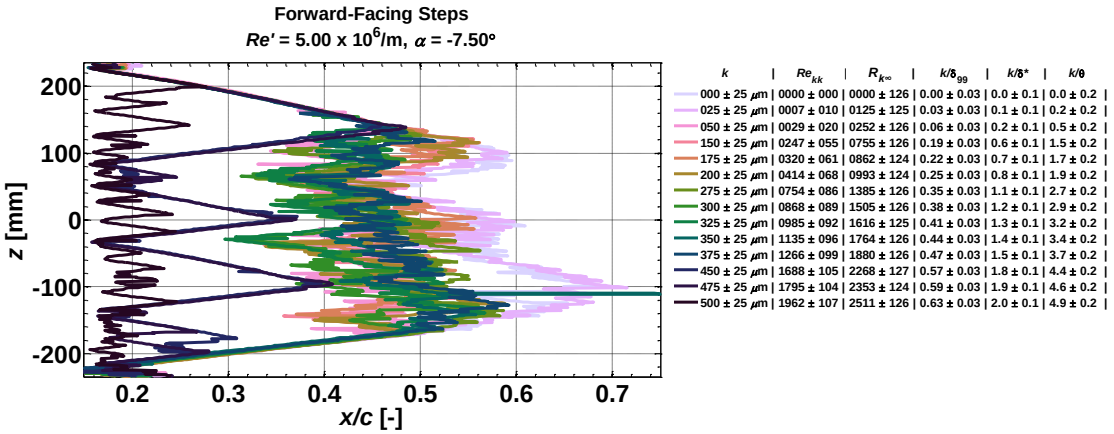

Fig. 149 Appendix: Forward-facing step, *Re´* = 5.00 x 10^6/m, α = -7.50°

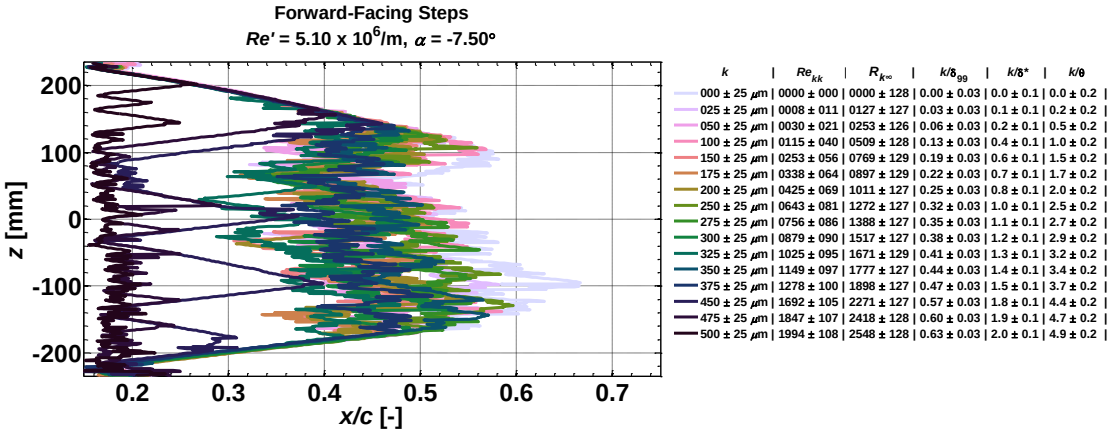

Fig. 150 Appendix: Forward-facing step, *Re´* = 5.10 x 10^6/m, α = -7.50°

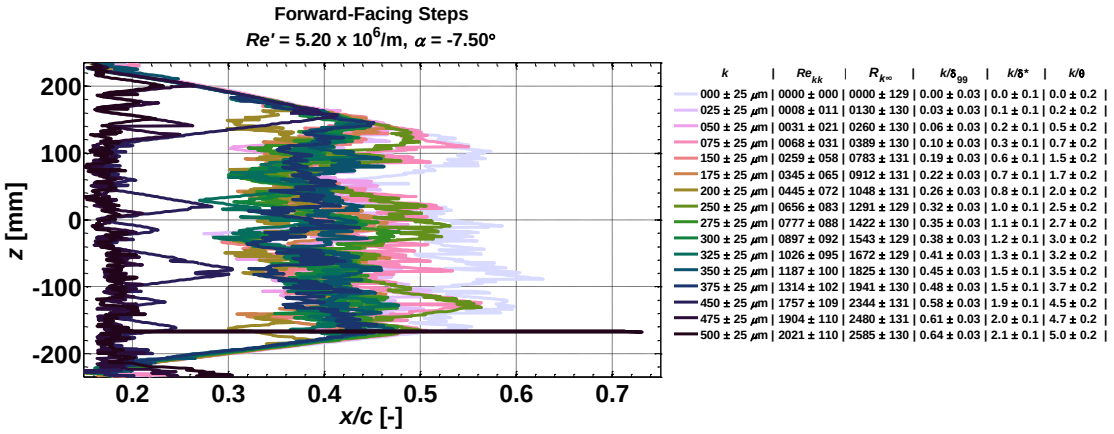

Fig. 151 Appendix: Forward-facing step, *Re´* = 5.20 x 10^6/m, α = -7.50°

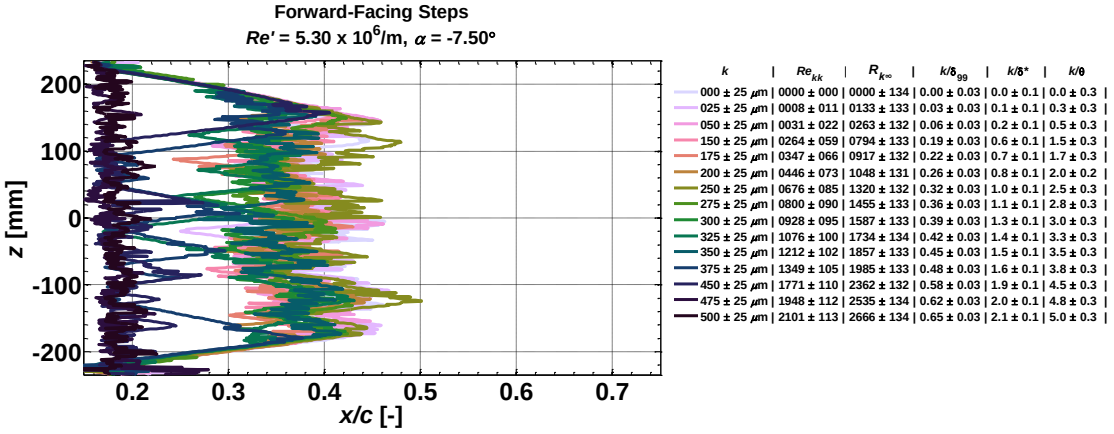

Fig. 152 Appendix: Forward-facing step, *Re´* = 5.30 x 10^6/m, α = -7.50°

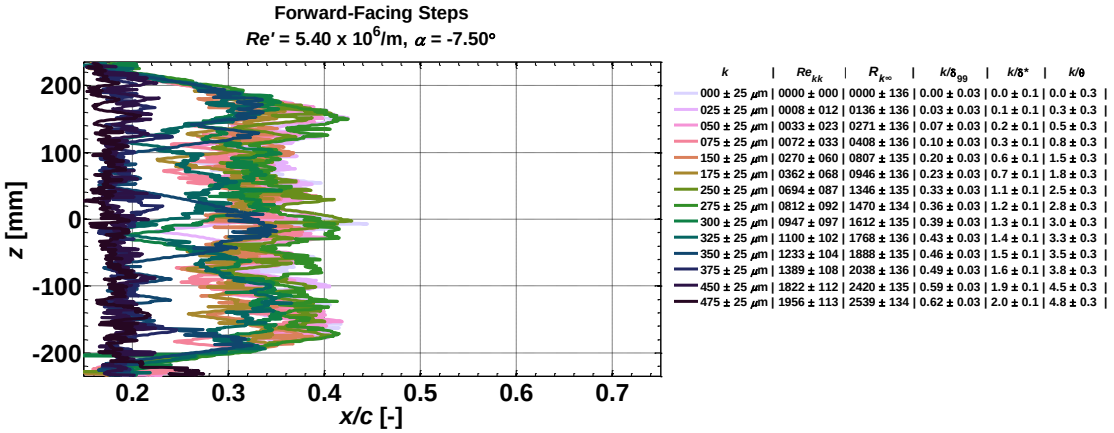

Fig. 153 Appendix: Forward-facing step, *Re´* = 5.40 x 10^6/m, α = -7.50°

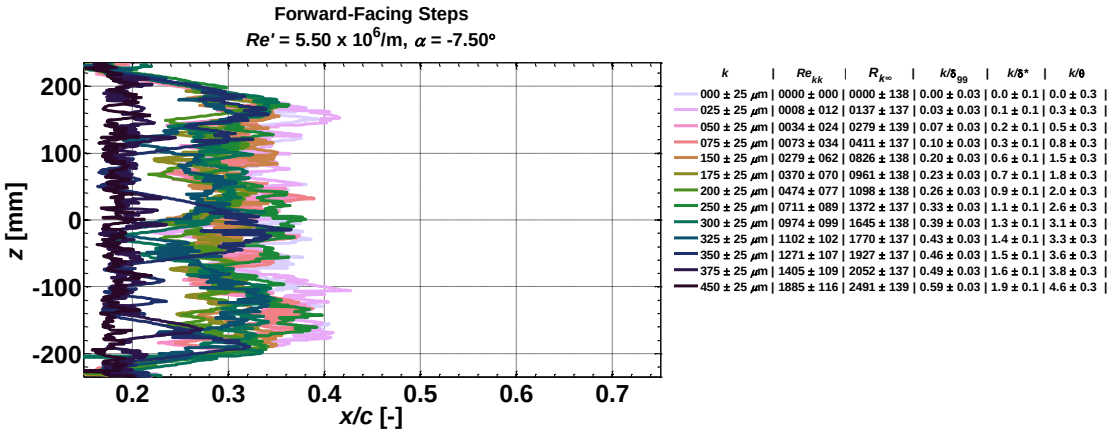

Fig. 154 Appendix: Forward-facing step, *Re´* = 5.50 x 10^6/m, α = -7.50°

APPENDIX G

WIND-TUNNEL HOTWIRE RESULTS

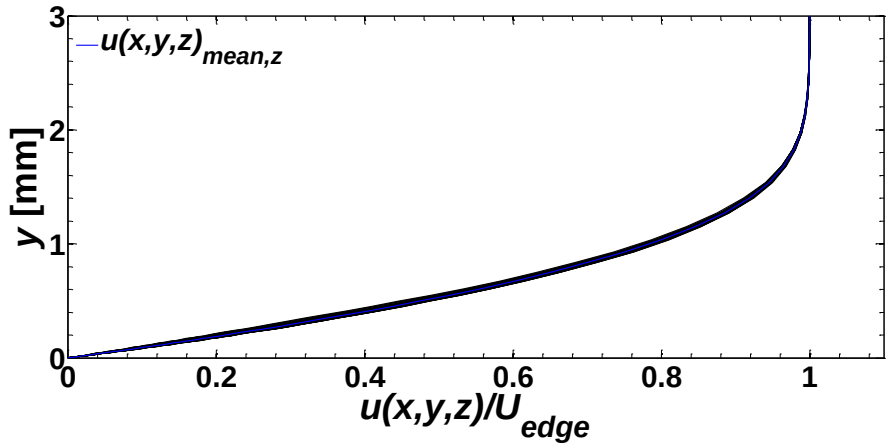

Fig. 155 Appendix: Boundary-layer velocity profiles, k = 0 µm, x/c = 0.18

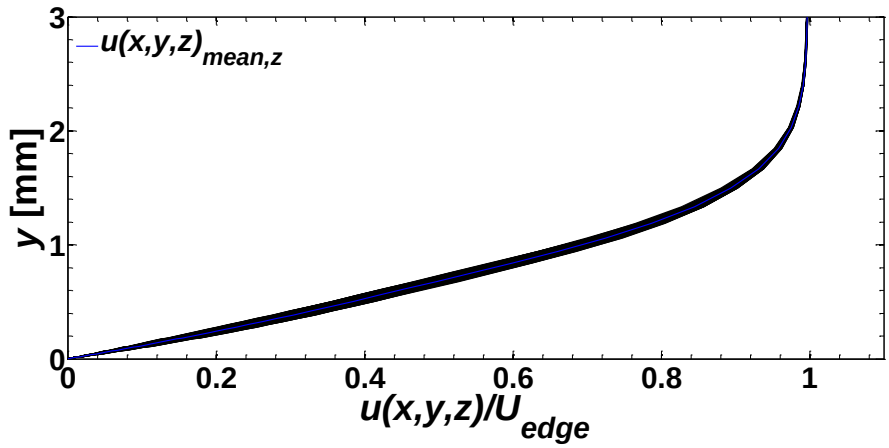

Fig. 156 Appendix: Boundary-layer velocity profiles, k = -1,525 µm, x/c = 0.18

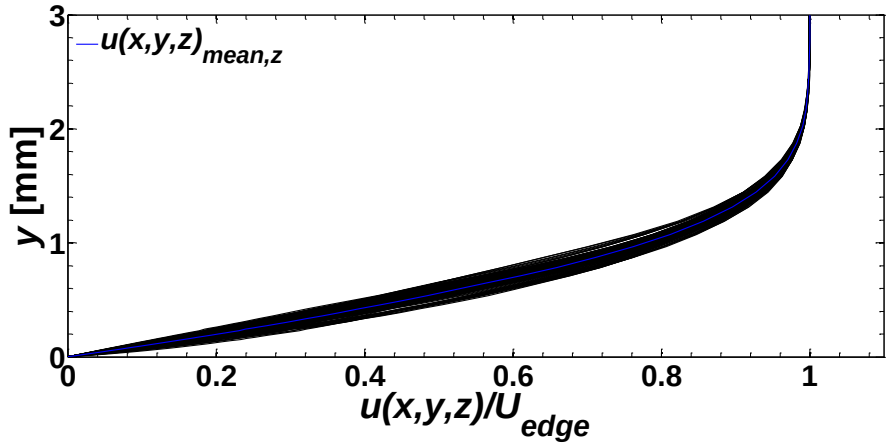

Fig. 157 Appendix: Boundary-layer velocity profiles, k = 1,775 µm, x/c = 0.18

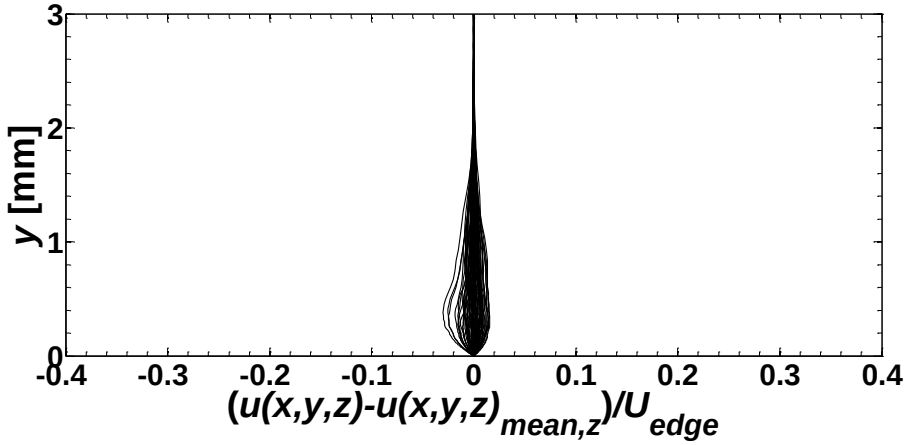

Fig. 158 Appendix: Steady disturbance profiles, k = 0 µm, x/c = 0.18

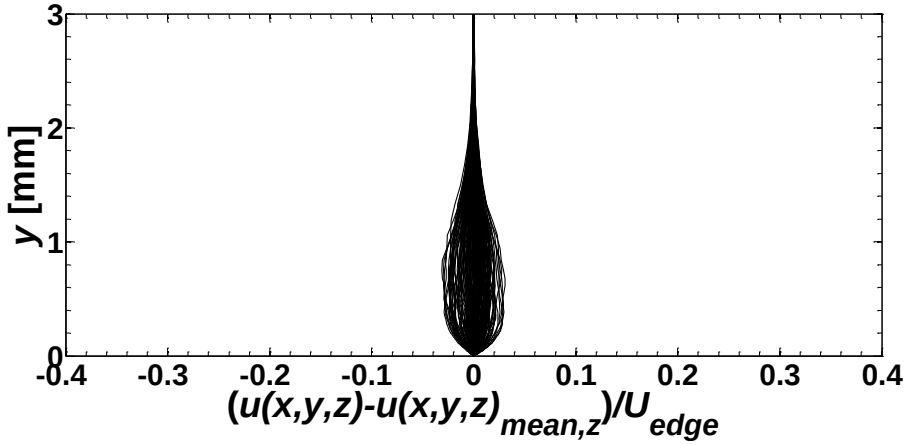

Fig. 159 Appendix: Steady disturbance profiles, k = -1,525 µm, x/c = 0.18

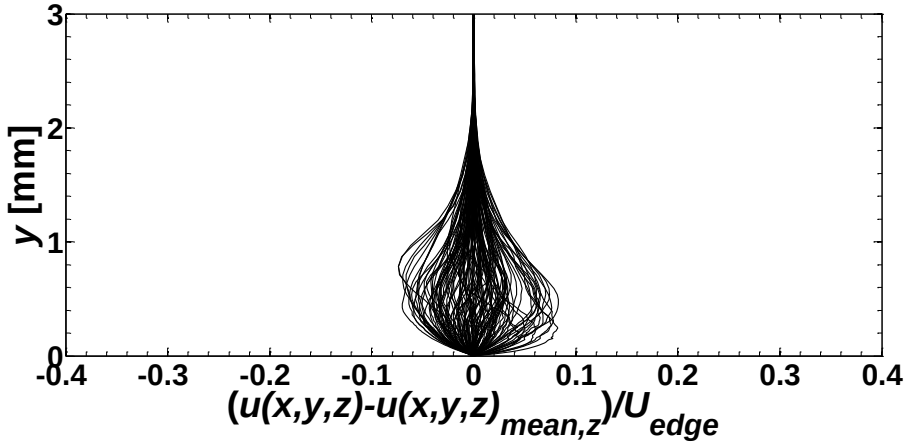

Fig. 160 Appendix: Steady disturbance profiles, k = 1,775 µm, x/c = 0.18

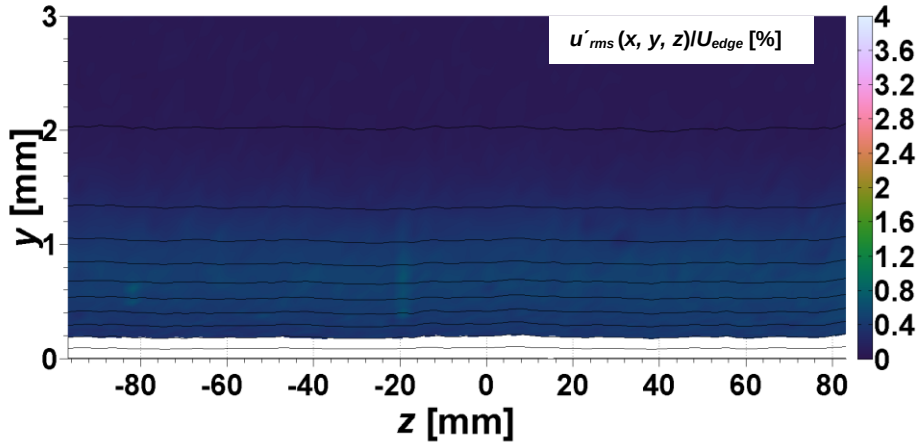

Fig. 161 Appendix: Unsteady velocity contours, k = 0 µm, x/c = 0.18, Δz = 2.5 mm

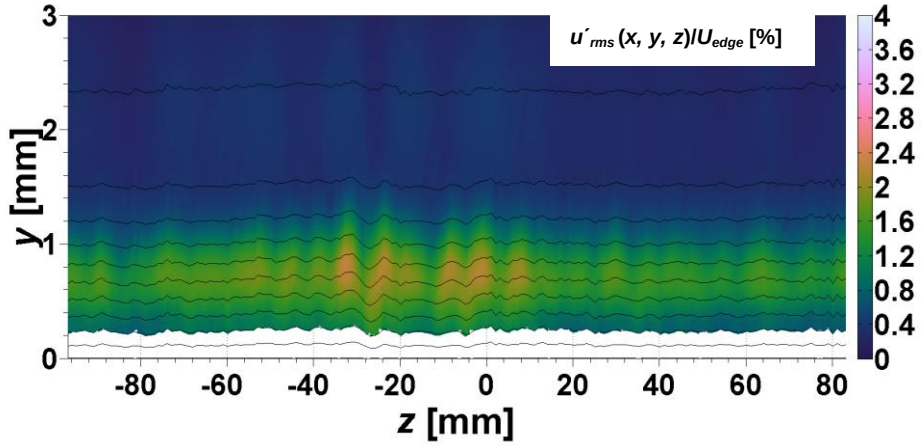

Fig. 162 Appendix: Unsteady velocity contours, k = -1,525 µm, x/c = 0.18, Δz = 1 mm

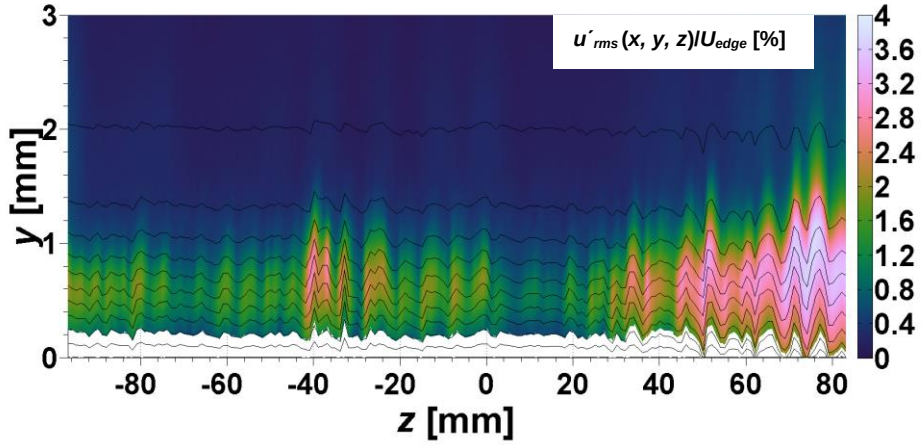

Fig. 163 Appendix: Unsteady velocity contours, k = 1,775 µm, x/c = 0.18, Δz = 1 mm

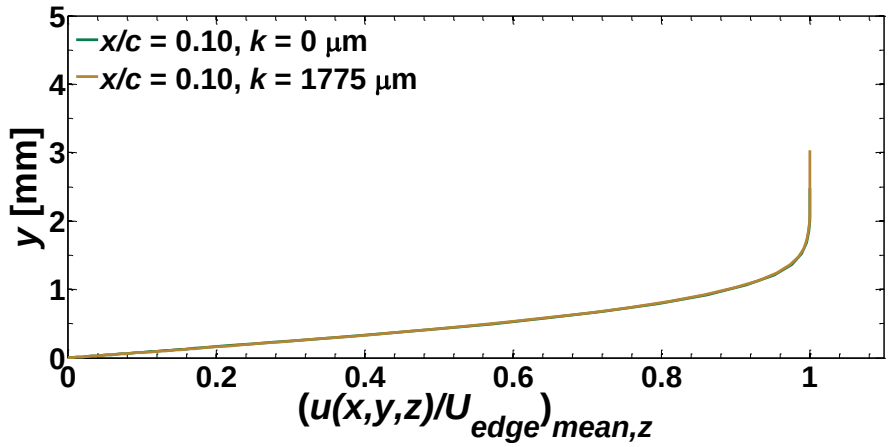

Fig. 164 Appendix: Boundary-layer velocity profiles, *x/c* = 0.10

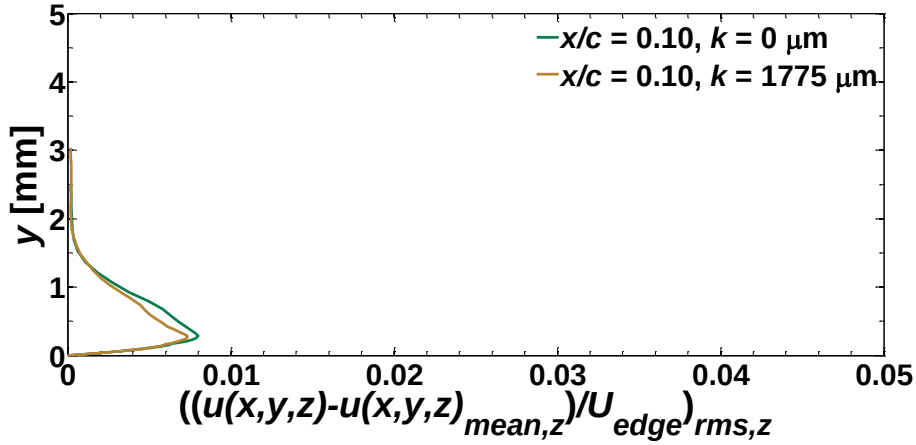

Fig. 165 Appendix: Steady disturbance profiles, *x/c* = 0.10

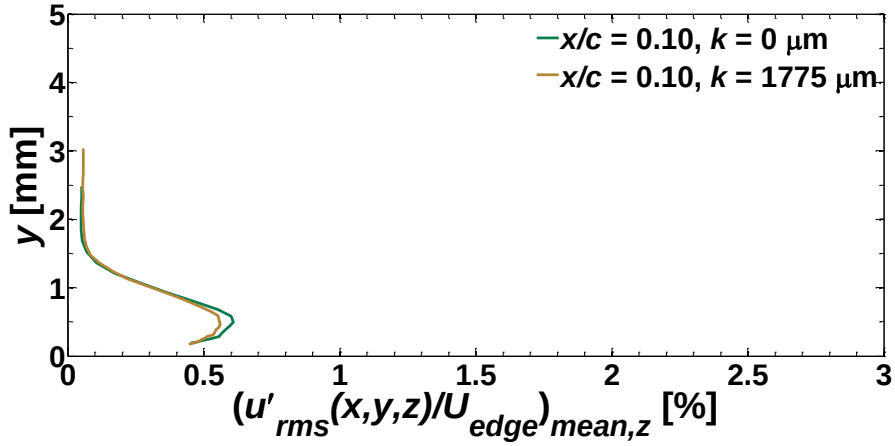

Fig. 166 Appendix: Unsteady disturbance profiles, *x/c* = 0.10

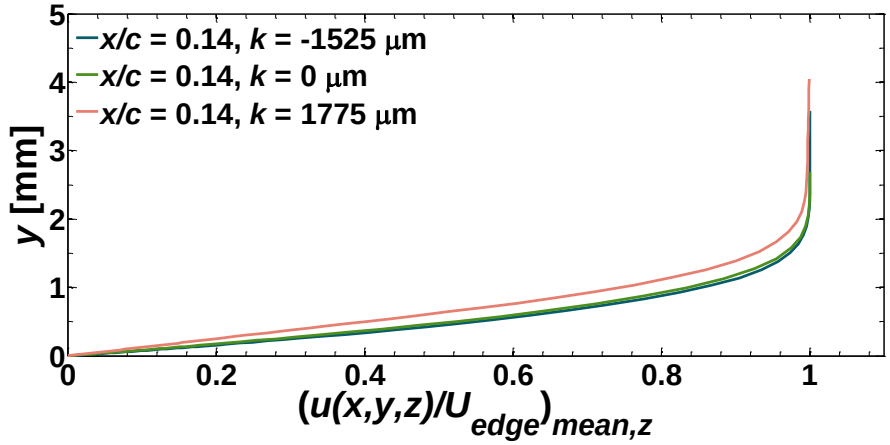

Fig. 167 Appendix: Boundary-layer velocity profiles, *x/c* = 0.14

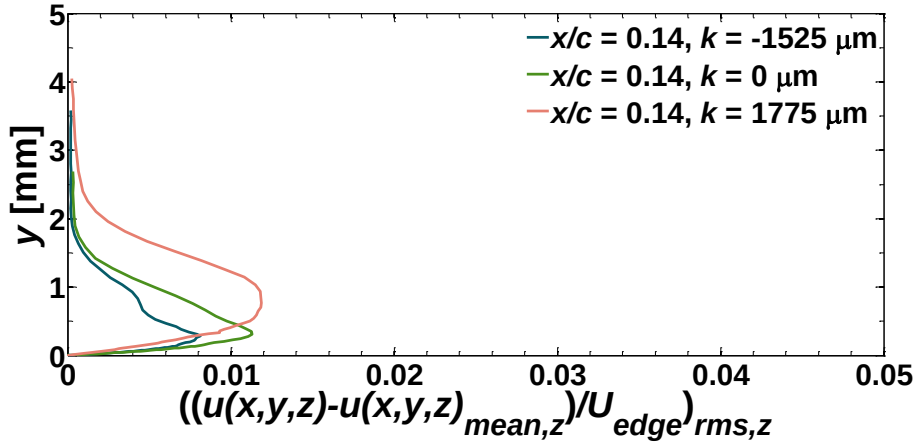

Fig. 168 Appendix: Steady disturbance profiles, *x/c* = 0.14

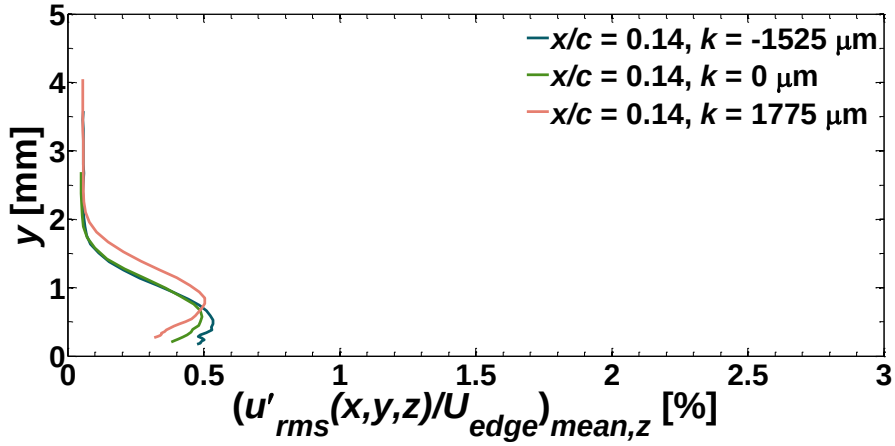

Fig. 169 Appendix: Unsteady disturbance profiles, *x/c* = 0.14

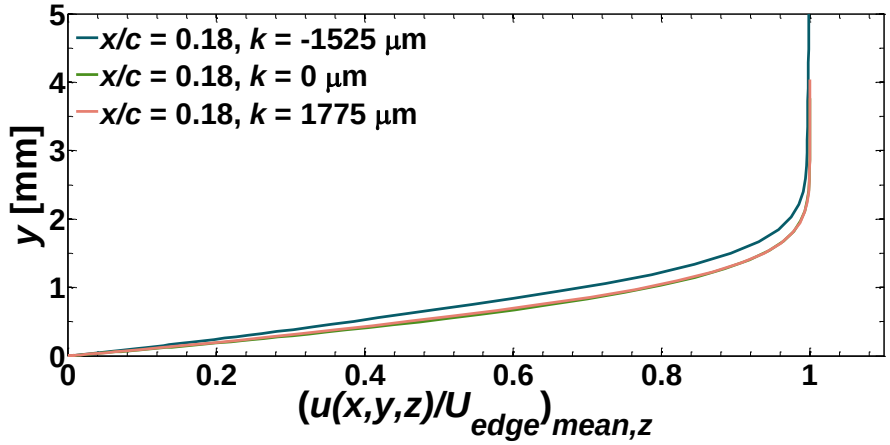

Fig. 170 Appendix: Boundary-layer velocity profiles, *x/c* = 0.18

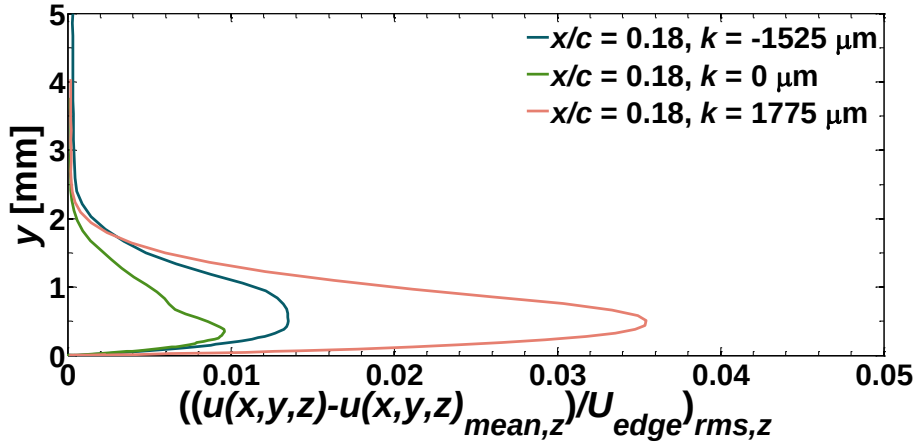

Fig. 171 Appendix: Steady disturbance profiles, *x/c* = 0.18

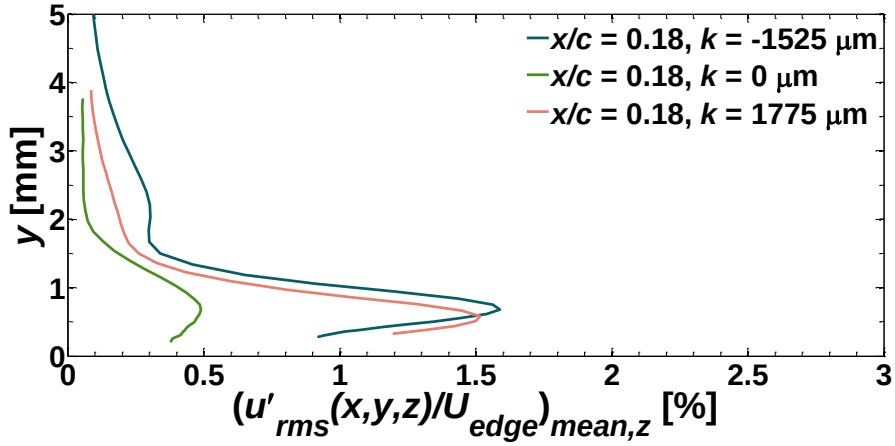

Fig. 172 Appendix: Unsteady disturbance profiles, *x/c* = 0.18

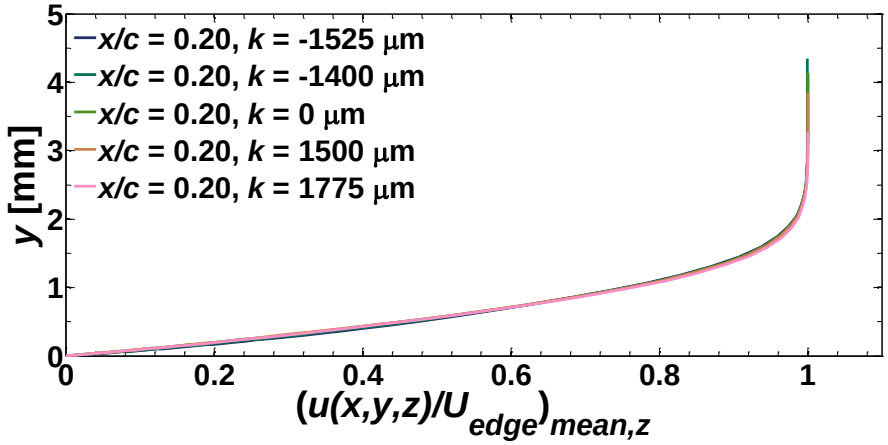

Fig. 173 Appendix: Boundary-layer velocity profiles, *x/c* = 0.20

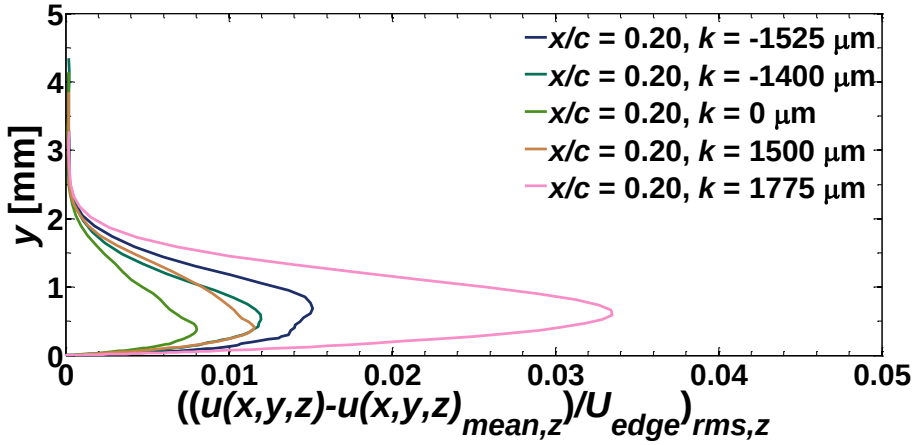

Fig. 174 Appendix: Steady disturbance profiles, *x/c* = 0.20

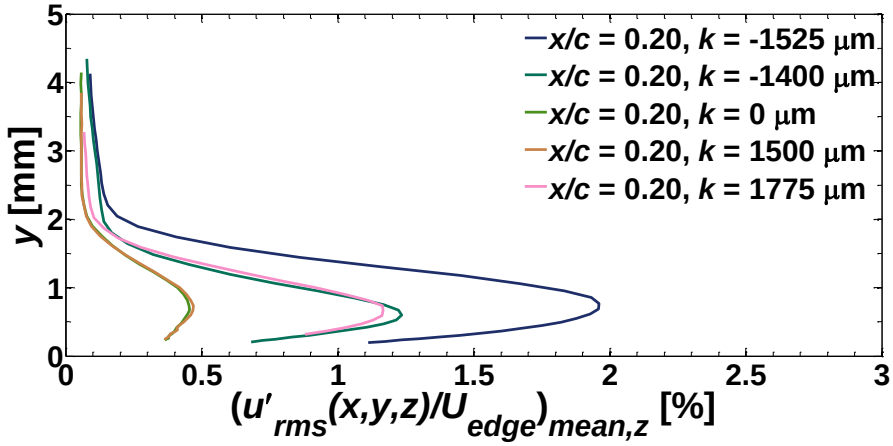

Fig. 175 Appendix: Unsteady disturbance profiles, *x/c* = 0.20